

# 2016

## Accomplishments and Opportunities





## ON THE COVER

The NCNR's neutron source provides a valuable research tool for a wide variety of scientific fields from biological systems, engineering materials, to magnetic structures, and more. The cover features data from only a few of the experiments highlighted in this report.

# 2016 NIST Center for Neutron Research Accomplishments and Opportunities

NIST Special Publication 1208

*Robert M. Dimeo, Director*

*Steven R. Kline, Editor*

December 2016

U.S. Department of Commerce

*Penny Pritzker, Secretary*

National Institute of Standards and Technology

*Willie May, Under Secretary of Commerce for  
Standards and Technology and Director*



## **DISCLAIMER**

Certain commercial entities, equipment, or materials may be identified in this document in order to describe an experimental procedure or concept adequately. Such identification is not intended to imply recommendation or endorsement by the National Institute of Standards and Technology, nor is it intended to imply that the entities, materials, or equipment are necessarily the best available for the purpose. Error bars in figures represent one standard deviation unless otherwise stated.

National Institute of Standards and Technology  
Special Publication 1208, 88 pages  
(December 2016)  
CODEN: NSPUE2

This publication is available free of charge from:  
<https://doi.org/10.6028/NIST.SP.1208>



# Table of Contents

## ii FOREWORD

## 1 THE NIST CENTER FOR NEUTRON RESEARCH

## 2 NIST CENTER FOR NEUTRON RESEARCH INSTRUMENTS

## 4 NCNR IMAGES 2016

## HIGHLIGHTS

## BIOLOGY

- 6 The role of molecular complexity in regulating biophysical processes, E. Kelley, *et al.* (CHRS)
- 8 Neutron reflectometry studies of membrane-bound tubulin reveal an amphipathic helical binding motif, D. Hoogerheide, *et al.*

## CHEMICAL PHYSICS

- 10 Toward increasing the density of hydrogen in the pores of metal-organic frameworks, T. Runčevski, *et al.*
- 12 Critical factors driving the high volumetric uptake of methane in  $\text{Cu}_3(\text{btc})_2$ , Z. Hulvey, *et al.*
- 14 Enhancements in superionic conduction properties in Lithium and Sodium *closo*-dodecaborate salts via substitutional and morphological modifications, T. J. Udovic, *et al.* (CHRS)
- 16  $\text{SiF}_6$ -pillared metal-organic frameworks for highly effective acetylene capture from ethylene, X. Cui, *et al.*
- 18 A novel route to achieving high thermoelectric performance in oxide materials, L. K. Lamontagne, *et al.*

## CONDENSED MATTER

- 20 Realization of ground-state artificial skyrmion lattices at room temperature, D. A. Gilbert, *et al.*
- 22 Combined time-reversal and lattice symmetry breaking in a cubic antiferromagnet  $\text{GdPtBi}$ , T. Suzuki, *et al.*
- 24 Beyond the interface limit: structural and magnetic depth profiles of voltage-controlled magneto-ionic heterostructures, D. A. Gilbert, *et al.*
- 26 The vibrations of methylammonium ions as local probe of ferroelectric ordering in hybrid halide perovskite; a combined neutron scattering and first-principles study, B. Ipek, *et al.*
- 28 Quadrupole order in the frustrated pyrochlore  $\text{Tb}_{2+x}\text{Ti}_{2-x}\text{O}_{7+y}$ , H. Takatsu, *et al.*
- 30 Upward dispersing magnetic resonance mode in superconducting  $\text{Ce}_{1-x}\text{Yb}_x\text{CoIn}_5$ , Y. Song, *et al.* (CHRS)

## ENGINEERING PHYSICS

- 32 Effects of pre-strain and load reversal in shear testing of an interstitial free steel, T. Gnäupel-Herold, *et al.*

## NEUTRON PHYSICS

- 34 Precision measurement of the radiative beta-decay of the free neutron, M. J. Bales, *et al.*

## SOFT MATTER

- 36 Structure, viscoelasticity, and interfacial dynamics of a model polymeric bicontinuous microemulsion, R. J. Hickey, *et al.*
- 38 Tuning dispersion-aggregation transition and wetting-dewetting in polymer nanocomposites, A. Jayaraman, *et al.* (CHRS)
- 40 Gelation transitions of colloidal systems with bridging attractions, G. Yuan, *et al.* (CHRS)
- 42 Connecting polymer-solvent interactions to structural transformations during solvent vapor annealing of block polymer thin films, C. K. Shelton, *et al.* (nSOFT)
- 44 Nano-deformation of sphere-forming thermoplastic elastomers during uniaxial extension, C. R. López-Barrón, *et al.*
- 46 Megasupramolecules, M-H. Wei, *et al.* (CHRS)

## ADVANCES IN MEASUREMENT

- 48 Dielectric RheoSANS for the simultaneous interrogation of rheology, microstructure, and electronic properties of complex fluids, J. J. Richards, *et al.*
- 49 Ultra small-angle neutron scattering with azimuthal asymmetry, X. Gu, *et al.* (CHRS)
- 50 Application of small-angle scattering data to improve biomolecular docking success rate using Rosetta, J. A. Snyder, *et al.*
- 51 A second-generation low-background gamma-ray spectrometer, R. M. Lindstrom
- 52  $\mu\text{RheoSANS}$  for measurement of complex fluids structure at high shear rates, J. Weston, *et al.* (nSOFT)

## 53 NEUTRON SOURCE OPERATIONS

## 55 FACILITY DEVELOPMENT

## 58 SERVING THE SCIENCE AND TECHNOLOGY COMMUNITY

## 61 THE CENTER FOR HIGH RESOLUTION NEUTRON SCATTERING (CHRS)

## 64 2016 AWARDS

## 67 PUBLICATIONS: AUGUST 1, 2015 TO JULY 31, 2016

## 83 INSTRUMENTS AND CONTACTS

## 85 NIST CENTER FOR NEUTRON RESEARCH CONTACTS

# Foreword

I am delighted to present to you this year's annual report for the NIST Center for Neutron Research, containing a selection of the NCNR's accomplishments and opportunities for 2016.

It was a very good year for facility operations: the reactor operated at full power for 265 days with 96.5 % reliability. Both cold sources operated with excellent reliability.

Two major instrument development efforts – vSANS and CANDOR – were the focus of much effort this past year. With major procurements awarded, extensive site preparation complete, and instrument installation well underway, both instruments are scheduled to deliver first neutrons in 2017. The addition of vSANS and CANDOR to the instrument suite will enable new capabilities for users in terms of speed and flexibility of neutron scattering measurements.

New capabilities for users are not just limited to construction of new instruments. Also reported here is a new capability for the simultaneous measurement of dielectric relaxation and rheology while performing small angle neutron scattering measurements. In addition, the new “octo-strain” and shear device tested last year are now in operation on the BT8 engineering diffractometer. Finally, you will read about a new micro-flow SANS capability that is allowing users to obtain macromolecular structure information with SANS for fluids at extremely high flow rates. Developments such as these result from user input, augment our existing measurement capabilities and advance science. We also collaborate with other neutron facilities in



this important aspect of neutron scattering instrumentation. In September, the University of Maryland and the NCNR hosted over 80 attendees for the 9th International Workshop on Sample Environment at Scattering Facilities. This workshop, which was held at Liberty Mountain near Gettysburg, PA, brought together scientists, engineers, and technicians to exchange experience, form collaborations, and discuss new ideas in this essential component to user facility operations.

As ever, the reason for the NCNR is to enable excellent science that comes from the many researchers who use our facility. You will find many exciting research highlights in the pages that follow. I hope that you enjoy reading them as much as I have.

# The NIST Center for Neutron Research

**N**eutrons provide a uniquely effective probe of the structure and dynamics of materials ranging from water moving near the surface of proteins to magnetic domains in memory storage materials. The properties of neutrons (outlined below) can be exploited using a variety of measurement techniques to provide information not otherwise available. The positions of atomic nuclei in crystals, especially of those of light atoms, can be determined precisely. Atomic motion can be directly measured and monitored as a function of temperature or pressure. Neutrons are especially sensitive to hydrogen, so that hydrogen motion can be followed in H-storage materials and water flow in fuel cells can be imaged. Residual stresses such as those deep within oil pipelines or in highway trusses can be mapped. Neutron-based measurements contribute to a broad spectrum of activities including engineering, materials development, polymer dynamics, chemical technology, medicine, and physics.

The NCNR's neutron source provides the intense, conditioned beams of neutrons required for these types of measurements. In addition to the thermal neutron beams from the heavy water moderator, the NCNR has two liquid hydrogen moderators, or cold sources which supply neutrons to three-fourths of the instruments. One is a large area moderator and the other is smaller, but with high brightness.

There are currently 28 experiment stations: 12 are used for neutron physics, analytical chemistry, or imaging, and 16 are beam facilities for neutron scattering research. The subsequent pages provide a schematic description of our instruments. More complete descriptions can be found at [www.ncnr.nist.gov/instruments/](http://www.ncnr.nist.gov/instruments/). Two new cold neutron instruments are under development, including a very small angle neutron scattering instrument (vSANS), and a quasi-white beam neutron reflectometer (CANDOR).

The Center supports important NIST measurement needs, but is also operated as a major national user facility with merit-based access made available to the entire U.S. technological community. Each year, about 2000 research participants from government, industry, and academia from all areas of the country are served by the facility (see pp. 58). Beam time for research to be published in the open literature is without cost to the user, but full operating costs are recovered for proprietary research. Access is gained mainly through a web-based, peer-reviewed proposal system with user time allotted by a beamtime allocation committee twice a year. For details see [www.ncnr.nist.gov/beamtime.html](http://www.ncnr.nist.gov/beamtime.html). The National Science Foundation and NIST co-fund the Center for High Resolution Neutron Scattering (CHRNS) that currently operates five of the world's most advanced instruments (see pp. 61). Time on CHRNS instruments is made available through the proposal system. Some access to beam time for collaborative measurements with the NIST science staff can also be arranged on other instruments.

## Why Neutrons?

Neutrons reveal properties not readily probed by photons or electrons. They are electrically neutral and therefore easily penetrate ordinary matter. They behave like microscopic magnets, propagate as waves, can set particles into motion, losing or gaining energy and momentum in the process, and they can be absorbed with subsequent emission of radiation to uniquely fingerprint chemical elements.

**WAVELENGTHS** – in practice range from  $\approx 0.01$  nm (thermal) to  $\approx 1.5$  nm (cold) ( $1 \text{ nm} = 10 \text{ \AA}$ ), allowing the formation of observable interference patterns when scattered from structures as small as atoms to as large as biological cells.

**ENERGIES** – of millielectronvolts, the same magnitude as atomic motions. Exchanges of energy as small as nano-electronvolts and as large as tenths of electronvolts can be detected between samples and neutrons, allowing motions in folding proteins, melting glasses and diffusing hydrogen to be measured.

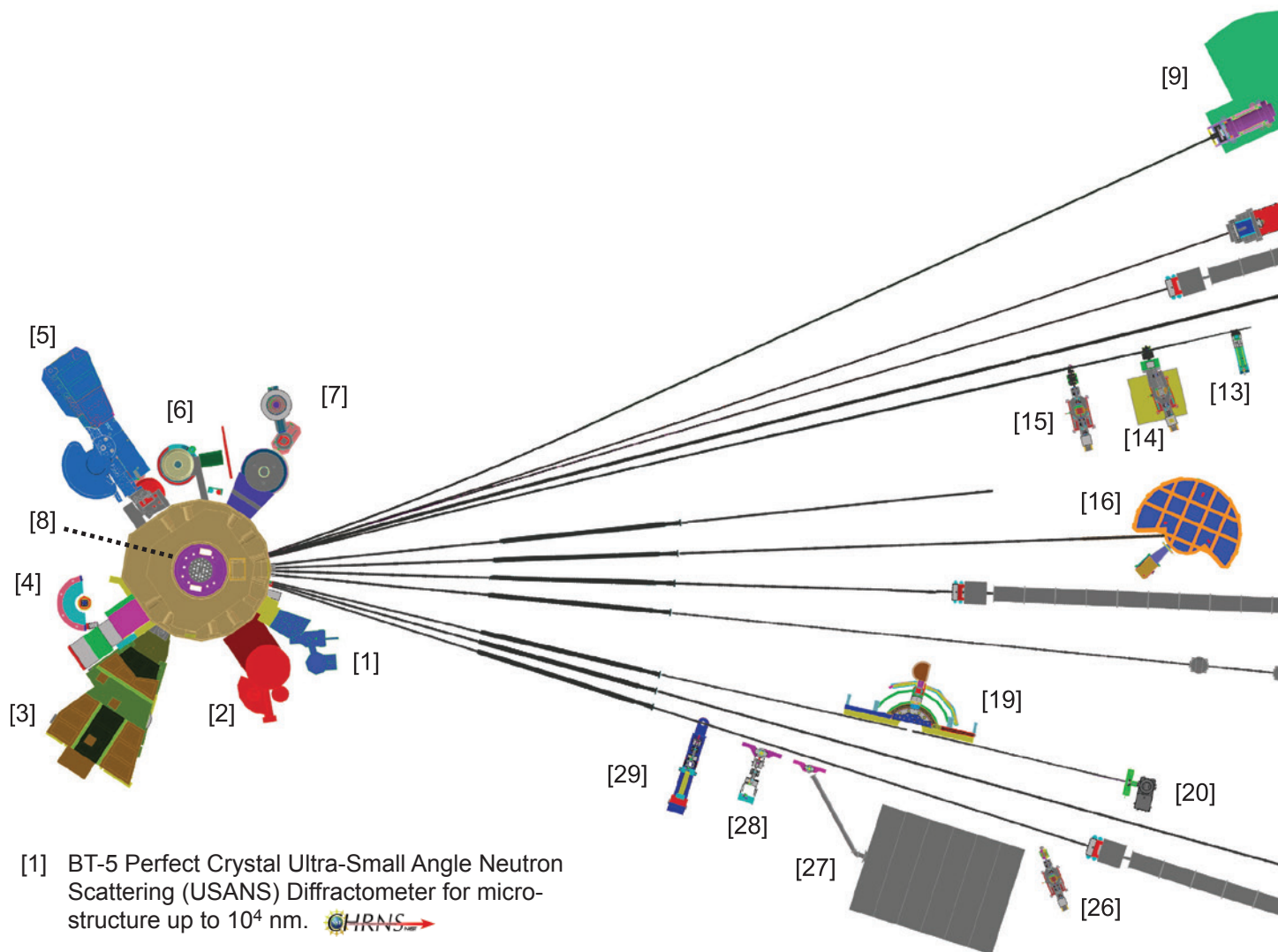
**SELECTIVITY** – in scattering power varies from nucleus to nucleus somewhat randomly. Specific isotopes can stand out from other isotopes of the same kind of atom. Specific light atoms, difficult to observe with X-rays, are revealed by neutrons. Hydrogen, especially, can be distinguished from chemically equivalent deuterium, allowing a variety of powerful contrast techniques.


**MAGNETISM** – makes the neutron sensitive to the magnetic moments of both nuclei and electrons, allowing the structure and behavior of ordinary and exotic magnetic materials to be detailed precisely.

**NEUTRALITY** – of the uncharged neutrons allows them to penetrate deeply without destroying samples, passing through walls that condition a sample's environment, permitting measurements under extreme conditions of temperature and pressure.

**CAPTURE** – characteristic radiation emanating from specific nuclei capturing incident neutrons can be used to identify and quantify minute amounts of elements in samples as diverse as ancient pottery shards and lake water pollutants.

# NIST Center for Neutron Research Instruments *(as of December 2016)*




[1] BT-5 Perfect Crystal Ultra-Small Angle Neutron Scattering (USANS) Diffractometer for micro-structure up to  $10^4$  nm. 

[2] BT-4 Filter Analyzer Neutron Spectrometer with cooled Be/Graphite filter analyzer for chemical spectroscopy and thermal triple axis spectrometer.

[3] BT-2 Neutron Imaging Facility for imaging hydrogenous matter in large components such as water in fuel cells and lubricants in engines, in partnership with General Motors and DOE.


[4] BT-1 Powder Diffractometer with 32 detectors; incident wavelengths of 0.208 nm, 0.154 nm, and 0.159 nm, with resolution up to  $\Delta d/d \cong 8 \times 10^{-4}$ .


[5] BT-9 Multi Axis Crystal Spectrometer (MACS II), a cold neutron spectrometer for ultra high sensitivity access to dynamic correlations in condensed matter on length scales from 0.1 nm to 50 nm and energy scales from 2.2 meV to 20 meV. 

[6] BT-8 Residual Stress Diffractometer optimized for depth profiling of residual stresses in large components.

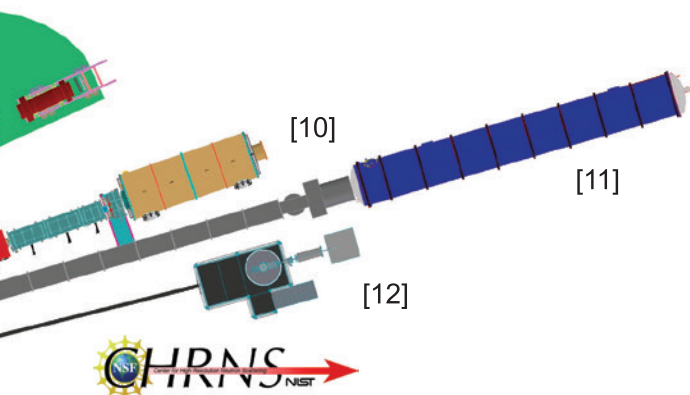
[7] BT-7 Thermal Triple Axis Spectrometer with large double focusing monochromator and interchangeable analyzer/detectors systems.

[8] VT-5 Thermal Neutron Capture Prompt Gamma-ray Activation Analysis Instrument used for quantitative elemental analysis of bulk materials including highly hydrogenous materials ( $\cong 1\%$  H) such as foods, oils, and biological materials.

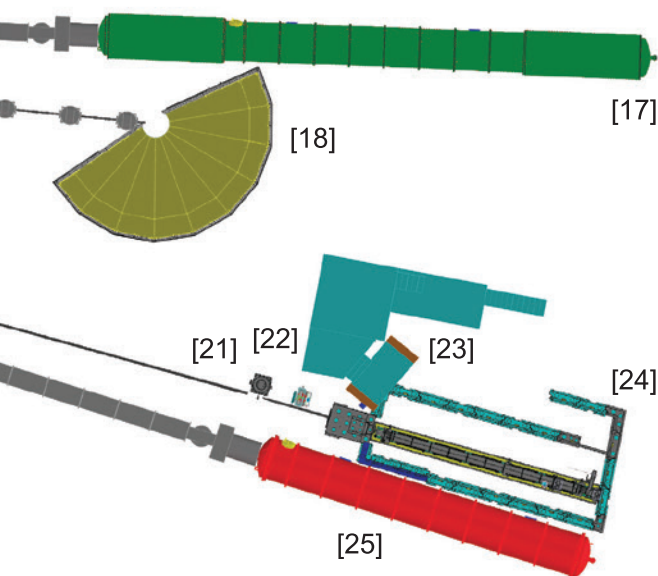
[9] NG-A Neutron Spin-Echo Spectrometer (NSE) for measuring dynamics from 5 ps to 100 ns. 

[10] NG-B 10 m SANS for macromolecular structure measurements. 






The Center for High Resolution Neutron Scattering (CHRS) is a partnership between NIST and the National Science Foundation that develops and operates neutron scattering instrumentation for use by the scientific community. The following instruments are part of the Center: 1 (USANS), 5 (MACS II), 9 (NSE), 11 (NG-B 30m SANS), and 16 (HFBS).



[15] NG-D Polarized Beam Reflectometer (PBR) for measuring reflectivities as low as  $10^{-8}$  to determine subsurface structure.

[16] NG-2 Backscattering Spectrometer (HFBS) high intensity inelastic scattering instrument with energy resolution  $< 1 \mu\text{eV}$ , for studies of motion in molecular and biological systems. 

[17] NG-3 VSANS Single measurement investigation of lengths from 1 nm to 2 micron. (installation in progress)

[18] NG-4 Disk Chopper Time-of-Flight Spectrometer for diffusive motions and low energy dynamics. Wavelengths from  $\approx 0.18 \text{ nm}$  to  $2.0 \text{ nm}$  and energy resolutions from  $\approx 2 \text{ meV}$  to  $< 10 \mu\text{eV}$ .

[19] NG-5 Spin-Polarized Triple Axis Spectrometer (SPINS) using cold neutrons with position sensitive detector capability for high-resolution studies.

[20] NG-5 Cold Neutron Depth Profiling for profiling of subsurface elemental composition.

[21] NG-6 Precision measurement of the magnetic dipole moment of the neutron.

[22] NG-6 Precision measurement of neutron flux.

[23] NG-6 LAND detector development.

[24] NG-6 Cold Neutron Imaging Facility for imaging hydrogenous matter in large components such as water in fuel cells and lubricants in engines.


[25] NG-7 30 m SANS for microstructure measurements, in partnership with ExxonMobil and University of Minnesota's IPrime.

[26] NG-7 PHADES Cold neutron test station.

[27] NG-7 Neutron Interferometry and Optics Station with perfect crystal silicon interferometer. A vibration isolation system provides exceptional phase stability and fringe visibility.

[28] NG-7 Neutron Physics Interferometry Test Bed for quantum information science.

[29] NG-7 Horizontal Sample Reflectometer allows reflectivity measurements of free surfaces, liquid/vapor interfaces, as well as polymer coatings.

[11] NG-B 30 m SANS for microstructure measurements. 

[12] NG-C aCORN Neutron physics station for measurement of the correlation parameter between the electron and anti-neutrino in neutron beta decay.

[13] NG-D Cold neutron capture Prompt Gamma Activation Analysis, for quantitative elemental analysis of bulk materials.

[14] NG-D MAGIK off-specular reflectometer for studies of thin-film samples with in-plane structure.

# NCNR Images 2016



Dusan Sarenac (U. Waterloo, Canada), Wangchun Chen (UMD/NCNR), and Michael Huber (NCNR) discuss their experiment at PHADES.



James Pressley (U. Pennsylvania) gets assistance loading samples from NCNR's Grethe Jensen at NGB-30m SANS.



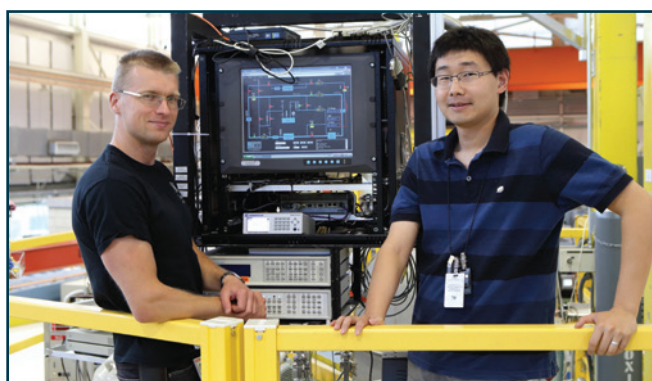
Viacheslav Li (U. Hawaii) is confident that the miniTimeCube neutrino detector is ready to go.



Joshua Graybill and Chandra Shahi (NCNR) at the NG6 Neutron Physics Station, adjusting the electronics for the far UV radiation neutron detector.



NCNR's Craig Brown explains the science at DCS to Montgomery Blair HS students while Ziling (Ben) Xue and Shelby Stavretis (U. Tennessee Knoxville) collect their data.

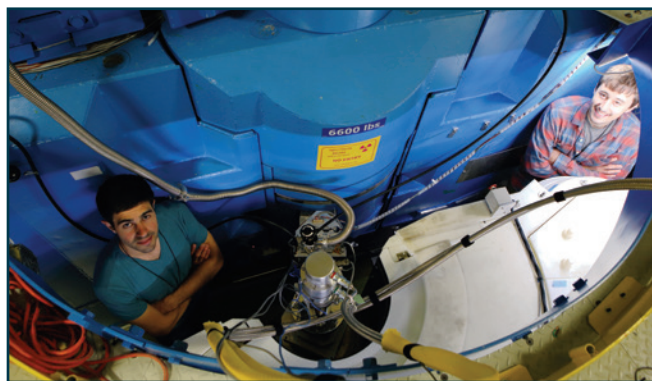


NCNR's Yegor Vekhov and Zhiling Dun (U. Tennessee Knoxville) at DCS, monitoring the dilution refrigerator.





Amber Larson (U. Maryland) collects powder diffraction data from a Hollandite sample at BT1.



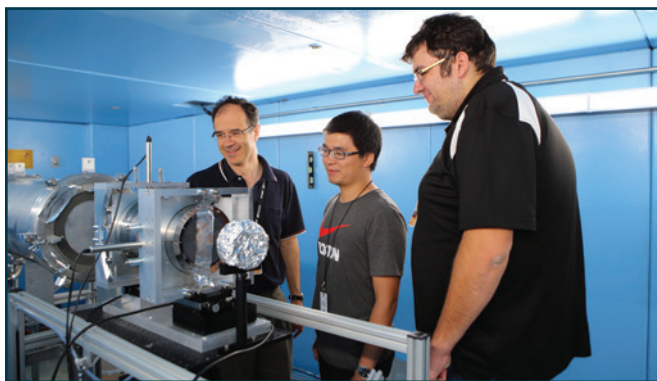
Aryeh Gold-Parker (SLAC National Accelerator Laboratory) and Ian Smith (Stanford University) at MACS preparing to measure phonon dispersion in perovskites.



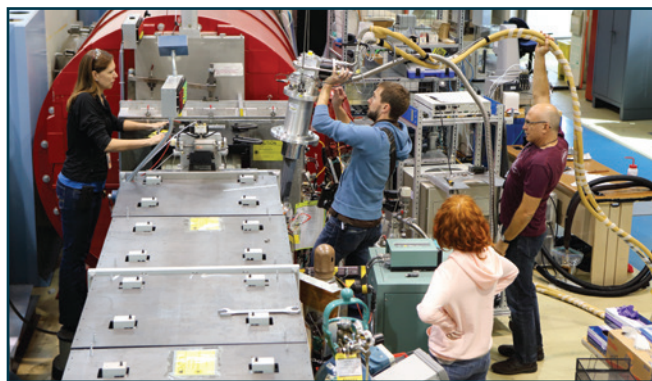
Patrick Corona and Nino Ruocco (UCSB) prepare their hydrogel samples for rheo-SANS experiments at NGB-30m SANS.



Ben Heacock (North Carolina State U.) and Robert Haun (Tulane U.) are measuring the coherent scattering length of  $^4\text{He}$  at the NG7 Neutron Interferometer.



Boris Khaykovich and Huarui Wu from MIT, and Samuel Richardson (NASA summer intern) are characterizing their latest Wolter optics at the NG6 Cold Neutron Imaging Facility.



At NG7 SANS, NCNR's Kathryn Krycka and Jeff Krzywon prepare the CCR for Dario Arena and Corisa Kons (U. South Florida) and their study of interfaces of magnetic materials.

# The role of molecular complexity in regulating biophysical processes

E. G. Kelley,<sup>1</sup> R. Ashkar,<sup>1,2,3</sup> R. Bradbury,<sup>1,4</sup> P. D. Bulter,<sup>1,5</sup> and M. Nagao<sup>1,4</sup>

Once thought to simply be a passive matrix housing the myriad proteins that carry out the cellular functions necessary for life, the lipid membrane is now understood to play a vital role in those activities. Indeed, the lipid membrane fluidity and flexibility govern a host of processes from the very local diffusion of lipids and proteins that facilitate cell signaling and communication to the large scale deformations that allow red blood cells to flow through small capillaries. At the intermediate scale, collective membrane motions involving tens to hundreds of lipids, such as bending and thickness fluctuations, overlap with the nanometer length scale and nanosecond time scales of protein motions necessary for their activity. Moreover, these mesoscale dynamics are governed by the same elastic properties that determine the energy required for large scale membrane deformations necessary for cell functions such as cell growth and division.

While it is clear that membrane dynamics are essential for biological function, the roles of the numerous components and overall membrane composition in tuning its elastic properties are not well understood. To date, the majority of detailed characterization has focused on model membrane systems composed of a single lipid species of interest to link subtle differences in the lipid chemical structure to changes in the membrane structure and dynamics. Here we gradually increase the complexity of the model system and mix lipids with different tail lengths, dimyristoylphosphatidylcholine (DMPC, 14 carbon tails) and distearoylphosphatidylcholine (DSPC, 18 carbon tails), to study the effects of tail length mismatch and begin to tackle the role of molecular complexity, via lipid composition, on the collective lipid dynamics.

Using neutron spin echo spectroscopy (NSE), we measure both the collective bending and thickness fluctuations in our mixed lipids membranes (Fig 1). The NSE decay constants,  $\Gamma$ , for a fluid bilayer composed of an equimolar mixture of DMPC and DSPC are shown in Fig. 2. For a mixture of protiated lipids in  $D_2O$ , the data show a  $q^3$  dependence as predicted for membranes undergoing bending fluctuations, and the slope is then related to the bending modulus,  $\kappa$  [1,2]. The membrane bending modulus,  $\kappa$ , is arguably one of the most important biophysical constants that characterizes

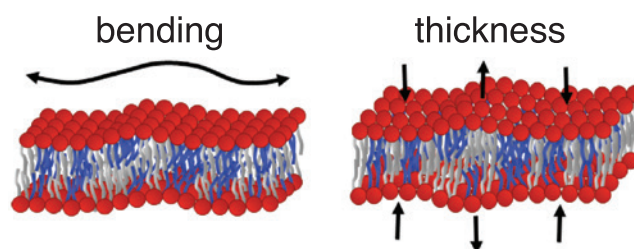


**FIGURE 1:** Illustration of collective bending and thickness fluctuations in lipid membranes.

the stiffness of lipid membranes and the energetic cost of large-scale deformations of the membrane, such as the formation of highly curved structures necessary for endocytosis as cells take in nutrients. Remarkably, our NSE results demonstrate that  $\kappa$  can be tuned by simply mixing lipids with different tail lengths. As seen in Fig. 3a, the mixed lipid bilayers are softer (lower  $\kappa$ ) than either of the pure component membranes.

To experimentally highlight the contribution of thickness fluctuation dynamics in NSE, the lipid tails were contrast matched to the surrounding solvent, emphasizing the collective dynamics of the headgroups. The thickness fluctuations are then seen as a peak in the plot of  $\Gamma$  versus  $q$  (Fig. 2), with the peak width being related to the amplitude of the thickness fluctuations. Once again, we find that the membrane dynamics are highly dependent on the lipid composition, (Fig. 3b) as the amplitude of the fluctuations in each of the pure component membranes are approximately equal, but less than in the mixed lipid bilayers [1,2].

Theoretical and computational studies have suggested that the thickness fluctuation amplitude,  $\sigma_d = \Delta d_t / d_t$  in which  $d_t$  is the thickness of the hydrophobic tail region, is related to another elastic property of the membrane: the area compressibility modulus,  $K_A$ . Assuming that the bilayer volume compressibility is much smaller than the area compressibility (i.e.  $\Delta V/V \ll \Delta A/A$ ) the amplitude is given by  $\sigma_d^2 = k_b T / K_A A_0$  [3]. In this expression,  $k_b$  is the Boltzmann constant,  $T$  is the temperature, and  $A_0$  is the area per lipid headgroup. In other words, the amplitude will be large when  $K_A$  is low and it is easier to compress the membrane laterally.

<sup>1</sup> NIST Center for Neutron Research, National Institute of Standards and Technology, Gaithersburg, MD 20899

<sup>2</sup> University of Maryland, College Park, MD 20742

<sup>3</sup> Oak Ridge National Laboratory, Oak Ridge, TN 37831

<sup>4</sup> Indiana University, Bloomington, IN 47498

<sup>5</sup> University of Delaware, Newark, DE 19716



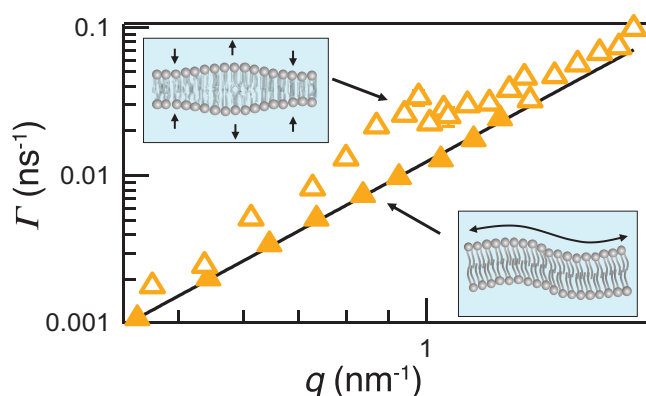


**FIGURE 2:** The  $q$ -dependence of the NSE decay constant,  $\Gamma$ , for fluid lipid bilayers containing a mole fraction of 50 % long-tail DSPC lipid. The solid line shows a  $q^3$  dependence and the insets illustrate the contrast conditions used to measure the bending and thickness fluctuations.

Importantly,  $K_A$  is also directly related to the bending modulus,  $\kappa$ , through the well-established expression:  $\kappa \propto d_t^2 K_A$ , [4]. This relationship implies that the membrane will be softer and easier to bend when  $K_A$  is low.

Therefore, the enhanced dynamics in the mixed lipid bilayers seen as a reduction in  $\kappa$  and increase in  $\sigma_d$  are most likely due to a reduction in  $K_A$  upon mixing lipids with different acyl chain lengths. These results suggest that the hydrophobic mismatch between the different tail lengths leads to less efficient lipid packing and increases the area per molecule compared to a single component bilayer, allowing the mixed bilayers to stretch and compress more easily in the lateral direction and ultimately making the membrane more dynamic.

Thus, using the unique ability of NSE to measure both the bending and thickness fluctuations, we were able to explicitly relate an enhancement in the dynamics to a reduction in the area expansion modulus and ultimately differences in the membrane structure upon mixing lipids with different acyl chain lengths. These results highlight the importance of lipid composition in tailoring the membrane properties with important implications for understanding the role of lipid diversity in tuning cell functions. Indeed, a single membrane may contain thousands of different lipid molecules, varying in hydrophilic headgroup structure, charge, glycosylation and hydrophobic tail length, number, saturation and asymmetry, with more than 40,000 chemically distinct lipid molecules identified to date [5].

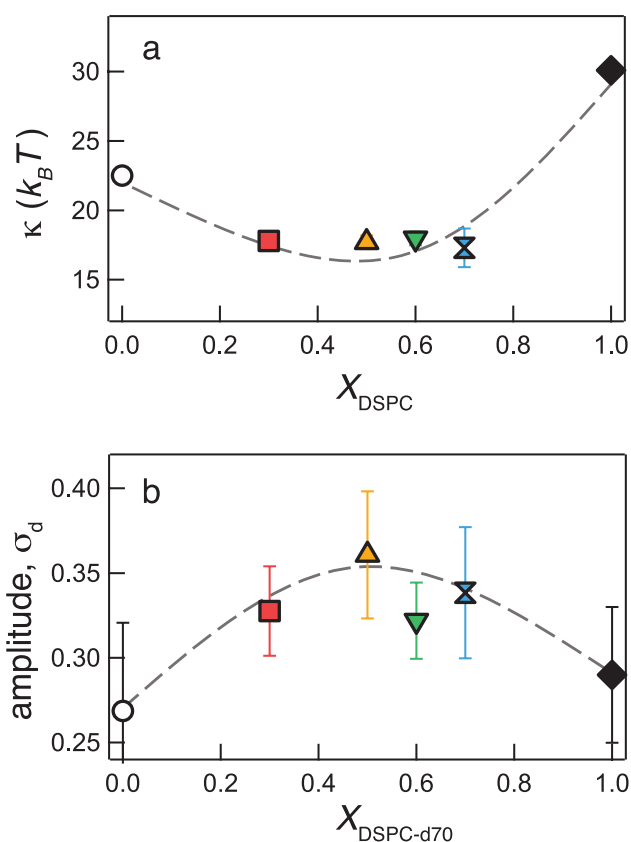


**FIGURE 3:** Mixed lipid membrane (a) bending modulus and (b) thickness fluctuation amplitude as a function of mole fraction of long-tail DSPC lipid. The dashed lines are added to guide the eye.

## References

- [1] A. C. Woodka, P. D. Butler, L. Porcar, B. Farago, M. Nagao, *Phys. Rev. Lett.* **109**, 058102 (2012).
- [2] R. Ashkar, M. Nagao, P. D. Bulter, A. C. Woodka, M. K. Sen, T. Koga, *Biophys. J.* **109** (1), 106 (2015).
- [3] E. Lindahl, O. Edholm, *Biophys. J.* **79** (1), 426 (2000).
- [4] D. Boal, *Mechanics of the Cell*, Cambridge University Press, 2nd edn., 267 (2012).
- [5] LIPID MAPS Structure database (LMSD), [www.lipidmaps.org/data/structure](http://www.lipidmaps.org/data/structure)

# Neutron reflectometry studies of membrane-bound tubulin reveal an amphipathic helical binding motif

D. P. Hoogerheide,<sup>1</sup> S. Yu. Noskov,<sup>2</sup> D. Jacobs,<sup>3</sup> L. Bergdoll,<sup>4</sup> V. Silin,<sup>5</sup> D. Worcester,<sup>1</sup> J. Abramson,<sup>4,6</sup> H. Nanda,<sup>1,7</sup> T. K. Rostovtseva,<sup>3</sup> and S. M. Bezrukov<sup>3</sup>

**B**ilayer lipid membranes (BLMs) form barriers that separate the interior from the exterior of the cell and divide the cell into specialized compartments called organelles. Proteins that are embedded into BLMs, known as membrane proteins, play diverse roles, including the transportation of various ions, metabolites, proteins, DNA, etc., across the BLMs, thus providing communication pathways between cells and between organelles inside cells. This function is so crucial for health and disease that while membrane proteins account for about 20 % of known proteins [1], they comprise 70 % of known drug targets [2]. In humans, mitochondria are the organelles responsible for energy conversion, with two main purposes: to store energy, and to produce heat that maintains body temperature. However, mitochondria themselves are also the sources of the reactive oxygen species that damage mitochondria, mitochondrial DNA, and other cellular components. Therefore, maintaining the appropriate conditions that provide sufficient energy for cellular functions and limit the production of chemically damaging reactive oxygen species is crucial for cell life and death. Recent evidence indicates that the regulation of this equilibrium is accomplished at least in part by a complex of the mitochondrial voltage-dependent anion channel (VDAC), a passive transport channel of the mitochondrial outer membrane (MOM), and dimeric tubulin [3], which is best known as a structural protein in microtubules. The association of tubulin with the MOM is particularly suggestive given the role of microtubule-targeting drugs (MTDs) in chemotherapy [4]. In this work we shed light on the role of dimeric tubulin in regulating mitochondrial bioenergetics by investigating the binding of tubulin to biomimetic mitochondrial membranes using a combination of neutron reflectometry (NR) and molecular dynamics (MD) simulations [5].

Tubulin is a heterodimer comprising  $\alpha$  and  $\beta$  subunits, which have similar spatial arrangements but different amino acid sequences. In microtubules, the exposed end is always the  $\beta$  subunit; as a result, all MTDs bind to the  $\beta$  subunit [4]. Remarkably, in an *in vitro* system the rate of interaction between tubulin and a single VDAC channel was observed to depend strongly on the lipid composition of the BLM in which VDAC was embedded. In particular, the interaction rate increased by two orders of magnitude if a lamellar (i.e. preferring a flat membrane geometry) dioleoylphosphatidylcholine

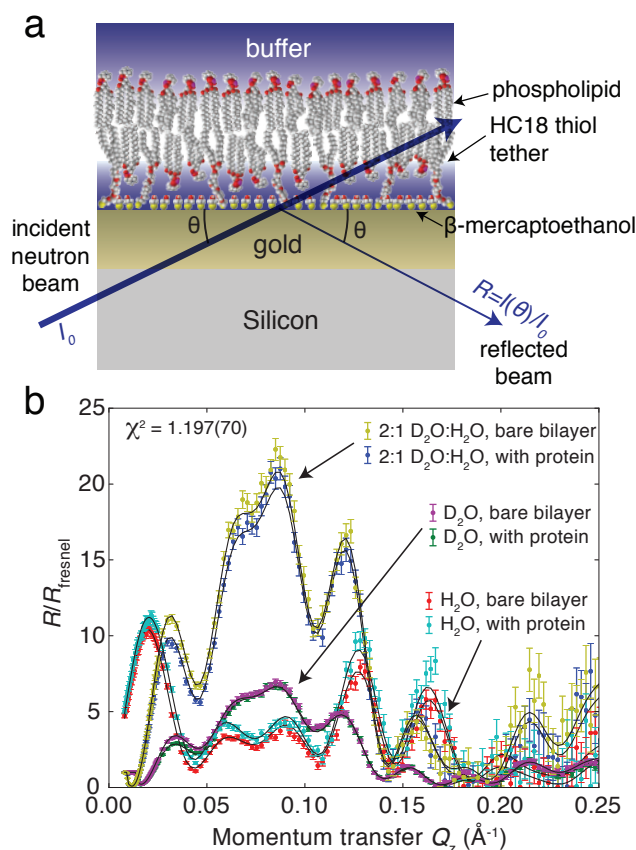


**FIGURE 1:** Neutron reflectometry (NR) experiment with a sparsely tethered lipid bilayer membrane (stBLM). (a) Schematic of the stBLM and scattering geometry. Sparse tethering is achieved by using  $\beta$ -mercaptoethanol as a spacer molecule. (b) NR data, showing the differences between the three deuteration levels of the buffer solutions. Data are normalized to the Fresnel reflectivity expected from a silicon/buffer interface. Solid lines show the fit to a theoretical model of the bilayer with bound tubulin.

(DOPC) membrane was replaced with the non-lamellar (preferring a curved membrane geometry) dioleoylphosphatidylethanolamine (DOPE) [6], suggesting that tubulin is able to distinguish between these two lipid species. Furthermore, these results indicate that the first step of the VDAC-tubulin interaction involves tubulin binding to the lipid membrane surface.

<sup>1</sup> NIST Center for Neutron Research, National Institute of Standards and Technology, Gaithersburg, MD 20899

<sup>2</sup> University of Calgary, Calgary, AB, Canada, T2N 1N4

<sup>3</sup> Eunice Kennedy Shriver National Institute of Child Health and Human Development, National Institutes of Health, Bethesda, MD 20892

<sup>4</sup> University of California Los Angeles, Los Angeles, CA 90095

<sup>5</sup> University of Maryland, Rockville, MD 20850

<sup>6</sup> Institute for Stem Cell Biology and Regenerative Medicine, National Centre for Biological Sciences–Tata Institute of Fundamental Research, Bellary Road, Bangalore-560065, Karnataka, India

<sup>7</sup> Carnegie Mellon University, Pittsburgh, PA 15213

In this study, we determined the orientation of membrane-bound tubulin—and hence the face of the tubulin molecule that is in contact with the membrane surface—by NR on sparsely tethered BLMs (stBLMs). NR reports on the depth profile of the interfacial components, including the stBLM and any membrane-bound tubulin (Figure 1a). Thus, NR is well suited to determine the spatial extent of the protein in and away from the BLM and yields a potential family of binding surfaces to be investigated by computational methods and amino acid sequence analysis.

For these experiments, an stBLM was composed of a 1:1 molar ratio of DOPC:DOPE. This lipid composition closely mimics the mitochondrial outer membrane, in which the ratio of PC to PE headgroups is about 3:2. The stBLM was bathed in an aqueous 1 mol/L KCl solution buffered at pH 7.4 by 5 mM HEPES. The reflectivity of the stBLM was measured using 4.75 Å neutrons on the NCNR NG7 horizontal reflectometer. To provide contrast between the various components of the stBLM system, a sequence of reflectometry measurements was performed using buffers in 100 % D<sub>2</sub>O, 100 % H<sub>2</sub>O, and a 2:1 D<sub>2</sub>O:H<sub>2</sub>O mixture. This procedure was then repeated in the presence of 600 nM tubulin dimers (a physiologically relevant concentration).

The reflectivity data (Figure 1b) were then fit to an stBLM model (Figure 2a). Because it accounts for known molecular volumes, molecular connectivity, and stoichiometric constraints, the model is highly constrained. To determine the orientation of the tubulin dimer on the lipid substrate, the expected scattering profile was calculated for various Euler rotations of the known X-ray crystal structure of tubulin. Due to the elongated geometry of the tubulin dimer, the NR profile is very sensitive to the tilt angle  $\beta$  (Figure 2b), allowing a precise determination of this tilt angle,  $\approx 60^\circ$ , from the optimization of the experimental NR data to the stBLM/tubulin model.

To complement the NR results, molecular dynamics simulations were performed to confirm the orientation of  $\alpha$ -tubulin on a DOPE membrane. A range of possible orientations were evaluated using a coarse-grained model of the protein; likely orientations were then optimized using atomistic simulations. The tilt angle of the tubulin on the membrane surface is consistent with that observed by NR, while the atomistic nature of the simulations allows us to identify the particular domain of the tubulin protein that is responsible for binding to the membrane surface. A comparison of the MD and NR results is shown in Figure 2b.

The binding sequence is shown in green in Figure 2b. Notably, it is on the  $\alpha$ -tubulin subunit, rather than on the  $\beta$ -tubulin subunit which is conventionally targeted by chemotherapeutics. When associated with the membrane, this amino acid sequence likely adopts an  $\alpha$ -helical structure which has opposing hydrophobic and hydrophilic faces, i.e. an amphipathic helix. Such helices are oriented at the interface between the polar lipid headgroups and the hydrophobic lipid tails. We have also shown [5] that the affinity of this helix to the mixed PC/PE membranes considered here depends strongly on the amount of PE lipid. This suggests that the lipid composition of the mitochondrial outer membrane could regulate tubulin binding, which in turn modulates VDAC permeability and consequently mitochondrial function. We hypothesize that this selectivity for the uncharged PE lipids may have developed to overcome electrostatic

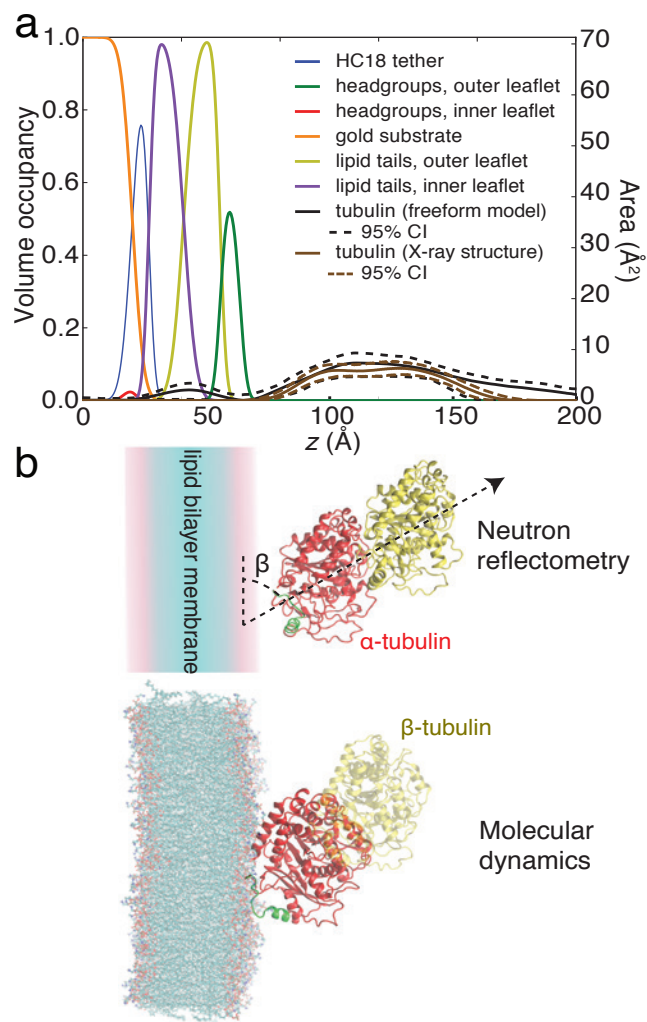


**FIGURE 2:** Results of modeling the tubulin-stBLM system. (a) Volume occupancy representation showing the position of various chemical species. (b) Visual representation of the structure of membrane-bound tubulin as determined by NR (top) and atomistic molecular dynamics simulations of the  $\alpha$ -tubulin subunit (bottom). The Euler angle  $\beta$  is  $\approx 60^\circ$ . The  $\alpha$ -tubulin subunit is shown in red; the  $\beta$ -tubulin subunit in yellow; and the binding site in green.

repulsion between the negatively charged components of the mitochondrial outer membrane and the tubulin molecule.

## References

- [1] M. S. Almen, K. J. Nordstrom, R. Fredriksson, and H. B. Schioth, *BMC Biology* **7**, 50 (2009).
- [2] M. A. Yildirim, K.-I. Goh, M. E. Cusick, A.-L. Barabasi, and M. Vidal, *Nat. Biotechnol.* **25**, 1119 (2007).
- [3] T. K. Rostovtseva, K. L. Sheldon, E. Hassanzadeh, C. Monge, V. Saks, S. M. Bezrukov, and D. L. Sackett, *Proc. Natl. Acad. Sci.* **105**, 18746 (2008).
- [4] J. J. Field, A. B. Waight, and P. D. Senter, *Proc. Natl. Acad. Sci.* **111**, 13684 (2014).
- [5] D. P. Hoogerheide, S. Y. Noskov, D. Jacobs, L. Bergdoll, V. Silin, D. Worcester, J. Abramson, H. Nanda, T. K. Rostovtseva, and S. M. Bezrukov, *Nat. Struct. Mol. Biol.*, submitted (2016).
- [6] T. K. Rostovtseva, P. A. Gurnev, M. Y. Chen, and S. M. Bezrukov, *J. Biol. Chem.* **287**, 29589 (2012).



# Toward increasing the density of hydrogen in the pores of metal-organic frameworks

T. Runčevski,<sup>1,2</sup> M. T. Kapelewski,<sup>1,2</sup> R. M. Torres-Gavosto,<sup>1,2</sup> J. D. Tarver,<sup>3,4</sup> C. M. Brown,<sup>3,5</sup> J. R. Long<sup>1,2,6</sup>

The use of hydrogen as a fuel in light-duty vehicles would offer a significantly cleaner alternative to gasoline, natural gas, or electric, grid-powered vehicles. However, the low energy density of gaseous hydrogen currently requires storage at very high pressures in order to achieve reasonable driving ranges. An alternative to this method is to store hydrogen at lower pressures in a porous adsorbent, in which the hydrogen interactions with the internal surfaces of the material result in a higher density of stored hydrogen than for pure compression to the same pressure.

One class of porous materials that has been well studied for hydrogen storage is metal-organic frameworks (MOFs). These three-dimensional materials are built of metal ions connected by tunable organic linkers, which facilitates the installation of highly selective functionalities into the framework pores and hence the design of structures tuned for specific applications. For hydrogen storage, the incorporation of metal centers with open coordination sites can lead to strong affinities for hydrogen and enhanced storage densities, as the positively charged metal centers strongly interact with guest hydrogen molecules [1-3]. However, the most promising metal-organic frameworks still fall short of the Department of Energy hydrogen storage targets. Therefore, new adsorbents must be designed with an even higher density of open metal coordination sites in order to meet these targets. Using gas dosing in powder neutron diffraction experiments, we were able to demonstrate, for the first time, the interaction of two hydrogen molecules with a single metal center in a metal-organic framework.

We have recently reported the storage of hydrogen in the MOF known as  $\text{Mn}_2(\text{dsbdc})$  (where the organic ligand is  $\text{dsbdc}^{4-} = 2,5\text{-disulfido-1,4-benzenedicarboxylate}$  and Mn stands for manganese). While the organic linker used here is similar to that used to generate the well-studied  $\text{M}_2(\text{dobdc})$  series ( $\text{dobdc}^{4-} = 2,5\text{-dioxo-1,4-benzenedicarboxylate}$ ), this material has a unique structure in which the pores exhibit infinite chains of manganese ions, wherein every other manganese is bound by framework organic ligands and two removable solvent molecules. Upon heating the material under vacuum, it is possible to remove these solvent molecules and expose two open sites at the metal capable

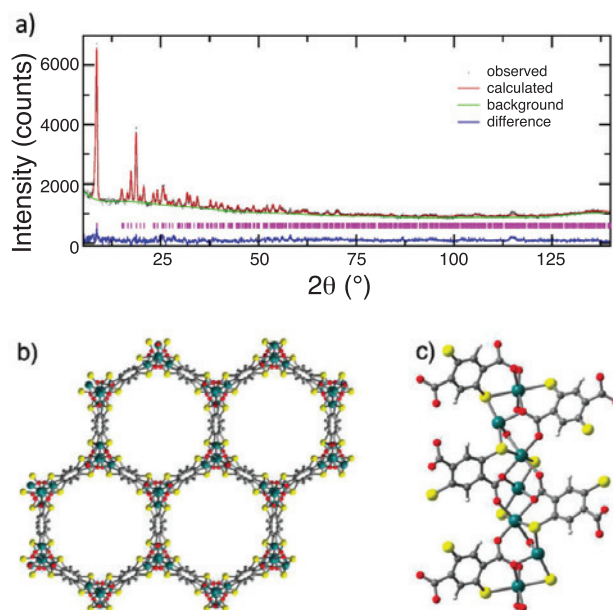


**FIGURE 1:** (a) Rietveld refinement plot for the crystal structure of  $\text{Mn}_2(\text{dsbdc})$ . The neutron diffraction intensity as a function of scattering angle ( $2\theta$ ) is represented by black dots, the best fit with a red line, background as a green line, the difference curve with a blue line, and the Bragg positions with vertical bars. (b) Crystal structure of  $\text{Mn}_2(\text{dsbdc})$  showing the one-dimensional hexagonal pores along the crystallographic  $c$ -axis. (c) A portion of a single helix of alternating six-coordinate and four-coordinate metal nodes, with blue-green, yellow, red, grey, and white spheres representing Mn, S, O, C, and H atoms, respectively.

of binding hydrogen, which we were able to confirm through neutron diffraction (Figure 1) and inelastic neutron scattering experiments (Figure 2).

The hydrogen storage properties of this material were measured via hydrogen adsorption experiments carried out at 77 K and 87 K. The isotherms resulting from these measurements were fit with the dual-site Langmuir model to determine the heat of adsorption of hydrogen in the structure, which was found to be  $-6.5$  kJ/mol for all measured loadings.

<sup>1</sup> Department of Chemistry, University of California, Berkeley, Berkeley, CA 94720

<sup>2</sup> Materials Sciences Division, Lawrence Berkeley National Laboratory, Berkeley, CA 94720

<sup>3</sup> NIST Center for Neutron Research, National Institute of Standards and Technology, Gaithersburg, MD 20899

<sup>4</sup> National Renewable Energy Laboratory, 15013 Denver West Parkway, Golden, CO 80401

<sup>5</sup> University of Delaware, Newark, DE 19716

<sup>6</sup> Department of Chemical and Biomolecular Engineering, University of California, Berkeley, Berkeley, CA 94720

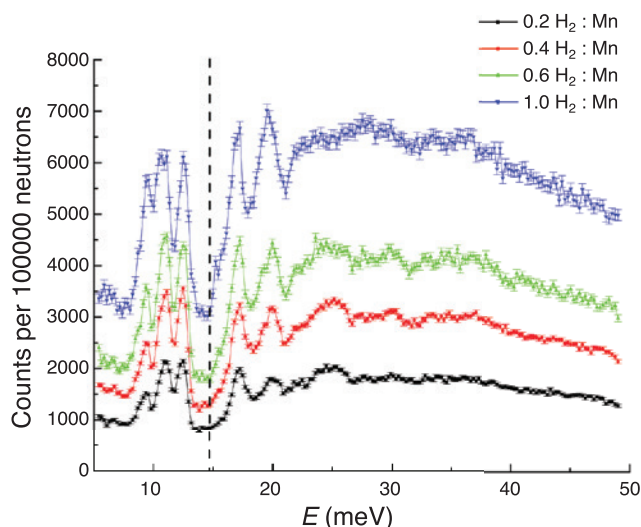


**FIGURE 2:** Inelastic neutron scattering spectra of low dosing of  $\text{H}_2$  in  $\text{Mn}_2(\text{dsbdc})$ . The spectra are labelled as a ratio of all Mn in the system; the number of  $\text{H}_2$  molecules per open-Mn is twice this value.

While this value of the binding enthalpy is not quite as large as those exhibited by other MOFs, the advantage of this material is that it can bind two hydrogen molecules per manganese center, as verified by powder neutron diffraction experiments. In order to facilitate these measurements, it was necessary to use an isotope of hydrogen, namely deuterium ( $\text{D}_2$ ), which was introduced into the material at loadings of 0.7  $\text{D}_2$  and 1.4  $\text{D}_2$  per metal center. The manganese– $\text{D}_2$  distances were found to be 3.40(4) Å and 3.07(3) Å, respectively, and these distances correspond to a binding strength of  $-5.6$  kJ per molar equivalent of  $\text{D}_2$  as found in the hydrogen adsorption experiments. Furthermore, we used inelastic neutron scattering to characterize  $\text{Mn}_2(\text{dsbdc})$  dosed with  $\text{H}_2$  and confirmed that the two  $\text{H}_2$  molecules are indeed binding to the metal center. Figure 2 illustrates that the rotational spectrum for adsorbed hydrogen is somewhat perturbed from the free-rotor value of 14.7 meV [4]. More importantly, the spectrum is scalable from low coverage to well above 1.4  $\text{H}_2$ :open-Mn indicating that the two hydrogens are similarly perturbed when adsorbed at this open-Mn.

We additionally sought to demonstrate that the binding of multiple gas molecules to the metal centers extends beyond  $\text{H}_2$ . Using X-ray and powder neutron diffraction, respectively, we found that samples of  $\text{Mn}_2(\text{dsbdc})$  dosed with  $\text{CD}_4$  (the deuterium analogue of methane) and  $\text{CO}_2$  showed similar gas binding at the open metal coordination sites as with  $\text{D}_2$ .

The applicability of this strategy to a variety of different gas molecules demonstrates its viability and promise as a long-term strategy for increasing the density of gas molecules bound in the

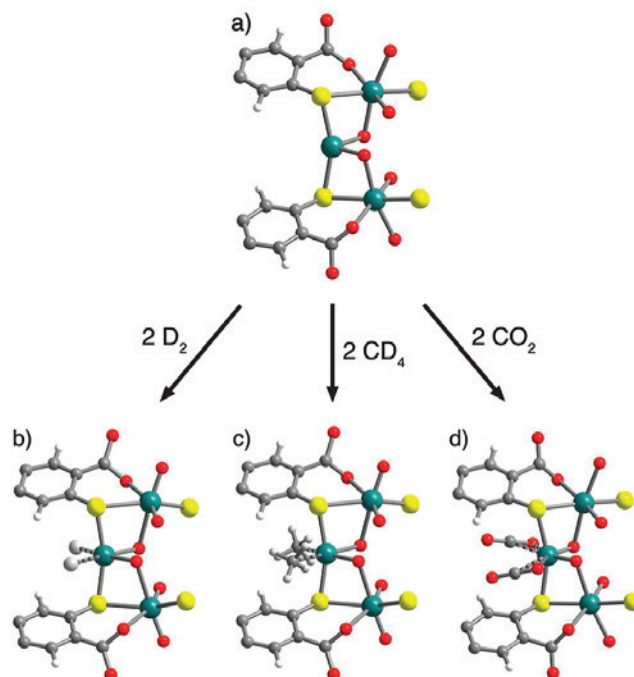


**FIGURE 3:** A portion of the crystal structure of  $\text{Mn}_2(\text{dsbdc})$  presented around the four-coordinate  $\text{Mn}^{2+}$  center in (a) activated, (b) 0.7  $\text{D}_2$  dosed, (c) 0.4  $\text{CD}_4$  dosed, and (d) 0.13  $\text{CO}_2$  dosed samples (per four-coordinate metal ion). Blue-green, yellow, red, gray, and small white spheres represent Mn, S, O, C, and D or H atoms, respectively. Large white spheres in (b) represent the centroids of  $\text{D}_2$  molecules.

pores of metal-organic frameworks. Importantly, these neutron diffraction and inelastic neutron scattering results demonstrate the interaction of two hydrogen molecules with a single metal center in a MOF for the very first time [5]. This is a step toward significantly increasing both the binding enthalpy and storage density of  $\text{H}_2$  in porous materials to levels approaching the DOE targets for on-board hydrogen storage in fuel cell vehicles.

## References

- [1] M. Dinca, W. S. Han, Y. Liu, A. Dailly, C. M. Brown, J. R. Long, *J. Am. Chem. Soc.* **128**, 16876 (2006).
- [2] Y. Liu, J.-H. Her, A. Dailly, A. J. Ramirez-Cuesta, D. A. Neumann, C. M. Brown, *J. Am. Chem. Soc.* **130**, 11813 (2008).
- [3] K. Sumida, S. Horike, S. S. Kaye, Z. R. Herm, W. L. Queen, C. M. Brown, F. Grandjean, G. J. Long, A. Dailly, J. R. Long, *Chem. Sci.* **1**, 184 (2010).
- [4] C. M. Brown, Y. Liu, T. Yildirim, V. K. Peterson, C. J. Kepert, *Nanotechnology* **20**, 204025 (2009).
- [5] T. Runčevski, M. T. Kapelewski, R. M. Torres-Gavosto, J. D. Tarver, C. M. Brown, J. R. Long, *Chem. Commun.* **52**, 8251 (2016).

# Critical factors driving the high volumetric uptake of methane in $\text{Cu}_3(\text{btc})_2$

Z. Hulvey,<sup>1,2</sup> B. Vlaisavljevich,<sup>3</sup> J. A. Mason,<sup>3</sup> E. Tsvion,<sup>3,4</sup> T. P. Dougherty,<sup>1,5</sup> E. D. Bloch,<sup>3</sup> M. Head-Gordon,<sup>3,4</sup> B. Smit,<sup>3,6</sup> J. R. Long,<sup>3,4</sup> and C. M. Brown<sup>1,7</sup>

A variety of economic and environmental factors have sparked interest in the use of natural gas, composed primarily of methane ( $\text{CH}_4$ ), as an alternative transportation fuel to petroleum. However, its use in on-board vehicular applications is severely limited by its relatively low volumetric energy density. The development of adsorption-based systems where high surface area materials store large volumes of  $\text{CH}_4$  at ambient conditions would allow for the use of smaller, lightweight tanks that could be integrated into smaller vehicles such as passenger cars. Metal-organic frameworks (MOFs) have attracted substantial attention as materials for these types of adsorption applications due to their high surface areas and chemically tunable pore dimensions and surface functionality. It has been shown through multiple adsorption studies that  $\text{Cu}_3(\text{btc})_2$  ( $\text{btc}^{3-} = 1,3,5\text{-benzenetricarboxylate}$ ; HKUST-1) exhibits one of the highest volumetric capacities for  $\text{CH}_4$  in a MOF at 35 bar and 25 °C [1, 2]. Its structure consists of binuclear copper(II) paddlewheel units connected through the carboxylate linkers to form a three-dimensional pore structure. An axial water molecule on each  $\text{Cu}^{2+}$  ion can be removed to leave an open coordination site that can attract different gas molecules. The pore structure contains three distinct types of cavities: two large pores with diameters of about 11 Å and 13 Å, which contain the open  $\text{Cu}^{2+}$  sites exposed to the pore surface; and an octahedral cage (diameter  $\approx 5$  Å) accessible through triangular windows from the largest pore. An isostructural Cr analog can be synthesized that displays a slightly higher surface area and interesting adsorption behavior for gases such as  $\text{H}_2$ ,  $\text{O}_2$ , and  $\text{CO}_2$ , but has yet to be investigated for  $\text{CH}_4$  uptake.

Correlating structural features with adsorption behavior is a critical part of the evaluation of adsorptive materials and must be accomplished using a variety of experimental techniques. Powder diffraction experiments have been used to determine binding sites for many gas molecules in MOFs, including  $\text{CH}_4$  in  $\text{Cu}_3(\text{btc})_2$  [3,4]. These studies have determined that  $\text{CH}_4$  adsorption occurs in both the octahedral cages and at the open metal sites; however, the data in these reports did not clearly identify the relative affinity, or order of filling, of these sites. It is of particular interest to determine whether the  $\text{CH}_4$  molecule prefers a perfectly sized cage to enhance adsorbate–adsorbent

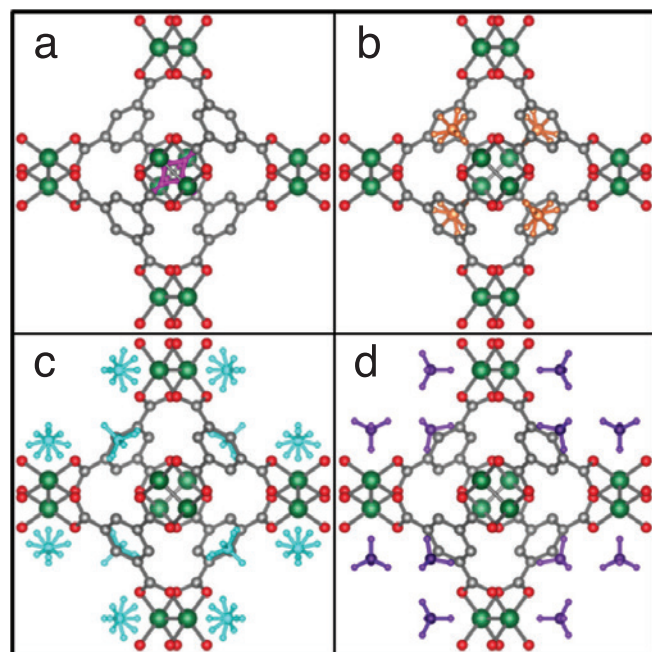


**FIGURE 1:** Structure of approximately half of the unit cell of  $\text{Cr}_3(\text{btc})_2$  dosed with 2.2  $\text{CD}_4$  per Cr atom viewed down the  $a$ -axis. Green, grey, and red spheres represent Cr, C, and O atoms, respectively; H atoms are omitted for clarity.  $\text{CD}_4$  molecules are shown at the octahedral cage site (a, pink) the window site (b, orange), the metal site (c, cyan), and the fourth site (d, purple).

contacts or an enhanced electronic interaction at an open metal coordination site, or if these structural characteristics are of relatively equal importance. Furthermore, any differences found in the adsorptive behavior of  $\text{Cu}_3(\text{btc})_2$  and  $\text{Cr}_3(\text{btc})_2$  would clarify the nature of the  $\text{CH}_4$ –open metal site interaction. Additional computational studies of adsorption in MOFs can assist in explaining experimental observations and build on experimental foundation to predict adsorptive behavior in other materials. These theoretical studies have become an extremely important tool to guide synthetic efforts in the design of porous materials, as once adsorptive behavior can be adequately predicted entire libraries of thousands of possible structures can be screened for their properties to expose beneficial structural features.

<sup>1</sup> NIST Center for Neutron Research, National Institute of Standards and Technology, Gaithersburg, MD 20899

<sup>2</sup> University of Maryland, College Park, MD 20742

<sup>3</sup> University of California, Berkeley, CA 94720

<sup>4</sup> Lawrence Berkeley National Laboratory, Berkeley, CA 94720

<sup>5</sup> Georgetown University, Washington, DC 20057

<sup>6</sup> Ecole Polytechnique Fédérale de Lausanne, Lausanne, Switzerland

<sup>7</sup> University of Delaware, Newark, DE 19716



Neutron diffraction structures were determined at various loadings of  $\text{CD}_4$  in  $\text{Cu}_3(\text{btc})_2$  and  $\text{Cr}_3(\text{btc})_2$ . Data analysis indicated that the initial adsorption site is at the windows to the octahedral cages in both  $\text{Cu}_3(\text{btc})_2$  and  $\text{Cr}_3(\text{btc})_2$ . With increased dosing to 1.5  $\text{CD}_4$  per metal atom, additional nuclear density was found inside the octahedral cages and at the metal sites in a similar fashion for both materials. At the highest dose of 2.2  $\text{CD}_4$  per metal atom, the first three binding sites described above are fully occupied, and a fourth site begins to populate in the 11 Å diameter pore. This site is located above the outside of the ligands that form the surface of the octahedral cages and essentially represents the filling of the surface of one of the large pores (Figure 1).

The major conclusions evident from the combination of the adsorption and diffraction data are that adsorption mechanisms are essentially identical for  $\text{Cu}_3(\text{btc})_2$  and  $\text{Cr}_3(\text{btc})_2$ , and that the binding sites in and around the octahedral cage are favored over both metal sites. We infer that the main reason  $\text{Cu}_3(\text{btc})_2$  has a slightly higher volumetric uptake compared to  $\text{Cr}_3(\text{btc})_2$  is due to its slightly smaller unit cell. It is not immediately clear why  $\text{CH}_4$  adsorption occurs first at the octahedral cage and window sites, rather than at the metal sites as is perhaps expected. In an effort to better understand the origins of this surprising sequential filling of adsorption sites, a detailed computational analysis was performed for  $\text{CH}_4$  binding in  $\text{Cr}_3(\text{btc})_2$  and  $\text{Cu}_3(\text{btc})_2$ .

Binding energies for  $\text{CH}_4$  were determined by periodic DFT calculations at the window and metal sites and converted to binding enthalpies by applying harmonic vibrational corrections. The calculated difference in energy between the window and metal sites is consistent with the observation in our NPD results that the window sites are occupied first. We hypothesized that the strength of  $\text{CH}_4$  binding at the  $\text{Cu}^{2+}$  sites might be effectively increased by intermolecular interactions with  $\text{CH}_4$  molecules already adsorbed at the nearby window sites. The effect of lateral  $\text{CH}_4$ – $\text{CH}_4$  interactions has been shown by other researchers to be important given that  $\text{CH}_4$ – $\text{CH}_4$  distances are quite short in this topology. Recomputing the binding energy at the metal site and decomposing the interactions between the  $\text{CH}_4$  molecules reveals that the presence of one  $\text{CH}_4$  alone increases the binding strength by  $-1.28$  kJ/mol. However, if the structures of both  $\text{CH}_4$  molecules are allowed to relax, as opposed to only the  $\text{CH}_4$  at the metal site, binding at the metal site increases further leading to an enhancement of  $-5.49$  kJ/mol (or  $-2.74$  kJ/mol per  $\text{CH}_4$ ). Furthermore, at the configuration from NPD with the highest loading, the  $\text{CH}_4$  at the metal site interacts with not one but eight  $\text{CH}_4$  molecules. While the absolute value of this energy should be thought of as a rough approximation, this result emphasizes the importance of the cumulative effect of interactions between neighboring  $\text{CH}_4$  molecules. Due to these interactions, the effective binding energy at the metal site is not that different from the binding energy at the window site, further explaining why a dual-site Langmuir isotherm was not necessary to fit the adsorption data.

Total volumetric  $\text{CH}_4$  adsorption isotherms computed with grand canonical Monte Carlo (GCMC) describe the experimental isotherms presented above very well (Figure 2). We extended

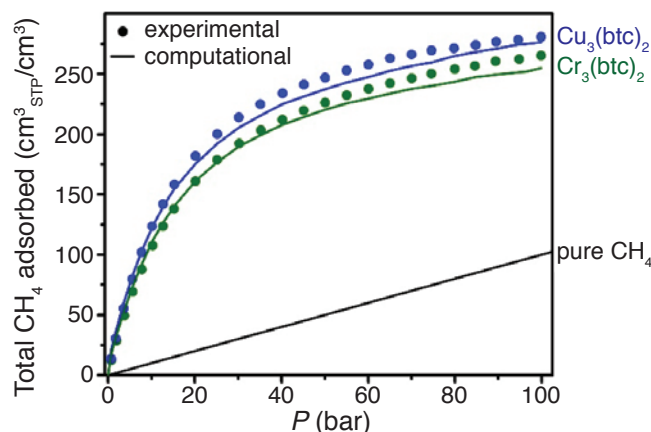


**FIGURE 2:** Experimental and calculated isotherms of total volumetric uptake for  $\text{Cu}_3(\text{btc})_2$  (green) and  $\text{Cr}_3(\text{btc})_2$  (blue). Experimental results are shown as circles, and the shifted-UFF isotherm as solid lines.

these calculations to evaluate  $\text{CH}_4$  adsorption in some structural variations of  $\text{Cu}_3(\text{btc})_2$  and  $\text{Cr}_3(\text{btc})_2$  and to gain insight into the possibility of developing an improved adsorbent. We found that while binding enthalpies are increased by ligand substitution, deliverable capacity decreases in all cases from the non-functionalized materials. Additionally, even if we could artificially increase or decrease the heat of adsorption as much as 6 kJ/mol, there is no significant increase in the deliverable capacity beyond what is calculated for the actual  $\text{Cu}_3(\text{btc})_2$  structure. In other words,  $\text{Cu}_3(\text{btc})_2$  already has the ideal binding enthalpy required to maximize the deliverable capacity.

To date,  $\text{Cu}_3(\text{btc})_2$  has shown the most promise of any MOF as a  $\text{CH}_4$  storage material for relevant industrial applications. In this work, we have carried out a thorough investigation regarding the underlying mechanistic reasons for its high volumetric uptake, combining several types of experimental and computational data. The fact that enhancement of  $\text{CH}_4$  binding at its open metal site is mostly due to  $\text{CH}_4$ – $\text{CH}_4$  interactions between adjacent adsorbed molecules is a very important conclusion that should assist future research into new materials for this application. The structure of  $\text{Cu}_3(\text{btc})_2$  has just the right combination of features to maximize both  $\text{CH}_4$ –framework and  $\text{CH}_4$ – $\text{CH}_4$  interactions for optimum delivery capacity. Furthermore, this work highlights the level of mechanistic understanding that can be achieved when experimental and computational techniques are combined. This approach is currently being expanded to other adsorption applications in other MOF systems.

## References

- [1] J. A. Mason, M. Veenstra, J. R. Long, *Chem. Sci.* **5**, 32 (2014).
- [2] Y. Peng, V. Krungleviciute, I. Eryazici, J. T. Hupp, O. K. Farha, T. Yildirim, *J. Am. Chem. Soc.* **135**, 11887 (2013).
- [3] M. Dincă, A. Dailly, C. M. Brown, D. A. Neumann, J. R. Long, *J. Am. Chem. Soc.* **128**, 16876 (2006).
- [4] Z. Hulvey, K. V. Lawler, Z. Qiao, J. Zhou, D. Fairen-Jimenez, R. Q. Snurr, S. V. Ushakov, A. Navrotsky, C. M. Brown, P. M. Forster, *J. Phys. Chem. C* **117**, 20116 (2013).

# Enhancements in superionic conduction properties in Lithium and Sodium *closo*-dodecaborate salts via substitutional and morphological modifications

T. J. Udovic,<sup>1</sup> W. S. Tang,<sup>1,2</sup> H. Wu,<sup>1</sup> W. Zhou,<sup>1</sup> V. Stavila,<sup>3</sup> M. Matsuo,<sup>4</sup> A. Unemoto,<sup>4</sup> and S. Orimo<sup>4</sup>

Finding replacement solid-state electrolytes with sufficiently high conductivities and stabilities are the elusive answer to the inherent shortcomings of organic liquid electrolytes prevalent in today's rechargeable batteries. We recently found that solid sodium and lithium salts of the divalent icosahedral  $B_{12}H_{12}^{2-}$  anion, indeed, possess the requisite (super)ionic conductivities comparable to liquid electrolytes, but only above their high order-disorder phase transition temperatures near 530 K and 620 K, respectively. Making them more applicable to future solid-state-battery technologies requires much lower transition temperatures closer to ambient operating temperatures. We have been able to accomplish this in two different ways: (i) by replacing the  $B_{12}H_{12}^{2-}$  anions with chemically modified monovalent  $CB_{11}H_{12}^{-}$  anions [1] (see Fig. 1) and (ii) by ball-milling the salts to generate nanosized disordered crystallite morphologies [2].

Figure 1 shows the ionic conductivity data for the modified  $NaCB_{11}H_{12}$  and  $LiCB_{11}H_{12}$  salts and ball-milled  $Na_2B_{12}H_{12}$  compared with those for pristine  $Na_2B_{12}H_{12}$  and  $Li_2B_{12}H_{12}$ .  $NaCB_{11}H_{12}$  and  $LiCB_{11}H_{12}$  display dramatically lower respective superionic transition temperatures near 380 K and 400 K and

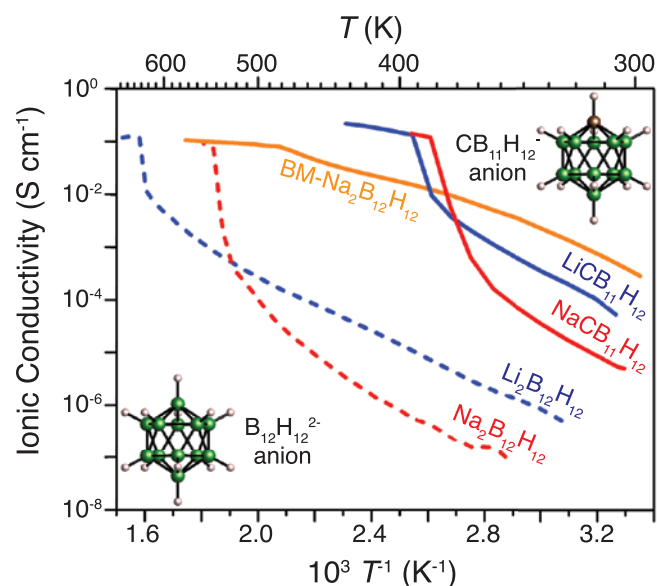


**FIGURE 1:** Ionic conductivities for  $NaCB_{11}H_{12}$ ,  $LiCB_{11}H_{12}$ , and ball-milled  $Na_2B_{12}H_{12}$  compared with those for pristine  $Na_2B_{12}H_{12}$  and  $Li_2B_{12}H_{12}$ . Adapted from [1, 3].

order-of-magnitude higher conductivities compared to their divalent-anion cousins. Moreover, ball-milled  $Na_2B_{12}H_{12}$  (unlike pristine  $Na_2B_{12}H_{12}$ ) maintains superionic conductivity well below 530 K down to room temperature.

Neutron scattering methods were used to characterize the various structures as well as the high anion reorientational mobilities in the disordered superionic phases. These high mobilities are believed to facilitate rapid cation diffusive motions through the interstitial channels of these materials. The 4 K neutron vibrational spectra from FANS for ordered  $NaCB_{11}H_{12}$  and  $LiCB_{11}H_{12}$  shown in Fig. 2a are in good agreement with the DFT-simulated phonon densities of states (PDOS) of the orthorhombic structures determined by diffraction. As suggested by the simulated PDOS of the isolated  $CB_{11}H_{12}^{-}$  anion, the neutron vibrational spectrum is clearly sensitive to the structural arrangement.

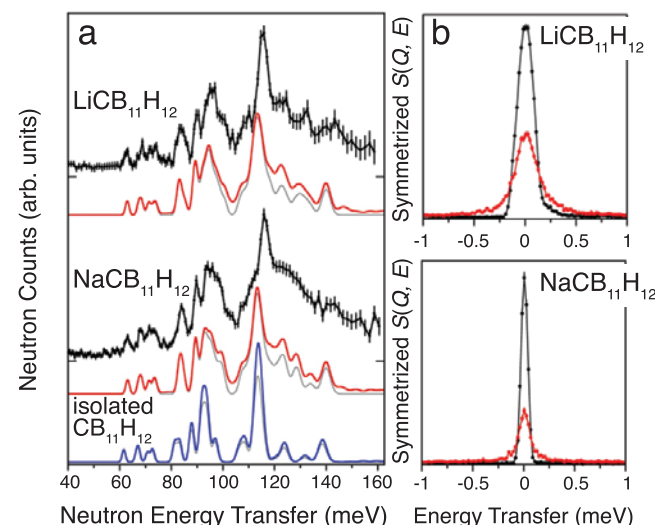


**FIGURE 2:** (a) Neutron vibrational spectra (black) of  $NaCB_{11}H_{12}$  and  $LiCB_{11}H_{12}$  at 4 K compared to the simulated one-phonon (gray) and one+two-phonon (red) densities of states from the DFT-optimized orthorhombic structures (red), and the isolated  $CB_{11}H_{12}^{-}$  anion (blue). (b) QENS spectra from DCS with 4.1 Å neutrons ( $Q = 1.35 \text{ \AA}^{-1}$ ) showing the anion-reorientation-induced broadening in red for  $NaCB_{11}H_{12}$  (at 375 K) and  $LiCB_{11}H_{12}$  (at 433 K) compared to the resolution-limited elastic-scattering peaks in black observed at 200 K, below the order-disorder phase transitions. (N.B., lower instrumental resolution was used for  $LiCB_{11}H_{12}$ ) Adapted from [1].

<sup>1</sup> NIST Center for Neutron Research, National Institute of Standards and Technology, Gaithersburg, MD 20899

<sup>2</sup> University of Maryland, College Park, MD 20742

<sup>3</sup> Energy Nanomaterials, Sandia National Laboratories, Livermore, CA 94551

<sup>4</sup> Institute for Materials Research, Tohoku University, Sendai, Japan



Preliminary QENS measurements for natural-boron  $\text{NaCB}_{11}\text{H}_{12}$  and  $\text{LiCB}_{11}\text{H}_{12}$  confirm orders of magnitude jumps in anion orientational mobilities to between  $10^{10}$  and  $10^{11}$  reorientational jumps  $\text{s}^{-1}$  in the disordered phases, as reflected in Fig. 2b by the transformation from purely resolution-limited elastic component peaks at 200 K to ones with significant quasielastic broadening at 433 K and 375 K, respectively. For both materials, the observed fraction of scattering that is quasielastic above  $Q = 1 \text{ \AA}^{-1}$  appears to be of the order of 0.8 or more, suggesting that we are observing anion small-angle-jump reorientations akin to that observed for  $\text{Na}_2\text{B}_{12}\text{H}_{12}$ , [3] which is thought to entail a distribution of individual anion motions ranging from one-axis to multi-axis reorientations. The quasielastic linewidths suggest that the monovalent anions are on the order of 60 % more mobile than their divalent analogs. Such higher relative  $\text{CB}_{11}\text{H}_{12}^-$  reorientational mobilities compared to  $\text{B}_{12}\text{H}_{12}^{2-}$  are likely a consequence of relatively weaker cation-anion (Coulombic) interactions as well as, on average, one-half fewer near-neighbor cations for the  $\text{CB}_{11}\text{H}_{12}^-$  anion.

For ball-milled  $\text{Na}_2\text{B}_{12}\text{H}_{12}$ , in agreement with the conductivity data in Fig. 1, both X-ray and neutron powder diffraction confirm the stabilization of the disordered superionic pseudo-bcc phase down to at least 5 K. Neutron fixed-window scans (FWSs) and QENS measurements for pre- and post-ball-milled  $\text{Na}_2^{11}\text{B}_{12}\text{H}_{12}$  are shown in Fig. 3. The FWSs in Fig. 3a reflect  $\text{B}_{12}\text{H}_{12}^{2-}$  anion reorientational jump frequencies on the order of  $10^8 \text{ s}^{-1}$  already by  $\approx 240 \text{ K}$  to  $250 \text{ K}$  after ball-milling (as evidenced by the onset of more significant intensity dropoff), which is consistent with the observed presence of the superionic phase.

In comparison, pristine  $\text{Na}_2\text{B}_{12}\text{H}_{12}$  displays hysteretic FWS behavior and high reorientational mobility only at considerably higher temperatures. QENS spectra of ball-milled  $\text{Na}_2\text{B}_{12}\text{H}_{12}$  were measured between 270 K and 400 K and could be fit to a primary Lorentzian component linewidth  $(2\hbar)/\tau_1$  ranging between 0.27  $\mu\text{eV}$  and 11  $\mu\text{eV}$  fwhm, respectively. This narrow Lorentzian component dominated at lower  $Q$  values, with increasing contributions from one and probably more broader Lorentzian components at larger  $Q$  values, which is again compatible with a small-angle jump mechanism [3]. Anion reorientational jump correlation frequencies derived from the QENS spectral broadening (Fig. 3b) are in excellent agreement with the Arrhenius dependence observed for pristine  $\text{Na}_2\text{B}_{12}\text{H}_{12}$  above its phase transition at higher temperatures. Combined data yield an activation energy for reorientation of 270(3) meV, the same value obtained for pristine bcc  $\text{Na}_2\text{B}_{12}\text{H}_{12}$  from NMR measurements.

The measured elastic fraction of the total QENS spectrum (i.e., the elastic incoherent structure factor, EISF) at 400 K at  $0.84 \text{ \AA}^{-1}$  (using DCS with 11  $\mu\text{eV}$  resolution) was estimated to be  $\approx 0.48$ . Assuming a similar reorientational mechanism as for pristine disordered  $\text{Na}_2\text{B}_{12}\text{H}_{12}$ , [3] this EISF value is consistent with 20 % to 25 % of the anions being relatively immobile in an ordered monoclinic phase at this temperature. Moreover the continued decrease in the FWS in Fig. 3a upon heating above 340 K

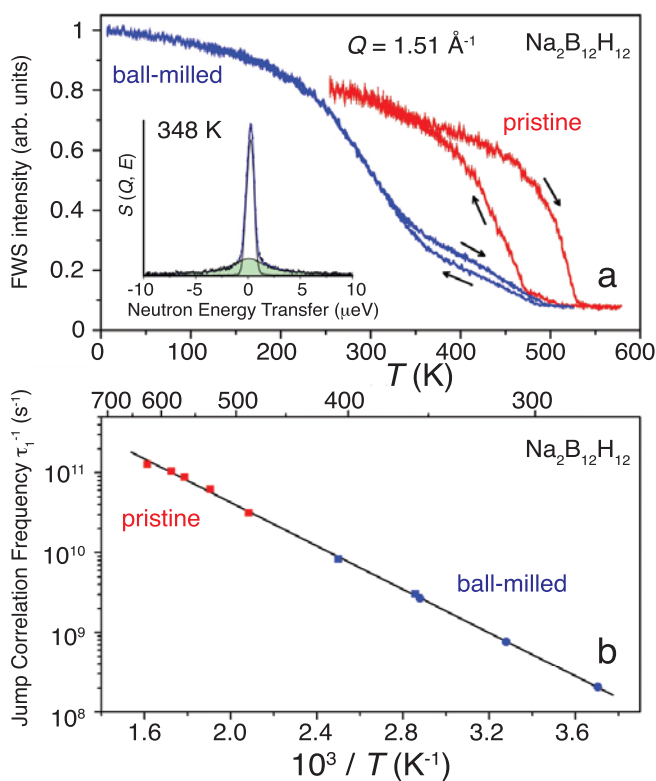


**FIGURE 3:** (a) Neutron fixed-window scans (HFBS, neutron momentum transfer  $Q = 1.51 \text{ \AA}^{-1}$ ) for  $\text{Na}_2^{11}\text{B}_{12}\text{H}_{12}$  before (red) and after (blue) ball-milling for 72 h. Inset: QENS spectrum (348 K,  $Q = 1.51 \text{ \AA}^{-1}$ ) showing Lorentzian broadening (green) due to rapid anion reorientational motions ( $\approx 3 \times 10^9$  jumps  $\text{s}^{-1}$ ) for the ball-milled material. (b) Arrhenius plot of the jump correlation frequency ( $\tau_1^{-1}$ ) vs.  $T^{-1}$  determined for ball-milled  $\text{Na}_2^{11}\text{B}_{12}\text{H}_{12}$  (blue symbols) compared to  $\tau_1^{-1}$  values for pristine  $\text{Na}_2\text{B}_{12}\text{H}_{12}$ . Squares and circles denote measurements on DCS and HFBS instruments, respectively. All data points fit well to a single line with an activation energy for reorientation of 270(3) meV. Adapted from [3].

indicates that this remaining “immobile” phase fraction converts to the superionic phase over a broad temperature range until its completion above 500 K. This transitioning fraction is reversible, as evidenced by the observed hysteretic FWS cooling behavior.

Looking forward, we are exploring analogous chemical and morphological modifications of related  $\text{Na}_2\text{B}_{10}\text{H}_{10}$  and  $\text{Li}_2\text{B}_{10}\text{H}_{10}$  anion-cluster salts and their effects on transition temperatures, anion reorientational mobilities and mechanisms, and resulting cation mobilities as well as molecular dynamics studies to understand the possible link between these orientational anion motions and the observed superionic conductivity.

## References

- [1] W. S. Tang, A. Unemoto, W. Zhou, V. Stavila, M. Matsuo, H. Wu, S. Orimo, T. J. Udovic, *Energy Environ. Sci.* **8**, 3637 (2015).
- [2] W. S. Tang, M. Matsuo, H. Wu, V. Stavila, A. Unemoto, S. Orimo, T. J. Udovic, *Energy Storage Mater.* **4**, 79 (2016).
- [3] N. Verdal, T. J. Udovic, V. Stavila, W. S. Tang, J. J. Rush, A. V. Skripov, *J. Phys. Chem. C* **118**, 17483 (2014).

# SiF<sub>6</sub>-pillared metal-organic frameworks for highly effective acetylene capture from ethylene

X. Cui,<sup>1</sup> K. Chen,<sup>2</sup> H. Xing,<sup>1</sup> Q. Yang,<sup>1</sup> R. Krishna,<sup>3</sup> Z. Bao,<sup>1</sup> H. Wu,<sup>4</sup> W. Zhou,<sup>4</sup> X. Dong,<sup>5</sup> Y. Han,<sup>5</sup> B. Li,<sup>6</sup> Q. Ren,<sup>1</sup> M. J. Zaworotko,<sup>2</sup> and B. Chen<sup>6</sup>

Due to the worldwide demand for plastic, ethylene (C<sub>2</sub>H<sub>4</sub>) is the most widely produced organic compound in the world, with well over 100 million tons of it manufactured each year, largely by refining crude oil. Newly made ethylene is not pure enough to make polyethylene because the refinement process also creates a substantial amount of acetylene (C<sub>2</sub>H<sub>2</sub>), which can poison the catalysts used in the polymerization process. The conventional industrial solution is to convert the undesirable acetylene into ethylene, but this step requires the use of palladium as a catalyst and consumes a significant amount of energy. A promising alternative technology is to use porous adsorbent materials to capture acetylene from ethylene. We recently discovered that a subfamily of metal-organic frameworks (MOFs) called “SIFSIX MOFs” can effectively remove the contaminant acetylene from ethylene, with unprecedented C<sub>2</sub>H<sub>2</sub> adsorption capacity and C<sub>2</sub>H<sub>2</sub>/C<sub>2</sub>H<sub>4</sub> selectivity [1].

SIFSIX MOFs are comprised of metal ions (e.g., Cu<sup>2+</sup>, Zn<sup>2+</sup> etc.), pyridine-containing organic linkers, and preformed SiF<sub>6</sub><sup>2-</sup> (hexafluorosilicate, SIFSIX). In Figure 1, the building units and the crystal structure of a prototypical SIFSIX compound, SIFSIX-1-Cu (1 = 4,4'-bipyridine), is shown schematically as an example. The metal ions coordinate with pyridine in the organic linkers, forming 2-D square grid layers (parallel to crystallographic *a-b* plane). Along crystallographic *c*-axis, the SiF<sub>6</sub> units coordinate with the metal ion and function as pillars between the 2-D metal-organic grids, resulting in 3-D extended framework structures. SIFSIX MOFs are highly versatile: by changing the length of the organic linkers, the metal node, and/or framework interpenetration, the pore sizes within this family of materials can be systematically tuned.

Several SIFSIX MOFs, including SIFSIX-1-Cu, SIFSIX-2-Cu (2 = 4,4'-dipyridylacetylene), SIFSIX-2-Cu-*i* (*i* = interpenetrated), SIFSIX-3-Ni (3 = pyrazine), and SIFSIX-3-Zn, were investigated for C<sub>2</sub>H<sub>2</sub> capture. First, the C<sub>2</sub>H<sub>2</sub> adsorption isotherm was measured for these materials. SIFSIX-2-Cu-*i* rapidly adsorbs C<sub>2</sub>H<sub>2</sub> at very low pressure (≤ 0.05 bar), indicating that SIFSIX-2-Cu-*i* offers promise for C<sub>2</sub>H<sub>2</sub> capture when it is a minor component in a gas mixture. SIFSIX-1-Cu exhibits extraordinary C<sub>2</sub>H<sub>2</sub> uptake (8.5 mmol/g) at 298 K and 1 bar, which is higher than the previous benchmark, Fe-MOF-74 [2].

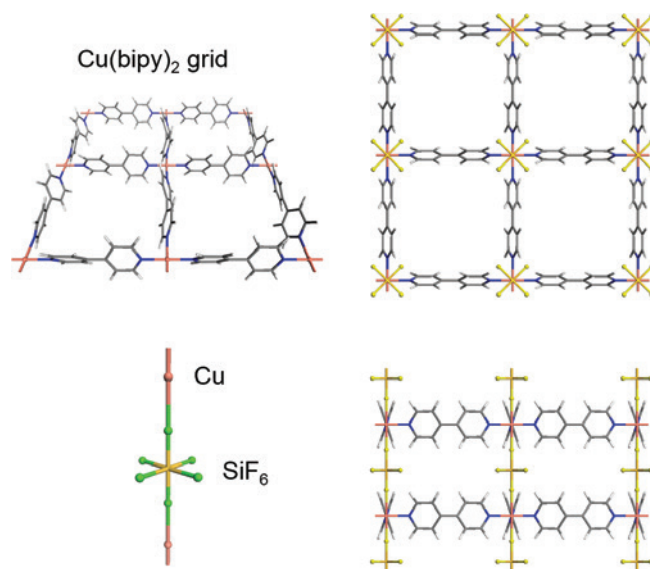


**FIGURE 1:** Schematic structure of SIFSIX-1-Cu. LEFT: The MOF building blocks. RIGHT: [001] and [100] views of the MOF crystal lattice. Color code: Cu, orange; Si, yellow; F, green; O, red; N, blue; C, gray; H: white.

In order to understand the exceptional C<sub>2</sub>H<sub>2</sub> adsorption in these materials, we conducted detailed first-principles DFT-D (dispersion-corrected density-functional theory) calculations. In SIFSIX-1-Cu, C<sub>2</sub>H<sub>2</sub> molecules are bound through strong C-H...F hydrogen (H) bonding and van der Waals (vdW) interactions with the 4,4'-bipyridine linkers (Fig. 2). The DFT-D calculated static adsorption energy ( $\Delta E$ ) is 44.6 kJ/mol. Each unit cell of SIFSIX-1-Cu contains four equivalent exposed F atoms and each exposed F atom binds one C<sub>2</sub>H<sub>2</sub> molecule. The distance between neighboring adsorbed C<sub>2</sub>H<sub>2</sub> is ideal for them to synergistically interact with each other through multiple H<sup>δ+</sup>...C<sup>δ-</sup> dipole-dipole interactions, further enhancing the energy of adsorption. As four C<sub>2</sub>H<sub>2</sub> molecules are adsorbed per unit cell, the  $\Delta E$  of C<sub>2</sub>H<sub>2</sub> increases to 47.0 kJ/mol. The strong binding of C<sub>2</sub>H<sub>2</sub> at F atoms and the geometric arrangement of SiF<sub>6</sub><sup>2-</sup> anions enables the efficient packing of four C<sub>2</sub>H<sub>2</sub> molecules per unit cell and extraordinary C<sub>2</sub>H<sub>2</sub> uptake at 298 K and 1 bar.

<sup>1</sup> Zhejiang University, Hangzhou 310027, China

<sup>2</sup> University of Limerick, Limerick, Republic of Ireland

<sup>3</sup> University of Amsterdam, Science Park 904, 1098 XH Amsterdam, The Netherlands

<sup>4</sup> NIST Center for Neutron Research, National Institute of Standards and Technology, Gaithersburg, MD 20899

<sup>5</sup> King Abdullah University of Science and Technology, Thuwal 23955-6900, Saudi Arabia

<sup>6</sup> University of Texas at San Antonio, One UTSA Circle, San Antonio, TX 78249

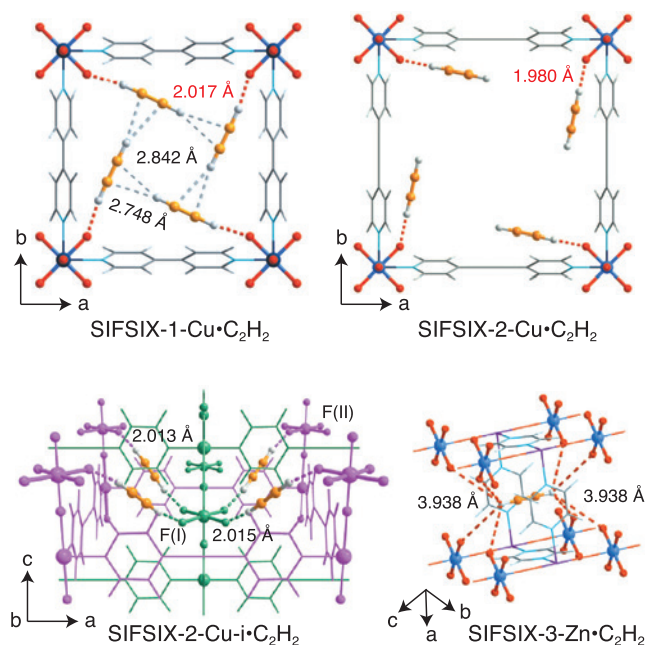


**FIGURE 2:** DFT-D calculated  $C_2H_2$  adsorption binding sites in SIFSIX-1-Cu, SIFSIX-2-Cu, SIFSIX-2-Cu-i (the different nets are highlighted in magenta and green for clarity), and SIFSIX-3-Zn. Color code: F, red; Si, light blue; C, gray; H, light gray; N, sky blue; Cu, dark teal; Zn, violet; C (in  $C_2H_2$ ), orange.

$C_2H_2$  adsorption is notably weaker in the wider pore material SIFSIX-2-Cu versus that in SIFSIX-1-Cu. The  $C-H\cdots F$  H-bonding interaction from  $SiF_6^{2-}$  sites is of the same nature in these isoreticular networks (Fig. 2), while vdW interactions between  $C_2H_2$  and the organic linker in SIFSIX-2-Cu is weaker compared to that in SIFSIX-1-Cu. However, in the twofold interpenetrated structure of SIFSIX-2-Cu-i, one  $C_2H_2$  molecule can be simultaneously bound by two F atoms from different nets through cooperative  $C-H\cdots F$  H-bonding, which enables the strongest energy of  $C_2H_2$  binding ( $\Delta E$ : 52.9 kJ/mol) yet observed in SIFSIX materials. The strong adsorption energy of SIFSIX-2-Cu-i contributes to its extremely high uptake capacity at low pressure.

The weakly basic  $SiF_6^{2-}$  sites and their geometric arrangement enable strong binding with weakly acidic  $C_2H_2$  molecules. Because  $C_2H_2$  is more acidic than  $C_2H_4$  and the geometry is more optimal for  $C_2H_2$  binding, there are much stronger interactions with  $C_2H_2$  than  $C_2H_4$  ( $\Delta E$  in SIFSIX-1-Cu: 44.6 kJ/mol vs. 27.2 kJ/mol, SIFSIX-2-Cu-i: 52.9 kJ/mol vs. 39.8 kJ/mol). The calculated H-bond distances between  $C_2H_4$  and  $SiF_6^{2-}$  sites are 2.541 Å and 2.186 Å in SIFSIX-1-Cu and SIFSIX-2-Cu-i, respectively, which are longer than those between  $C_2H_2$  and  $SiF_6^{2-}$  sites.

To experimentally validate our DFT-D calculation results, high-resolution neutron powder diffraction data were collected on  $C_2D_2$ -loaded samples of SIFSIX-1-Cu• $4C_2D_2$  and SIFSIX-2-Cu-i• $1.7C_2D_2$  at 200 K to establish the structure of the  $C_2H_2$  binding sites through Rietveld refinements. We found that each unit cell of SIFSIX-1-Cu is filled with four  $C_2D_2$  molecules

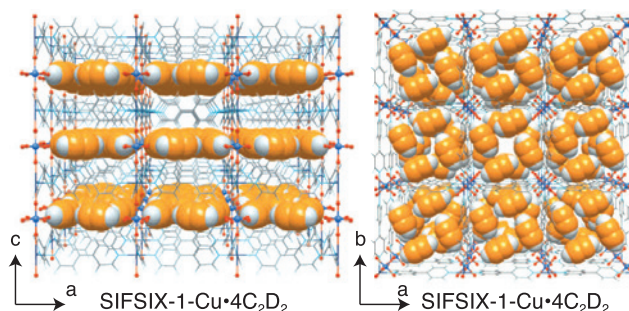


**FIGURE 3:** Neutron crystal structure of SIFSIX-1-Cu• $4C_2D_2$  at 200 K from Rietveld analysis.

that are arranged in an ordered planar structure (Fig. 3), consistent with the DFT-D modeling results.  $C-D\cdots F$  H-bonding occurs between  $C_2D_2$  and  $SiF_6^-$  anions (2.063 Å), and  $D^{\delta+}\cdots C^{\delta-}$  distances between neighboring  $C_2D_2$  molecules are 3.063 Å and 3.128 Å. In SIFSIX-2-Cu-i, each  $C_2H_2$  interacts with two  $SiF_6^-$  anions via dual  $C-D\cdots F$  H-bonding (2.134 Å). These values are also in excellent agreement with our DFT-D predictions.

Next, transient breakthrough simulations were conducted on these materials in order to evaluate  $C_2H_2/C_2H_4$  separation performances in column adsorption processes. Two  $C_2H_2/C_2H_4$  mixtures (1/99 and 50/50) were used as feeds to mimic the industrial process conditions. Clean separations are realized with all five SIFSIX MOFs studied in this work. SIFSIX-2-Cu-i efficiently removes trace  $C_2H_2$  from  $C_2H_4$  gas (1/99) whereas SIFSIX-1-Cu demonstrates excellent  $C_2H_2$  capacity with an uptake of 5533 mmol/L from 50/50 mixture,  $\approx 37\%$  greater than that of Fe-MOF-74. We further examined these materials in actual adsorption processes for both 1/99 and 50/50 mixtures through experimental breakthrough studies. Highly efficient separations for  $C_2H_2/C_2H_4$  mixtures were indeed realized. For the capture of  $C_2H_2$  from the 1/99 mixture, the concentration of  $C_2H_2$  in the gas exiting the adsorber for up to 140 minutes was measured to be below  $2 \times 10^{-6}$  g/g and the purity of  $C_2H_4$  was  $> 99.998\%$ , surpassing the industrial requirement (i.e.,  $C_2H_2$  below  $5 \times 10^{-6}$  g/g).

In summary, SIFSIX materials exhibit unprecedented  $C_2H_2$  capture performance. We attribute it to the existence of sweet-spots in pore chemistry and pore size that enable highly specific recognition of  $C_2H_2$  and high uptake to occur in the same material. Neutron diffraction combined with first-principles calculations have played a critical role in understanding the acetylene capture mechanism in these materials.

## References

- [1] X. Cui, K. Chen, H. Xing, Q. Yang, R. Krishna, Z. Bao, H. Wu, W. Zhou, X. Dong, Y. Han, B. Li, Q. Ren, M. J. Zaworotko, B. Chen, *Science* **353**, 141 (2016).
- [2] E. D. Bloch, W. L. Queen, R. Krishna, J. M. Zadrozny, C. M. Brown, J. R. Long, *Science* **335**, 1606 (2012).



# A novel route to achieving high thermoelectric performance in oxide materials

L. K. Lamontagne,<sup>1,2</sup> G. Laurita,<sup>2</sup> M. W. Gaultois,<sup>2,3</sup> M. Knight,<sup>2</sup> C. M. Brown,<sup>4</sup> and R. Seshadri<sup>1,2,3</sup>

Thermoelectric materials are capable of converting waste heat into useable electricity and have the potential to increase the efficiency of many technologies. These materials develop an electrical potential when subjected to a temperature gradient because of the Seebeck effect and conversely develop a thermal gradient when subjected to an electrical potential through the Peltier effect. Devices made from such thermoelectric materials are currently used for refrigeration and heating and are being widely explored for waste heat recovery [1]. To be effective, these materials must have low electrical resistivities to conduct the charge carriers with minimal loss, and a high Seebeck coefficient to produce sufficient voltages. Additionally, they should have minimal lattice thermal conductivity, because the thermal gradient must be maintained. These properties combine in a dimensionless thermoelectric figure of merit  $zT$  given by the formula  $zT = S^2T/(\rho\kappa)$  where  $S$  is the Seebeck coefficient,  $\rho$  the electrical resistivity, and  $\kappa$  the total thermal conductivity, measured at temperature  $T$ . These properties are highly dependent, with metals possessing low electric resistivities yet near zero Seebeck coefficients, and insulators with large Seebeck coefficients but prohibitively high electrical resistivities. Finding new materials with optimal balances of these properties is key to understanding and improving thermoelectric efficiency.

Oxide materials possess many attractive qualities for use in high temperature waste heat recovery in air such as scavenging waste heat from car exhaust to improve vehicle fuel efficiency. They are preferred for such applications, as they are generally lightweight and air stable. Neutrons are crucial to structural studies of oxide thermoelectrics because the relatively low atomic number of the oxygen atoms makes X-ray characterization problematic. Oxide materials have not yet reached the level of performance of current state-of-the-art thermoelectrics, in part due to higher thermal conductivities compared to those of other material families, but additionally as a result of low power factors ( $S^2/\rho$ ). While many oxides possess favorable Seebeck coefficients, finding oxides with the necessary metallic conductivities while retaining these high Seebeck coefficients has proven to be difficult [2]. Currently, the highest-performing oxide materials are  $p$ -type complex cobalt oxides that sprung from the discovery of high thermopower in metallic  $\text{NaCoO}_2$  [3]. These compounds possess metallic resistivities yet retain high Seebeck coefficients. A key feature

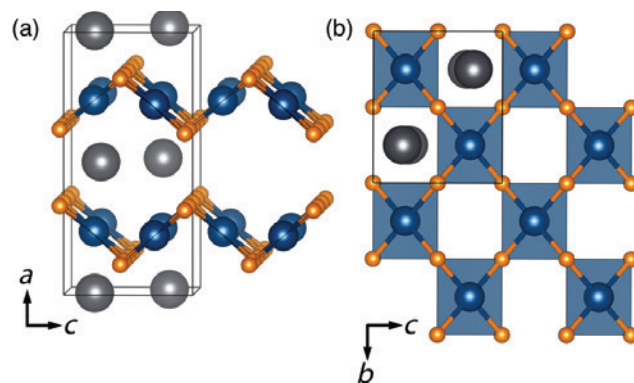


**FIGURE 1:** Depictions of the orthorhombic *Imma* (space group #74) crystal structure of  $\text{PbPdO}_2$ . (a) Corrugated layers of corner-connected  $\text{PdO}_4$  square planes, arranged in a checkerboard pattern as seen in the top view in panel (b). Pb atoms (large spheres) are four-coordinate with O, capping  $\text{PbO}_4$  square pyramids between the  $\text{Pd—O}$  layers.

in all of the promising cobalt oxides are  $\text{CoO}_2$  layers comprising mixed valent  $\text{Co}^{3+}$  and  $\text{Co}^{4+}$ . The highly correlated, mixed valent cobalt ions provide the necessary electrical properties and the layered structure results in a low thermal conductivity, giving rise to a modestly high thermoelectric performance.

$\text{PbPdO}_2$ , shown in Figure 1, is an attractive material for thermoelectric investigation because of the layered nature of the Pd square-planar units and heavy Pb atoms (suggesting potentially lower thermal conductivity) and the possibility for hole doping, which has been successful in other palladium oxide materials (suggesting control of electrical properties). In this study [4], we have prepared polycrystalline  $\text{PbPd}_{1-x}\text{Li}_x\text{O}_2$  ( $0 \leq x \leq 0.08$ ) in an effort to hole dope the material. Structural characterization was performed through neutron diffraction experiments collected on the BT-1 high resolution powder diffractometer and were coupled with electronic and thermal transport measurements to assess the thermoelectric performance.

Refinement of structural models against neutron diffraction patterns (Figure 2) was necessary not only because of the abundance of oxygen in the structure, but also to confirm the location and amount of Li substitution. Neutron diffraction

<sup>1</sup> Materials Department, University of California, Santa Barbara, CA 93106

<sup>2</sup> Materials Research Laboratory, University of California, Santa Barbara, CA 93106

<sup>3</sup> Department of Chemistry and Biochemistry, University of California, Santa Barbara, CA 93106

<sup>4</sup> NIST Center for Neutron Research, National Institute of Standards and Technology, Gaithersburg, MD 20899

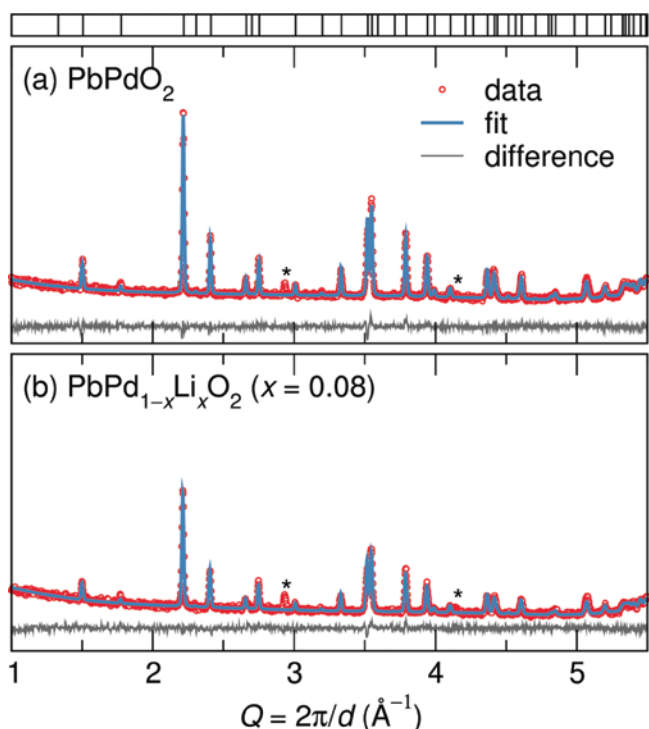


**FIGURE 2:** Refinements of neutron diffraction data of (a) stoichiometric  $\text{PbPdO}_2$  and (b) the nominally Li-substituted  $\text{PbPd}_{0.92}\text{Li}_{0.08}\text{O}_2$  (Li mole fraction of 8 %), showing the quality of the fits. The top panel indicates the Bragg reflection marks for  $\text{PbPdO}_2$ . Asterisks mark the positions of reflections from the vanadium sample can.

revealed that for a nominal  $x = 0.08$  sample, a Li content of  $x = 0.04$  was achieved, and confirmed that it was substituted onto the Pd site in the material. This successful incorporation of Li had a dramatic effect on the electrical properties, shown in Figure 3. It was observed that even for the nominal  $x = 0.02$  Li substitution, the material is metallic, as the resistivity dropped by an order of magnitude compared to that of stoichiometric  $\text{PbPdO}_2$ . The resistivity decreases slightly further for the  $x = 0.04$  sample, but remains roughly unchanged for higher substitution amounts, supporting the refined Li occupancy values from neutron diffraction. The Seebeck coefficient for the Li-substituted samples remains greater than  $100 \mu\text{V/K}$  at room temperature. The Seebeck coefficient increases with increasing temperature, approaching  $200 \mu\text{V/K}$  at  $800 \text{ K}$ . The electrical resistivity and Seebeck coefficient of these Li-substituted materials is nearly identical to values reported for polycrystalline  $\text{NaCoO}_2$  [5]. The origins of the electrical properties in our materials differ from those of the cobalt oxides, suggesting alternate methods for achieving high thermoelectric performance in oxides.

The thermal conductivity was measured in order to calculate  $zT$  and evaluate the overall thermoelectric performance of the stoichiometric and  $x = 0.04$  materials. At the highest measured temperature, the values for both samples approach  $2.5 \text{ W m}^{-1} \text{ K}^{-1}$ . Combined with the electrical properties, a  $zT = 0.12$  at  $600 \text{ K}$  was observed for the  $x = 0.04$  sample. The material is stable to

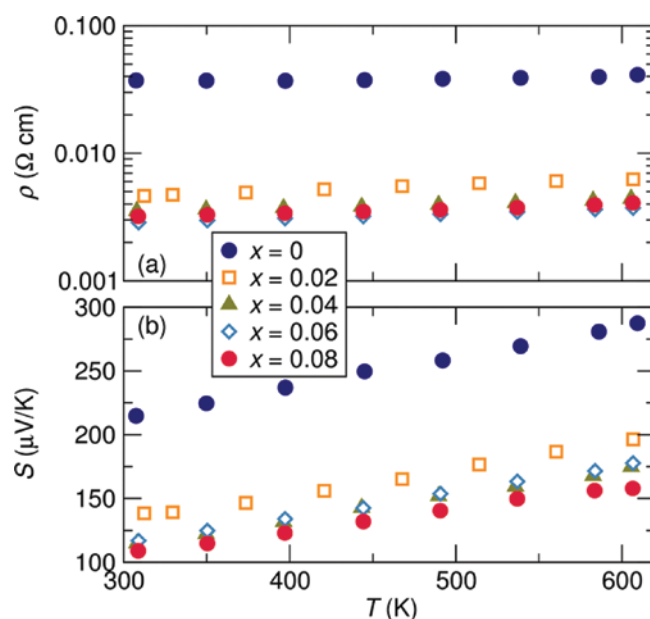


**FIGURE 3:** (a) Resistivity and (b) Seebeck coefficient for  $\text{PbPd}_{1-x}\text{Li}_x\text{O}_2$ . The resistivity drops by one order of magnitude with a mole fraction of 2 % Li-substitution ( $x$ ), while the Seebeck coefficient drops by  $100 \mu\text{V/K}$ . The Seebeck coefficients of the Li-substituted samples increase with temperature and approach  $200 \mu\text{V/K}$  at  $600 \text{ K}$ .

temperatures higher than those within experimental constraints, and this value is predicted to be even greater at more elevated temperatures.

In conclusion, we report the structural characterization and thermoelectric properties of Li-substituted  $\text{PbPO}_2$ . Neutron diffraction played an essential role in confirming the substitution amount and location of the Li dopant. Thermoelectric measurements indicate that our materials display similar electrical properties to those of some of the current high performing oxide thermoelectrics. Our findings suggest potentially new avenues to achieving high-performing oxide thermoelectric materials and encourage the search for such properties in oxides of metals more earth-abundant than the ones studied here.

## References

- [1] G. J. Snyder, E. S. Toberer, *Nat. Mater.* **7** (2), 105 (2008).
- [2] M. W. Gaultois, T. D. Sparks, C. K. H. Borg, R. Seshadri, W. D. Bonificio, D. R. Clarke, *Chem. Mater.* **25** (15), 2911 (2013).
- [3] I. Terasaki, Y. Sasago, K. Uchinokura, *Phys. Rev. B* **56** (20), R12685 (1997).
- [4] L. K. Lamontagne, G. Laurita, M. W. Gaultois, M. Knight, L. Ghadbeigi, T. D. Sparks, M. E. Gruner, R. Pentcheva, C. M. Brown, R. Seshadri, *Chem. Mater.* **28** (10), 3367 (2016).
- [5] K. Fujita, T. Mochida, K. Nakamura, *Jpn. J. Apply. Phys.* **40** (7R), 4644 (2001).

# Realization of ground-state artificial skyrmion lattices at room temperature

D. A. Gilbert,<sup>1,2</sup> B. B. Maranville,<sup>2</sup> A. L. Balk,<sup>3,4</sup> B. J. Kirby,<sup>2</sup> P. Fischer,<sup>5,6</sup>  
D. T. Pierce,<sup>3</sup> J. Unguris,<sup>3</sup> J. A. Borchers,<sup>2</sup> and K. Liu<sup>1</sup>

Moore's Law has been the icon of the computer revolution for nearly 50 years, but recent challenges with heat management and miniaturization have signaled its impending end. Spintronics – data and logic technologies that use the electron spin, in addition to the electron charge – offer a new approach to ultra-low power information technologies that may reinvigorate Moore's Law. One promising spintronic technology is the magnetic skyrmion. Skyrmions are specialized configurations of magnetic moments into topologically-protected structures; a typical skyrmion structure, shown in Fig. 1, possesses a core and perimeter with opposite out-of-plane spin orientations, and a closed, continuous in-plane winding of magnetic moments between. These structures can be realized on the atomic scale, moved with very low electrical current densities, and are robust against moderate perturbations including stray fields and system defects. These make skyrmions very attractive for ultra-low power, high-density data storage and logic technologies. A key challenge to the development of skyrmion-based memory and logic devices is achieving skyrmion structures stable at ambient conditions (room temperature and no magnetic field).

Recently, we have realized ground-state magnetic skyrmions stable at ambient conditions by nanopatterning [1]. Specifically, cobalt nanodots with diameters of 560 nm and heights of 30 nm are patterned. The magnetic 'vortex' configuration within these dots, shown in Fig. 1 (red), form a closed winding structure, with an out-of-plane core, which is stable over a wide range of temperatures. However, a vortex lacks an out-of-plane perimeter, distinguishing it from a skyrmion. By placing a vortex-state nanodot on top of a magnetic film, the loop structure and core can be imprinted into the film. Thus, by designing a film with an out-of-plane orientation, the imprinted structure at the interface has a closed loop structure with an out-of-plane core and perimeter, e.g. a skyrmion. To prove this claim and demonstrate its viability for application, three pieces of evidence must be shown: (1) the direction of circulation of the loop structure, called the circularity, must be controllable, (2) the orientation of the core, called the polarity, relative to the perimeter must be controllable, and (3) the loop structure must, in-fact, be imprinted into the film underlayer.

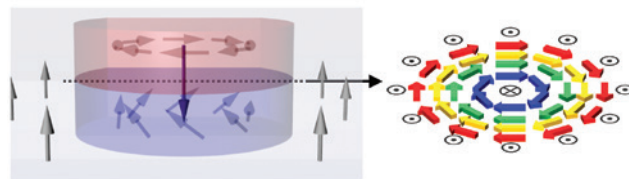


**FIGURE 1:** Diagram of an artificial skyrmion. Vortex dot is shown in red. The imprinted region (blue) that forms a skyrmion with the underlayer is shown in grey.

Samples were prepared by a three-step process. In step one, multilayer films of  $[\text{Co}(0.5 \text{ nm})/\text{Pd}(1 \text{ nm})]_{10}$  were grown on naturally oxidized Si substrates; the multilayer structure gives the film a preferred out-of-plane orientation - called the perpendicular magnetic anisotropy (PMA). In the second step, hexagonal arrays of nano-holes with a diameter of 560 nm and center-to-center spacing of 1000 nm were patterned into a  $\approx 400$  nm thick polymer layer that was spin-coated onto the Co/Pd film. The holes are shaped like a circle, with one side made flat; the asymmetric structure has been previously used to realize circularity control. Next, the sample was irradiated by 1 keV  $\text{Ar}^+$  plasma, which suppresses the PMA in the regions exposed by the holes, while the regions still protected by polymer retain their PMA. During the third step, 32 nm of Co was deposited into the holes and the polymer mask removed, realizing asymmetric Co dots grown over the irradiated regions. Once the sample was fabricated, the skyrmion state was configured by a designed field sequence. First, the Co/Pd underlayer was saturated in the positive out-of-plane direction using a large out-of-plane magnetic field. Then, the out-of-plane field was removed and a small in-plane magnetic field was applied to saturate the dots parallel to the flat edge. At this point a small out-of-plane magnetic field was applied anti-parallel to the underlayer. The in-plane magnetic field was removed, nucleating a vortex, with the core biased to be anti-parallel to the underlayer. Lastly, the out-of-plane magnetic field was removed, leaving the system at remanence (no magnetic field) in a vortex state dot, with a core anti-parallel to the underlayer, and the region under the dot having no PMA.

<sup>1</sup> University of California, Davis, CA 95616

<sup>2</sup> NIST Center for Neutron Research, National Institute of Standards and Technology, Gaithersburg, MD 20899

<sup>3</sup> Center for Nanoscale Science and Technology, National Institute of Standards and Technology, Gaithersburg, MD 20899

<sup>4</sup> University of Maryland, College Park, MD 20742

<sup>5</sup> Lawrence Berkeley National Laboratory, Berkeley, CA 94720

<sup>6</sup> University of California, Santa Cruz, CA 94056



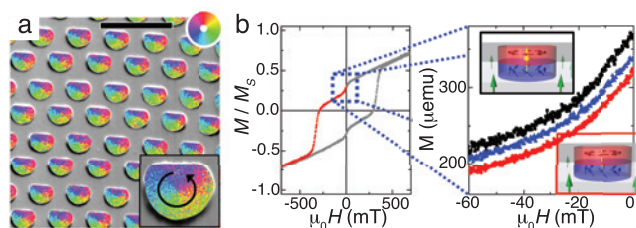


**FIGURE 2:** (a) SEMPA image of the asymmetric dot array. Color wheel indicates magnetization direction. (b) Remnant magnetization curve, with the core parallel, anti-parallel, and random relative to the underlayer, shown in black, red and blue, respectively ( $1 \text{ emu} = 10^{-3} \text{ A m}^2$ ).

As stated above, circularity control was achieved by using the asymmetric dot structure. Applying an in-plane magnetic field parallel to the flat edge of the dot defines the nucleation site for the vortex and thus the circularity. Micrographs taken using scanning electron microscopy with polarization analysis (SEMPA) are shown in Fig. 2(a). The colors indicate the direction of the magnetization; the common color wheel for each of the dots indicates a common circularity of the magnetization. Other magnetic imaging technique and magnetometry measurements confirm the circularity control seen in SEMPA.

Recalling the magnetic field sequence to set the skyrmion state, polarity control is determined during the vortex nucleation by the small magnetic field applied anti-parallel to the underlayer. To demonstrate polarity control, the remanent magnetization was measured with the core parallel and anti-parallel to the underlayer. Specifically, the sample was prepared as discussed above, with the core anti-parallel to the underlayer and the out-of-plane magnetization measured as the magnetic field was decreased from remanence to negative saturation. In this case the magnetization of the core and perimeter are opposite, and thus subtract when measured together. Then, the sample was prepared again, but with the biasing field applied parallel to the underlayer. In contrast to the former case, the magnetization from the core and underlayer are expected to be parallel and add together. In a third measurement no biasing field was applied and the polarity was random. Indeed, as shown in Fig. 2(b), the skyrmion state, with the core and underlayer anti-parallel, has the smallest magnetization; the vortex state with the core and the underlayer oriented parallel has the largest magnetization; the random polarity falls in-between the parallel and anti-parallel configurations. This confirms the biasing field indeed defines the polarity.

Lastly, and arguably most crucially, the imprinting of the skyrmion was demonstrated using polarized neutron reflectometry (PNR), performed on the MAGIK reflectometer. PNR is a technique that uses scattering to extract depth-profiles from layered systems and possesses sensitivity to nuclear and magnetic features. The measured data are shown as dots in Fig. 3(a). A model was made to simulate the nominal structure and the reflectivity pattern calculated. By iteratively changing the model and comparing the calculated reflectivity to the data, the model converges on an accurate representation of the physical system. The

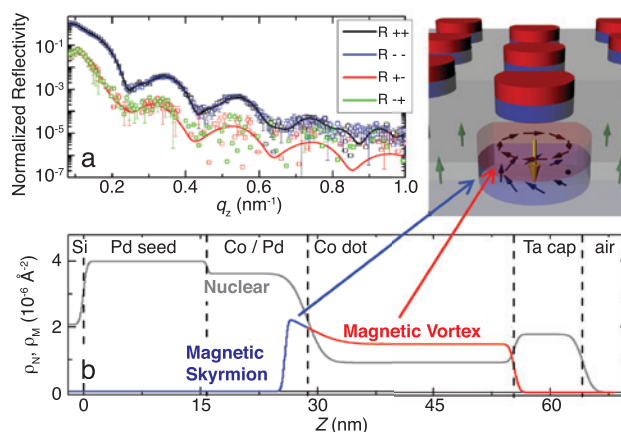


**FIGURE 3:** (a) Measured (dots) and simulated (lines) reflectometry, and (b) converged depth profile.

converged model is shown in Fig. 3(b), and the corresponding reflectometry is shown as the solid lines in Fig. 3(a), which agree well with the experimental data ( $\chi^2 < 1.2$ ). The converged model correctly identifies the designed structure, giving confidence in its accuracy. More importantly, the model identifies the magnetization of the Co dot - as expected - but also shows that the magnetization extends  $\approx 3 \text{ nm}$  below the [Co/Pd]/Co-dot interface. This imprinted magnetic feature is the first direct evidence of the imprinted magnetic skyrmion. Further, the imprinted skyrmion is expected to be stable while the dots and underlayer are stable (ambient conditions up-to approximately  $300^\circ \text{C}$ , and  $300 \text{ mT}$ ). Theoretical modeling using NIST's object oriented micromagnetic framework (OOMMF) confirms that the imprinted structure extends  $2 \text{ nm}$  into the underlayer.

In summary, we have successfully achieved room temperature artificial skyrmion lattices in the ground state over extended areas, defining a platform for exploring skyrmion properties and behaviors as well as the use of skyrmion lattices in novel technological concepts. The system is constructed by fabricating circularity controlled Co nanodots on a selectively irradiated Co/Pd underlayer with PMA. Circularity control is imposed by the fabrication of asymmetric dots and confirmed by microscopy. Polarity control is realized by the application of a small out-of-plane magnetic field during the vortex nucleation, and demonstrated in the magnetization curves. The imprinted skyrmion lattice in the Co/Pd is directly confirmed by PNR, and is quantitatively consistent with micromagnetic simulations. These artificially constructed skyrmion lattices are stable over a wide range of magnetic fields and temperatures, including room temperature and zero magnetic field. These foundational results present a new path in skyrmion research on the meso-scale, at and above room temperature.

## Reference

- [1] D. A. Gilbert, B. B. Maranville, A. L. Balk, B. J. Kirby, P. Fischer, D. T. Pierce, J. Unguris, J. A. Borchers, K. Liu, Nature Communications **6**, 8462 (2015).

# Combined time-reversal and lattice symmetry breaking in a cubic antiferromagnet GdPtBi

T. Suzuki,<sup>1</sup> R. Chisnell,<sup>2</sup> A. Devarakonda,<sup>1</sup> Y.-T. Liu,<sup>1</sup> W. Feng,<sup>3</sup> D. Xiao,<sup>4</sup> J. W. Lynn,<sup>2</sup> and J. G. Checkelsky<sup>1</sup>

**M**agnetic order, electronic structure, and electrical transport are strongly intertwined in correlated materials. The symmetries of a particular correlated state dictate different classes of charge transport phenomena that may be observed. For example, in a material that has ferromagnetic order where time-reversal symmetry is broken, electrons acquire a velocity transverse to electric current and magnetization. This effect (known as the anomalous Hall effect) originates from both spin-dependent scattering and intrinsic quantum mechanical properties of the electronic wave function (Berry curvature) of the filled bands. The latter contribution becomes significant if the electronic band structure has band-crossing points that develop energy gaps with the breaking of time-reversal symmetry. In the fully quantum limit in two dimensions (2D) where the Fermi level is located within such a gapped region, the anomalous Hall conductivity is quantized in units of  $e^2/h$ , where  $e$  is electron charge and  $h$  is Planck's constant, which has been observed experimentally in the ferromagnetic topological insulator  $\text{Cr}_x(\text{Bi,Sb})_2\text{Te}_3$  [1].

More complex ordered materials such as antiferromagnets can also exhibit the anomalous Hall effect; this is most commonly seen when the constituent spins have a non-coplanar ordering pattern with finite net scalar spin chirality  $\chi_{ijk} = \vec{S}_i \cdot (\vec{S}_j \times \vec{S}_k)$ , where  $\vec{S}_n$  are spins [2]. In addition, if the spins have an ordering pattern that breaks the combined time-reversal and lattice symmetry of the material, the Berry curvature of the filled bands can contribute to the anomalous Hall effect as in ferromagnets [3]. This last phenomenon has been recently explored in materials with a kagome network, but its applicability to a general class of materials is an open question.

Recently, we found that the antiferromagnet GdPtBi shows a large anomalous Hall conductivity and used elastic neutron scattering and electronic structure calculations to confirm it belongs to this newest class of effects [4]. GdPtBi has a half-Heusler structure composed of a face centered cubic Gd sublattice responsible for magnetism of the system and a nonmagnetic zinc blende PtBi sublattice (Fig. 1). Theoretical calculations have revealed that the electronic band structure near the Fermi level is mainly determined by the PtBi sublattice and has band touching around

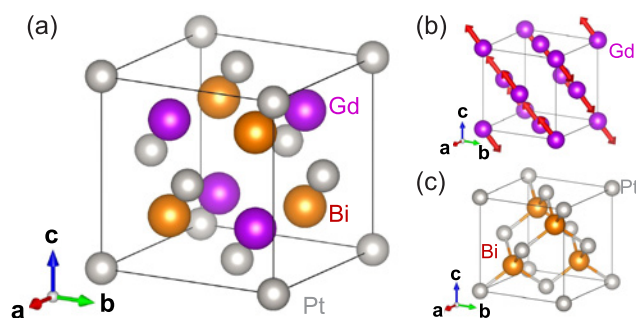


**FIGURE 1:** (a) Crystal structure of GdPtBi, which is composed of (b) a magnetic Gd face centered cubic sublattice and (c) a PtBi zinc-blende sublattice. Red arrows in (b) show the type-II antiferromagnetic ordering pattern.

the Fermi level similar to that of the topologically non-trivial material HgTe. A critical difference between HgTe and GdPtBi is the existence of localized magnetic moments, which affect the electronic structure via magnetic ordering. It is known that this compound exhibits antiferromagnetic ordering below  $T_N = 9$  K, where the Gd moments order ferromagnetically in the (111) plane and are coupled antiferromagnetically along the [111] direction (called type-II ordering) in zero magnetic field, as shown in Fig. 1(b) [5]. From the Curie-Weiss fitting of the high temperature magnetization data, the Weiss temperature  $Q_{CW} \gg -38$  K. This gives a moderate frustration parameter  $f = \theta_{CW}/T_N \approx 4$ , implying that there are other magnetically ordered states with comparable energy. It has been proposed theoretically for the face centered cubic structure that such a spin system may exhibit an anomalous Hall effect originating from scalar spin chirality  $\chi_{ijk}$  if the spins order in a multiple- $q$  spin structure with  $q \parallel \langle 001 \rangle$  [6]. To elucidate whether the observed anomalous Hall effect originates from the scalar spin chirality or the Berry curvature mechanisms, the magnetic structure in finite field needs to be determined experimentally.

We have performed elastic neutron scattering measurements using  $^{160}\text{Gd}$ -enriched GdPtBi single crystals on the triple-axis spectrometer BT-7 at the NIST Center for Neutron Research. Figure 2(a) shows the temperature dependence of the (0.5 0.5 0.5) magnetic Bragg peak intensity in zero magnetic field. This peak

<sup>1</sup> Massachusetts Institute of Technology, Cambridge, MA 02139

<sup>2</sup> NIST Center for Neutron Research, National Institute of Standards and Technology, Gaithersburg, MD 20899

<sup>3</sup> Beijing Institute of Technology, Beijing 100081, China

<sup>4</sup> Carnegie Mellon University, Pittsburgh, PA 15213



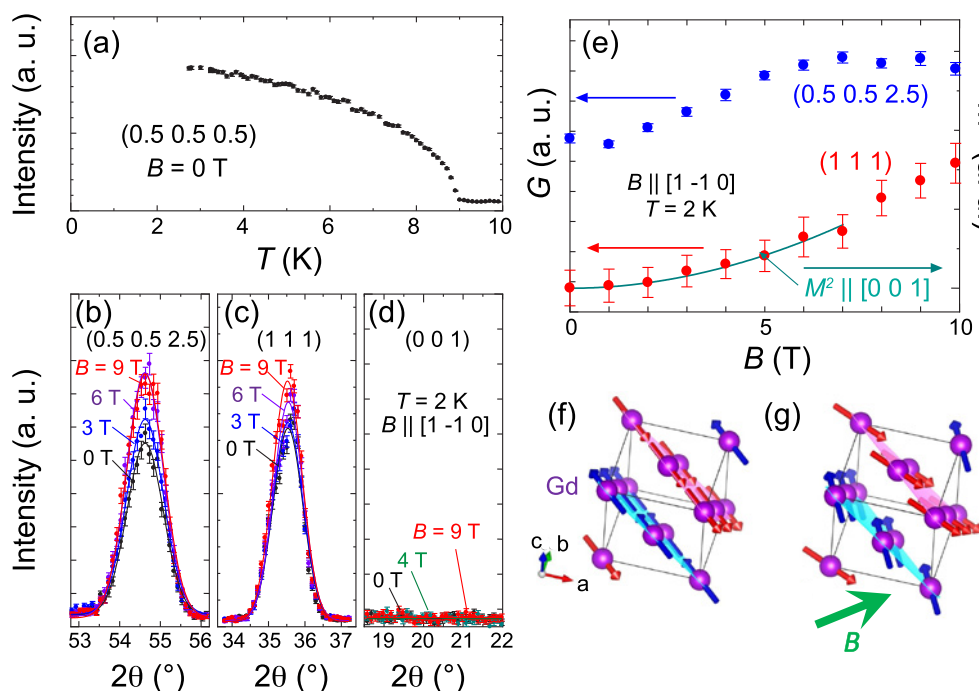


**FIGURE 2:** (a) Temperature dependence of the (0.5 0.5 0.5) magnetic Bragg peak intensity in zero magnetic field. Magnetic ordering occurs at  $T_N = 9$  K. (b), (c), and (d) show the profile of the (0.5 0.5 2.5), (1 1 1), and (0 0 1) Bragg peaks in several magnetic fields, respectively. The solid lines denote the fitting results of the profile to a single Gaussian function. (e) Integrated Gaussian area of (0.5 0.5 2.5) and (1 1 1) Bragg peaks as a function of magnetic field,  $G$ . The solid line shows the square of magnetization. (f) and (g) show the deduced magnetic structure in zero magnetic field and finite field, respectively.

is allowed in the presence of type-II antiferromagnetic ordering. The intensity increases with decreasing temperature below  $T_N = 9$  K as expected. The evolution of the magnetic Bragg peak (0.5 0.5 2.5) from the type-II ordering with applied magnetic field is shown in Fig. 2(b). The intensity increases up to 6 T and shows saturation above that field. This tendency is seen more clearly in the integrated Gaussian area obtained by fitting the profile to a single Gaussian function versus magnetic field, as shown in Fig. 2(e). We have performed the measurements at all half-integer (HHL) with  $Q < 3.7 \text{ \AA}^{-1}$  and observed the same trend. Figure 2(c) shows the profile of the (111) peak originating from the nuclear Bragg scattering as well as the magnetic one from the ferromagnetic component of the spin ordering, whose intensities are additive. The magnetic intensity increases with increasing magnetic field and the increase of the integrated Gaussian area scales with the square of the magnetization (Fig. 2(e)). We have also examined the possibility of the multiple- $q$  spin structure with  $q \parallel \langle 001 \rangle$ , but no evidence for the presence of such a structure was obtained, as shown in Fig. 2(d).

The spin structure deduced from the obtained results is shown in Figs. 2(f) and 2(g). The spins align antiferromagnetically in zero field and cant toward the magnetic field direction in finite field. As the canting represents a ferromagnetically ordered component in the spin structure, the symmetry requirement for finite anomalous Hall effect (that the combined time-reversal and lattice symmetry should be broken) is fulfilled.

Furthermore, spin-dependent electronic band calculations based on the magnetic structure revealed that the band crossing point existing in the collinearly ordered state is lifted along the high symmetry direction and Weyl points possibly appear by spin canting caused by applied magnetic field. Both features in the electronic structure may contribute to the Berry curvature and the resulting large anomalous Hall effect. This mechanism that has been extensively investigated in ferromagnetic system is therefore now a new target for study in antiferromagnets which host a rich variety of complex orders. The current study extends the generality of the mechanism to the half-Heusler antiferromagnet and demonstrates the ubiquity of the role of Berry phase in symmetry-broken system.

## References

- [1] C. -Z. Chang *et al.*, Science **340**, 167 (2013).
- [2] N. Nagaosa *et al.*, Rev. Mod. Phys. **82**, 1539 (2010).
- [3] H. Chen, Q. Niu, A. H. MacDonald, Phys. Rev. Lett. **112**, 017205 (2014).
- [4] T. Suzuki *et al.*, accepted in Nature Phys. DOI:10.1038/NPHYS3831.
- [5] R. A. Müller *et al.*, Phys. Rev. B **90**, 041109(R) (2014).
- [6] R. Shindou, N. Nagaosa, Phys. Rev. Lett. **87**, 116801 (2001).

# Beyond the interface limit: structural and magnetic depth profiles of voltage-controlled magneto-ionic heterostructures

D. A. Gilbert,<sup>1</sup> A. J. Grutter,<sup>1</sup> E. Arenholz,<sup>2</sup> K. Liu,<sup>3</sup> B. J. Kirby,<sup>1</sup> J. A. Borchers,<sup>1</sup> and B. B. Maranville<sup>1</sup>

Oxidation is a common process that changes virtually every quality of a material, including optical, mechanical, electrical, thermal, and magnetic properties. For example, metals are typically shiny, ductile, conductive, and can be magnetic, while metal oxides can be matte or transparent, brittle, insulating, and are frequently non-magnetic. Controlling oxidation by electric fields offers an opportunity for manipulating the material properties with the flip of a switch. This is the premise behind both memristors, which use a voltage to control oxygen distributions and tune electrical conductivity, and magneto-ionic devices [1-5], which similarly use a voltage to tune magnetic properties. These technologies work by recognizing that metal oxides are ionic solids with oxygen atoms that have a net charge and thus are sensitive to electric fields. Applying a strong electric field can thus alter the oxygen ion distribution, changing the material properties. Recent investigations [1, 2] have demonstrated magneto-ionic control in ultra-thin Hall bar structures (thicknesses < 1 nm). In these studies, the films prefer to have the magnetization oriented out of the plane of the film; using an electric field to drive oxygen into the interface with a neighboring oxide material causes the magnetization to rotate into the plane of the film. Devices built on this control have been proposed for ultra-high density, low-power data storage technologies. However, for broader applications, ion-based control must be demonstrated in thicker films with bulk-like properties, and it is unclear how the magneto-ionic control mechanism works in this regime.

In this work, we demonstrated magneto-ionic effects in comparably thick (15 nm) cobalt films [5]. Using an applied voltage, oxygen was driven from a  $\text{GdO}_x/\text{AlO}_x$  film into the neighboring Co film, which then becomes non-ferromagnetic  $\text{CoO}_x$ . Magnetometry revealed that, while some of the magnetic properties are recovered, others are not. Using polarized neutron reflectometry (PNR), the depth-resolved oxygen distribution and magnetization were directly mapped, providing a physical picture to explain the observed behavior.

Thin-films with a structure  $\text{Si}/\text{Pd}(50\text{ nm})/\text{AlO}_x(1000\text{ nm})/\text{GdO}_x(2\text{ nm})/\text{Co}(15\text{ nm})/\text{Pd}(20\text{ nm})$  were grown by sputtering and e-beam evaporation at the Center for Nanoscale Science and Technology. Electro-thermal (E+T) conditioning was performed by heating the sample to 230 °C and applying 40 V across the Pd layers for 15 min. The measured PNR reflection and

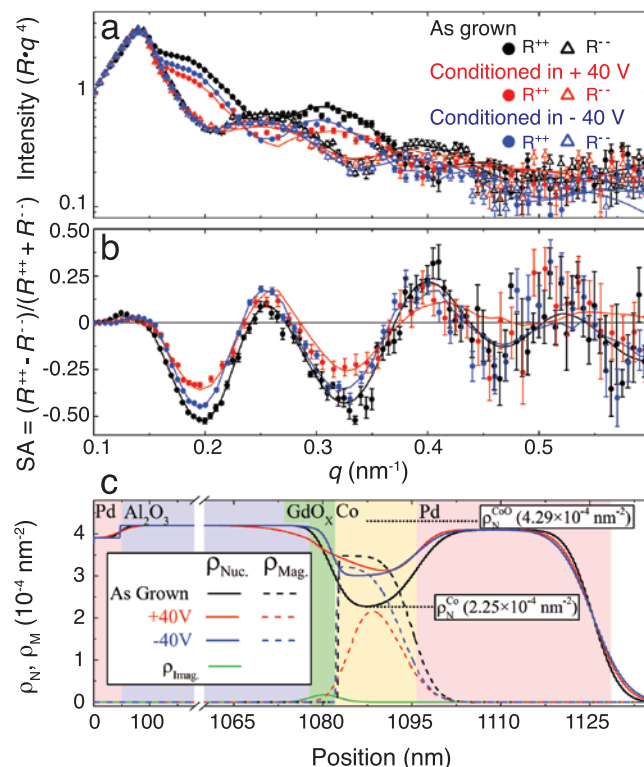


**FIGURE 1:** (a) Fitted PNR data scaled by  $q^4$  and (b) spin asymmetry for the sample as-grown and after electro-thermal conditioning. (c) Depth-dependent real and imaginary nuclear SLD ( $\rho_N$  and  $\rho_{\text{imag}}$ ), and magnetic SLD ( $\rho_M$ ) extracted from the PNR. In (a) and (b) the experimental data are shown as symbols, and the lines are fits corresponding to the depth profile shown in (c).

spin-asymmetry (SA) for the as-grown sample, the sample after applying + 40 V (anode on the top surface), and sequential - 40 V are shown in Figs. 1(a) and (b), respectively. The SA, which is proportional to the product of the magnetization and nuclear scattering length density (SLD), is shown to decrease after the + 40 V treatment and partly recover after subsequently applying - 40 V. Using the Refl1d software package, models for the three treatments (as-grown, after + 40 V, and after sequential +/- 40 V) were fitted in parallel, Fig. 1(c). The fitted model for the as-grown sample closely matches the designed structure and the bulk nuclear SLD for these materials, lending confidence to its accuracy. After the initial + 40 V treatment the nuclear SLD increases in the Co layer, the  $\text{GdO}_x/\text{Co}$  interface becomes much broader, and the

<sup>1</sup> NIST Center for Neutron Research, National Institute of Standards and Technology, Gaithersburg, MD 20899

<sup>2</sup> Advanced Light Source, Lawrence Berkeley National Laboratory, Berkeley, CA 94720

<sup>3</sup> University of California, Davis, CA 95616

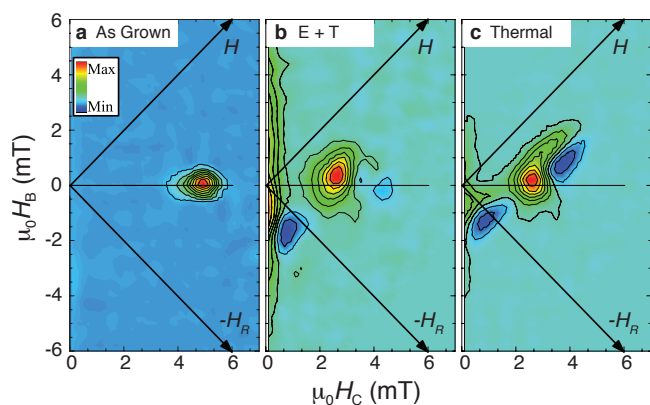


**FIGURE 2:** FORC distributions for the sample (a) as-grown, (b) after +/- 40 V conditioning, and (c) after thermal-only conditioning.

magnetic SLD decreases (38 %), most prominently at the interface (80 %). This is consistent with oxygen being moved by the electric field from the  $\text{GdO}_x$  layer into the Co layer, forming non-magnetic  $\text{CoO}_x$ . Subsequently applying - 40 V restored the sharp nuclear interface and most of the magnetism (92 %). However, oxygen migration was irreversible for thicknesses greater than 10 nm. Measurements performed using a thermal-only treatment showed a much smaller effect, demonstrating that the electric field moves oxygen into and out of the Co layer depending on its polarity.

Magnetic first order reversal curve (FORC) measurements of the as-grown sample, the +/- 40 V sample, and a thermally treated sample (230 °C for 30 minutes) are shown in Fig. 2. The FORC plots, in a general sense, are a map of all hysteretic events that exist within a system and provide detailed information regarding the magnetic reversal process. The FORC distribution for the as-grown sample shows only a single feature, indicating a single magnetic phase. By comparison the electro-thermal and thermal-only samples show two features, with a new feature located at  $H_C = 0$  that specifically identifies reversible features. In general, reversible features indicate the absence of hysteresis and are often manifest when the magnetism is measured along a hard axis. We suggest that the new reversible phase is the result of a decoupling between grains within the Co film plane. Specifically, the film is comprised of many nano-scale magnetic grains, each with their own randomly oriented magnetocrystalline anisotropy. Typically, magnetic exchange coupling between neighboring grains can cause the film to behave as a single coherent structure. The small amount of residual oxygen may be interrupting the exchange interaction, allowing the magnetocrystalline anisotropy of each grain to dictate its orientation.

We suggest the reduced exchange interaction and irreversibility for thicknesses of > 10 nm is due to a screening effect of the electric field, as shown in Fig. 3. Specifically, the + 40 V electro-thermal treatment moved oxygen deep into the film, diffusing quickly at grain surfaces and more slowly in the bulk. During the - 40 V treatment the oxygen migrated quickly off of the grain surface,

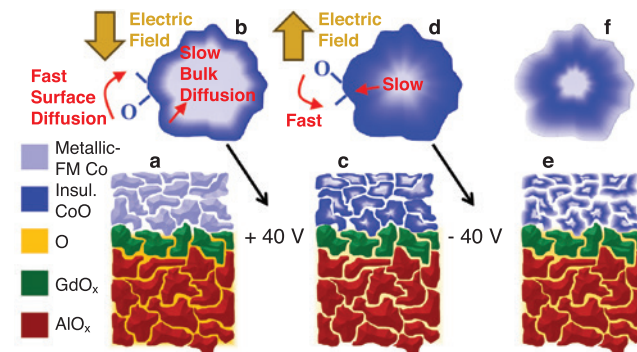


**FIGURE 3:** Cross-section view of (a) the as grown film, (b) a single grain during + 40 V treatment, (c) the film after + 40 V treatment, (d) a single grain during subsequent - 40 V treatment, and (e, f) cross section and grain after - 40 V treatment. Colors identify  $\text{AlO}_x$  (red),  $\text{GdO}_x$  (green), metallic FM Co (light blue), insulating non-FM  $\text{CoO}_x$  (blue), and interstitial oxygen (orange); large gold arrow indicates the electric field. Illustration (e) emphasizes fast surface migration, identified by the red arrows, and slow bulk diffusion, indicated by the grey arrows.

leaving a metallic Co shell. This shell screens the electric field via the Faraday effect, thus halting any further migration and trapping oxygen within each grain and deeper in the film. This mechanism suggests an unexplored role of the microstructure, and a potential limit to these technologies.

In summary, we have realized a thin film magneto-ionic device built on a thick (15 nm) Co film. Semi-reversible control of the magnetism resulting from oxygen migration was demonstrated and directly mapped using polarized neutron reflectometry. First order reversal curve measurements showed that the nominally similar sample possessed two phases, while the as-grown sample had only one. Based on a fundamental understanding of the nature of electric fields and oxygen migration, a physical picture was presented which supports the results. This work thus demonstrates that ionic devices with 'active' layers thicker than a few atom layers are still viable, thus opening new opportunities for future ion-based technologies.

## References

- [1] U. Bauer, L. Yao, A. J. Tan, P. Agrawal, S. Emori, H. L. Tuller, S. v. Dijken, G. S. D. Beach, *Nature Mater.* **14**, 174 (2015).
- [2] C. Bi, Y. Liu, T. Newhouse-Ilige, M. Xu, M. Rosales, J. W. Freeland, O. Mryasov, S. Zhang, S. G. E. t. Velthuis, W. G. Wang, *Phys. Rev. Lett.* **113**, 267202 (2014).
- [3] D. A. Gilbert, J. Olamit, R. K. Dumas, B. J. Kirby, A. J. Grutter, B. B. Maranville, E. Arenholz, J. A. Borchers, K. Liu, *Nature Commun.* **7**, 11050 (2016).
- [4] A. J. Grutter, D. A. Gilbert, U. S. Allan, E. Arenholz, B. B. Maranville, J. A. Borchers, Y. Suzuki, K. Liu, B. J. Kirby, *Appl. Phys. Lett.* **108**, 082405 (2016).
- [5] D. A. Gilbert, A. J. Grutter, E. Arenholz, K. Liu, B. J. Kirby, J. A. Borchers, B. B. Maranville, *Nature Commun.* **7**, 12264 (2016).



# The vibrations of methylammonium ions as local probe of ferroelectric ordering in hybrid halide perovskite; a combined neutron scattering and first-principles study

B. Ipek,<sup>1,2</sup> L. Hung<sup>1</sup>, C. M. Brown<sup>1,2</sup> T. Yildirim,<sup>1</sup> B. J. Foley,<sup>3</sup> T. Chen,<sup>4</sup> J. J. Choi,<sup>3</sup> and S. H. Lee<sup>4</sup>

Solar cells based on the hybrid halide perovskite  $\text{CH}_3\text{NH}_3\text{PbI}_3$  have achieved efficiencies as high as 20 %. Despite tremendous work on these systems [1], it is still not clear what role the  $\text{CH}_3\text{NH}_3^+$  (methylammonium, MA) cations play in enhancing solar cell performance. For instance, while the most stable form of  $\text{MAPbI}_3$  is non-polar, it has been suggested that the organic cation dipoles may also orient into ferroelectric domains, which affect the electronic band structure and slow carrier recombination. The ability to probe local dipole dynamics and ferroelectricity would greatly improve our understanding and assessment of this hypothesis. To shed some light on the influence of the MA cations, we present a combined neutron scattering and first-principles computation study of the structure and dynamics of  $\text{MAPbI}_3$  [2].

The temperature-dependent powder diffraction data from  $\text{MAPbI}_3$  show two phase transitions (Fig. 1). For  $T > 300$  K to 335 K, the structure is cubic with space group  $P4mm$ . The system changes to a tetragonal phase with symmetry  $I4cm$  below 300 K, and with further cooling below  $\approx 160$  K transforms to an orthorhombic phase with space group  $Pnma$ . The lattice parameters, bond angles, and atomic positions were determined by full structural Rietveld refinement [2]; the refinement and difference plots indicate a very good fit to the powder diffraction data (Fig. 2). Focusing on the low-temperature orthorhombic phase, each unit cell contains four symmetry-related  $\text{CH}_3\text{NH}_3^+$  molecules with C-N bonds confined to the ac-plane (see insets to Fig. 1 and Fig. 2). The molecules at sites 1-4 (inset to Fig. 2) have orientations L (C to the left of N in the c-axis projection) or R (C to the right of N). The non-polar ground state is labeled LLRR. We also examined three other symmetry-distinct orientations of the four dipole moments in the unit cell, i.e., RRRR, LLRL, and LRRR. First-principles computations show that the energy difference between the non-polar LLRR phase and the other possible ferroelectric phases is quite small, on the order of a few meV per atom, and the barrier between them is around 0.3 eV. Hence local dipole dynamics should be present, and less commonly, ferroelectric domains may form.

The observed inelastic neutron scattering (INS) spectrum is shown in Figure 3 in comparison to computed one- and two-phonon spectra for the non-polar (LLRR) orientation. The agreement

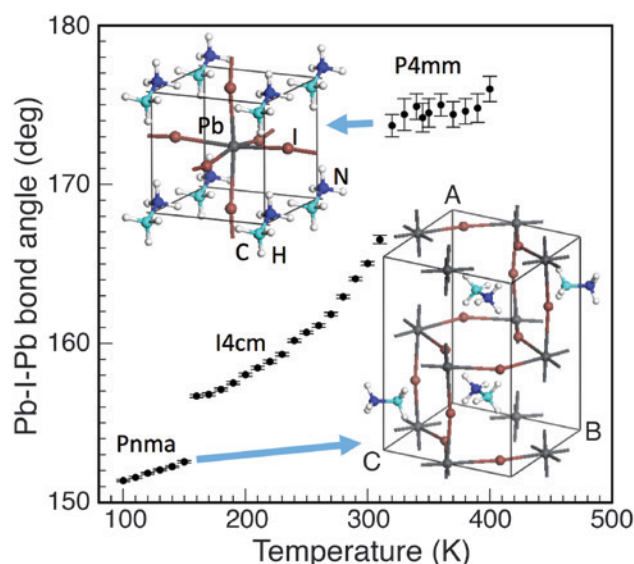


**FIGURE 1:** The Pb-I-Pb bond angle versus temperature, indicating two successive phase transitions between cubic ( $P4mm$ ), tetragonal ( $I4cm$ ), and orthorhombic ( $Pnma$ ) symmetries. The insets show the cubic (top) and low-temperature (bottom) structures of  $\text{CH}_3\text{NH}_3\text{PbI}_3$ .

between the measured data and calculations is good; in particular, we notice significant multi-phonon scattering in the observed spectrum. The phonons below 25 meV are mainly  $\text{PbI}_3$  sub-lattice phonons, while those above 25 meV are the vibrational modes of the MA cations. Diagonalizing the dynamical matrix with and without the off-diagonal coupling terms, we find that there is strong coupling between the low-energy  $\text{PbI}_3$  modes and MA rotational modes. The  $\text{CH}_3\text{NH}_3^+$  ion thus controls the final structure and dynamics due to its strong hydrogen bonding and steric (i.e. space filling) effects, even while it is decoupled electronically from the  $\text{PbI}_3$  bands. The lowest energy vibrational mode of the MA is found to be around 39 meV, corresponding to the twisting of  $\text{CH}_3/\text{NH}_3$  groups around the C-N bond. Near 100 meV, another significant high-energy mode corresponds to the bending of the  $\text{CH}_2\text{—CH}$  bond/ $\text{NH}_2\text{—CH}$  bond angles.

Figure 4 shows the calculated INS spectra for the symmetry-distinct cation orientations and the overall dipole moment of each system. These results demonstrate that the lattice

<sup>1</sup> NIST Center for Neutron Research, National Institute of Standards and Technology, Gaithersburg, MD 20899

<sup>2</sup> University of Delaware, Newark, DE 19716

<sup>3</sup> Department of Chemical Engineering, University of Virginia, Charlottesville, VA 22904

<sup>4</sup> Department of Physics, University of Virginia, Charlottesville, VA 22904

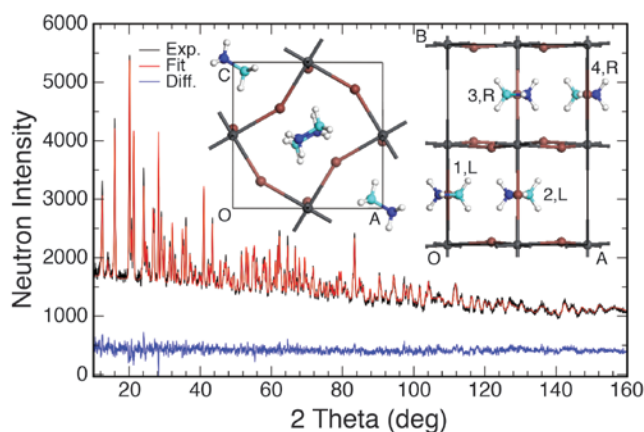


**FIGURE 2:** Neutron powder diffraction (black), refinement (red), and difference plots (blue) at 5K of  $\text{CD}_3\text{NH}_3\text{PbI}_3$ . The insets show the structure along the  $b$ -axis (left) and  $c$ -axis (right).

dynamics are sensitive to the local ordering of the MA dipoles in the structure. In the cases of RRRR and LRRR, there are two and four non-equivalent MA ions in the cell, respectively, and therefore the  $\text{CH}_3/\text{NH}_3$  twisting mode energies are split. There are also significant changes to the low-energy modes of the  $\text{PbI}_3$  sub-lattice due to strong  $\text{CH}_3\text{NH}_3$ - $\text{PbI}_3$  interactions. Hence we propose measuring the  $\text{CH}_3\text{NH}_3^+$  twisting mode energies to obtain a local probe of the local dipole moment orientations.

In conclusion, we have revealed the role of organic  $\text{CH}_3\text{NH}_3^+$  ions in determining the structural and dynamical properties of the hybrid halide perovskites. Even though  $\text{CH}_3\text{NH}_3^+$  is disconnected electronically from the band structure of the  $\text{PbI}_3$  sub-lattice, it controls the  $\text{PbI}_3$  network geometry due to structural interactions and space filling effects. The ground state is non-polar, but ferroelectric states where the dipole moments are ordered in parallel are very close in energy, with small barriers of  $\approx 0.3$  eV. The spontaneous dipole moment is dominated by the off-centering of the MA ions with respect to the  $\text{PbI}_3$  framework rather than due to dipole moment of the MA ions itself. We find that the  $\text{CH}_3/\text{NH}_3$  twisting mode energy is especially sensitive to the ordering of the  $\text{CH}_3\text{NH}_3^+$  ions with dipole moments, and that it shifts and splits significantly depending on the surrounding MA orientations. We therefore propose using the vibrational dynamics of MA ions as a local probe of the dipole ordering. Under an electric field, one may stabilize different ferroelectric domains that can be monitored via the vibrational spectrum of MA. Such ferroelectric ordering, and its impact on the performance of the hybrid halide perovskite solar cells, could then be accurately quantified and understood.

## References

- [1] T. M. Brenner, D. A. Egger, L. Kronick, G. Hodes, and D. Cahen, *Nature Rev. Materials*, doi: 10.1038/natrevmats.2015.7 (2016).
- [2] B. Ipek, L. Hung, C. M. Brown, T. Yildirim, B. J. Foley, T. Chen, J. J. Choi, S. H. Lee, X. Luo, arXiv: 1609.07xxx (to appear in *Phys. Rev. B*, rapid comm.).

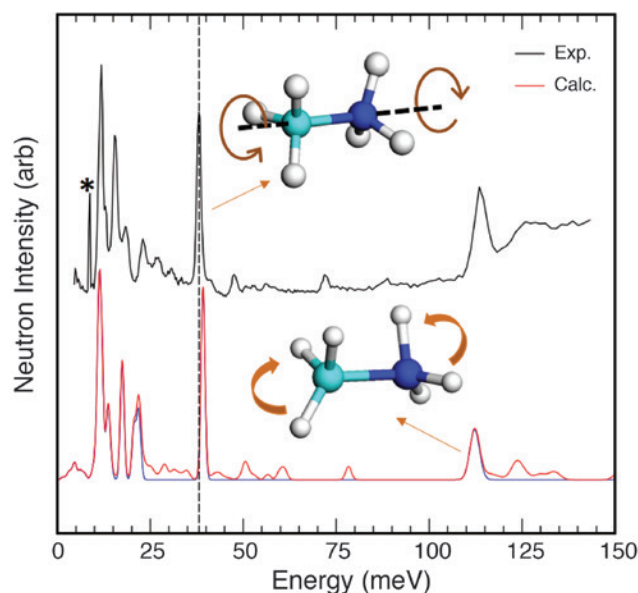


**FIGURE 3:** Experimental (black) and calculated one- (blue) and two-phonon (red) inelastic neutron scattering spectra. The peak labeled as “\*” is due to  $\lambda/2$  contamination from the low energy monochromator. The insets show the  $\text{CH}_3/\text{NH}_3$  twisting (top) and bending modes (bottom).

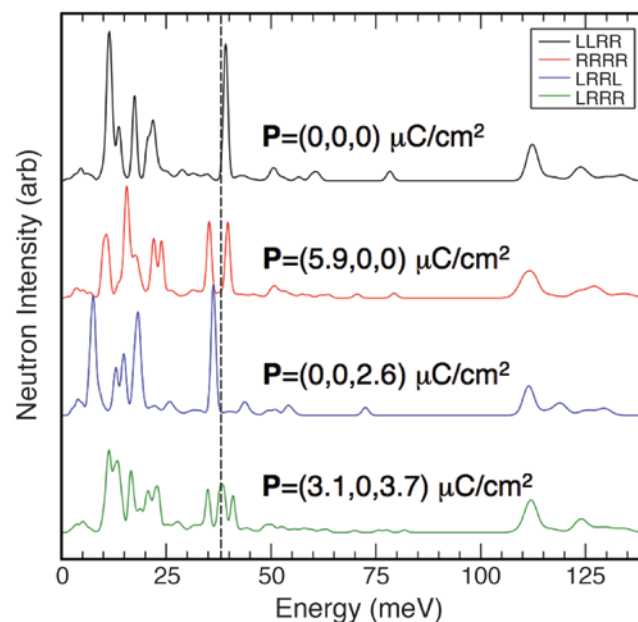


**FIGURE 4:** The calculated inelastic neutron scattering spectra for four different orientations of the  $\text{CH}_3\text{NH}_3^+$  molecules in the unit cell, which reflect the sensitivity of the  $\text{CH}_3/\text{NH}_3$  twisting mode energy on the surrounding dipole orientations.  $P$  is the overall dipole moment.

# Quadrupole order in the frustrated pyrochlore $\text{Tb}_{2+x}\text{Ti}_{2-x}\text{O}_{7+y}$

H. Takatsu,<sup>1,2</sup> S. Onoda,<sup>3,4</sup> S. Kittaka,<sup>5</sup> A. Kasahara,<sup>5</sup> Y. Kono,<sup>5</sup> T. Sakakibara,<sup>5</sup> Y. Kato,<sup>3,6</sup> B. Fak,<sup>7</sup> J. Ollivier,<sup>7</sup> J.W. Lynn,<sup>8</sup> T. Taniguchi,<sup>1</sup> M. Wakita,<sup>1</sup> and H. Kadowaki<sup>1</sup>

**M**agnetism in a solid typically arises as a consequence of the orbital state of unpaired electrons and the cooperative alignment of these spin and orbital magnetic moments. In contrast to this conventional magnetic order, ordered patterns of orbitals themselves can play an important role, particularly in *f*-electron materials, and create exotic new types of phases where novel properties emerge [1]. Though quite interesting, these new types of multipole orbital orders are difficult to probe because common techniques to elucidate the thermodynamic order parameter, such as neutron Bragg scattering or Mossbauer spectroscopy, couple directly only to the dipole moments and not the higher-order moments. Hence these new types of order are often referred to as “hidden order”, and have attracted a great deal of attention. One prototype class of materials where hidden order emerges is on the magnetically frustrated cubic pyrochlore lattice, such as  $\text{Tb}_{2+x}\text{Ti}_{2-x}\text{O}_{7+y}$  which is the system of present focus. We have investigated this system employing diffraction and inelastic neutron scattering, specific heat, magnetization, and Monte Carlo calculations, and have succeeded in demonstrating that the ordered state originates from electric quadrupole moments intrinsic to the  $\text{Tb}^{3+}$  ions [2]. This is the first example of electric quadrupole order in a frustrated magnetic systems, and opens new research directions for “frustrated quadrupole systems”.

The magnetic ground state of  $\text{Tb}_2\text{Ti}_2\text{O}_7$  (TTO) does not exhibit either the usual long range magnetic order, or a (frozen) spin glass, but rather exhibits fluctuating moments down to very low temperature (viz. 0.07 K) [3]. The pyrochlore structure consists of a corner-sharing network of tetrahedra that exhibit prototypical geometrical frustration [Fig. 1(a)]. A classical treatment of the magnetic system indicates that TTO should undergo a transition to magnetic (dipole) long range order (LRO) at about 1 K, and thus is considered a candidate quantum spin liquid (QSL). However, despite many theoretical and experimental studies, the actual nature of the ground state has remained elusive, partly owing to a sample dependence of the properties that depend very sensitively on the precise stoichiometry of the system. For example, it was found that some crystals showed a

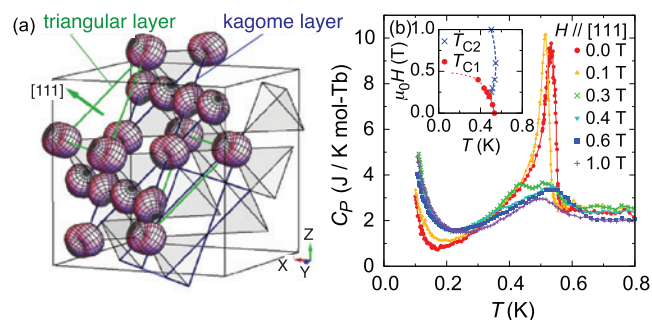


**FIGURE 1:** (a) Schematic view of the deformation of the *f*-electron charge density due to the quadrupole order on the pyrochlore lattice of  $\text{Tb}_2\text{Ti}_2\text{O}_7$ . Distorted spheres represent the charge distribution around  $\text{Tb}^{3+}$  ions. This long range ordered pattern indicates the order of quadrupole moments of  $\text{Tb}_2\text{Ti}_2\text{O}_7$ . The [111] direction is characteristic for the direction of the two dimensional structure consisting of alternative stacks between the triangular and kagome lattices. (b) Temperature dependence of the observed specific heat  $C_p(T, H)$  for  $H||[111]$  using the single crystal of  $\text{Tb}_{2.005}\text{Ti}_{1.995}\text{O}_{7+y}$ . The sharp peak appears at 0.53 K in zero field, indicating the phase transition. Inset of (b) represents a phase diagram made by peak positions of  $C_p(T, H)$ .

clear specific-heat peak at  $\approx 0.4$  K suggesting a phase transition, but without magnetic LRO. Indeed recent studies on polycrystalline samples revealed a dramatic sensitivity to the *x*-value of  $\text{Tb}_{2+x}\text{Ti}_{2-x}\text{O}_{7+y}$ , where a mysterious order appears in the vicinity of the QSL state ( $x > -0.0025 = x_c$ ), although the origin of the QSL and its relation to the order were not clear.

Therefore it is essential to be able to fine-tune the composition of high quality single crystals, and we have recently succeeded in this synthesis. This has enabled the elucidation of the key ingredients of the hidden order using a crystal with  $x = 0.005$  ( $T_c = 0.53$  K). Figure 1(b) shows the *T* dependence of specific heat under an applied magnetic field along the [111] direction, up to 1 T. Since the [111] direction is one of the characteristic directions of the pyrochlore lattice [Fig. 1(a)], it should be a good direction to observe typical behavior of the ordered state. Indeed, the sharp peak at  $T_c$  survives only up to 0.1 T, turning into broad double

<sup>1</sup> Tokyo Metropolitan University, Hachioji-shi, Tokyo 192-0397, Japan

<sup>2</sup> Kyoto University, Kyoto 615-8510, Japan

<sup>3</sup> RIKEN Center for Emergent Matter Science (CEMS), Wako, Saitama 351-0198, Japan

<sup>4</sup> Condensed Matter Theory Laboratory, RIKEN, Wako, Saitama 351-0198, Japan

<sup>5</sup> Institute for Solid State Physics, University of Tokyo, Kashiwa 277-8581, Japan

<sup>6</sup> Department of Applied Physics, University of Tokyo, Bunkyo, Tokyo 113-8656, Japan

<sup>7</sup> Institute Laue Langevin, BP 156, F-38042 Grenoble, France

<sup>8</sup> NIST Center for Neutron Research, National Institute of Standards and Technology, Gaithersburg, MD 20899



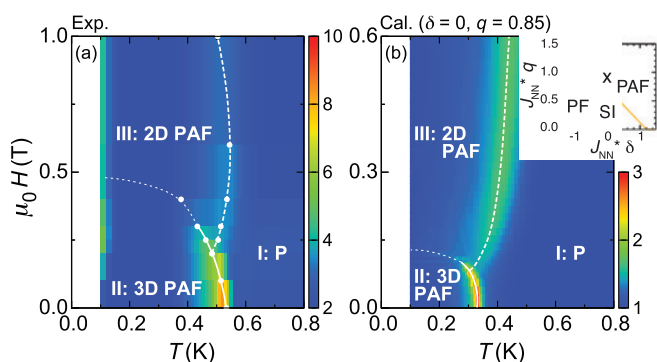


**FIGURE 2:** (a)  $H$ - $T$  map of specific heat  $C_p(T, H)$  for  $\text{Hf}[111]$ . Filled circles in the map are peak positions of  $C_p(T, H)$ . Solid, dashed, and dotted lines are guides to the eyes. (b) Calculated results of specific heat  $C(T, H)$ . Inset of (b) is a phase diagram of the effective model on the basis of the pseudospin-1/2 Hamiltonian for pyrochlore systems with non-Kramers ions. Two quadrupole phases, the planar antiferropseudospin (PAF) and planar ferropseudospin (PF) phase, exist in the vicinity of the spin ice (SI) phase. Classical SI is replaced by a U(1) QSL in quantum theory. The cross mark indicates the typical values of  $(\delta, q) = (0, 0.85)$ , which is used for the calculation of  $C(T, H)$  shown in (b). Calculated result qualitatively reproduces the experimental result of (a). Labels in maps indicate assigned states; i.e., (I) a paramagnetic paraquadrupole state, (II) a three dimensional (3D) PAF state, and (III) a two dimensional (2D) PAF state.

peaks at 0.3 T. The  $H$  dependence of the higher peak ( $T_{C2}$ ) exhibits a similar behavior for the  $H$  dependence of the peak of systems showing a hidden or multipole order [Inset of Fig. 1(b), Fig. 2(a)]. It is also found that the spectrum of inelastic neutron scattering and magnetization both show abrupt changes in accordance with the ordered state.

An interesting theoretical scenario has been recently proposed by Onoda and Tanaka to understand this behavior [4]. They consider a pseudospin-1/2 Hamiltonian for pyrochlore systems with non-Kramers ions such as  $\text{Tb}^{3+}$  (or  $\text{Pr}^{3+}$ ), and show that transverse super-exchange interactions between quadrupole moments, which are set into the spin ice Hamiltonian as an additional term, play the driving force of the order, transforming it into a type of a quadrupole order in the vicinity of a SL state. We therefore analyzed the experimental data based on this model, and found that the data can be reproduced by parameters in an electric quadrupole phase located very close to the phase boundary between the quadrupolar and U(1) QSL states [Fig. 2(b)]. This result also agrees with the interpretation of the previous experimental result that the minute change of  $x$  of  $\text{Tb}_{2+x}\text{Ti}_{2-x}\text{O}_{7+y}$  brings about the change in states between QSL and LRO. These results indicate that the problem of the hidden order in TTO can now be reconsidered as the novel problem of quadrupole order on the frustrated pyrochlore lattice with the non-Kramers ion of  $\text{Tb}^{3+}$ . These results also suggest that the putative SL state of TTO studied for more than decade could be the U(1) QSL.

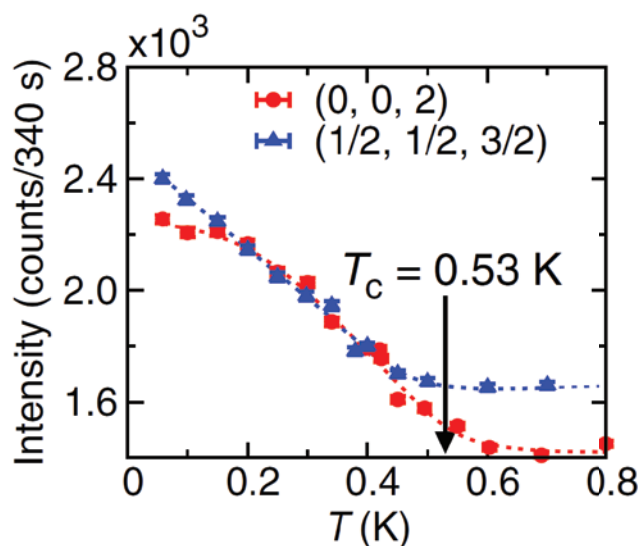


**FIGURE 3:** Temperature dependence of intensities of the single-crystal neutron Bragg scattering at the (002) and  $(1/2, 1/2, 3/2)$  Bragg peak positions.

All the above comparisons between the experiments and theories reveal that the low temperature ordered state of TTO is quadrupole in nature. Although neutrons do not couple directly to the primary order parameter for this type of order, important clues to the order are nevertheless evident. In particular, weak reflections develop at the forbidden (002) position and at the superlattice type  $(1/2, 1/2, 3/2)$  position [Fig. 3], and polarized neutron data on BT7 reveal that *both* of them are magnetic. The long-range ordered magnetic moments of these reflections are only  $\approx 0.1 m_B$ , too small to be the primary order parameter. It appears that the (002) reflection develops simultaneously with the quadrupole order, with an order parameter characterized by the wave vector  $k = 0$  that is induced by higher order terms neglected in the theoretical model. On the other hand, the  $(1/2, 1/2, 3/2)$  reflection (also observed in a powder sample) exhibits a different  $T$  dependence, suggesting it has a different physical origin. Since electric quadrupolar orders are related to the deformation of  $f$ -electron charge density, these naturally couple to displacements of ligand ions and may induce cooperative Jahn-Teller (JT) effects, providing new pathways to investigate these multipole order parameters. Moreover, the model parameters suggest that this composition of TTO is very close to the putative spin-liquid state. Investigations in the context of a Higgs transition, and following the evolution of the system to the nearby U(1) quantum spin liquid state are fascinating future directions to explore.

## References

- [1] P. Santini *et al.*, Rev. Mod. Phys. **81**, 807 (2009).
- [2] H. Takatsu *et al.*, Phys. Rev. Lett. **116**, 217201 (2016).
- [3] J. S. Gardner, M. J. P. Gingras, J. E. Greedan, Rev. Mod. Phys. **82**, 53 (2010).
- [4] S. Onoda, Y. Tanaka, Phys. Rev. Lett. **105**, 047201 (2010).

# Upward dispersing magnetic resonance mode in superconducting $\text{Ce}_{1-x}\text{Yb}_x\text{CoIn}_5$

Y. Song,<sup>1</sup> J. Van Dyke,<sup>2</sup> I. K. Lum,<sup>3,4,5</sup> B. D. White,<sup>4,5</sup> S. Jang,<sup>3,4,5</sup> D. Yazici,<sup>3,4,5</sup> L. Shu,<sup>6,7</sup> A. Schneidewind,<sup>8</sup> P. Čermak,<sup>8</sup> Y. Qiu,<sup>9</sup> M. B. Maple,<sup>3,4,5</sup> D. K. Morr,<sup>2</sup> P. Dai<sup>1</sup>

Pairing of electrons into Cooper pairs in conventional superconductivity is mediated by phonons. In unconventional superconductors including cuprates, iron pnictides, and heavy fermion superconductors such as  $\text{CeCoIn}_5$ , the ‘pairing glue’ is likely to be magnetic fluctuations. In the superconducting state of these unconventional superconductors, a prominent magnetic resonant mode appears at the antiferromagnetic wave vector at energies that roughly scale with the superconducting transition temperatures ( $T_c$ ). The magnetic resonance mode is a ‘common thread’ for unconventional superconductors [1] and revealing its nature is a prerequisite for understanding the mechanism of superconductivity mediated by spin fluctuations.

The magnetic resonance mode is commonly interpreted as a spin-exciton [2], although it has also been proposed to be a remnant magnon-like mode revealed due to reduction of damping in the superconducting state. In the spin-exciton picture, the magnetic resonance mode can be calculated from structures of the Fermi surface and the superconducting order parameter. For cuprates with d-wave pairing symmetry, the magnetic resonance mode exhibits a prominent downward dispersion while in iron pnictides with s-wave pairing symmetry the mode displays an upward dispersion. In both cases experimentally measured dispersion agrees with what is expected in the spin-exciton picture.

Superconductivity in  $\text{CeCoIn}_5$  ( $T_c = 2.3$  K) has d-wave pairing symmetry similar to the cuprates, and the resonance is expected to display a downward dispersion as in the cuprates. Our results on MACS instead clearly demonstrate a prominent upward dispersion, as shown by constant-energy slices of magnetic scattering at several energy transfers in Figure 1. With increasing energy transfer from  $E = 0.5$  meV in Figure 1 (a) to 1.0 meV in Figure 1 (d), the magnetic resonance mode disperses out, exhibiting a ring-like features at  $E = 1.0$  meV. The dispersive feature is only observed in the superconducting state, whereas

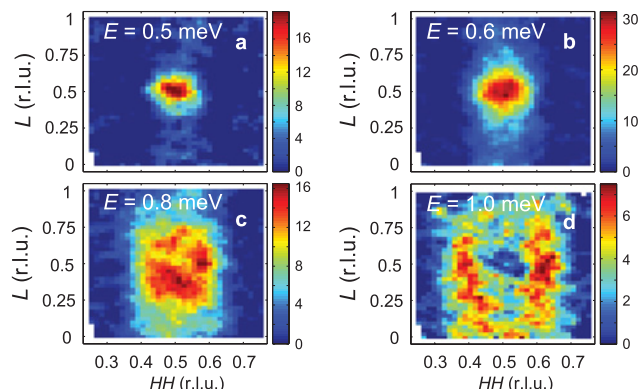


**FIGURE 1:** Constant-energy maps of inelastic neutron scattering cross sections for  $\text{CeCoIn}_5$  measured on MACS cold neutron spectrometer for several energies transfers, (a)  $E = 0.5$  meV, (b)  $E = 0.6$  meV, (c)  $E = 0.8$  meV and (d)  $E = 1.0$  meV. The data at  $T = 0.1$  K ( $T < T_c$ ) after subtracting the data at  $T = 2.5$  K ( $T > T_c$ ) is shown; all observed features correspond to the magnetic resonance mode.

in the normal state ( $T > T_c$ ) magnetic excitations are centered at  $Q = (0.5, 0.5, 0.5)$  for all measured energies.

It has been shown that the electronic structure of  $\text{CeCoIn}_5$  is significantly modified by Yb doping. If the magnetic resonance mode is a spin-exciton which results from the Fermi surface and the superconducting gap structure, then it should be strongly affected if the Fermi surface or the superconducting gap structure is modified dramatically. Our results on MACS reveal that the dispersion of the magnetic resonance mode remains robust with Yb doping, although considerably broadened, as shown in Fig. 2. For both  $\text{Ce}_{0.95}\text{Yb}_{0.05}\text{CoIn}_5$  ( $T_c = 2.25$  K) and  $\text{Ce}_{0.7}\text{Yb}_{0.3}\text{CoIn}_5$  ( $T_c = 1.5$  K) the magnetic resonance modes exhibit clear upward dispersions, as shown in Fig. 2 (a) – (d). More strikingly, the dispersion hardly changes compared to  $\text{CeCoIn}_5$ , as shown in Fig. 2 (e) – (g). Therefore, despite the changes of electronic structure with Yb doping, the dispersion of the resonance remains robust.

<sup>1</sup> Rice University, Houston, TX, 77005

<sup>2</sup> University of Illinois at Chicago, Chicago, IL 60607

<sup>3</sup> Materials Science and Engineering Program, University of California, San Diego, La Jolla, CA 92093

<sup>4</sup> Department of Physics, University of California, San Diego, La Jolla, CA 92093

<sup>5</sup> Center for Advanced Nanoscience, University of California, San Diego, La Jolla, CA 92093

<sup>6</sup> State Key Laboratory of Surface Physics, Department of Physics, Fudan University, Shanghai 200433, China

<sup>7</sup> Collaborative Innovation Center of Advanced Microstructures, Fudan University, Shanghai 200433, China

<sup>8</sup> Jülich Center for Neutron Science JCNS, Forschungszentrum Jülich GmbH, Outstation at MLZ, D-85747, Garching, Germany

<sup>9</sup> NIST Center for Neutron Research, National Institute of Standards and Technology, Gaithersburg, MD 20899



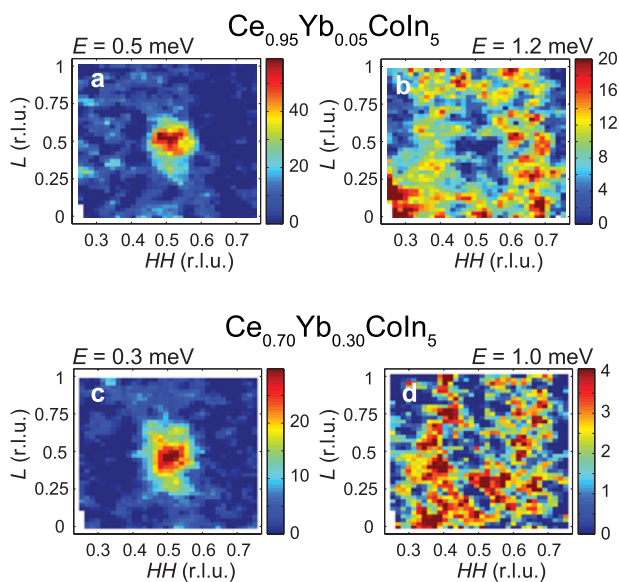


**FIGURE 2:** Constant-energy maps for  $\text{Ce}_{0.95}\text{Yb}_{0.05}\text{Coln}_5$  ( $T_c = 2.25$  K) at (a)  $E = 0.5$  meV and (b)  $E = 1.2$  meV. The data at  $T = 1.0$  K ( $T < T_c$ ) after subtracting data at  $T = 2.4$  K ( $T > T_c$ ) is shown. Similarly, constant-energy maps are shown for  $\text{Ce}_{0.70}\text{Yb}_{0.30}\text{Coln}_5$  ( $T_c = 1.5$  K) at (c)  $E = 0.3$  meV and (d)  $E = 1.0$  meV. The data at  $T = 0.3$  K ( $T < T_c$ ) after subtracting data at  $T = 2.0$  K ( $T > T_c$ ) is shown. Summarizing the results for  $\text{Ce}_{1-x}\text{Yb}_x\text{Coln}_5$  measured on MACS, the dispersions are summarized for (e)  $x = 0$ , (f)  $x = 0.05$  and (g)  $x = 0.30$ . Identical solid cyan curves are shown in each panel to demonstrate dispersion of the magnetic resonance mode in  $\text{Ce}_{1-x}\text{Yb}_x\text{Coln}_5$  is robust against Yb doping.

The observation of a prominent upward rather than downward dispersion of the magnetic resonance mode and insensitivity of the dispersion to changes in electronic structure both challenge the view of the mode being a spin-exciton. Our results suggest it is likely the mode could be magnon-like excitations and the robust dispersion reflects a robust effective nearest neighbor exchange coupling in this system, although our observation can be due to either itinerant or local magnetism. This idea is in agreement with the fact the magnetic resonance mode in  $\text{Ce}_{1-x}\text{Yb}_x\text{Coln}_5$  display strong  $L$ -modulation, as can be seen in Fig. 1 and Fig. 2, in contrast to the cases of cuprates and iron pnictides where the mode form rods along  $L$ . In addition, as shown in Fig. 3 the dispersion of the magnetic resonance mode in  $\text{Ce}_{1-x}\text{Yb}_x\text{Coln}_5$  resembles the dispersion of spin waves in antiferromagnetically ordered  $\text{CeRhIn}_5$ , although with a slightly reduced dispersion velocity. The reduced dispersion velocity in

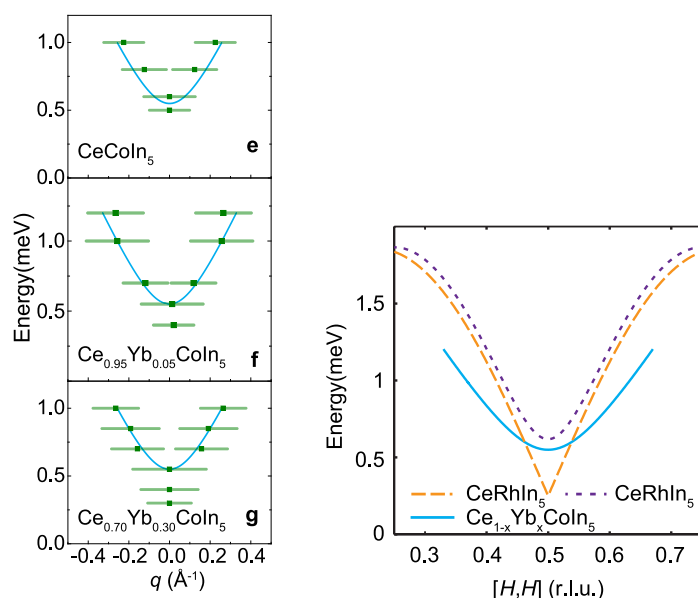


**FIGURE 3:** Comparison of spin waves in  $\text{CeRhIn}_5$  with the dispersive magnetic resonance mode in  $\text{Ce}_{1-x}\text{Yb}_x\text{Coln}_5$ . The dashed lines are dispersions of spin waves from two independent previous works on  $\text{CeRhIn}_5$  and the solid line is the dispersion shown in Fig. 2 (e) – (g).

$\text{Ce}_{1-x}\text{Yb}_x\text{Coln}_5$  compared to  $\text{CeRhIn}_5$  is reminiscent of similar results in cuprates where upon doping the dispersion of magnetic excitations is found to soften.

In summary, using MACS we have established a robust upward dispersion for the magnetic resonance mode in  $\text{Ce}_{1-x}\text{Yb}_x\text{Coln}_5$ . Our observation challenges the common view that the magnetic resonance mode in  $\text{CeColn}_5$  is a spin-exciton, and suggests the presence of magnon-like excitations being a common feature of unconventional superconductors.

## References

- [1] D. J. Scalapino, Rev. Mod. Phys. **84**, 1383 (2012).
- [2] M. Eschrig, Adv. Phys. **55**, 47 (2006).

# Effects of pre-strain and load reversal in shear testing of an interstitial free steel

T. Gnäupel-Herold

In 2009 President Obama proposed a new national fuel program that mandates a gradual rise in fuel economy to an average mileage (cars and light trucks) of 54.5 mpg by 2025. This goal is about 50 % higher than the 2016 mandate posing a serious challenge to the automotive industry. Industries are pursuing two major themes to achieve this ambitious goal: (1) more efficient engine technologies with hybrids and plug-in electrics, and (2) broad spectrum efforts to reduce vehicle weight. Automotive lightweighting requires the use of new materials that combine two properties: elongation to large strains and high strength. The first describes the capacity to stretch during forming or under crash conditions while the second (strength) is crucial to allow thinner gages that bring weight reduction. While these materials have been developed, wide adoption in car body parts has been slowed by a severe lack of data regarding their deformation behavior. Such knowledge is essential because the stresses necessary to strain a metal sheet into a part with a precisely defined shape must also be known precisely.

The measurement of plastic stress-strain properties ( $\sigma(\epsilon)$  laws) is straightforward in uniaxial deformation but very difficult in two dimensions with additional complications in path changes, e.g. sequences of straining in different directions. The reason for this difficulty is evident in Figure 1 through the highly inhomogeneous distribution of shear strains. The sub-millimeter spatial resolution of the strain field is made possible through in-situ digital image correlation (DIC). Neutron diffraction is the complement to the strain from DIC – a neutron beam is focused on the center of the sample in the near-homogenous strain region, and the elastic lattice strains measured by diffraction provide the stress tensor. This experiment is enabled by a novel straining device specifically built for neutron diffraction with in-situ DIC [1]. Here, shear is achieved by mutually perpendicular compressive and tensile stresses of equal magnitude. The relative standard deviation  $\sigma_{rel}$  of strains in the entire sample is almost eight times larger than in the beam-exposed center ( $\sigma_{rel}^{full} = 0.38$  vs.  $\sigma_{rel}^{beam} = 0.05$ ), which precludes the use of averaging force sensor data.

The combination of DIC and neutron diffraction stress analysis can provide new insights into the shear test as commonly used in sheet metal testing. Specifically, a large difference between the local  $\sigma_{xy}(\epsilon_{xy})$  law (subscript xy = shear) and the average is revealed with the largest spread found between load cell based stresses

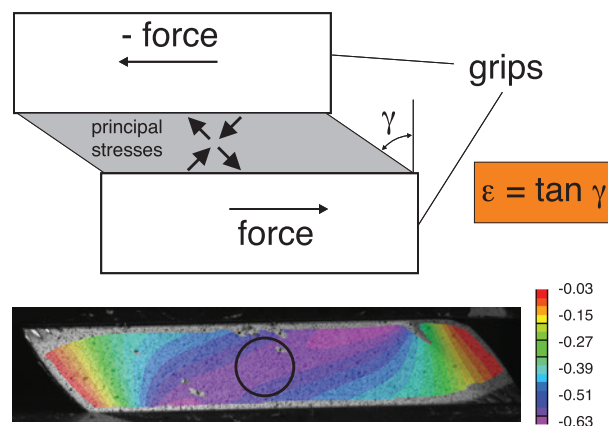


**FIGURE 1:** Shear test (top) and resulting strain field (bottom) of a pure shear deformation of an interstitial-free steel. The circle indicates the neutron measurement area. The arrows in the sketch (top) indicate the direction of the principal stresses in shear (45° inclination at the start of straining).

of two very similar samples as shown in Figure 2. This difference hints at a considerable effect of the specimen geometry on the average stress obtained from the load cell.

The stresses measured by neutron diffraction on the other hand are very similar – as they should be for samples of the same material. The implication is that neutron diffraction provides data with better accuracy for an important sheet metal forming test, and the consequences extend beyond the monotonic  $\sigma_{xy}(\epsilon_{xy})$  curves. While the forming of an automotive body part involves shear it rarely does so in pure form with the exception of deep drawing such as beverage cans. Monotonic  $\sigma_{xy}(\epsilon_{xy})$  curves are therefore just one piece of the puzzle of large strain deformation. However, sequences of tensile stretching and compressive shortening are common in forming, and that is where the shear test finds another use. Reversals between forward and backward shear are very easy to perform even at large strains and without buckling which restricts the utility of uniaxial load reversal tests (the problem of compressive buckling was first investigated by Leonard Euler more than 250 years ago). The effects of reverse deformation after some plastic strain has already been accumulated (the pre-strain) can be described as a yield drop, i.e. the magnitude of stress necessary to initiate

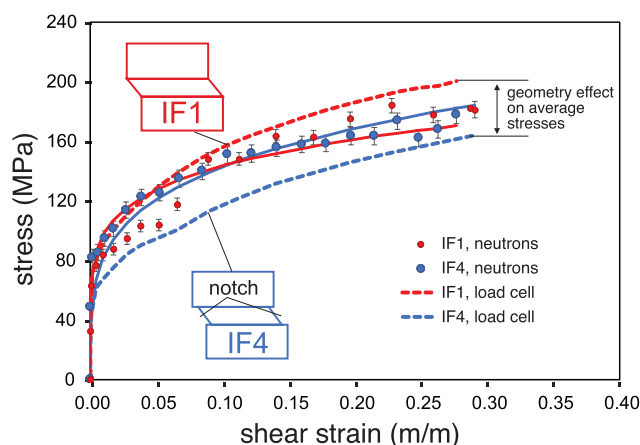


**FIGURE 2:** Comparison of neutron stresses and stresses from force sensor data through  $\sigma = F / A$  ( $F$ = force;  $A$  = cross section). The two samples are interstitial free steel with IF1 (red) as a simple rectangle shape and IF4 (blue) with notches machined to facilitate a more homogenous strain field. IF4 showed tearing which explains the much lower stresses.

plastic deformation in the *opposite* direction is lower. This observation is known as the Bauschinger effect. Its importance lies in the fact that the magnitude of the yield drop depends, among other factors, on the pre-strain as shown in Figure 3. The basic mechanism responsible can be understood through the concept of back stress created by dislocation networks that are arranged in stable cells within grains. The back stresses, sometimes called long range internal stresses (LRIS), increase with plastic strain and they act against the external applied stress – if the applied stress is reversed the back stresses now aid the movement of free dislocations, hence the stress necessary to produce reverse strain is now lower. The inset in Figure 3 describes the yield stress before and after load reversal. The yield drop is the difference between the (absolute) yield stress in forward shear and immediately after reversal of shear. The yield stress in forward shear (inset, red graph) can be described by a power law type behavior ( $\sigma_{\text{yield}} = A\epsilon^n$  with  $200 < A$  (MPa)  $< 400$  and  $0.1 < n < 0.4$ , depending on whether deformation occurs in forward or reverse shear). It should be noted that the hardening coefficient  $n$  is smaller in reversal. This is another consequence of the Bauschinger effect, and it is called work hardening stagnation

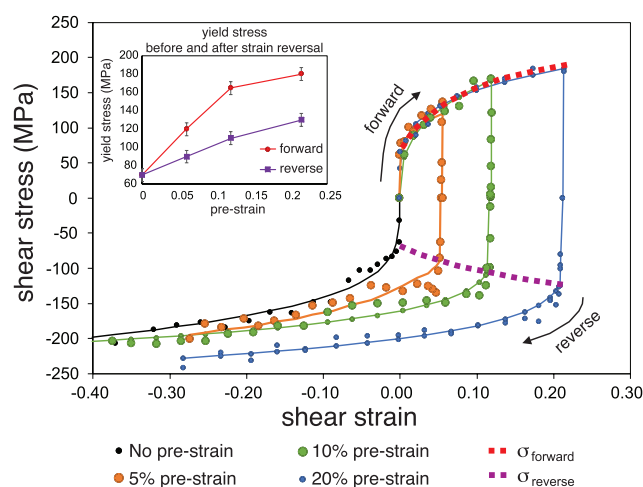


**FIGURE 3:** Stress-strain curves  $\sigma_{xy}(\epsilon_{xy})$  with different amounts of pre-strain (forward shear) and reverse shear. The inset summarizes the yield stresses extracted from the curves.

expressed by the lower increase in stress after reversal. The law describing the yield stress after reversal (purple graph in the inset) appears to be nearly linear suggesting that the yield drop becomes smaller at even larger strains  $> 0.22$ ; however, it is unlikely to continue in this manner at larger pre-strains; rather, a similar plateau for the reverse yield stress can be expected, most likely leading to a plateau in the yield drop for strains  $> 0.2$ .

The observations made here regarding the effects of pre-strain and load reversal are not new in qualitative terms; however, the magnitudes of stress and strain have been put on a much sounder footing through the simultaneous use of digital image correlation strain measurement and neutron diffraction stress determination. Both methods offer spatial resolution as a remedy to the inherent inhomogeneity of stress and strain fields in multiaxial testing.

## Reference

- [1] T. Gnäupel-Herold, J. Milner, S. Hallock, submitted to Nuclear Instruments and Methods A.



# Precision measurement of the radiative beta-decay of the free neutron

M. J. Bales,<sup>1, 2</sup> R. Alarcon,<sup>3</sup> C. D. Bass,<sup>4</sup> E. J. Beise,<sup>5</sup> H. Breuer,<sup>5</sup> J. Byrne,<sup>6</sup> T. E. Chupp,<sup>1</sup> K. J. Coakley,<sup>7</sup> R. L. Cooper,<sup>8</sup> M. S. Dewey,<sup>4</sup> S. Gardner,<sup>9</sup> T. R. Gentile,<sup>4</sup> D. He,<sup>9</sup> H. P. Mumm,<sup>4</sup> J. S. Nico,<sup>4</sup> B. O'Neill,<sup>3</sup> A. K. Thompson,<sup>4</sup> and F. E. Wietfeldt<sup>10</sup>

In the six decades since the first measurement of the neutron lifetime, the study of neutron beta decay has provided increasingly precise tests of the Standard Model and important input to cosmology and other areas of physics [1]. Precision measurements of neutron observables, such as the lifetime and the spin-electron asymmetry coefficient, currently allow for comparisons with theory with a precision below 1 %. The Standard Model predicts that the decay of the free neutron can produce one or more detectable radiative photons in addition to a proton, an electron, and an antineutrino. Here we summarize the results of the RDK II experiment [2], which includes the first precision test of the shape of the photon energy spectrum and a substantially improved determination of the branching ratio. This demonstrates that measurements of the neutron's radiative decay mode can probe new physics. A measurement of the photons' circular polarization could reveal information about the Dirac structure of the weak current [3, 4], and a possible source of time-reversal violation would be apparent in a triple-product correlation between the antineutrino, electron, and photon [5]. Increased precision would allow a test of a heavy baryon chiral perturbation theory calculation [4].

In contrast with the long history of most neutron beta-decay measurements, experimental studies of neutron radiative beta decay are relatively recent [6]. In 2006 the RDK I collaboration reported the first definitive observation of radiative decay. The RDK II experiment improved upon its predecessor by reducing statistical uncertainties through the use of additional photon detectors, improving the understanding of systematic uncertainties through detailed energy response studies of the detectors, and significantly extending the detectable photon energy range to between 0.4 keV and the 782 keV photon energy endpoint. Radiative photons from neutron decay originate from either electron, proton, or vertex bremsstrahlung. Electron bremsstrahlung dominates while higher order terms contribute less than 1 % to the branching ratio [4].

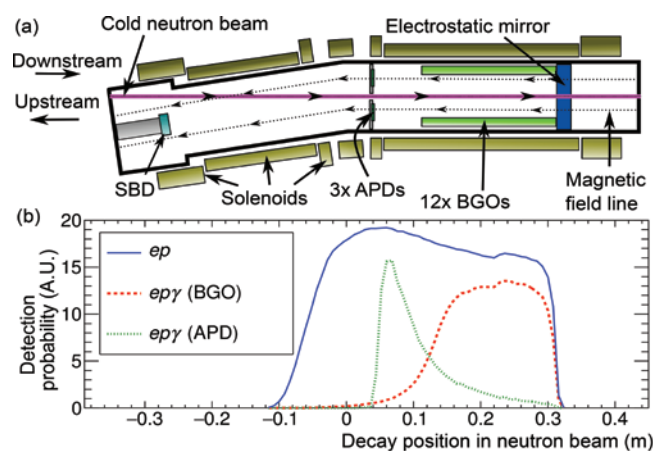


**FIGURE 1:** (a) A cross-sectional diagram of the RDK II detection apparatus from above. The neutron beam (pink) traveled from left to right through the active region defined by the fields (dashed lines) created by the solenoids (gold) and the electrostatic mirror (blue). Protons and electrons follow the field lines to the SBD (light blue). Radiative photons were detected by twelve bismuth germanate (BGO) crystals (green) and three large area avalanche photodiodes (APDs). (b) Detection probability in independent arbitrary units (A.U.) for electron-proton ( $ep$ ) and electron-proton-photon ( $ep\gamma$ ) detection coincidence for either the BGO or direct APD detectors. This plot is approximately aligned with the diagram above.

The RDK II experiment operated at the NG-6 fundamental physics end-station at the NCNR for one year, with a typical neutron fluence rate of  $1.1 \times 10^8 \text{ s}^{-1}$ . The cold neutron beam was guided to the experiment as in RDK I but with increased neutron collimation to decrease backgrounds and systematic uncertainties in decay locations. The neutron beam passed through a strong magnetic field produced by a set of superconducting solenoids that were used to guide charged decay products to a detector. As shown in Fig. 1(a), the detection region was defined by a 9.5 degree bend in the magnetic field and a ring of aluminum maintained at +1400 V that served as an electrostatic mirror. The mirror created an +800 V barrier at the center of the beam to protons. The magnetic field

<sup>1</sup> University of Michigan, Ann Arbor, MI 48104

<sup>2</sup> Physikdepartment, Technische Universität München, D-85748, Germany

<sup>3</sup> Arizona State University, Tempe, AZ 85287

<sup>4</sup> National Institute of Standards and Technology, Gaithersburg, MD 20899

<sup>5</sup> University of Maryland, College Park, MD 20742

<sup>6</sup> University of Sussex, Brighton, BN1 9QH, UK

<sup>7</sup> National Institute of Standards and Technology, Boulder, CO 80305

<sup>8</sup> Indiana University, Bloomington, IN 47408

<sup>9</sup> University of Kentucky, Lexington, KY 40506

<sup>10</sup> Tulane University, New Orleans, LA 70118

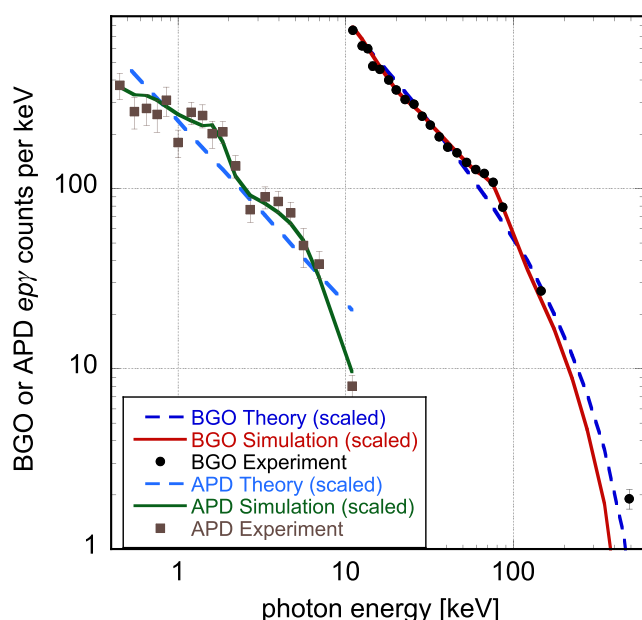


**FIGURE 2:** Pulse height spectra for radiative neutron decay. Plotted are the average background-corrected radiative photon counts for both the BGO and APD detectors versus photon pulse height. Pulse heights were determined relative to an electron-positron annihilation peak for the BGO detectors ( $511 = 511$  keV) and relative to a  $^{55}\text{Fe}$  source peak ( $5.9 = 5.9$  keV) for the APD detectors. The blue dashed lines shows the theoretical spectrum and the solid lines show the output of the simulation using the theoretical spectrum as input; both are scaled to the experimental data. The experimental data (black circles for BGO and brown squares for APD) include only the statistical uncertainty in the vertical error bars. The APD detectors were operated for a shorter time than the BGO detectors, hence the lower number of APD counts.

varied from 3.3 T to 4.6 T over the 34 cm distance between the bend and mirror.

Neutrons which decayed between the mirror and the bend produced electrons and protons capable of being detected by the apparatus. The electrons and protons followed adiabatic helical orbits about the field lines with maximum cyclotron radii of approximately 1 mm. Electrons emitted in the downstream direction typically escaped the active detection region undetected because their kinetic energies, typically hundreds of keV each, were likely sufficient to overcome the electrostatic mirror. Electrons emitted in the upstream direction followed the magnetic field to a silicon surface barrier detector (SBD) in a time on the order of nanoseconds. Protons were detected if emitted in either direction because the electrostatic mirror was sufficient to reflect all of them and traveled to the SBD in a time on the order of microseconds. The SBD was held at a  $-25$  kV potential to accelerate protons through the gold layer on its front surface.

Two separate photon detector arrays surrounded the neutron beam in the active region [7]. Photons with energies between 10 keV and 1000 keV were detected by a BGO detector array that consisted of twelve  $1.2$  cm  $\times$   $1.2$  cm  $\times$   $20$  cm bismuth germanate

(BGO) scintillator crystals optically coupled to avalanche photodiodes (APDs). The cryogenic environment (80 K) inside the detector served to both increase the BGO scintillators' light output and the APDs' gain while decreasing the APDs' noise. Photons with energies between 0.3 keV and 20 keV were directly detected by an APD array that consisted of three  $2.8$  cm  $\times$   $2.8$  cm APDs (without a scintillator).

The final data set consisted of 22 million electron-proton ( $ep$ ) detections, for which about 20,000 and 800 radiative photons were detected in coincidence ( $ep\gamma$ ) with the BGO and APD detectors, respectively. The dominant systematic uncertainties in this experiment were in the simulation's model registration, pulse shape discrimination, and photon detector energy response. As shown in Fig. 2, the BGO and APD spectra agreed well with the scaled spectra predicted by simulation. The branching ratio for the BGO range of 14.1 keV to 782 keV was measured to be  $0.00335 \pm 0.00005$  [statistical]  $\pm 0.00015$  [systematic], which agreed with the theoretical value of 0.00308 within 1.7 times the combined standard uncertainty. The branching ratio for the APD range of 0.4 keV to 14 keV was measured to be  $0.00582 \pm 0.00023$  [statistical]  $\pm 0.00062$  [systematic], which agreed with the theoretical value of 0.00515 within 1.0 times the combined standard uncertainty.

In summary, we have reported the first precise measurement of the radiative decay of the free neutron spanning three orders of magnitude in photon energy using two different detectors. As the precision is limited by systematic effects, the significantly better understanding of these effects obtained in this experiment provides a path towards an improved experiment with an uncertainty below 1 %. A future experiment could be considered that eliminates the magnetic field, which would allow for particle tracking and improved detection-volume definition. In addition, photon detectors with better proportionality could be implemented, and improvements in low-energy proton detection would allow better identification of proton and electron events. Utilizing a higher intensity cold neutron source should significantly improve the ability to study systematics while maintaining high statistical precision.

## References

- [1] D. Dubbers and M. G. Schmidt, *Rev. Mod. Phys.* **83**, 1111 (2011).
- [2] M. J. Bales *et al.*, *Phys. Rev. Lett.* **116**, 242501 (2016).
- [3] Y. Gaponov and R. Khafizov, *Nucl. Instrum. Methods A* **440**, 557 (2000).
- [4] V. Bernard, S. Gardner, U.-G. Meissner, and C. Zhang, *Phys. Lett. B* **593**, 105 (2004).
- [5] S. Gardner and D. He, *Phys. Rev. D* **87**, 116012 (2013); S. Gardner and D. He, *Phys. Rev. D* **86**, 016003 (2012).
- [6] R. L. Cooper *et al.*, *Phys. Rev. C* **81**, 035503 (2010); J. S. Nico, *Nature* **444**, 1059 (2006); M. Beck *et al.*, *JETP Lett.* **76**, 332 (2002).
- [7] R. L. Cooper *et al.*, *Nucl. Instrum. Methods A* **691**, 64 (2012).

# Structure, viscoelasticity, and interfacial dynamics of a model polymeric bicontinuous microemulsion

R. J. Hickey,<sup>1</sup> T. M. Gillard,<sup>2</sup> M. T. Irwin,<sup>2</sup> T. P. Lodge,<sup>1,2</sup> and F. S. Bates<sup>2</sup>

**T**ernary systems composed of two immiscible A and B homopolymers and a corresponding AB diblock copolymer are characterized by rich phase diagrams containing numerous morphologies and exhibiting an extraordinary range of structural dynamics. Under appropriate conditions such A/B/AB three-component mixtures will self-assemble into a thermodynamically stable polymeric bicontinuous microemulsion (BμE) with structural dimensions ranging from 10 nm to 500 nm. The polymeric BμE is globally isotropic, but contains locally correlated domains of A/B homopolymers mediated by AB diblock copolymers at the interface [1]. This fascinating state of molecular organization forms through a complex combination of interactions, and a comprehensive understanding of the BμE formation has yet to be realized.

Polymeric systems are very well suited for studying the fundamental nature of the BμE state. Judicious choice of the A and B polymers provides the advantage of isotopic labeling, which is essential for small-angle neutron scattering (SANS). We utilized a saturated hydrocarbon system comprised of poly(cyclohexylethylene) (C) and poly(ethylene) (E) homopolymers, and the corresponding CE diblock copolymer, in order to capitalize on this advantage [2].

We have used a combination of SANS and dynamic mechanical spectroscopy to reveal the structural and dynamical features that govern the BμE over a large (80 °C) temperature range [2]. Figure 1 summarizes schematically what we have deduced regarding the equilibrium structure that emerges as the C/E/CE mixture is cooled from a mean-field homogeneous state at high temperatures, to a fluctuating, highly structured, bicontinuous morphology at temperatures below approximately 150 °C ( $T_x$ ). As the temperature is reduced, the interfacial area per diblock copolymer chain of the BμE approaches that of the neat lamellar (LAM) diblock copolymer. With increasing temperature, the diblock-rich interface swells through homopolymer infiltration [2].

The structure of the BμE was evaluated over the temperature range 125 °C to 200 °C using SANS. As seen in Figure 2, the mixture produces a single prominent peak at all temperatures, which changes in intensity by two orders of magnitude and broadens between the highest and lowest temperatures. A nearly flat incoherent background intensity, estimated based on the weighted average of the scattering obtained from the pure

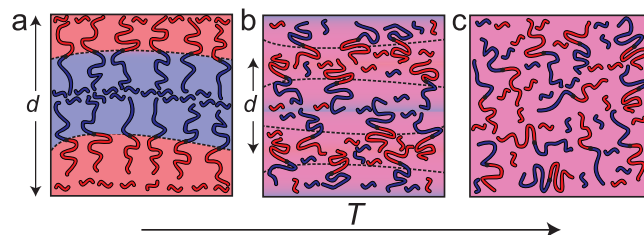


**FIGURE 1:** Scheme representing the change in the interfacial area per chain, domain spacing ( $d$ ), and degree of polymer intermixing with respect to temperature ( $T$ ) for the BμE sample. (a) At low temperatures ( $T \ll T_x$ ) the CE diblock copolymer packs at the interface with the same crowded areal density as the neat LAM forming diblock copolymer. In this temperature regime, homopolymers are largely excluded from the interfacial region. (b) At intermediate temperatures ( $T \approx T_x$ ) homopolymers penetrate into the interfacial region, leading to an increase in the surface area per diblock chain and a reduction in  $d$ . (c) At significantly increased temperatures ( $T \gg T_x$ ), the system reaches a mean-field homogeneously mixed state.

homopolymers, was subtracted from the acquired data, resulting in Figure 2. The background corrected scattering patterns were fit with the Teubner-Strey (T-S) model [3],

$$I(q) = \frac{1}{a_2 + c_1 q^2 + c_2 q^4},$$

where  $q = 4\pi\lambda^{-1}\sin(\theta/2)$  ( $\lambda$  is the wavelength, and  $\theta$  is the scattering angle), and  $a_2$ ,  $c_1$ , and  $c_2$  are fitting coefficients. We obtained good agreement between the SANS results and the T-S model over a large  $q$ -range, as seen in Figure 2. The model fails to quantitatively reproduce the coherent scattering intensity for  $q > 0.04 \text{ \AA}^{-1}$ , which is attributed to Gaussian coil scattering ( $I(q) \sim q^{-2}$ ) due to the hydrogen labeled C (h-C) blocks of the CE diblock copolymer, a consequence of the imperfect contrast matching with the deuterated C (d-C) homopolymer.

From the SANS data in Figure 2, we were able to quantitatively determine the temperature-dependent density of the CE diblock copolymer at the C/E homopolymer interface. To do this, we first estimated the interfacial area per diblock copolymer chain ( $A_c$ ) from estimates of the interfacial area per unit volume ( $S$ ) of the BμE.  $A_c$  is related to  $S$  for the BμE, and to the LAM and disordered (DIS) states in the CE diblock copolymer.  $S$  can be extracted from any 2-phase system using Porod's law and the scattering invariant [4]. However, the experimental SANS

<sup>1</sup> Department of Chemistry, University of Minnesota, Minneapolis, MN 55455

<sup>2</sup> Department of Chemical Engineering and Materials Science, University of Minnesota, Minneapolis, MN 55455



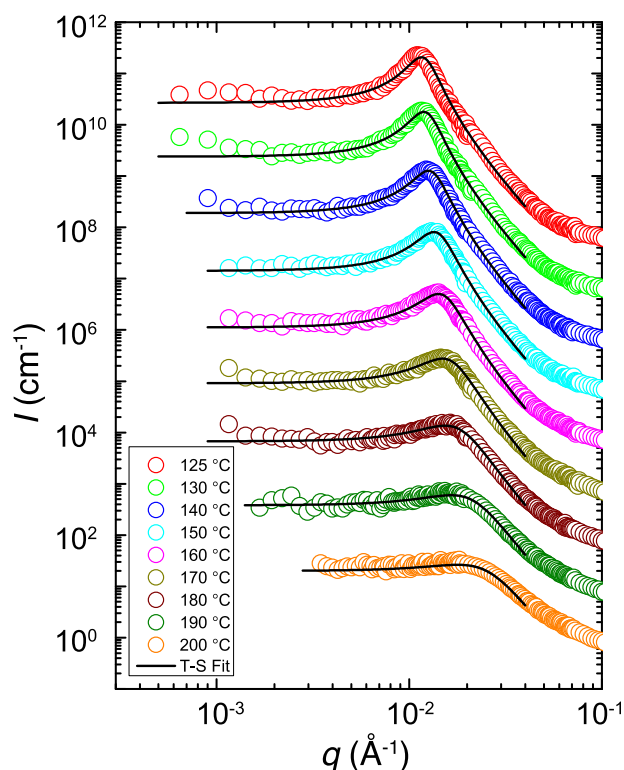


**FIGURE 2:** Background subtracted SANS data with optimized fits to the 3-parameter T-S model (solid curves). The data at 200 °C are in absolute units. The other scattering patterns (190 °C to 125 °C) have been vertically shifted successively by factors of 10.

data at high  $q$  (Figure 2) are dominated by scattering from the h-C blocks within the d-C homopolymer domains and by contributions from the incoherent background. This precludes reliable extraction of  $S$  using a direct application of Porod's law. Therefore, we have taken advantage of the excellent quality of the T-S fits to the SANS data and used these fitted functions to estimate the scattering invariant, and to calculate  $S$  and  $A_c$ , assuming these functions apply over all values of  $q$ .

For comparison, we have estimated  $A_c$  for the neat CE diblock copolymer in the LAM and DIS states for comparison with the B $\mu$ E, using  $S_{\text{LAM}} = q^*/\pi$  and  $S_{\text{DIS}} = 0.5q^*$ . Values of  $q^*$  were determined from SAXS data obtained from previously reported work [5], and the associated  $S$  values were converted to  $A_c$  and are plotted in Figure 3. Remarkably, the area per block copolymer chain for the B $\mu$ E asymptotically approaches that of the CE chains in the undiluted LAM morphology in the low temperature limit. Hence, we conclude that cooling the ternary mixture deep into the bicontinuous channel,  $T \ll T_x$ , leads to the expulsion of homopolymer from the interfacial region as illustrated in Figure 1a.

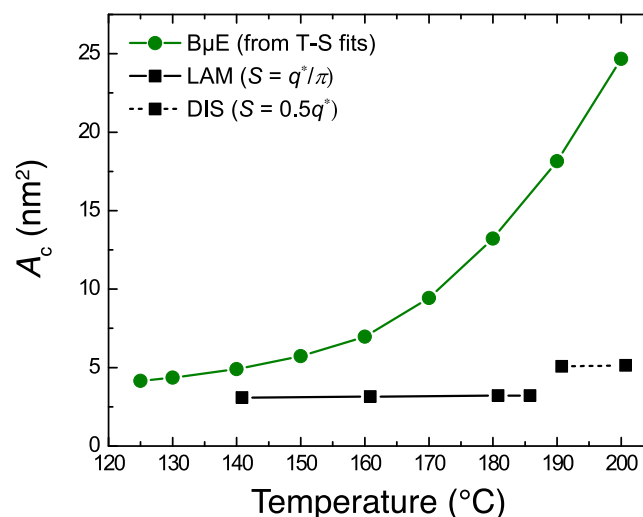


**FIGURE 3:** Temperature dependence of the interfacial area per CE diblock copolymer chain ( $A_c$ ) for the B $\mu$ E and neat CE samples.  $A_c$  was calculated for the B $\mu$ E sample from the T-S function shown in Figure 2.

These results offer new insights regarding the local properties of the interface and the extent of polymer intermixing in the B $\mu$ E, as summarized in Figure 1. Although the B $\mu$ E is globally disordered at all levels of segregation, the molecular environment of the interface resembles that of the neat CE diblock copolymer in the LAM morphology at lower temperatures: the interface becomes saturated with block copolymer, largely excluding the C and E homopolymers from the interfacial region, creating a situation analogous to the dry brush limit. These findings provide fresh insights into the thermodynamic driving forces responsible for the formation of B $\mu$ E and highlight opportunities to better understand this fascinating state of self-assembly.

## References

- [1] F. S. Bates, W. W. Maurer, P. M. Lipic, M. A. Hillmyer, K. Almdal, K. Mortensen, G. H. Fredrickson, T. P. Lodge, *Phys. Rev. Lett.* **79**, 849 (1997).
- [2] R. J. Hickey, T. M. Gillard, M. T. Irwin, T. P. Lodge, F. S. Bates, *Soft Matter* **12**, 53 (2016).
- [3] M. Teubner, R. Strey, *J. Chem. Phys.* **87**, 3195 (1987).
- [4] O. Glatter, O. Kratky, *Small Angle X-ray Scattering*. Academic Press: New York, 1982.
- [5] R. J. Hickey, T. M. Gillard, T. P. Lodge, F. S. Bates, *ACS Macro Lett.* **4**, 260 (2015).

# Tuning dispersion-aggregation transition and wetting-dewetting in polymer nanocomposites

A. Jayaraman,<sup>1,2</sup> R. Krishnamoorti,<sup>3</sup> T. B. Martin,<sup>1</sup> and P. Butler<sup>1,4</sup>

**P**olymer nanocomposites are soft materials composed of a bulk polymer matrix with dispersed nanoscale organic/inorganic particles that are added to modify and improve the mechanical, optical, electrical, and/or thermal properties of the polymer matrix. Driven by the need to develop functionally superior polymer nanocomposites, significant effort has been directed towards linking the molecular-level design of the nanoparticles and polymer to the resulting polymer nanocomposite morphology and understanding the thermodynamics driving the morphology. One way to tailor the composite morphology, specifically dispersion or aggregation of the particles in the polymer matrix, is to densely graft the nanoparticle with polymer chains (graft chains) that are chemically identical to the matrix polymer. Past simulation and experimental studies have shown that the delicate balance of enthalpic and entropic driving forces arising from the interplay of graft and matrix polymer molecular weight ratios, particle size or curvature, grafting density, flexibility of graft and matrix polymers, dispersity in graft and matrix molecular weights dictates the phase transition from dispersed to aggregated states [1-5].

Previous studies have also delineated the connection between the dispersion-aggregation transition to the extent of mixing of the graft and matrix polymer chains [1-5]. When the graft chains are wet (dewet) by the matrix chains, the nanocomposite is driven towards dispersed (aggregated) morphologies. Furthermore, when the graft and matrix polymers are chemically identical, the graft chains are wet by matrix chains and as a result dispersed morphologies are observed only at high graft to matrix polymer molecular weight ratios. Many applications where particle dispersion is desired, however, require matrix chains of fairly large molecular weights which then require long graft chains to achieve a high graft to matrix polymer molecular weight ratios needed for wetting. Grafting large molecular weight polymer chains on nanoparticles is a challenge synthetically, and the large graft chain molecular weights also limit the particle volume fraction in the composite. Thus, there has been a need for new molecular-level design rules that enable wetting of the grafted layer and in turn, particle dispersion even at low graft to matrix polymer molecular weight ratios. One such design rule is to choose graft and matrix chemistries with attractive interactions between the graft and matrix monomers, so as to energetically drive the

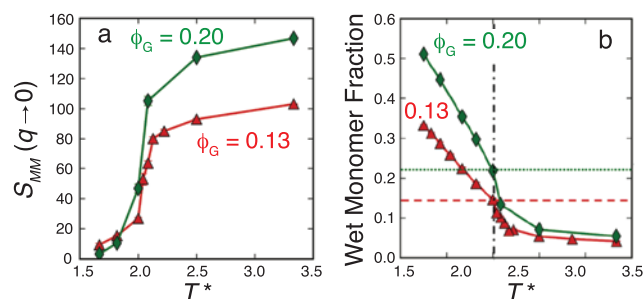


**FIGURE 1:** Simulations: (a) Low- $q$  value of the matrix-matrix structure factor and (b) wet monomer fraction versus reduced temperature,  $T^*$  from simulations of particles of diameter  $D = 5d$  (where  $d$  is the size of the Kuhn segment) grafted with “G” homopolymer chains of length  $N_{\text{graft}} = 10$  and grafting density  $\Sigma = 0.76$  chains/ $d^2$  in a “M” homopolymer matrix of length  $N_{\text{matrix}} = 50$  at a total volume fraction  $\eta = 0.35$  and with blend composition  $\phi_G = 0.13$ , and  $0.20$ . In part (b) the dispersion-aggregation transition temperature (vertical dot-dashed line) and the wet monomer fraction for the athermal  $\phi_G = 0.13$  and  $0.20$  blends (horizontal dashed and dotted lines) are also denoted. The error bars in parts (a) and (b) are standard deviations calculated from 50 uncorrelated configurations for each system; the error bars when not visible are smaller than the size of the symbol.

matrix chains to wet the graft chains even at low graft to matrix molecular weight ratios. In our recent work, using coarse-grained simulations and small angle X-ray and neutron scattering (SAXS and SANS) experiments we studied polymer nanocomposites where the graft-matrix polymer pair exhibit lower critical solution temperature (LCST) behavior, driving the composite to exhibit dispersed morphologies even when the graft molecular weight was smaller than the matrix molecular weight [6]. Interestingly, this process revealed an unexpected result about the coupling between the wetting-dewetting and dispersion-aggregation transitions. We found that in chemically dissimilar graft-matrix polymer nanocomposites, the wetting-dewetting transition occurs gradually with increasing temperature and is distinct from the sharp dispersion-aggregation (phase separation) transition, unlike other work with chemically similar graft-matrix nanocomposites where the two transitions are treated analogously.

In this recent work, the coarse-grained molecular dynamics (CGMD) simulations used a generic model that represents chemically dissimilar graft-matrix polymer pairs that exhibit

<sup>1</sup> Department of Chemical and Biomolecular Engineering, University of Delaware, Newark, DE 19716

<sup>2</sup> Department of Materials Science and Engineering, University of Delaware, Newark, DE 19716

<sup>3</sup> University of Houston, Houston, TX 77004

<sup>4</sup> NIST Center for Neutron Research, National Institute of Standards and Technology, Gaithersburg, MD 20899

a LCST phase behavior. The experiments focused on a specific system of deuterated polystyrene (dPS) grafted silica nanoparticles (diameter  $\approx 15$  nm) in a poly(vinyl-methyl-ether) (PVME) matrix as dPS-PVME blends have been shown to exhibit miscibility at room temperature, and a LCST phase behavior with increasing temperatures. In the simulations, the dispersion to aggregation transition was characterized both using simulation snapshots rendered with visual molecular dynamics (VMD) [7] as well as partial structure factors which showed an upturn with increasing temperature as  $q \rightarrow 0$ , indicative of the onset of particle aggregation. Since the simulations were run at discrete temperatures, the dispersion-aggregation phase transition was marked as the temperature where the onset of the low- $q$  upturn in these partial structures was seen. The low- $q$  value of the partial structure factor as a function of temperature exhibited a sharp transition over a small temperature range, indicating a first-order dispersion-aggregation transition (Figure 1a). The extent of matrix chains wetting the graft chains was calculated using two different methods: monomer concentration profiles and wet monomer fraction. Both methods concurred that with increasing temperature the wetting to dewetting was gradual and onset of dewetting occurred at temperatures below the dispersion to aggregation transition (Figure 1b).

To complement the simulations, SAXS and SANS studies were conducted as a function of temperature on critical volume fraction blends of 226k PVME (80 % by volume) with 33k dPS-grafted silica particles (grafting density = 0.7 chains/nm<sup>2</sup>). These scattering techniques provide structural information that covers a broad range of length scales and enabled a direct comparison to the simulation results. Since the X-ray contrast between the polymers is small and their contrast with the silica particles dominate the SAXS data, the observed peaks in the SAXS data were used to track the correlations between silica particles and therefore monitor the changes in wetting of the dPS brushes on the silica

particles. Separately, since the largest contrast for neutrons are between dPS and PVME and because of the small amount of silica particles in the scattering volume, the bulk phase behavior (and aggregation) of the dPS-grafted silica in PVME was monitored using the low- $q$  behavior in SANS. Figure 2 shows the results from both SAXS and SANS experiment and confirm the conclusions from simulations regarding a sharp first-order dispersion-aggregation transition (blue circles in Figure 2) and gradual wetting to dewetting transition (black triangles in Figure 2).

Simulations showed further that there is a critical extent of wetting which marks the onset of dispersion-aggregation transition; this critical extent of wetting is equal to the extent of wetting of an equivalent chemically identical or athermal nanocomposite (shown in Figure 1b with horizontal dashed lines). Since the wetting-dewetting transition for chemically different graft-matrix composites occurs over a range of temperatures rather than a distinct temperature, there are many “partially wet” and “partially dewet” states that occur between the “fully wet” and “fully dewet” states. This means that one could tune the extent of wetting, i.e., the extent of mixing between the graft and matrix chains, within the aggregated and dispersed morphologies by varying the chemical properties of the system, such as graft-matrix interactions or graft/matrix composition, at specific graft and matrix chain lengths. Fine control over the extent of wetting-dewetting in polymer nanocomposites presents useful control knob for tuning rheological properties that are strongly dependent on the mixing/entanglement of the graft and matrix chains [8-11]. Aside from these exciting new results in the field of polymer nanocomposites, this work also demonstrates the power of simulations and scattering methods to unravel the structure and thermodynamics of complex soft matter that enable engineering and production of new and unique materials with enhanced properties.

## References

- [1] P. F. Green, *Soft Matter* **7**, 7914 (2011).
- [2] R. Krishnamoorti, *MRS Bulletin* **32**, 341 (2007).
- [3] C. Chevigny *et al.*, *Macromolecules* **44**, 122 (2011).
- [4] B. Lin, T. B. Martin, A. Jayaraman, *ACS Macro Lett.* **3**, 628 (2014).
- [5] T. B. Martin, P. M. Dodd, A. Jayaraman, *Phys Rev Lett.* **110**, 018301 (2013).
- [6] T. B. Martin, K. I. S. Mongcopa, R. Ashkar, P. Butler, R. Krishnamoorti, A. Jayaraman, *J. Am. Chem. Soc.* **137**, 10624 (2015).
- [7] W. Humphrey, A. Dalke, K. Schulten, *J Molec. Graphics* **14**, 33 (1996).
- [8] S. K. Kumar, N. Jouault, B. Benicewicz, T. Neely, *Macromolecules* **46**, 3199 (2013).
- [9] N. Jouault, P. Vallat, F. Dalmas, S. Said, J. Jestin, F. Boué, *Macromolecules* **42**, 2031 (2009).
- [10] K. M. Lee, C. D. Han, *Polymer* **44**, 4573 (2003).
- [11] Q. Zhang, L. A. Archer, *Langmuir* **18**, 10435 (2002).

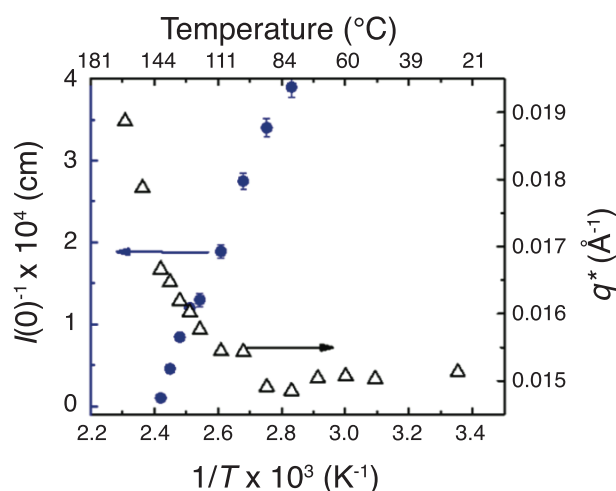


**FIGURE 2:** Shown is the temperature dependence of reciprocal of the extrapolated zero wavevector intensity ( $I^{-1}(0)$ ) from SANS and primary scattering peak position ( $q^*$ ) from SAXS for experimental blends of a 33k dPS-grafted silica (grafting density of 0.7 chains/nm<sup>2</sup>) with a 226k PVME blend at a volume fraction of PVME of 80 %.



# Gelation transitions of colloidal systems with bridging attractions

G. Yuan,<sup>1,2,3</sup> J. Luo,<sup>3</sup> C. C. Han,<sup>3</sup> and Y. Liu<sup>1,4</sup>

**S**tructural arrested transitions, such as the glass/gelation transition, describe the change of material from a liquid to a disordered solid state that is associated with a dramatic change of dynamic properties. Yet, despite its importance for a wide range of applications, the physical mechanisms of these transitions remain elusive. Spherical colloidal systems with a short-ranged attraction have long been used as ideal model systems to investigate glass/gelation transitions. While colloidal glass transitions typically take place at very large volume fraction, gelation transitions of spherical colloidal systems usually happen at relatively low concentrations.

A widely studied model colloidal system is the depletion-attraction system, where a short-ranged attraction between large colloidal particles is introduced by adding small polymer/colloidal particles. In general, a depletion attraction system can be considered a binary colloidal system with small solvent particles and large solute particles. There are no attractions between small and large particles in these systems. The added small particles can then introduce an effective attraction between large colloidal particles by an osmotic pressure effect.

Experiments using poly(methyl methacrylate) (PMMA) and polystyrene particles with a depletion-attraction have demonstrated that the gelation transition at a volume fraction of  $\approx 0.16$  coincides with the gas-liquid phase transition boundary [1]. It was proposed that the gelation transition of spherical colloidal systems with short-range attraction is due to the frustrated spinodal phase transition and not linked to the percolation transition. Because the equilibrium phase diagram of short-ranged attraction systems does not depend on the microscopic details of a system, the frustrated phase transition has now been widely considered a general theory for the gelation transition of spherical colloidal systems with a short-ranged attraction.

However, there are many experimental systems that can also be considered as binary colloidal systems, where the attraction between small and large particles are not negligible, and in some cases, very strong. The generalization of the physical mechanisms of gelation in a depletion-attraction system to other types of binary colloidal systems has not been carefully examined. Here, we studied the gelation transitions in a binary colloidal system

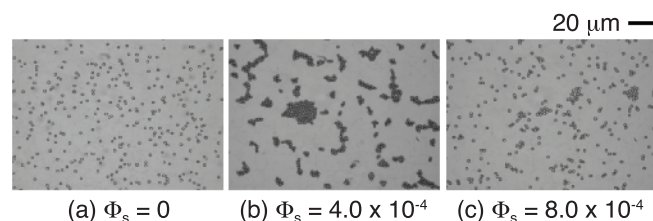


**FIGURE 1:** Optical microscopy images of dilute mixed suspensions with  $\Phi_L = 2.0 \times 10^{-3}$  at various  $\Phi_s$ . Under the optical microscope, only the large PS spheres are visible because the microgel size is much smaller than the wavelength of visible light.

where there is a strong attraction between small solvent and large colloidal particles [2]. The small particles can serve as a bridge to link neighboring particles. By varying the attraction strength between small and large particles, a binary colloidal system can gradually transition from a depletion-attraction system to a bridging attraction system.

The system investigated is composed of large hard polystyrene (PS) spheres ( $R_g = 960$  nm) and small soft poly (N-isopropylacrylamide) (PNIPAM) microgels ( $R_h = 140$  nm) in solvent. Here,  $R_g$  is the radius of gyration determined by neutron scattering (BT5-USANS, NCTR), and  $R_h$  is the hydrodynamic radius determined by dynamic light scattering. PNIPAM microgels can be reversibly adsorbed to the surface of PS spheres [3, 4]. Adding small particles enhances the effective attraction strength between large particles through the bridging of small particles until the attraction strength reaches a maximum value, after which adding more small particles slowly decreases the effective attraction strength [5-7]. This nontrivial dependence of the attraction strength on the small particle concentration results in a fundamental change of the aggregation and gelation behavior compared with depletion attraction systems.

The aggregation at low volume fraction is examined by microscopy as shown in Figure 1. Before adding small particles, large colloidal particles are uniformly dispersed in the solution (Fig. 1a). Adding small particles increases the effective attraction strength quickly resulting in the formation of large aggregates (Fig. 1b).

<sup>1</sup> NIST Center for Neutron Research, National Institute of Standards and Technology, Gaithersburg, MD 20899

<sup>2</sup> University of Akron, Akron, OH 44325

<sup>3</sup> Institute of Chemistry, Chinese Academy of Sciences, Beijing 100190, China

<sup>4</sup> University of Delaware, Newark, DE 19716

Further increasing the volume fraction,  $\Phi_S$ , of small microgel particles results in the large particles re-dispersing as shown in Fig. 1c.

When the volume fraction of large particles,  $\Phi_L$ , increases, the aggregate size induced by the bridging attraction can be large enough to form percolated clusters resulting in a gelation transition. At a given  $\Phi_L$ , the gelation transition is confirmed by measuring  $G'$  and  $G''$  at  $0.1 < \omega \text{ (rad/s)} < 100$ . When  $G'$  is larger than  $G''$  within the studied frequency range, a sample is considered in a gel state. With increasing  $\Phi_S$  at a given  $\Phi_L$ , a liquid-to-gel-to-liquid transition is observed for many samples. The gelation transition boundaries are identified for suspensions with  $\Phi_L$  ranging from 0.01 to 0.35.

In order to locate the experimental gelation boundary in the theoretical phase diagram, the effective interaction between large particles needs to be determined. As the size of the large PS sphere is on the micrometer scale, USANS is ideally suited to probe the inter-particle structure factor,  $S(q)$ . Fig. 2a shows USANS patterns obtained from mixed suspensions near the gelation boundaries. The USANS data are analyzed based on Baxter's one component sticky hard-sphere model after taking into account the instrument resolution. The analyzed Baxter's stickiness parameters,  $\tau$ , are represented by the reduced second virial coefficient  $B_2^*$  with  $B_2^* = 1-1/4\tau$ . In Fig. 2b, we show the gelation transition boundary (symbols) in the theoretical phase diagram of the adhesive hard sphere fluid. These results indicate that the formation of physical gel at intermediate volume fractions follows more closely to the percolation line and deviates from the gas-liquid transition line.

We have demonstrated that in bridging attraction systems, the physical mechanisms of gelation transitions at intermediate volume fractions are clearly different from depletion-attraction systems. Even though at small volume fraction (less than 10 %), the gelation from both systems seems to follow the gas-liquid transition line [6], the gelation transition at intermediate volume fraction is a kinetic driven effect for bridging attraction systems, not directly related to the gas-liquid separation. Our results imply that for many binary colloidal systems, the physical mechanisms of the gelation transition may depend on the nature of the attraction force between the solvent and solute particles. Furthermore, we demonstrate here that tuning the interaction strength between small solvent and large solute particles provides a new way to control the gelation boundary of a system relative to its gas-liquid transition line.

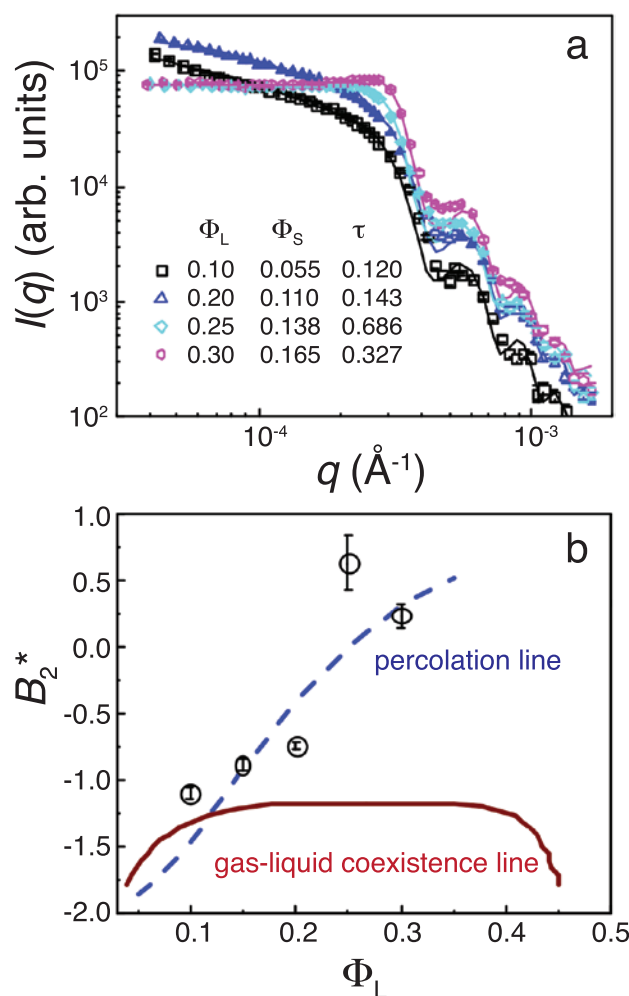


**FIGURE 2:** (a) Scattered intensity (symbols) and model fit (solid lines) from suspensions at different volume fraction along the gelation boundaries. (b) Open circles indicate the gelation boundaries in the general theoretical phase diagram of a hard sphere system with a short-ranged attraction. The blue dashed line and the red solid line are the theoretical percolation line and the gas-liquid coexistence line, respectively.

## References

- [1] P. J. Lu, E. Zaccarelli, F. Ciulla, A. B. Schofield, F. Sciortino, D. A. Weitz, *Nature*, **453**, 499 (2008).
- [2] G. Yuan, J. Luo, C. C. Han, Y. Liu, submitted (2016).
- [3] C. Zhao, G. Yuan, C. C. Han, *Soft Matter* **10**, 8905 (2014).
- [4] C. Zhao, G. Yuan, D. Jia, C. C. Han, *Soft Matter* **8**, 7036 (2012).
- [5] C. Zhao, G. Yuan, C. C. Han, *Macromolecules* **45**, 9468 (2012).
- [6] J. Luo, G. Yuan, C. Zhao, C. C. Han, J. Chen, Y. Liu, *Soft Matter* **11**, 2494 (2015).
- [7] J. Chen, S. R. Kline, Y. Liu, *J. Chem. Phys.* **142**, 084904 (2015).

# Connecting polymer-solvent interactions to structural transformations during solvent vapor annealing of block polymer thin films

C. K. Shelton,<sup>1</sup> R. L. Jones,<sup>2</sup> J. A. Dura,<sup>3</sup> and T. H. Epps, III<sup>1,4</sup>

Solvent vapor annealing (SVA) is a powerful technique for directing nanostructure ordering, orientation, and morphology in block polymer (BP) thin films for applications in emerging nanotechnologies such as nanolithographic masks, nanoporous membranes, nanotemplating, and organic optoelectronics. Swelling BP thin films with solvent vapor plasticizes polymer chains and reduces polymer glass transition temperatures ( $T_g$ s), thereby increasing chain mobility and allowing nanostructures to reorganize into well-ordered morphologies. With judicious control over factors including the solvent vapor composition, solvent vapor partial pressure, and swelling/deswelling pathways to influence the thermodynamics and kinetics of the polymer-solvent interactions, one can access a myriad of potential nanostructure conformations not obtainable by traditional thermal annealing alone. Additionally, SVA is ideal for BP systems that are susceptible to thermal transitions and degradation or require infeasible thermal annealing time scales. Therefore, we recently employed a combination of *in situ* small-angle neutron scattering (SANS) and neutron reflectivity (NR) to elucidate the importance of polymer-solvent interactions on morphology development during SVA of BP thin films [1]. Our results allowed us to glean key insights into the mechanisms of SVA and develop a more predictive approach to target desired nanostructure self-assembly.

Although the effects of SVA on BP self-assembly have been well researched, studies probing how solvent segregation into individual domains governs reorganization kinetics and thermodynamics have not been prevalent. Therefore, we used *in situ* neutron scattering to quantify the segregation of deuterated benzene (*d*-benzene) into the polystyrene (PS) and polyisoprene (PI) domains of PS-cylinder-forming poly(styrene-*b*-isoprene-*b*-styrene) (SIS) BP thin films as a function of atmospheric solvent concentration (solvent partial pressure divided by solvent vapor pressure [ $p/p_{\text{sat}}$ ]) [1]. Neutron scattering with solvent deuteration provided enhanced polymer-solvent contrast, in comparison to traditional X-ray experiments. From our neutron scattering analysis, we elucidated the full mechanism that describes how the number of stacked domains ( $n$ ) and the out-of-plane domain spacing ( $L_z$ ) changed as a function of film thickness and  $p/p_{\text{sat}}$  (Figure 1). The key factor in this mechanism was the amount of solvent in the PS block, a commonly ignored parameter that caused a transition between

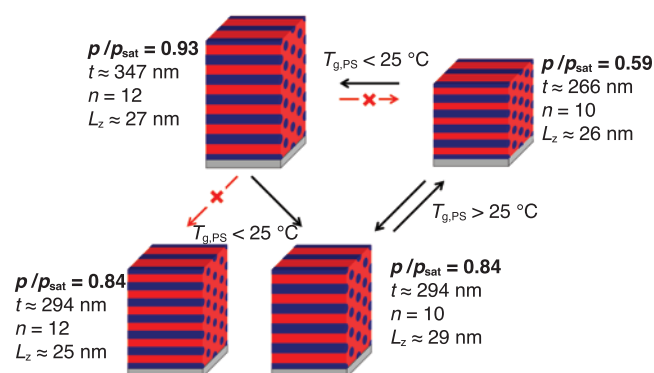


**FIGURE 1:** Schematic detailing the process by which SIS nanostructures restructure during SVA. SVA promoted layering of parallel PS cylinders by swelling the film to impart chain mobility *via* reduction of the  $T_g$  of the glassy PS domains below the annealing temperature (25 °C). To account for the film thickness ( $t$ ) reduction during solvent removal from  $p/p_{\text{sat}} = 0.93$  to  $p/p_{\text{sat}} = 0.84$ ,  $n$  decreased, rather than  $L_z$ , to prevent unfavorable compression of the SIS polymer chains. However, commensurability conditions from mismatches in  $t$  and  $n$  and an increased polymer-polymer interaction parameter ( $\chi_{\text{PS-PI}}$ ) led to slightly stretched layers ( $L_z = 27$  to  $L_z = 29$ ). When there was not enough solvent in the film to lower the PS  $T_g$  below 25 °C ( $p/p_{\text{sat}} \leq 0.59$ ),  $n$  could no longer adjust to account for thickness changes; instead, the average  $L_z$  decreased with the value of  $p/p_{\text{sat}}$  to account for the change in  $t$ .

a glassy PS state (kinetically trapped layers) and a non-glassy PS state (mobile layers); the PI domain is always non-glassy at room temperature. Primarily, we found that higher solvent concentrations in the PS domain lowered the  $T_g$  below room temperature, which increased the chain mobility and allowed the domains to rearrange and form the low energy domain spacing (modified slightly by commensurability). As the solvent concentration was decreased,  $T_g$  increased above room temperature,  $n$  was fixed, and  $L_z$  decreased as the film de-swelled. Interestingly, although the minority PS domain (cylinders) was the only glassy component at low solvent concentration, the non-glassy PI matrix was kinetically trapped as well and forced to conform to the same compressed  $L_z$ . This competition between polymer-solvent thermodynamics and kinetics resulted in an unexpected increase in  $L_z$  (27 nm to 29 nm) upon deswelling the film from a  $p/p_{\text{sat}}$  value of 0.93 to a  $p/p_{\text{sat}}$  value of 0.84, as there was sufficient *d*-benzene in the PS

<sup>1</sup> Department of Chemical and Biomolecular Engineering, University of Delaware, Newark, DE 19716

<sup>2</sup> Materials Science and Engineering Division, National Institute of Standards and Technology, Gaithersburg, MD 20899

<sup>3</sup> NIST Center for Neutron Research, National Institute of Standards and Technology, Gaithersburg, MD 20899

<sup>4</sup> Department of Materials Science and Engineering, University of Delaware, Newark, DE 19716



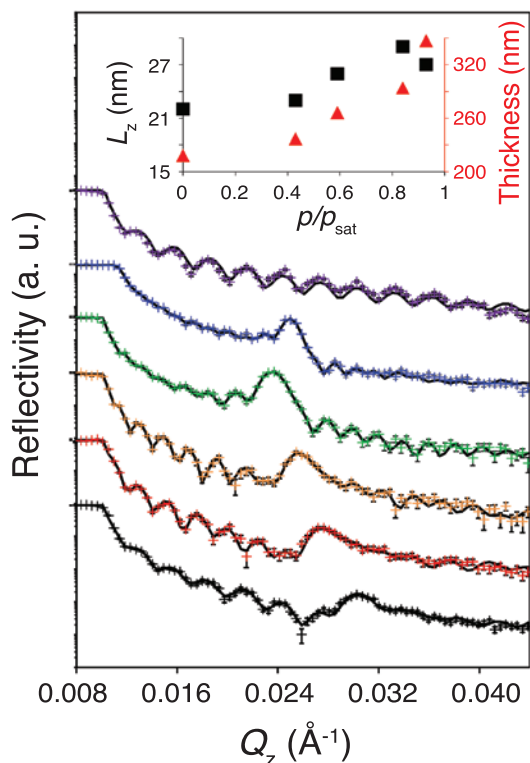


**FIGURE 2:** NR profiles (data point) and model fits (black lines) for *d*-benzene swollen SIS films at different  $p/p_{\text{sat}}$  in the order that they were run from top to bottom. Upon exposure to solvent vapor, the film increased in thickness ( $t$ ) due to solvent swelling and developed repeating parallel cylinder layers as evidenced by the narrowing of Kiessig fringes and the formation of a Bragg peak, respectively. In general,  $L_z$  decreased with the value of  $p/p_{\text{sat}}$ . However,  $L_z$  increased slightly from  $p/p_{\text{sat}} = 0.93$  to  $p/p_{\text{sat}} = 0.84$ . This effect was attributed to the reduction of  $n$  and subsequent incommensurability promoting slightly thicker layers. The inset plot shows how the film thickness and  $L_z$  change as a function of  $p/p_{\text{sat}}$ . The NR profiles have been vertically offset for clarity.

domain (51 % by mole and 40 % by mole, respectively) to lower the  $T_g$  of PS below 25 °C and impart chain mobility [2]. Therefore, the polymer chains were able to decrease  $n$  from 12 to 10 and maintain a favorable  $L_z$  at a reduced film thickness [3]. At the new  $n = 10$ , the layers were stretched slightly from 27 nm to 29 nm to achieve commensurability between the film thickness and  $L_z$  and to account for the slight increase in  $\chi_{\text{PS-PI}}$  when the solvent concentration in the film was reduced.

This unexpected transition from increasing to decreasing  $L_z$  during deswelling was determined from NR results obtained at the multi-angle grazing-incidence  $k$ -vector (MAGIK) reflectometer (Figure 2). The Bragg peak, which indicated the development of a periodic out-of-plane domain structure (parallel cylinders), shifted to a lower  $Q_z$  value going from the first ( $p/p_{\text{sat}} = 0.93$ ) to second ( $p/p_{\text{sat}} = 0.84$ ) solvent concentration and increased thereafter. This distinct shift signified an initial increase in  $L_z$ . Because the film thickness only decreased during deswelling,  $n$  had to decrease to maintain the low energy domain spacing. However  $L_z$  increased above this value to maintain commensurability with the film thickness,  $t$ . Following the initial increase in  $L_z$  the number of domains was fixed by the immobility of the PS domain, and  $L_z$  was forced to decrease with film thickness as solvent was removed.

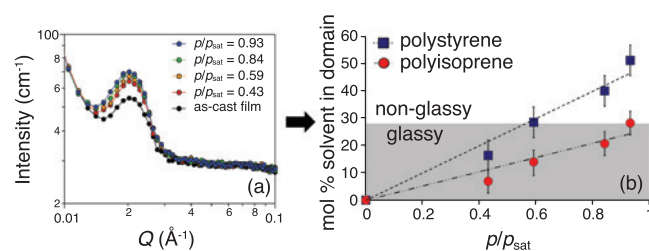


**FIGURE 3:** (a) SANS intensity profiles as a function of  $p/p_{\text{sat}}$ . (b) Solvent content in PS and PI domains calculated from broad peak model fits to SANS intensity profiles indicated that at a  $p/p_{\text{sat}}$  value of 0.59 the normalized *d*-benzene mol % in the PS domain (moles *d*-benzene in PS divided by moles *d*-benzene plus PS) was not high enough to reduce the  $T_g$  below 25 °C, which resulted in a glassy PS domain (gray shaded region) with limited mobility; the PI is always non-glassy at 25 °C.

To understand the cause of the structural transition, azimuthally averaged 1-D intensity profiles from *in situ* SANS, taken at the NGB 10 m SANS, (Figure 3a) were analyzed to quantify the solvent uptake in each domain as a function of  $p/p_{\text{sat}}$  (Figure 3b). Figure 3b revealed that at a  $p/p_{\text{sat}}$  value of 0.59, there was not a sufficient concentration of solvent to reduce the PS  $T_g$  below 25 °C (25-30) % by mole [2], and the PS domain transitioned to a glassy state. The  $p/p_{\text{sat}}$  value at which the glassy/non-glassy transition occurred matched with the  $p/p_{\text{sat}}$  value at which the restructuring mechanism, (measured with NR) changed, providing the final piece to the SVA mechanism.

In summary, we related measurable differences in  $L_z$ ,  $n$ , and film thickness to in-plane and out-of-plane solvent profiles determined with SANS and NR, respectively. The ability to add polymer-solvent contrast (via *d*-benzene) allowed us to relate both polymer-polymer and polymer-solvent interactions to the reorganization of nanostructures during SVA. Thus, we determined how solvent preferentially diffuses into individual domains, tracked solvent diffusion and nanostructure reorganization as a function of  $p/p_{\text{sat}}$ , and monitored the kinetic trapping of nanostructure reorganization with solvent removal. Finally, we demonstrated that  $L_z$  can be controlled by manipulating the solvent content in the film and the swelling/drying pathway. These outcomes help define several of the underlying mechanisms that govern self-assembly in BP thin films subjected to SVA, such as the mobility required to restructure the domain lattice, the impact of surface and interfacial roughness on commensurability constraints, the trapping of solvent in the film as a function of polymer mobility, and the selectivity of polymer and solvent at the free and substrate surfaces, which can facilitate the prediction of ideal solvent annealing conditions depending on the objectives.

## References

- [1] C. K. Shelton, R. L. Jones, J. A. Dura, T. H. Epps, III, (2016) in review.
- [2] J. E. Mark, Physical Properties of Polymers Handbook, (Springer Science & Business Media, LLC, New York, 2007) p. 191.
- [3] M. Luo, J. E. Seppala, J. N. L. Albert, R. L. Lewis, N. Mahadevapuram, G. E. Stein, T. H. Epps, III, Macromolecules **46**, 1803 (2013).

# Nano-deformation of sphere-forming thermoplastic elastomers during uniaxial extension

C. R. López-Barrón,<sup>1</sup> A. P. R. Eberle,<sup>2</sup> S. Yakovlev,<sup>1</sup> A.-J. Bons<sup>3</sup>

Elastomers' mechanical properties are greatly influenced by their microstructural features, e.g., cross-link density, type of crosslinking (physical or chemical), concentration and morphology of hard domains and/or nanofillers, etc. Therefore, engineering new elastomers with improved properties require deep understanding of the interrelations between mechanical response and microstructure evolution during deformation. To achieve this, in-situ nanostructure probes integrated with mechanical probes are needed. We present a method that combines small-angle neutron scattering (SANS), as the microstructure probe, with a commercial Sentmanat extensional rheometer (SER) that provides uniaxial deformation and measures the stress response from the sample (see Fig.1) [1].

Due to their commercial applicability, thermoplastic elastomers (TPEs) consisting of ABA-type triblock copolymers with styrenic end blocks and a rubbery middle block have been extensively studied. Most deformation studies of these TPEs are focused on systems with cylindrical and lamellar morphology [2], and very few on sphere-forming systems [3-5]. Among those studies, there is no consensus on whether the micro-deformation is affine or non-affine and whether the glassy domains deform or not. To elucidate such questions, we performed in-situ tensile-SANS measurements of sphere-forming blends of a SIS block copolymer with a low molecular weight deuterated polystyrene (dPS) during uniaxial deformation.

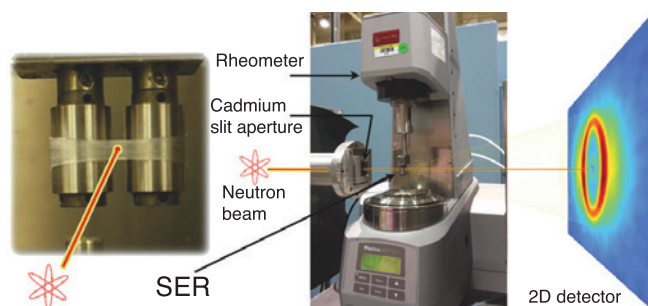


**FIGURE 1:** Left panel: photograph of the SER with a sample being stretched. Right panel: Rheometer with SER mounted in the NG7 30 m SANS instrument.

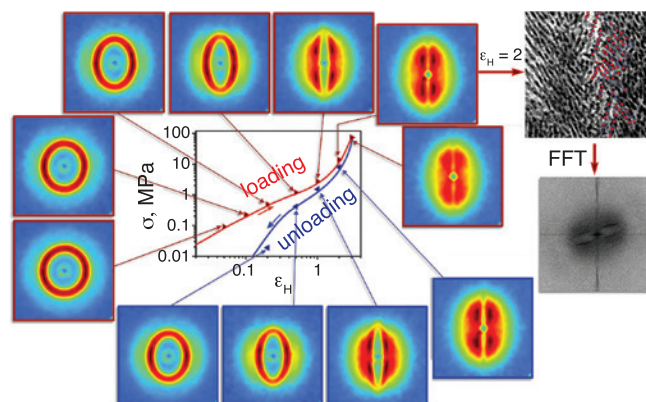


**FIGURE 2:** Stress-strain curves for the 5 % by weight dPS/SIS blends subjected to a load-unload cycle. The images are 2D SANS profiles at the strain values indicated by the arrows. Upper row corresponds to loading and lower row to unloading. Upper right: TEM micrograph of UV-cured 5 % dPS/SIS films subjected to uniaxial extension with Hencky strain of 2 and two dimensional fast Fourier transform image of the micrograph.

Figure 2 shows the stress-strain curve of the SIS/dPS blend measured in the rheometer, along with the 2D SANS profiles measured during the deformation. The initially isotropic circular profile (corresponding to a body-centered cubic lattice) becomes elliptical in the elastic and yield regimes, which indicates that the lattice is extended in the stretching direction (SD) and compressed in the transverse direction (TD). A new microstructural feature was observed at high elongations, namely the formation of quadrulobe patterns. These were previously observed in cylinder forming block copolymers [2, 6], in which their formation are associated to chevron-type arrangements of the cylinders. In our system the quadrulobes originate from the rearrangement of the glassy spheres into strings that orient into preferential angles inclined towards the stretching direction, as shown in the micrograph in Fig. 2.

Stress unloading is accompanied by the disappearance of the quadrulobe pattern and by the reduction of the anisotropy of the ellipsoidal scattering shapes. This indicates that the “oriented strings” configuration is not stable and the structure reverts to

<sup>1</sup> ExxonMobil Chemical Company, Baytown, TX 77520

<sup>2</sup> ExxonMobil Research and Engineering Company, Annandale, NJ 08801

<sup>3</sup> ExxonMobil Chemical Europe, Machelen, Belgium

the equilibrium BCC lattice structure once the stress is removed. This occurs due to the interconnectivity of the glassy domains via the rubbery middle block, which in turn is responsible for the elastic response of these materials. After unloading and complete removal of stress, a remnant deformation (evidenced by permanent anisotropy in the scattering peaks) is observed. This permanent deformation contributes to the permanent set measured macroscopically.

In order to determine the transition from affine to non-affine deformation, azimuthally averaged SANS intensities of circular sectors (with arc angle of  $20^\circ$ ) along SD and TD are computed for each strain probed during loading and unloading. 2D SANS profiles for the 5 % dPS/SIS blend at Hencky strain  $\epsilon_H = 0.5$  is shown in Fig. 3 with the circular sectors in SD ( $90^\circ$ ) and TD ( $0^\circ$ ) indicated as shaded areas, along with the azimuthally averaged sector 1D SANS profiles. The  $q$ -values corresponding to the scattering peaks measured in the sectors parallel to SD and TD are indicated as  $q_{SD}^*$  and  $q_{TD}^*$ , respectively. For  $\epsilon_H = 0$ ,  $q_{SD}^* = q_{TD}^* = q_0^*$ , which confirms that the initial structure is fully isotropic. Also expected is that  $q_{SD}^* < q_{TD}^*$  at  $\epsilon_H = 0$ , indicating an increase in inter-sphere spacing along SD and a contraction of the spacing along TD, as illustrated in the schematic drawing in Fig. 3. The changes in magnitude of the two vector components, with respect to the un-stretched state, are given by  $q_0^* / q_{SD}^*$  and  $q_0^* / q_{TD}^*$ , respectively. If the rearrangement of the polystyrene spheres is affine, then the ratio between the changes in length ( $L$ ) and width ( $W$ ) of the film must be the same as that between the vector component in SD and TD. To verify this, plots of  $\ln(W/W_0)$  versus  $\epsilon_H = \ln(\lambda) = \ln(L/L_0)$  (lines) along with plots of  $q_0^* / q_{TD}^*$  versus  $q_0^* / q_{SD}^*$  (symbols) are given in Figure 3 (lower panel). The deviation from the theoretical slope of  $-1/2$  indicates that the deformation is non affine above  $\epsilon_H > 0.3$ . Hence, the transition between affine and non-affine deformation is determined to be at  $\epsilon_H \approx 0.35$ . This transition preludes the appearance of quadrulobes in the SANS profiles which, as discussed above, is associated to the BCC-to-Chevron transition, and hence, non-affine deformation is not surprising.

Combining mechanical testing with SANS provides a very powerful tool to elucidate the structural origins of elastic response of nanostructured elastomers. We have shown that strain-hardening, hysteresis, permanent set, as well as affine to non-affine deformation transition are the result of rearrangement in the nanostructure of the sphere-forming block copolymer TPE studied [1]. These studies are being extended to other types of polymeric systems, such as polyolefins [7], and polymer melts, which lack contrast for other scattering techniques (e.g., SAXS).

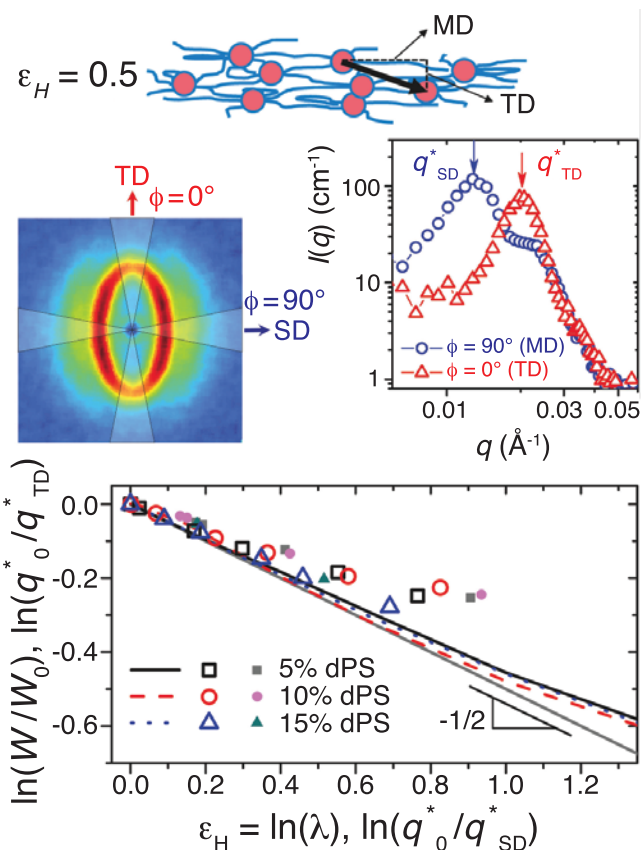


**FIGURE 3:** Upper panel: 2D SANS patterns and 1D azimuthally averaged SANS profiles corresponding to the sectors aligned in the TD and SD directions (shaded areas in the 2D patterns) for  $\epsilon_H = 0.5$ . Schematic cartoons shows the microstructural redistribution upon stretching. Lower panel: Normalized film width versus Hencky strain (lines), and normalized reciprocal scattering peak position in TD versus corresponding values in SD.

## References

- [1] C. R. López-Barrón, A. P. R. Eberle, S. Yakovlev, A. Bons, *Rheologica Acta* **55**, 103 (2016).
- [2] I. W. Hamley, *Journal of Physics: Condensed Matter* **13**, R643 (2001).
- [3] T. Inoue, M. Moritani, T. Hashimoto, H. Kawai, *Macromolecules* **4**, 500 (1971).
- [4] R. Seguela, J. Prud'homme, *Macromolecules* **21**, 635 (1988).
- [5] R. W. Richards, G. Welsh, *European Polymer Journal* **31**, 1197 (1995).
- [6] T. Pakula, K. Saijo, H. Kawai, T. Hashimoto, *Macromolecules* **18**, 1294 (1985).
- [7] C. R. López-Barrón, Y. Zeng, J. J. Schaefer, A. P. R. Eberle, T. P. Lodge, F. S. Bates, *Macromolecules* (Submitted).



# Megasupramolecules

M.-H. Wei,<sup>1</sup> B. Li,<sup>1</sup> R. C. Lhota,<sup>1</sup> R. L. A. David,<sup>1</sup> S. C. Jones,<sup>2</sup> V. Sarohia,<sup>3</sup> J. A. Schmitgal,<sup>4</sup> and J. A. Kornfield<sup>1</sup>

Ultralong polymers have remarkable properties that enable drag reduction in pipelines and control of drop breakup. For example, even at low concentrations ( $\approx 10$  to  $100 \times 10^{-6}$  g/g), ultralong polymers ( $>4 \times 10^6$  g/mol) dissolved in jet fuel reduce the risk of post-crash large, hot fireballs. By inhibiting mist formation, ultralong polymers reduce the droplet surface area through which fuel evaporates and, consequently, reduce the extent and intensity of the resulting fire. The longer the polymers, the more potent they become—and the more vulnerable. Stress accumulates along the chain, particularly in strong flows (e.g., passing through pumps), reaching levels that break the backbone [1]. Using statistical mechanics, we designed end-functional polymers that are individually short enough to survive routine handling and assemble into supramolecules to mimic ultralong polymers. They control mist—but reversibly separate under high stress to avoid degradation. To test the theoretical basis for these effects, small angle neutron scattering (SANS) was uniquely able to provide the necessary information on the supramolecular structure. The results support the theoretical model and open the way to design of further end-to-end associative polymers with unprecedented combinations of properties [2].

Flows through industrial pumps and filters typically break chains to pieces  $< 0.7 \times 10^6$  g/mol - too short to reduce drag or inhibit misting. We sought to use chains that are near, but shorter than, this limiting length and stick them together into very long, multimillion molecular weight supramolecules—“megasupramolecules” ( $M_w > 4 \times 10^6$  g/mol). There were conflicting demands that might have made it impossible. On one hand, literature shows that increasing backbone lengths beyond  $5 \times 10^4$  g/mol disfavors end-association. On the other hand, long chains are needed to disfavor formation of rings, which are ineffective, when used at the low concentrations relevant to fuel additives. To check the feasibility of building ultralong supramolecules at low concentration, we used a statistical mechanical lattice model to calculate the populations of linear and cyclic aggregates of end-associative polymers as a function of the association strength, backbone length, and concentration. The model predicted that using end-association of long chains is feasible—providing the required 50 ppm of megasupramolecules (Figure 1, A)—but only in a small window of parameter space. The backbone length must be long enough that a string of

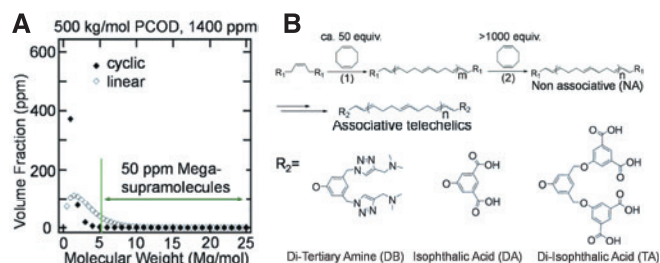


**FIGURE 1:** A) Theory predicts it is possible to produce long enough supramolecules ( $> 4$  Mg/mol) at sufficient concentration ( $50 \times 10^{-6}$  g/g) to confer mist control. B) Translating theoretical predictions into actual polymer molecules. Synthesis of end-functional nonassociative polymers: (1) Grubbs II, dichloromethane (DCM),  $40^\circ\text{C}$ , 1 hour; (2) Grubbs II, DCM,  $40^\circ\text{C}$ , until stir bar stops ( $> 5$  min), equivalents of COD for desired molecular weight. (middle) Postpolymerization conversion to end-associative polymers. (bottom) End group structures: DB, dibase; DA, diacid; TA, tetraacid.

8-10 reaches the length of ultralong polymers and short enough to not suffer from shear degradation. The association strength must be very strong to drive formation of megasupramolecules—but not too strong, or ineffective circular supramolecules will dominate over linear ones.

We set out to make the predicted molecules with structures suitable for use in fuel. We excluded salt- or metal-mediated associations; however, the required strength of end association ( $16\text{ kT}$  to  $18\text{ kT}$ ) was comparable to the strongest previously reported hydrogen-bond “stickers.” We turned to charge-assisted hydrogen bonds, each providing  $8\text{ kT}$  to  $9\text{ kT}$ : two tertiary amines on each end of the “dibase” (DB) chains and two carboxylic acids on each end of the “diacid” (DA, Figure 1, B bottom) chains can deliver the needed  $16\text{ kT}$  to  $18\text{ kT}$ . The model requires individual end-associative chains, approximately ten-times longer than previously examined end-functional “telehelix” chains. Although there was no precedent for making such long telechelics, we were able to expand the envelope of accessible chain lengths via two-step ring-opening metathesis polymerization (ROMP), using a chain transfer agent (CTA) to start and end each chain with a functional group. In some cases, the initial end groups ( $R_1$ ) are subsequently converted to associative groups ( $R_2$ ) acid- and base-ended chains (Figure 1, B).

<sup>1</sup> California Institute of Technology, Pasadena, CA 91125

<sup>2</sup> Electrochemical Technologies Group, Jet Propulsion Laboratory, Pasadena, CA 91109

<sup>3</sup> Office of the Chief Technologist, Jet Propulsion Laboratory, Pasadena, CA 91109

<sup>4</sup> U.S. Army RDECOM TARDEC, 6501 East 11 Mile Road, Warren, MI 48397

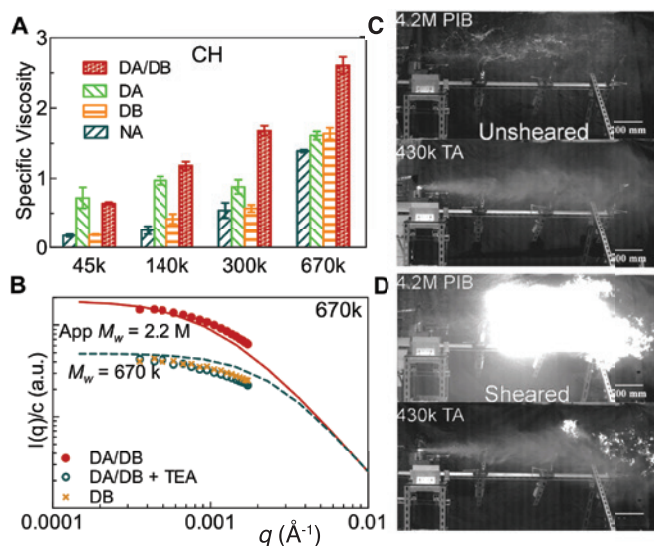


**FIGURE 2:** Evidence of association in solution and efficacy in mist control. A) Increase of specific viscosity for solutions at a weight fraction of 0.25 % of DA/DB polymers with 670k backbone relative to DB alone and nonassociative (NA) chains. B) Static light scattering at a weight fraction of 0.028 % (35 °C) shows supramolecules of  $M_w$  2200 kg/mol (2.2 M, solid circles), which separate into individual units (x) when a small-molecule tertiary amine, TEA, is added (open circles). Curves show predictions from theory for 1000 kg/mol polymers at  $1400 \times 10^{-6}$  g/g (solid, associative; dashed, NA). C and D). Impact test in presence of ignition sources (60 ms after impact, maximal flame propagation), Jet-A treated with conventional ultralong polymer 4.2M PIB (mass fraction of 0.35 %) or with end-associative 430k TA PCOD (mass fraction of 0.3 %). “Unsheared” is as-prepared, “sheared” is after  $\approx 60$  passes through fuel pump.

Assembly of DA/DB into large supramolecules is evident in cyclohexane, tetralin, and Jet-A, manifested by increased specific viscosity compared to the nonassociative controls at the same backbone length (Figure 2, A). Static light scattering results verify that this increase in viscosity is due to formation of supramolecules (Figure 2, B). The molecules were ready for testing in the conditions that motivated this research: severe flows that degrade ultralong polymers and high-speed impacts that produce devastating fuel mist fires. The supramolecules proved effective for mist control for improved fire safety (comparable to ultralong polymers, Figure 2, C and D top)—and their efficacy lasts even after  $> 50$  passes through a fuel pump (Figure 2, D bottom), which destroys ultralong polymers (Figure 2, C bottom). Furthermore, tests in an unmodified diesel engine indicate these associative polymers burn cleanly, without affecting power or efficiency—and provide a 12 % decrease in soot formation.

To test the fundamental premise of the theoretical model, measurements of the distribution of segment density in the megasupramolecules were needed. Deuterated cyclohexane provided neutron-scattering contrast relative to the hydrogenous

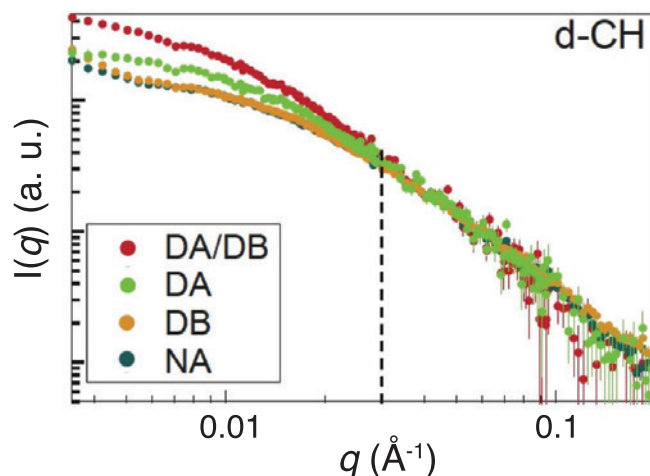


**FIGURE 3:** Concentration-normalized SANS intensities (25 °C) for 50 kg/mol polymers in  $d_{12}$ -cyclohexane at concentrations well below the overlap concentration of NA (2 mg/mL for NA and DB; 0.05 mg/mL for DA and DA/DB) show that DA/DB supramolecules adopt relatively open conformation. Dashed line is radius of gyration for NA.

polymer. In accord with theory, the resulting SANS patterns show megasupramolecules are *not* collapsed in solution (their conformation is as open as their nonassociative counterparts: scattering patterns are unchanged at  $q > 2\pi/R_g \approx 0.03(1/\text{\AA})$  in Figure 3). Furthermore, DA/DB association increases scattering at low  $q$  as though it formed longer linear chains, consistent with end-to-end, pairwise association.

By using a theoretical model for end-associative polymers, we were able to propose and synthesize polymers capable of self-assembling into long chains in solution and surviving high shear conditions, like repeated pumping. Neutron scattering, light scattering, and specific viscosity all confirm association of these polymers in solution. In practice, these carefully selected associative polymers do provide effective mist control. We verified that these mist control properties are due to the reversible separation of the chains through contrasting associative and nonassociative versions of these polymers, and by comparing the associative polymer’s mist control ability and a commercial long-chain polymer before and after shearing. These associative polymers are able to imitate the behavior of long-chain polymers, yet retain their efficacy despite high stress conditions, making them attractive additives for mist control.

## References

- [1] S. A. Vanapalli, S. L. Ceccio, M. J. Solomon, PNAS **103**, 16660 (2006).
- [2] M.-H. Wei, B. Li, *et al.*, Science **350**, 72 (2015).

# Dielectric RheoSANS for the simultaneous interrogation of rheology, microstructure, and electronic properties of complex fluids

J. J. Richards,<sup>1</sup> C. V. L. Gagnon,<sup>2</sup> J. R. Krzywon,<sup>1</sup> N. J. Wagner,<sup>3</sup> and P. D. Butler<sup>1</sup>

In situ measurements are an increasingly important tool to elucidate the complex relationship between nanoscale properties and macroscopic measurements. One important example is the electrical and mechanical properties of carbon black slurries. While carbon based nanocomposites have been studied for decades, an emerging application is their use as an electrically percolating network in semi-solid flow battery electrodes [1]. In this application, electrical conductivity must be maintained while the electrode is continuously pumped through an electrochemical flow cell. Under these conditions, it is highly desirable to maximize the conductivity of these suspensions while reducing their viscosity in order to minimize pumping losses. Our hypothesis is that the relationship between viscosity and conductivity is a direct product of material microstructure and colloidal interactions. To test this hypothesis, we seek a way to measure the electrical, mechanical, and microstructural response of carbon particles under arbitrarily complex deformations. To accomplish this, we have developed a new Dielectric RheoSANS environment.

The instrument consists of a Couette geometry mounted on an ARES G2 strain controlled rheometer enclosed in a modified Forced Convection Oven (FCO) shown Figure 1a. The carbon black slurry is confined between concentric titanium cylinders that are nearly transparent to neutrons. Both cylinders are electrically isolated from the rheometer. In a Dielectric RheoSANS experiment, the impedance response is measured by an impedance-capacitance (LCR) meter and stress response is measured by the rheometer. The control scheme for this procedure is shown in Figure 1b. and is made possible through a programmable Labview interface that measures signals from the LCR meter and the rheometer. An analog triggering protocol synchronizes those measurements to the SANS event mode acquisition. At the end of a preprogrammed set of shear conditions, the entire rheological, electrical and microstructural characteristics of the sample can be reconstructed and time binned in order to quantify changes in microstructure as a function of both the shear conditions and time.

An example raw data output from Dielectric RheoSANS experiment from a 3 % by mass Vulcan XC72 sample dispersed in hydrogenated propylene carbonate is shown in Figure 1c. From top to bottom Fig. 1c shows the rheological, electrical, and microstructural response of a single sample throughout the course of an acquisition. Using this approach, we are able to capture the liquid to gel transition that takes place as shear stress imposed on the carbon black suspension drops below the yield stress of the bulk gel. The instrument design and findings resulting from initial testing will

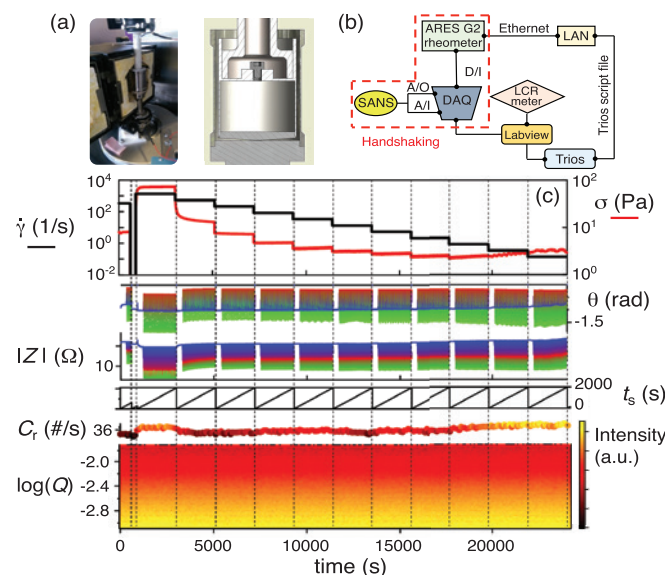


**FIGURE 1:** (a) (left) Picture of the dielectric Couette geometry contained within the FCO accessory and mounted onto an ARES G2 rheometer, (right) Schematic radial cross-section of dielectric Couette geometry. (b) Control scheme for Dielectric RheoSANS experiment detailing how synchronization of the three measurements is accomplished. (c) (top) shear rate,  $\dot{\gamma}$ , and shear stress,  $\sigma$ ; (middle) impedance magnitude,  $|Z|$ , and phase shift,  $\theta$ ; (bottom) neutron arrival time,  $t_s$ , detector count rate,  $C_r$ , and intensity (a. u.) vs.  $\log(Q)$ ; all as a function of measurement time throughout the acquisition of a single Dielectric RheoSANS experiment. Shown here is a flow sweep experiment consisting of a 600 s preshear and 300 s delay and then 11 logarithmically spaced programmed shear rates ranging from 1000 (1/s) to 0.1 (1/s), each 2100 s long. From the neutron time plot the synchronization scheme is evident as the detector clock was reset between each specified shear rate resulting in a hedgehog pattern emphasized here by vertical dotted lines through the plots.

appear in forthcoming publications [2, 3]. While the Dielectric RheoSANS instrument was developed to answer important questions related to flowability of carbon black suspensions, it has the potential to expand the study of other complex suspension behavior, and will soon be available for use within the user program.

## References

- [1] M. Duduta *et al.* Adv. Energy Mater. **1**, 511 (2011).
- [2] J. J. Richards, N. J. Wagner, P. D. Butler, Rev. Sci. Instrum, In preparation (2016).
- [3] J. J. Richards, J. Hipp, N. J. Wagner, P. D. Butler, Soft Matter, In preparation (2016).

<sup>1</sup> NIST Center for Neutron Research, National Institute of Standards and Technology, Gaithersburg, MD 20899

<sup>2</sup> University of Maryland, College Park, MD 20742

<sup>3</sup> University of Delaware, Newark, DE 19716



# Ultra small-angle neutron scattering with azimuthal asymmetry

X. Gu,<sup>1</sup> and D. F. R. Mildner<sup>2</sup>

The scattering vector range of small-angle neutron scattering using pinhole geometry may be extended to  $10^{-5} \text{ \AA}^{-1}$  using a double perfect crystal instrument [1]. The poor resolution in the direction normal to the scan direction enables increased intensity, but the slit-smeared data requires a correction before concatenation with the SANS data. The desmearing algorithm is valid only for azimuthally symmetric scattering, such that the scattering in the scan direction and the slit direction are the same. This presents a problem for the analysis of USANS data of asymmetric scattering systems. We offer a method [2] to modify asymmetric data that follow a power law such that the USANS data concatenate well with that obtained using pinhole SANS.

SANS measurements on thin shale sections cut both along the bedding plane and normal to bedding show power law scattering with an exponent  $n$ . The scattering from shale cut parallel to the bedding plane has azimuthal symmetry with circular contours on the two-dimensional detector that are averaged to obtain intensity  $I(Q)$  shown by the brown curve labeled X in Figure 1a. The perpendicular-cut scattering has elliptical contours. Sector averages are taken in directions parallel (Y curve in blue) and normal (Z curve in red) to bedding for the perpendicular-cut sample. Note that curves X and Y are coincident. The R curve in green is for the perpendicular-cut sample rotated continuously in the incident beam.

We assume that the  $Q$  dependence of the scattering is separable from the azimuthal dependence and the intensity may be written

$$I(Q, \varphi) = A_{\varphi} Q^{-n} \approx [a^{-2} \cos^2 \varphi + b^{-2} \sin^2 \varphi]^{-n},$$

where  $\varphi$  is the azimuthal angle relative to the normal to bedding. In the  $\varphi = 0$  (or Z) direction,  $I_Z(Q) = A_Z Q^{-n} \approx a^n Q^{-n}$ , and the  $\varphi = \pi/2$  (or Y) direction,  $I_Y(Q) = A_Y Q^{-n} \approx b^n Q^{-n}$ . The factor  $a/b$  corresponds to the ratio of the long and short semi-axes of the elliptical isointensity contours. The Z plot may be made coincident with the Y plot by multiplying the intensity values by  $(b/a)^n$ .

The slit-smeared USANS data also have power law scattering with an exponent  $m$ , such that  $m \approx n-1$ . Figure 1a also shows the slit-corrected USANS results indicating that the desmearing of the X and R data results in a smooth transition when concatenated with the SANS data. On the other hand, the Y curve is no longer

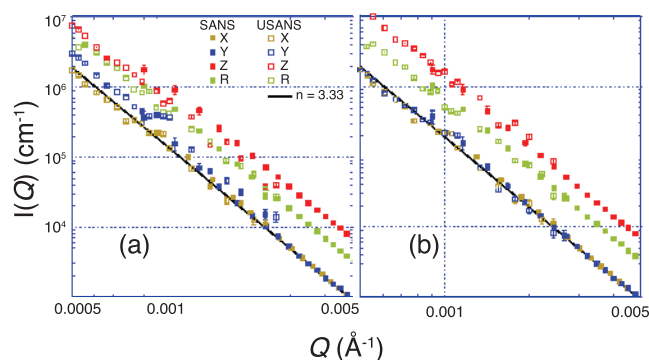


**FIGURE 1:** The desmeared USANS (open square symbols) and the SANS (filled square symbols) measurements in the vicinity of the overlap region (a) before and (b) after modification to the USANS data. The parallel-cut (brown X curve) and the rotational (green R curve) measurements show a smooth transition, whereas for the perpendicular-cuts before modification the Y blue curve (with the bedding plane in the horizontal) has an upward jump at the transition and the Z red curve (with the bedding plane in the vertical) has a downward jump. After modification, the transitions are no longer so abrupt. The line indicates the power law  $AQ^{-n}$  for the X and Y curves, where  $n = 3.33$ .

coincident with the X curve. When the two datasets are joined, the desmeared Y data have a positive shift in intensity, while the Z data have a negative shift.

An elliptical contour has a corresponding circular contour of radius  $r = (ab)^{1/2}$ , the geometric average of the two semi-axes of the contours obtained from the SANS measurement. We multiply the Y intensity data by a factor  $(b/r)^m = (b/a)^{m/2}$  and then perform the desmearing. Figure 1b shows that the modified USANS Y intensity concatenates well with the SANS Y data and is consistent with the USANS X data. Similarly, multiplying the USANS Z intensity data by a factor  $(a/r)^m = (a/b)^{m/2}$  before desmearing results in the modified data having good concatenation with the SANS data. This procedure results in an intensity for asymmetric scattering that is consistent over the wide  $Q$  range offered by the combined measurement.

## References

- [1] J.G. Barker *et al.*, J. Appl. Cryst. **38**, 1004 (2005).
- [2] X. Gu, D. F. R. Mildner, J. Appl. Cryst. **49**, 934 (2016).

<sup>1</sup> Pennsylvania State University, University Park, PA 16802

<sup>2</sup> NIST Center for Neutron Research, National Institute of Standards and Technology, Gaithersburg, MD 20899

# Application of small-angle scattering data to improve biomolecular docking success rate using Rosetta

J. A. Snyder,<sup>1</sup> P. Ghatti,<sup>2</sup> A. McAuley,<sup>2</sup> and J. E. Curtis<sup>1</sup>

**B**iological macromolecules often associate to form complexes in solution. Obtaining information on the orientation of each protein partner within a complex can help determine functionality in applications such as actin filaments, bacterial flagellar filaments, design of antibody complementarity determining regions (CDR) for targeted antigen epitope binding, and protein oligomerization. Most algorithms used to model small-angle scattering (SAS) data of protein complexes rely on the use of dummy-spheres and do not account for the physics of the system. One method that is widely used to predict protein complex formation is the Rosetta suite of “docking” computational physics programs. Prediction of protein-protein docking can be particularly challenging when no experimental data on the system is known. Hence it is necessary to do an initial global search of relative protein configurations, where many thousands of docking decoy structures are required. Typically, either shape complementarity or an interaction energy for the two partners is used to calculate a docking score for each relative configuration. We have developed a protocol [1], to be implemented as part of the SASSIE program [2], which combines predictive capabilities from molecular docking simulations combined with an analysis of experimental SAS data. This method will benefit both the Rosetta docking and SAS communities.

Most protein-protein docking strategies employ an initial low-resolution stage (LR), where the proteins are treated as rigid bodies where the amino acid side chains are not permitted to move with respect to each other. This is then followed by a high-resolution stage (HR) within the local configuration space of each decoy from the LR search, which is then treated at a level of higher accuracy. Side chain atoms are allowed to move in this stage. For HR docking, a near-native structure is defined by decoys having an interfacial root mean-squared deviation (IRMSD), relative to the native structure, of less than 4.0. Docking success is then defined by the occurrence of least three near-native decoys within the top five (interfacial) scored HR decoys.

Our protocol involves first performing a LR scan to generate tens of thousands of decoy structures. Four protein structures were selected for initial benchmark study. For one of these protein-protein complexes, the neuroligin-1/ $\beta$ -neurexin protein complex, experimental SAS data was available [3]. Theoretical SAS profiles are then calculated [2] for each structure and the resulting  $I(q)$ -plots are compared to experimental SAS data using reduced  $\chi^2$ . The  $\chi^2$  values are used along with the set of docking scores to divide the initial set of LR docking decoy structures into four sets.

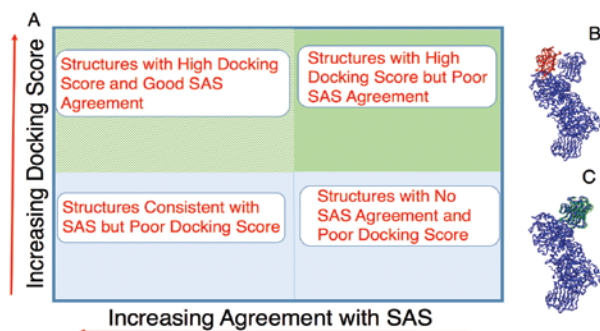


**FIGURE 1:** (A) Illustrative graph distinguishing set of structures for which use of docking alone would likely require selection from (green region) compared with a smaller set of structures (cross hatched region) representing both high likelihood of docking success and best agreement with SAS data (small  $\chi^2$ ). Resulting shape model fit to SAS data (B), and selected decoy structure from a LR docking which gives subsequent docking success (C), superposed on native neuroligin-1/ $\beta$ -neurexin protein complex (blue), respectively.

It is found that the set representing (both) high docking score and small  $\chi^2$  generate the largest number of docking successes when those decoys are used as input structures for the subsequent HR docking. This is illustrated in Fig. 1A. For the case of the neuroligin-1/ $\beta$ -neurexin protein complex, Fig. 1B shows the shape model obtained from a standard analysis of SAS data, superposed on the native structure, which has subsequently been solved [4]. Fig. 1C shows a model of one docking success, again superposed on the native structure. Comparing Fig. 1B to 1C represents the extent to which the shape model misplaces the orientation and relative position of the neurexin ligand by comparison to the structure representing a docking success that shows much better alignment relative to the known native structure.

These results show that SAS data may be used to assist the docking user in protein-protein docking with additional means of selectively filtering false positives among a set of decoy structures generated by a global docking search and provides the SAS user with a modeling strategy that includes an accounting of physical interactions.

## References

- [1] J. A. Snyder, P. Ghatti, A. McAuley, J. E. Curtis, Biophysical J. submitted (2016).
- [2] J. E. Curtis, S. Raghunandan, H. Nanda, S. Krueger. Computer Physics Communications **183**, 382-389 (2012).
- [3] D. Comoletti, *et al.*, Structure **15**, 693-705 (2007).
- [4] D. Arac, *et al.*, Neuron **20**, 992-1003 (2007).

<sup>1</sup> NIST Center for Neutron Research, National Institute of Standards and Technology, Gaithersburg, MD 20899

<sup>2</sup> Department of Analytical and Formulation Sciences, Amgen Inc., One Amgen Center Drive, Thousand Oaks, CA 91320

# A second-generation low-background gamma-ray spectrometer

R. M. Lindstrom

Nuclear analytical methods often need to be pushed to maximum sensitivity. Detection limits in gamma-ray spectrometry are improved by increasing the efficiency of the detector and by decreasing its background. A low-background gamma spectrometer system in a dedicated laboratory above ground at NIST has been in use for sensitive radioactivity measurements for more than twenty years [1]. Because the germanium detector, named Ty, is built of selected materials and is housed in an optimized shield of selected lead, its background is dominated by cosmic radiation even though it is located in the Reactor Building. Most of the background rate consists of a broad continuum from high-energy cosmic-ray muons. These muons also generate fast neutrons in the detector shield, which undergo inelastic scattering in the materials of the instrument, giving characteristic gamma peaks from isotopes of Fe, Cu, Pb, and the Ge detector itself.

One of the most useful criteria for selecting and using a Ge gamma-ray detector, in that it incorporates all the specifications of a spectrometer, was proposed by Cooper [2]. It may be rewritten [3] for the case of very low activity as

$$D(E) = \frac{A}{t\epsilon(E)\Gamma(E)} \left\{ \left[ 2tB(E)bR(E) + \frac{A^2}{4} \right] + \frac{A}{2} \right\}$$

where

$D(E)$  = minimum detectable disintegration rate, Bq

$A$  = reciprocal of the desired fractional precision (= 10 for 10 %)

$t$  = counting time, s

$\epsilon(E)$  = detector efficiency, counts/photon

$\Gamma(E)$  = gamma-ray yield, photons/decay

$R(E)$  = detector resolution (fwhm), keV

$b$  = peak integration width, in multiples of the resolution  $R$

$B(E)$  = background rate, counts  $s^{-1}keV^{-1}$

Another established low-background detector in this laboratory is operated in anticoincidence with a surrounding NaI scintillator. This procedure reduces the muon continuum by an average factor >15 between 500 keV and 2000 keV. Although the detection limit for single-photon nuclides is indeed improved by about the expected factor of four, this scheme is unsuitable for measuring nuclides with cascade decays: the detection limit for  $^{60}Co$  is in fact worse by a factor of two when anticoincidence is applied. In addition, with massive NaI closely surrounding the detector, this system is usable only for small-sized sources.



**FIGURE 1:** The second-generation detection system installed in the dedicated low-background counting room. The new Ge detector "Glen" is seen in the center of the shielding.

A new second-generation detector system is being constructed, with four improvements over the 1990 Ty detector.

- 1) The relative efficiency of the new Ge detector, named Glen, is 110 %, nearly three times that of the Ty system, at once improving the detection limit by more than 50 %.
- 2) The detector is shielded by 15 cm of pre-1945 iron rather than lead. Because the production rate of ( $\mu,n$ ) neutrons per kilogram of shielding is proportional to the atomic mass  $A$ , the fast-neutron flux is  $6 \times 10^{-3} \text{ cm}^{-2}s^{-1}$ , a factor 5 lower than in the lead shield of the Ty detector. There is ample room inside the 160L shield for bulky samples.
- 3) An umbrella of plastic scintillators covers three adjoining exterior faces of the shield, and is operated in anticoincidence with the central Ge to cancel the muon continuum by a factor of eight. Most of the remaining peaks in the background spectrum are due to radon, which is reduced by displacing the air inside the shield, either with nitrogen-filled pillows or by venting the detector Dewar into the shield.
- 4) The all-digital data acquisition system is capable of time-stamped list mode recording, enabling the signal shaping and logic timing to be optimally tuned.

As a result of these updates, the detection limit (or alternatively the required counting time for a given statistical uncertainty) has been improved by a factor of five over the old low-background spectrometer, the sample shape and size requirements are relaxed, and the background spectrum contains fewer interfering peaks.

## References

- [1] R. M. Lindstrom, D. J. Lindstrom, L. A. Slaback, J. K. Langland, Nucl. Instrum. Methods **A299**, 425 (1990).
- [2] J. A. Cooper, Nucl. Instrum. Methods **82**, 273 (1970).
- [3] R. M. Lindstrom, Appl. Radiat. Isotop. **43**, 263 (1992).



# $\mu$ RheoSANS for measurement of complex fluids structure at high shear rates

J. Weston,<sup>1</sup> D. Seeman,<sup>2</sup> S. D. Hudson,<sup>2</sup> and K. M. Weigandt<sup>2</sup>

Small angle neutron scattering measurements of complex fluids undergoing shear deformation have significantly enhanced our understanding of the structure-rheology relationships in materials [1]. Most rheoSANS measurements are made using Couette geometries due to the relatively simple flow field and the constraints of scattering geometry. However, Couette shear cells are typically limited to maximum shear rates on the order of  $10^4 \text{ s}^{-1}$ . This is well below some commonly encountered industrial applications such as spraying, injection, extrusion or lubrication processes, with shear rates approaching or above  $10^6 \text{ s}^{-1}$ . We have begun to develop thin slit rheometers for simultaneous SANS and rheology measurements in order to characterize structural changes at these much higher shear rates.

A prototype thin slit flow cell that is 100  $\mu\text{m}$  deep, 8 mm wide, and 35 mm long has been adapted for use in a neutron beam (Figure 1). Flow is driven by external rate controlled pumps (typically syringe pumps). Pressure sensors are installed inline before and after the flow cell to measure the pressure drop. The pressure drop is used to calculate the viscosity as a function of shear rate during the SANS experiment. The current device is suitable for measurements with pressure drop less than 700 kPa, but ongoing development is aimed at reaching pressures as high as 70 MPa [2]. Preliminary experiments used a 33 mmol/L cetylpyridinium chloride and 20 mmol/L sodium salicylate wormlike micelle solution in  $\text{D}_2\text{O}$ . A gear pump was used to recirculate the solution through the  $\mu$ RheoSANS apparatus and a thermal jacketed reservoir was used to extract excess heat generated from the pump motor and viscous heating. Example reduced 2D scattering patterns are plotted in Figure 2, left and center.

However, Poiseuille flow is more complicated than Couette flow and the shear rate is not constant through the sample. In fact, it varies from  $0 \text{ s}^{-1}$  in the center to a maximum at the wall (which increases with flow rate). Thus, the scattering represents an average structure over all of the shear rates in the flow cell. Knowing that, for continuous fluids, the shear stress ( $\tau$ ) decays linearly from a maximum at the wall to zero in the center of the channel we can deconvolute and isolate the scattering from the near wall sample (as shown in the equation) so long as there is scattering data from two different flow rates ( $Q$ ). Examples of the deconvoluted high shear scattering data is shown in Figure 2 (right).

$$I_{q_x, q_y}(\text{wall}) = \frac{1}{1 - \frac{\tau_{\text{wall}, n-1}}{\tau_{\text{wall}, n}}} \left[ I_{q_x, q_y}(Q_n) - \frac{\tau_{\text{wall}, n-1}}{\tau_{\text{wall}, n}} I_{q_x, q_y}(Q_{n-1}) \right]$$

As expected, at low flow rates when the scattering is isotropic applying the deconvolution does not have any effect on the

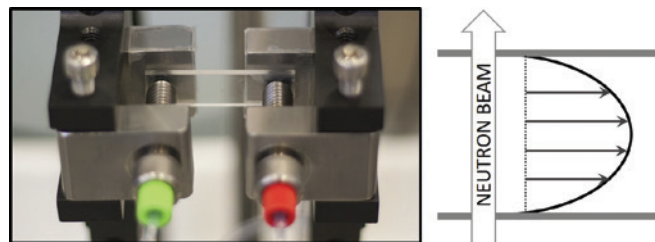


FIGURE 1: Left: Picture of prototype  $\mu$ RheoSANS device. Right: Schematic depicting velocity profile in thin slit relative to the incident neutron beam.

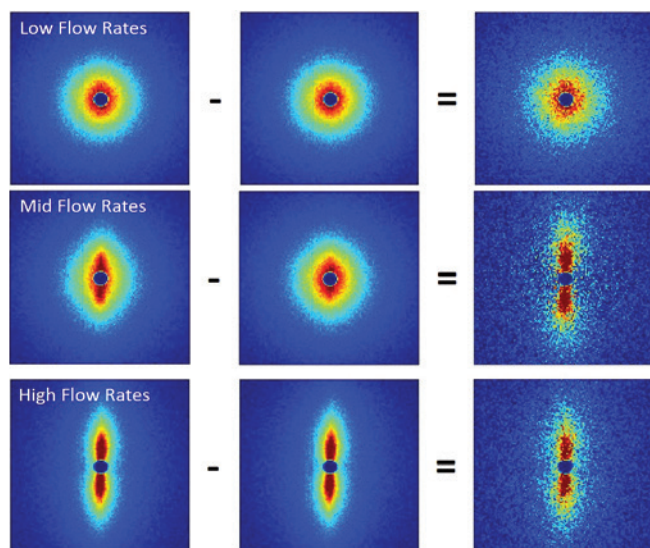


FIGURE 2: Example of 2D data deconvolution.

data. Similarly, at very high flow rates where the data is highly aligned in all but smallest region near the center of the channel, the deconvolution yields 2D data very similar to the original data set. However, at intermediate flow rates when the sample is transitioning from an unaligned to a maximally aligned state, there is significant variation in the micelle structure throughout the channel. Upon applying the deconvolution, it is qualitatively very clear that the near wall structure (high shear rate) is much more aligned relative to the bulk average structure at these flow rates.

## References

- [1] A.P. R Eberle, L. Porcar, Curr. Opin. Colloid Interface Sci., **17** (1), 33 (2012).
- [2] J. Weston, D. Seeman, S. D. Hudson, K. Weigandt, In Preparation (2016).

<sup>1</sup> Georgetown University, Washington, DC 20057

<sup>2</sup> NIST Center for Neutron Research, National Institute of Standards and Technology Gaithersburg, MD 20899

# Neutron Source Operations

## Reliability and Availability of the Reactor

The reactor operated 265 days during FY 2016, achieving a reliability of 96.5 %. The 4.4 days that were lost were due to three separate events: 1) a dropped fuel element, 2) the failure of an instrumentation power supply due to lightning and 3) a failure of a PLC in the cold source. Some of that lost time was made up by extending the reactor cycles.

## Liquid Deuterium Cold Source Status

The NBSR neutron source provides beams of thermal and cold neutrons for research in materials science, fundamental physics and nuclear chemistry. From its initial design, a large, 55 cm diameter beam port was included for the installation of a cold neutron source, and the NCNR has been steadily improving its cold neutron facilities for more than 25 years. Monte Carlo simulations have shown that upgrading to a liquid deuterium ( $\text{LD}_2$ ) source will provide an average gain of 1.5 between 4 Å and 9 Å with respect to the existing liquid hydrogen cold source, and a gain of 2 at the longest wavelengths. The conceptual design of the proposed source was presented in the 2012 NCNR Annual Report. Funding for the refrigerator and the cold source upgrade has been granted by the National Nuclear Security Administration of the Department of Energy as a mitigation strategy to offset the anticipated 10 % loss in neutron flux when the NBSR is converted to low-enriched uranium (LEU) fuel. The NCNR has been actively preparing for this fuel transition.

Many of the components necessary for the  $\text{LD}_2$  source have been procured. To manage the heat load on the  $\text{LD}_2$  cold source, a new, 7 kW helium refrigerator is being installed to provide the necessary cooling capacity. It is expected that acceptance testing will be completed later this year. The 16 m<sup>3</sup> ballast tank to store the deuterium at  $\approx 4$  bar when the refrigerator is not operating has been installed outside the guide hall; this provides a passively safe response to a refrigerator failure. A pair of deuterium condensers was obtained (Figure 1) and has since been integrated into two condenser assemblies (one spare) with completion of their vacuum and He containment jackets.

In FY 2017, it is expected that a final subcontract will be awarded for the turbine installation, testing and commissioning of the refrigerator. The new refrigerator will be used to operate the existing cold sources after its cooling capacity has been demonstrated. Also in FY 2017, detailed designs of the cryostat assembly components will be completed and the fabrication



**FIGURE 1:** Deuterium condensers prior to enclosure in vacuum and helium containment jackets.

of prototype vessels for testing will begin. Upon successful completion of tests on the prototypes, two complete cryostats will be fabricated. Because of contracting issues, it is now expected that installation of the  $\text{LD}_2$  source will not occur before 2021.

## Feasibility Studies for a Replacement Reactor

The NBSR, first critical on the 7th of December 1967, is currently licensed to operate until 2029, and then it will likely be re-licensed for 20 more years. The reactor will eventually need to be replaced however, to meet the ever-growing demand of the neutron scattering community. The demand is particularly great for cold neutron beams; more than 70 % of the research at the NCNR uses cold neutrons.

A reactor replacement study was initiated, and efforts to design a new research reactor optimized for cold neutron sources are currently underway. The primary purpose of the proposed new reactor is to provide high intensity cold neutron beams for scientific experiments. An innovative horizontally split compact core cooled and moderated by light water while reflected by heavy water is being investigated at this stage to achieve better flux performance [1]. The new reactor was designed for 20 MW thermal power and a 30 day refueling cycle for an equilibrium core condition to provide a cost-effective research facility.

A cut-away view of the reactor design is shown in Figure 2, illustrating the reactor components. An innovative horizontally split core scheme is employed in the design such that a thermal flux

trap between the core halves provides ideal locations to place cold neutron sources (CNS). The core itself is cooled and moderated by light water and surrounded by the heavy water reflector. The core halves are enclosed in two zirconium core boxes that separate heavy water and light water. Two vertical liquid deuterium cold neutron sources are placed in the flux trap located in the north and south sides of the core. Two CNS beam tubes are connected

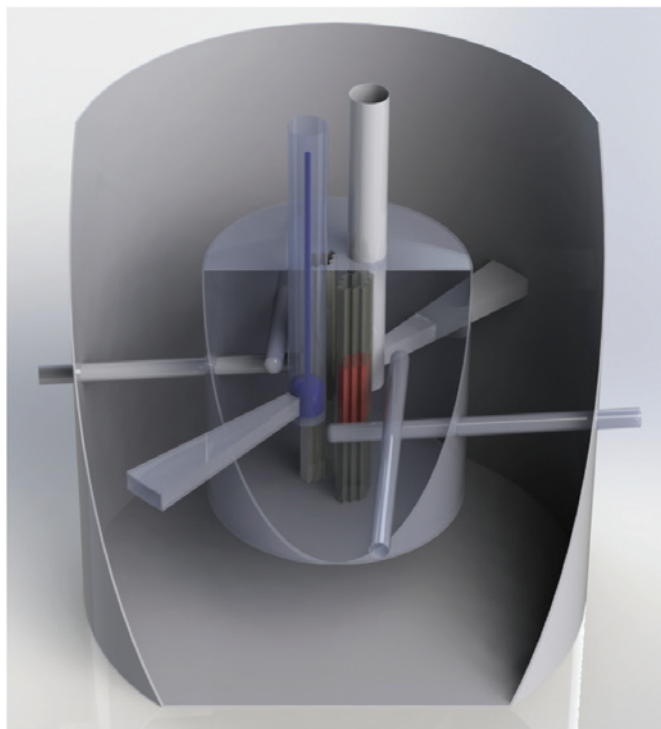


**FIGURE 2:** A cut-away view of the reactor with a split-core.

to the CNSs with guides pointing north and south. Four tangential thermal beam tubes are placed in the east and west sides of the core at different elevations. The split core consists of 18 MTR-type fuel elements in two horizontally split regions. Each region consists of 9 fuel elements and represents one half of the reactor core.

The most important figure of merit to evaluate the performance of a cold neutron source is the “brightness” of the source in the direction of the guides to various instruments. The calculated brightness of the vertical CNS in the split core compared to the actual performance of the existing large liquid hydrogen (LH<sub>2</sub>) CNS at the NCNR clearly shows that substantial gains can be achieved in brightness for the new design. Since the present NIST liquid hydrogen CNS has comparable performance per MW with most existing cold sources, the preliminary results indicate the performance of the vertical CNS in the split core has significant gains (a factor of  $\approx 3$ ) compared to nearly all currently available cold neutron sources. Some preliminary efforts made to optimize the CNS geometry indicate another 20 % to 40 % gain is possible.

The thermal neutron beam tubes are comparable to the existing NBSR beams. Only four are modelled in the present design. It may be possible to add additional thermal beams, or include one or two larger ports for some thermal neutron guides serving many instruments. The design is in a conceptual phase, and will change as engineering constraints continue to be introduced. A more detailed model, including a primary cooling loop is under development.

## Reference

- [1] Z. Wu, M. Carlson, R. E. Williams, S. O’Kelly, and J. M. Rowe, *Trans. Am. Nucl. Soc.*, **112**, 795 (2015).



# Facility Development

## Installations and Upgrades

Two major instrument development projects have dominated the efforts of the RFO group. First, work on the 40 m very Small Angle Neutron Scattering (vSANS) has been accelerating with designs, procurements, fabrications, installation, and testing continuing throughout 2016. By the end of 2016, vSANS will have installed, aligned, wired, and tested the pre-sample neutron beam delivery system, including the velocity selector and neutron/gamma shielding (bunker), cryogenically cooled crystalline Bi-Be filter, attenuator assembly, polarizer guide, and 11 pre-sample flight path boxes (Figures 1 and 2). The boxes contain the neutron guides, circular apertures, slit apertures, and magnetic guide fields, all under computer control. The 64 motors required is the largest motion control installation at the NCNR to date. The tube detectors arrays have been tested and the histogramming and management software has been written. However, contractor delays have pushed the delivery of the detector vessel back to late 2016, delaying the wiring and installation of the detectors on the front and middle carriages. The rear detector carriage will support



FIGURE 1: vSANS pre-sample flight path assembled and aligned.

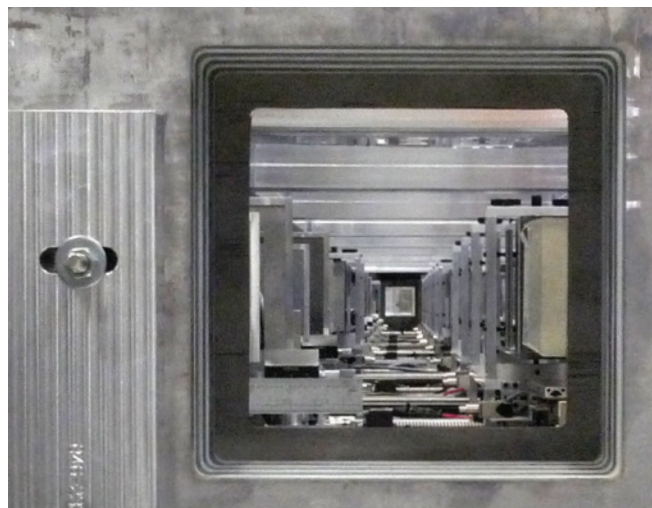
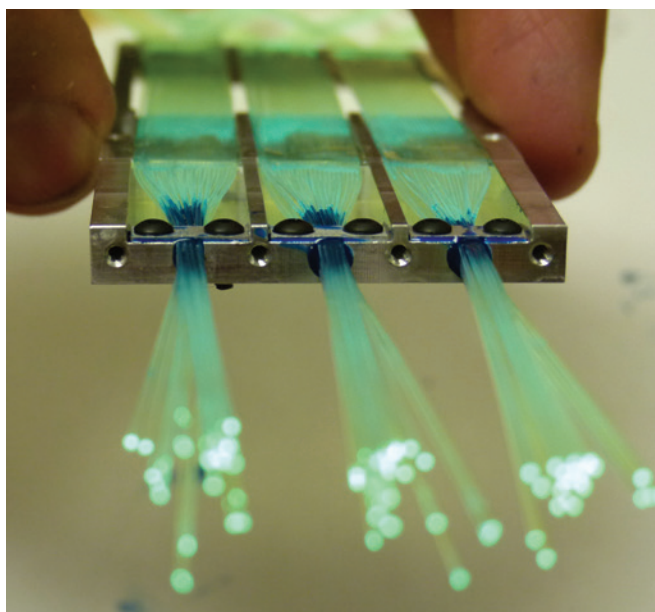


FIGURE 2: An upstream view through the vSANS guide boxes at NG-3.

a 2D detector that has been awarded and will be installed as part of phase II in 2017. We anticipate having the first neutrons on detector in April of 2017, the first SANS experiment June 2017, and full polarized beam SANS experiment by January 2018.

Activity at NG1 to prepare for the CANDOR Reflectometer has been ongoing. Physically, the detector test station has been relocated from NG1 to PHADES at NG7 to make room for CANDOR. Power, plumbing, and real estate have been re-configured or moved so that all beam line components from the beam delivery system to the sample position could be installed and aligned. This includes major components such as the converging guide, monochromator, Be/Bi filter, and apertures. Many more parts have been procured and are assembled and tested as they arrive.

The first full scale test of the chromatically optimized neutron detector for the CANDOR instrument was performed on SPINS this year. In this detector array, (Figures 3 and 4) 54 highly ordered pyrolytic graphite (HOPG) crystals are set at different takeoff angles to diffract neutrons into  $^6\text{LiF:ZnS(Ag)}$  scintillator based proportional counters (described in the 2014 Annual Report). The test involved varying the incident energy of the beam entering the array and monitoring the output of the scintillator detectors. The results are consistent with simulation, but have revealed the need for extraordinary precision in assembly and alignment. With the successful testing, efforts have focused on completing the full 30-array detector package.



**FIGURE 3:** Close-up of the wavelength shifting fibers of a CANDOR detector.

We anticipate to have the first neutrons on the CANDOR detector September 2017, first specular reflection experiment January 2018, full polarized beam operation March 2018, and non-specular capability available June 2018.

Several other upgrade and installation projects have also been completed in 2016. A new velocity selector for BT-7 has been received from Airbus and all performance testing has been completed. Design and fabrication of all components needed to install the velocity selector is nearing completion, and installation is scheduled for December 2016. The Neutron Spin Echo instrument at NG-A saw performance gains as the helium cooling system was tested and adjusted so the large 8-inch correction coil amperage could be increased from 50 A to 62.5 A and the current in the small and middle correction coils increased proportionally, giving the same proportional increase in the maximum accessible experiment Fourier time.

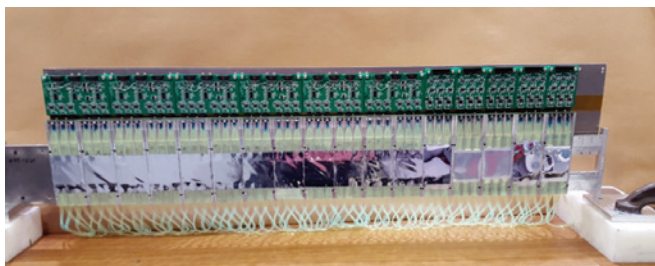


**FIGURE 4:** CANDOR prototype detector array showing the arrangement of the silicon photomultipliers and preamplifiers.

## Helium Spin Filters

The NCNR supports an active program to develop and provide  $^3\text{He}$  neutron spin filters (NSFs) to support measurement capabilities using polarized neutrons. Polarized beam experiments are routinely carried out on the BT-7 thermal neutron triple-axis spectrometer, the small-angle neutron scattering instruments, and the multi-axis crystal spectrometer (MACS). During the past year, the NCNR's spin filter program serviced 26 user experiments, for a total of 102 days of beam time, 116 bar-liters of polarized  $^3\text{He}$  gas, and 99 polarized  $^3\text{He}$  cells.

The NCNR and the PML have focused on deploying one of the worlds most powerful wide-angle neutron polarization analysis capabilities on MACS. We have implemented a reliable procedure to demagnetize the instrument after the use of superconducting magnets that permits  $^3\text{He}$  relaxation times on MACS close to the intrinsic values observed off-line. Several important polarized beam MACS experiments performed last year benefitted from these long relaxation times, and are yielding important scientific results. We have redesigned and built two new NMR-based  $^3\text{He}$  polarization flippers to address intermittent unreliable behavior in the first prototype device. They have been tested and are reliable, and are available for routine polarized MACS experiments. Figure 5 shows one of the  $^3\text{He}$  NMR flippers, which is a very compact, integrated neutron polarizer and flipper device.

We have expanded the development of the horseshoe-shaped wide-angle cells, which provide polarization analysis of the entire  $220^\circ$  range of scattering angles on MACS with a single analyzer cell. We have fabricated two such cells, available for routine polarized MACS experiments. These cells can improve polarized neutronic performance further by about 40 % compared to the current polarized MACS setup. These cells will employ a dedicated new cryostat with a smaller diameter tail, which is under construction. Concurrently, we are developing a polarized MACS capability that utilizes a CCR and a horseshoe cell to enable scientific applications for soft matter.

In a traditional polarized neutron reflectometer with a single incident wavelength, a supermirror is used for polarization analysis of specular reflection, whereas a  $^3\text{He}$  spin analyzer is needed for diffuse reflection. However, the simultaneous use of several wavelengths and multi-scattered beams in the CANDOR instrument requires a  $^3\text{He}$  spin analyzer for all experiments. We have collaborated with the CANDOR instrument responsables and engineering team on a conceptual design of the  $^3\text{He}$  spin analyzer. In phase I, we will operate with traditional, remotely polarized  $^3\text{He}$  cells to establish the polarized beam capability. An in-situ analyzer is under development for future experiments. We have also developed a polarized neutron capability using a superconducting magnet that allows for polarized beam experiments on BT-7 at sample magnetic fields up to 2 T, opening up many new scientific opportunities.



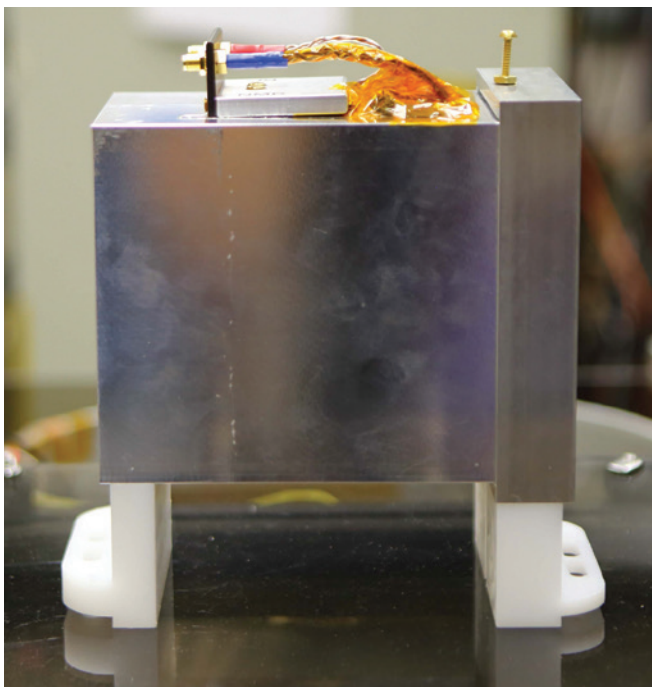


**FIGURE 5:** A recently developed, compact  $^3\text{He}$  polarizer with an integrated adiabatic fast passage NMR-based neutron spin flipper. The  $^3\text{He}$  polarization flipping efficiency has been determined to be  $3 \times 10^{-4}$  per flip.

## Data Acquisition Software

The New Instrument Control Environment (NICE) is a Java-based data acquisition package that incorporates a highly versatile scripting capability to enable end user adaptations to be coded under all the major scientific programming languages. This year, the graphical user interface (GUI) for SANS was completely overhauled. Its favorable user reviews spurred deployment at the NGB 30 m SANS, and now NICE has been deployed for full-time use on all three of the SANS instruments. This brings the total number of NCNR instruments controlled by NICE to eight. A special, polarized beam GUI has recently been tested on NG7 SANS, with good feedback. For vSANS, NICE is currently in testing, running with the existing hardware and incorporating new hardware as it is added. For CANDOR, gathering of software requirements is nearly complete.

## Data Analysis Software

During the past year, many improvements have been made to the Data Analysis and Visualization Environment (DAVE) software package. The DAVE suite is the primary software package used on many of the neutron inelastic instruments at the NCNR for experiment planning, data visualization, reduction and analysis. A long overdue infrastructure overhaul was made when the entire source code was migrated from CVS on SourceForge, where it has resided for more than a decade, to an internal NIST repository running Git. This change was essential for

reliability and better version control and management of the code repository for current and future developers. Besides the usual maintenance work that is necessary for a project of this maturity, there were new functionality and updates made in the areas of data reduction and analysis. To enhance usability, we have been gradually coalescing on two common interfaces for the data reduction modules representing each of the supported instruments in DAVE. This year it was the turn of the HFBS instrument; the data reduction modules covering dynamic and fixed window scan analysis were updated and new features added based on user requests. The new program modules provide an enriched user interaction experience and facilitate visual comparing and contrasting of multiple datasets. Built-in functions for momentum distribution analysis and a parametric empirical baseline function have been added to PAN. In addition, basic algebraic operations can now be applied to the fitted parameters making it straightforward to represent the results in ways that are more informative or amenable to further analysis.

Version 4.0 of the SASView data analysis program has been released. This release has a completely new modeling interface, making it easier for researchers to add their own models and share models with others. Models can be created using python or using C. In either case, features such as polydispersity on shape parameters are automatically available. Calculations can also take advantage of the extra computing capabilities on the CPU or on the graphics card to calculate patterns more quickly, often realizing several orders of magnitude speed improvement over SASView 3.1.

Reductus is the new reduction software for the NCNR reflectometers. Being web-based, the latest version of this software is automatically available to all users. The program links to the publicly available data from the NCNR, making it easy to retrieve and examine files. Reduction templates can be saved and shared, complete with all the parameters set by the user, completely capturing data provenance. All stages of the data reduction are visible, with the output available at each step, so problems in the final reduced data can be traced back to the step where they appear.

Funded jointly by the NSF and EPSRC, the CCP-SAS project is focused on developing an easy-to-use open-source modeling package that enables users to generate physically accurate atomistic models, calculate scattering profiles and compare results to experimental scattering data sets in a single web-based software suite. SASSIE-web is now available to the international scattering community. Several workshop and training sessions have taken place at scattering centers and scientific meetings. To date, over thirty-seven manuscripts using our software products on a variety of structural biology and soft-matter problems have been published. With hundreds of users the goals of the next year are to enable the software to utilize high performance computational methods to model scattering data.



# Serving the Science and Technology Community

The mission of the NIST Center for Neutron Research is to assure the availability of neutron measurement capabilities to meet the needs of U.S. researchers from industry, academia and other U.S. government agencies. To carry out this mission, the NCNR uses several different mechanisms to work with participants from outside NIST, including a competitive proposal process, instrument partnerships, and collaborative research with NIST.

## Proposal System

Most of the beam time on NCNR instruments is made available through a competitive, peer-review proposal process. The NCNR issues calls for proposals approximately twice a year. Proposals are reviewed at several different levels. First, expert external referees evaluate each proposal on merit and provide us with written comments and ratings. This is a very thorough process where several different referees review each proposal. Second, the proposals are evaluated on technical feasibility and safety by NCNR staff. Third, we convene our Beam Time Allocation Committee (BTAC) to assess the reviews and to allocate the available instrument time. Using the results of the external peer review and their own judgment, the BTAC makes recommendations to the NCNR Director on the amount of beam time to allocate to each approved experiment. Approved experiments are scheduled by NCNR staff members in consultation with the experimenters.

The current BTAC members are:

- Andrew Allen (NIST Ceramics Division)
- Jeffrey Allen (Michigan Technological University)
- Collin Broholm (The Johns Hopkins University)
- Leslie Butler (Louisiana State University)
- Thomas Epps (University of Delaware)
- Kushol Gupta (University of Pennsylvania)
- Valery Kiryukhin (Rutgers University)
- Ramanan Krishnamoorti (University of Houston)
- Jennifer Lee (National Institutes of Health)
- Raul Lobo (University of Delaware)
- Janna Maranas (The Pennsylvania State University)
- Steven May (Drexel University)
- Lilo Pozzo (University of Washington)

- Stephan Rosenkranz (Argonne National Laboratory)
- Gila Stein (University of Houston)
- Stephen Wilson (University of California Santa Barbara)

## Partnerships

The NCNR may form partnerships with other institutions to fund the development and operation of selected instruments. These partnerships, or “Participating Research Teams”, may have access to as much as 75 % of the available beam time on the instrument, depending on the share of total costs borne by the team. A minimum of 25 % of the available beam time is always made available through the NCNR proposal program to all users. Partnerships are negotiated for a fixed period (usually three years) and may be renewed if there is mutual interest and a continued need. These partnerships have proven to be an important and effective way to expand the research community’s access to NCNR capabilities.

## Collaboration with NIST

Some time on all instruments is available to NIST staff in support of our mission. This time is used to work on NIST research needs, instrument development, and promoting the widespread use of neutron measurements in important research areas, particularly by new users. As a result of these objectives, a significant fraction of the time available to NIST staff is used collaboratively by external users, who often take the lead in the research. Access through such collaborations is managed through written beam time requests. In contrast to proposals, beam time requests are reviewed and approved internally by NCNR staff. We encourage users interested in exploring collaborative research opportunities to contact an appropriate NCNR staff member.

## Research Participation and Productivity

The NCNR continued its strong record of serving the U.S. research community this year. Over the 2016 reporting year, 2536 research participants benefited from use of the NCNR. (Research participants include users who come to the NCNR to use the facility as well as active collaborators, including co-proposers of approved experiments, and co-authors of publications resulting from work performed at the NCNR.) As the number of participants has grown, the number of publications per year has increased in proportion.

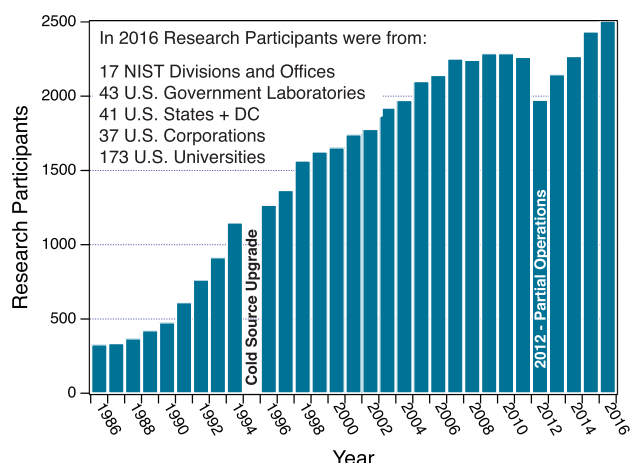


FIGURE 1: Research participants at the NCNR 1986 - 2016.

## 2016 NCNR Proposal Program

In response to the last two calls for proposals (calls 33 and 34) for instrument time, we received 708 proposals, of which 405 were approved and received beam time. For the most recent call, the oversubscription, i.e., the ratio of days requested on all proposals to the days available, was 2.0 on average. Proposal demand has grown constantly since the NCNR first began accepting proposals in 1991, and has more than doubled in the past decade. The following table shows the data for several instrument classes.

Instrument class	Proposals	Days requested	Days allocated
SANS and USANS	261	892	476
Reflectometers	97	673	360
Spectrometers	304	2038	877
Diffraction	26	93	70
Imaging	20	123	80
Total	708	3819	1863

## Users Group

The NCNR Users Group (NUG) provides an independent forum for all facility users to raise issues to NCNR management, working through its executive officers to carry out this function. The current members of the NUG Executive Committee are Alan Nakatani (Dow Chemical, chair), Michael Crawford (University of Delaware), Amber Larson (University of Maryland, student/postdoc member), Michael Mackay (University of Delaware), Megan Robertson (University of Houston), Rafael Verduzco (Rice University) and Igor Zaliznyak (Brookhaven National Laboratory).

The NUG conducted a user survey in the fall of 2015. There were more than 450 responses the majority of whom are CHRNS users. Overall the results are encouraging with 5 of the 6 general categories

## Panel of Assessment

The major organizational components of NIST are evaluated annually for quality and effectiveness by the National Research Council (NRC), the principal operating agency of both the National Academy of Sciences and the National Academy of Engineering. A panel appointed by the NRC convened at the NCNR on July 7-8, 2015. Their findings are summarized in a published report, "An Assessment of the National Institute of Standards and Technology Center for Neutron Research: Fiscal Year 2015," which is available at <https://www.nap.edu/catalog/21878/an-assessment-of-the-national-institute-of-standards-and-technology-center-for-neutron-research>. The panel members included Peter Green (University of Michigan, chair), Frank Bates (University of Minnesota), Bruce Gaulin (McMaster University), Janos Kirz (Lawrence Berkeley National Laboratory), V. Adrian Parsegian (University of Massachusetts Amherst), Sunhil Sinha (University of California at San Diego). A new panel is expected to convene at the NCNR in 2018.

## The Center for High Resolution Neutron Scattering (CHRNS)

CHRNS is a national user facility that is jointly funded by the National Science Foundation and the NCNR. Its primary goal is to maximize access to state-of-the-art neutron scattering instrumentation for the research community. It operates five neutron scattering instruments at the NCNR, enabling users from around the nation to observe dynamical phenomena involving energies from  $\approx 30$  neV to  $\approx 10$  meV, and to obtain structural information on length scales from  $\approx 1$  nm to  $\approx 10$   $\mu$ m. A more detailed account of CHRNS activities may be found on pp 61 of this report.

## Partnerships for Specific Instruments

### NG-7 SANS Consortium

A consortium that includes NIST, the ExxonMobil Research and Engineering Company, and the Industrial Partnership for Research in Interfacial and Materials Engineering (IPRIME) led by the University of Minnesota, operates, maintains, and conducts research at the NG-7 30m SANS instrument. The consortium uses 57 % of the beam time on this instrument, with the remaining 43 % allocated to the general scientific community through the NCNR's proposal system. Consortium members conduct independent research programs primarily in the area of large-scale structure in soft matter. For example, ExxonMobil has used this instrument to deepen their understanding of the underlying nature of ExxonMobil's products and processes, especially in the fields of polymers, complex fluids, and petroleum mixtures.

### ***The nSoft Consortium***

Formed in August 2012, the nSoft Consortium allows member companies to participate with NIST in the development of advanced measurements of materials and manufacturing processes, and develop their own expertise in state-of-the-art measurement technologies to include in their analytical research programs. nSoft develops new neutron-based measurement science for manufacturers of soft materials including plastics, composites, protein solutions, surfactants, and colloidal fluids. Members receive access to leading expertise and training support in neutron technology and soft materials science at NIST. Contact: Ron Jones, nSoft Director, [rljones@nist.gov](mailto:rljones@nist.gov), 301-975-4624.

### ***NIST / General Motors – Neutron Imaging***

An ongoing partnership and collaboration between General Motors and NIST, which also includes Honda Motors through GM's partnership with Honda, continues to yield exciting results using neutron imaging. Neutron imaging has been employed to visualize the operation of fuel cells for automotive vehicle applications. Neutron imaging is an ideal method for visualizing hydrogen, the fuel of electric vehicle engines. These unique, fundamental measurements provide valuable material characterizations that will help improve the performance, increase the reliability, and reduce the time to market introduction of the next generation electric car engines. 25 % of the time on the BT-2 Neutron Imaging Facility is made available to the general scientific community through peer-reviewed proposals.

### **Interagency Collaborations**

The Smithsonian Institution's Nuclear Laboratory for Archaeological Research is part of the Anthropology Department at the National Museum of Natural History. It has had a longstanding and productive partnership with the NCNR, during which time it has chemically analyzed over 43,100 archaeological artifacts by Instrumental Neutron Activation Analysis (INAA), drawing extensively on the collections of the Smithsonian, as well as on those of many other institutions in this country and abroad. Such chemical analyses provide a means of linking these diverse collections together in order to study continuity and change involved in the production of ceramic and other artifacts.

The Center for Food Safety and Applied Nutrition, U.S. Food and Drug Administration (FDA), maintains laboratory facilities at the NCNR providing agency-wide analytical support for food safety and food defense programs. Neutron activation and low-level gamma-ray detection techniques yield multi-element and radiological information about foods and related materials and provide a metrological foundation for FDA's field investigations and for radiological emergency response planning.



# The Center for High Resolution Neutron Scattering (CHRNA)

The Center for High Resolution Neutron Scattering is a national user facility that is jointly funded by the National Science Foundation through its Division of Materials Research (grant number DMR-1508249) and by the NCNR. The core mission of CHRNA is fourfold: (i) to develop and operate neutron scattering instrumentation, with broad application in materials research, for use by the general scientific community; (ii) to promote the effective use of the CHRNA instruments by having an identifiable staff whose primary function is to assist users; (iii) to conduct research that advances the capabilities and utilization of CHRNA facilities; and (iv) to contribute to the development of human resources through educational and outreach efforts. The purpose of this partnership is to maximize access to state-of-the-art neutron scattering instrumentation for the academic research community using the NCNR's proposal system. Proposals to use the CHRNA instruments are critically reviewed on the basis of scientific merit and/or technological importance.

Following the submission of a new proposal to NSF and a site visit in January 2015, the CHRNA agreement was renewed for five years beginning on September 1, 2015. The success of the proposal was based on CHRNA's demonstrated ability to advance neutron scattering measurement capabilities and its prominent role in expanding, educating, and diversifying the community of researchers who use neutron methods. As part of the new agreement, the portfolio of instruments supported by CHRNA will continue to evolve to ensure that the scientific capabilities exceed or are comparable to the best worldwide. Input for these new directions was obtained from the scientific community through a variety of mechanisms including a user survey administered by the NCNR User Group (NUG) in the fall of 2015.

## Scattering Instruments

During FY 2016, CHRNA supported operation of the following instruments: the NG-B 30 m Small Angle Neutron Scattering (SANS) instrument, the Ultra-Small Angle Neutron Scattering (USANS) instrument, the Multi-Angle Crystal Spectrometer (MACS), the High Flux Backscattering Spectrometer (HFBS), and the Neutron Spin-Echo (NSE) spectrometer. Combined, CHRNA instruments can provide structural information on a length scale of  $\approx 1$  nm to  $\approx 10$   $\mu$ m, and dynamical information on energy scales from  $\approx 30$  neV to  $\approx 10$  meV. The CHRNA agreement continues programs in instrument operations and development on HFBS, NSE, and MACS, which boasts the world's highest monochromatic cold-neutron flux and is now the premier instrument in the world for investigations of quantum magnetism. As part of the CHRNA agreement, two innovative instruments, vSANS and CANDOR, will be folded into CHRNA as the installation and commissioning of these new instruments progress. The data rates provided by the multiplex detector assembly of the CANDOR reflectometer will exceed those available elsewhere in the world by perhaps an order of magnitude. The versatile vSANS instrument will cover extensive nano-to-meso length scales in a single measurement, eliminating the need for combined experiments on uSANS and SANS in many cases. uSANS and SANS will thus be phased out of CHRNA following the commissioning of vSANS and CANDOR.

## Research

The wide ranges of instrument capabilities available in CHRNA support a very diverse scientific program, allowing researchers in materials science, chemistry, biology, and condensed matter



**FIGURE 1:** Participants and instructors in the NCNR 2016 Summer School "Methods and Applications of Small Angle Neutron Scattering and Neutron Reflectivity."



**FIGURE 2:** The 2016 SURF students.

physics to investigate materials such as polymers, metals, ceramics, magnetic materials, porous media, fluids and gels, rock formations, and biological molecules.

In the most recent Call for Proposals (call 34), 197 proposals requested CHRNA instruments, and 109 of these proposals received beam time. Of the 967 days requested for the CHRNA instruments, 503 were awarded. Roughly half of the users of neutron scattering techniques at the NCNR use CHRNA-funded instruments, and approximately one third of NCNR publications (see the “Publications” section on p. 67), over the current one-year period, are based on research performed using these instruments. This report contains several highlights of these CHRNA publications. See the labeled highlights in the table of contents.

### Scientific Support Services

In FY 2016, CHRNA provided scientific support in three critical areas: sample environment, chemical laboratories, and the production and delivery of polarized neutron beams. The laboratory staff continues to equip and maintain user laboratories and routinely assists users with sample preparations. The staff also ensures that users have the tools and supplies they need for a successful experiment.



**FIGURE 3:** David Hoogerheide (NCNR) explains the finer points of neutron reflectometry to Damian Kreske from Richard Montgomery High School on the Polarized Beam Reflectometer (PBR).

The CHRNA Sample Environment team provides users with the equipment and training needed to make neutron measurements under external conditions of temperature, pressure, magnetic field, humidity, and fluid flow. Two new Peltier blocks, which will allow for more efficient temperature changes in routine SANS experiments, are currently in the commissioning stages. In addition, a new heat shield extension and vacuum shroud extension were added to the HFBS closed-cycle refrigerator enabling temperatures of 800 K at the sample position.

As a result of the CHRNA support for the NCNR effort in  $^3\text{He}$  spin filters, full polarized beam capabilities are available to users of the MACS and SANS instruments within the CHRNA suite. Currently, both instruments make frequent use of record-breaking  $^3\text{He}$  spin analyzer cells with specialized geometries. It is also notable that CHRNA runs the only SANS program in the U.S. that routinely operates with full polarization analysis, and MACS provides the most intense polarized cold neutron beam with the largest scattering angle coverage for polarization analysis. From August 2015 through July 2016, the  $^3\text{He}$  Spin Filter team serviced 13 user experiments on the CHRNA instruments MACS and SANS. In the future, both the vSANS instrument and CANDOR will produce spin-polarized incident beams using a double-V supermirror polarizer (efficiency of  $> 95\%$ ), along with an RF spin flipper (efficiency of  $99.5\%$ ), and will be spin-analyzed by a  $^3\text{He}$  spin filter.

### Education and Outreach

This year the Center for High Resolution Neutron Scattering sponsored a variety of educational programs and activities tailored to specific age groups and professions. The twenty-second annual summer school, held on June 27 – July 1, 2016 was entitled “Methods and Applications of Small Angle Neutron Scattering and Neutron Reflectivity.” Forty graduate and postdoctoral students from 27 universities participated in the school. Lectures, research seminars and were highlighted for a wide variety of neutron measurement techniques. The guest lecturers were Prof. Michael Hore from Case Western University, Prof. Steve May from Drexel University, and Dr. Marilia Cabral from the Memorial Sloan Kettering Cancer Center. The evaluations were excellent and student feedback was very positive.



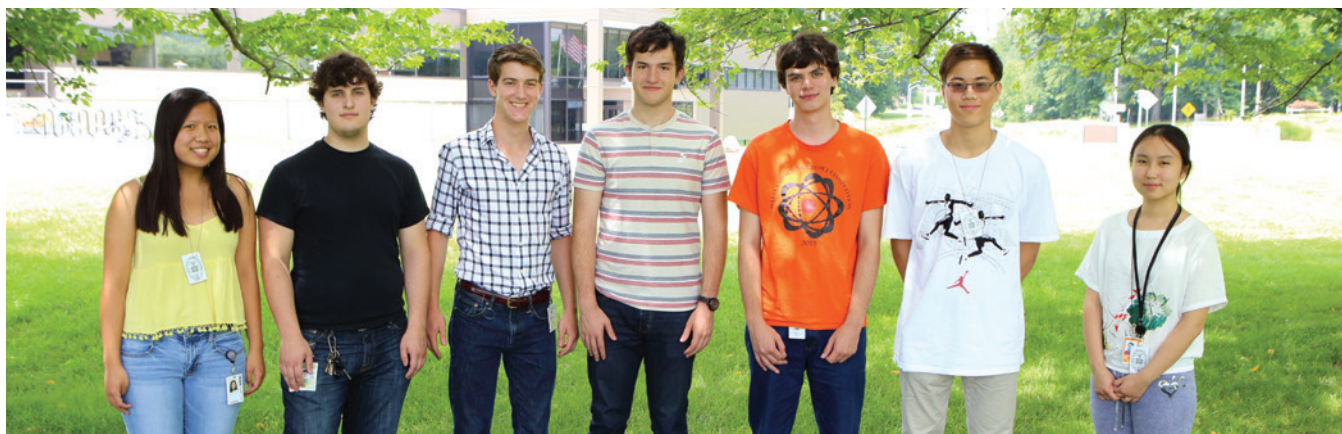


**FIGURE 4:** The 2016 SHIP interns.

As part of its expanding education and outreach effort, CHRNS offers the opportunity to request travel support for an additional graduate student to participate in the experiment to university-based research groups with BTAC-approved experiment proposals. This support is intended to enable new graduate students, for example, to acquire first-hand experience with a technique that they may later use in their own research. Announcements of this program are sent to all of the university groups whose experiment proposals receive beam time from the BTAC. Recipients of the announcement are encouraged to consider graduate students from under-represented groups for this opportunity. The program is also advertised on the NCNR's website at <http://www.ncnr.nist.gov/outreach.html>.

As in previous years, CHRNS participated in NIST's Summer Undergraduate Research Fellowship (SURF) program. In 2016 CHRNS hosted 14 SURF students, including two returning SURF interns from the previous year and two previous participants in the SHIP program. The students participated in research projects such as selective gas adsorption in metal organic frameworks, characterization of nanoparticle architecture in composite polymers, optimization of the cold neutron source design for a proposed new research reactor, and refining a Markov Chain Monte Carlo algorithm for fitting reflectometry data. They presented their work at the NIST SURF colloquium in early August 2016 in sessions moderated by programming officers from the National Science Foundation.

The NCNR initiated a Research Experiences for Teachers (RET) program in the summer of 2010. As part of the new agreement, the program was expanded to include two teachers from Montgomery County, MD: Damian Kreske, a biology teacher from Richard Montgomery High School, and Marie G. Paul, a chemistry teacher from Wheaton High School. Mr. Kreske investigated the formation of self-assembled biological monolayers with neutron reflectivity in collaboration with Dr. David Hoogerheide and Dr. Frank Heinrich from the NCNR. Ms. Paul studied the surfactant-polymer interactions using SANS under the guidance of Dr. Katie Weigandt. Both Mr. Kreske and Ms. Paul highlighted their research in oral presentations at the NCNR in early August. Those in attendance were particularly

intrigued by Ms. Paul's commentary on her future application of the skills learned during the summer to Project Based Learning (PBL) activities in her classroom.

### Elementary, Middle, and High School Activities

The Summer High school Intern Program (SHIP) is a very successful, competitive NIST-wide program for students who are interested in performing scientific research during the summer. CHRNS hosted seven high school interns from local Maryland schools, including two returning students from the previous year. The students studied the formation of streptavidin-immunoglobulin G complexes, explored methods to improve the model smoothing in reflectometry fitting, utilized augmented reality to visualize octahedral tilts in perovskite structures, and manufactured radial collimators with a 3-D printer. The results of the students' summer investigations were highlighted in a NIST-wide poster session in early August, as well as in a well-attended oral symposium at the NCNR.

The annual Summer Institute for Middle School Science Teachers brings middle school science teachers from across the United States to NIST for two weeks in order to give them a better understanding of the scientific process. Each year, CHRNS hosts the teachers for a one-day introduction to neutron scattering with a presentation that describes how neutrons are produced and how they are used to improve our understanding of materials at the atomic scale. This year the Summer Institute hosted twenty-four teachers from five states, including South Dakota and California. On July 19th, the teachers learned about the types of experiments performed using neutron methods after having toured the neutron guide hall and seeing several neutron instruments. To bring home projects suitable for middle school students, they then learned how to grow crystals of "alum" (hydrated aluminum potassium sulfate). Throughout the day and at lunchtime, the teachers had the opportunity to interact with staff members.

A large number of specialized tours for middle school, high school, and university students were also offered throughout the year.



# 2016 Awards



The 2016 **Clifford G. Shull** Prize from the Neutron Scattering Society of America has been awarded to the NCNR's **Chuck Majkrzak**. The award was presented at the 8th American Conference on Neutron Scattering held in July 2016. Chuck is recognized "For leadership in the development, application, and establishment of neutron reflectivity as an essential measurement tool for nanoscale materials."



The NCNR's **Yun Liu** was awarded the 2016 **Science Prize** by the Neutron Scattering Society of America, presented at the 8th American Conference on Neutron Scattering. The citation reads: "For the discovery of dynamic cluster ordering in complex colloidal and protein systems using neutron scattering." The NSSA Science Prize recognizes a major scientific accomplishment or important scientific contribution within the last 5 years using neutron scattering techniques.



**Craig Brown** of the NCNR, along with Jeff Long of UC Berkeley, received the 2016 **Hydrogen Storage Award** from DOE's Hydrogen and Fuel Cells Program. This award recognizes Craig and Prof. Long for their "decades of dedication and achievements in adsorbent-based hydrogen storage materials development and characterization. Craig used neutron diffraction experiments to characterize and subsequently confirm the results, which offer a pathway for significantly improved hydrogen storage capacity for adsorbent-based hydrogen storage materials."



**P. Douglas Godfrin**, University of Delaware, is the recipient of the 2016 Prize for **Outstanding Student Research** of the Neutron Scattering Society of America (NSSA) with the citation: "For seminal neutron scattering studies of concentrated protein solutions and protein dynamics with application to biopharmaceutical engineering."



NCNR's **Nick Butch** received the 2016 **Katharine B. Gebbie Young Investigator Award** presented by the NIST chapter of Sigma Xi. Nick is being recognized for "seminal contributions to the study of unconventional superconductors, topological insulators, and other quantum matter."



**Dennis Nester** of the NCNR received the 2015 NIST **Colleagues' Choice Award**. The Colleagues' Choice Award honors the outstanding achievements and contributions made by selected individuals in support of the NIST mission as determined by their colleagues. Dennis is being recognized "For dedicated support of safe and reliable NCNR cold neutron source operation and invaluable assistance to hundreds of NIST staff and visitors."



The NCNR's **Joseph Curtis** was selected by the Secretary of Commerce to receive the **Silver Medal**. Joseph is being recognized "For developing and making globally available the SASSIE software suite used to model complex biological molecules from small-angle scattering data."



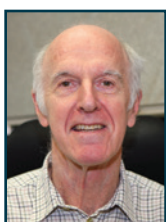
**Doug Ogg**, **Jim Moyer**, and **Mike Rinehart** of the NCNR received the Department of Commerce **Bronze Medal** Award for their work on the MACS detector/analyzer installation. The specific citation for the award is "For the mechanical design, installation, and alignment of a complex neutron analyzer and detection system on the NCNR Multi-Axis Crystal Spectrometer."



NCNR's **Liz Kelley** received the **Most Outstanding Poster** Award in the area of Biology/Biotechnology for her poster entitled "Towards understanding the role of lipid diversity in tuning biomembrane dynamics" at the annual Sigma Xi Post-doc poster presentation.



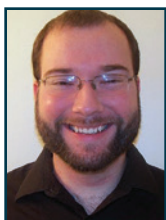
**Michelle Jamer** of the NCNR won the **Best Poster** prize at the Gordon Research Conference on Multiferroics and Magnetoelectric Materials in Lewiston, Maine. She won the award for her poster titled "Probing the depth dependent magnetization of FeGa/NiFe multilayers using polarized neutron reflectometry."



**John R. D. Copley** of the NCNR has been named a 2016 **NSSA Fellow** "For outstanding research on the physics of liquids and fullerenes and major contributions to neutron instrument development and scattering data analysis."



**Michelle Calabrese** of the University of Delaware received a **student poster award** at the American Conference on Neutron Scattering in July. Her poster was titled "Using spatiotemporal small angle neutron scattering to determine the effect of micellar branching on non-linear shear flow phenomena and instabilities."



**Jacob LaManna** of the Neutron Physics Group was named runner-up in the category of Physics/Engineering at the annual **Sigma Xi Post-doc poster** presentation for his poster "Simultaneous multimodal neutron and X-ray imaging for multiphase quantifications in engineering and material science."



**Julie Borchers** has been recognized for **Outstanding Service** to the Neutron Scattering Society of America. Julie served on the NSSA Executive Committee as Secretary from 1999-2002 and most recently as Vice-President from 2010-2014.



**Dan Hussey** of the Neutron Physics Group was awarded the **Arthur S. Flemming Award** for his pioneering work in neutron imaging. The Flemming Awards, which were established by the Downtown Jaycees in 1948, honor outstanding federal employees with 3 to 15 years of federal service for their exceptional contributions to the federal government.



**Thomas H. Epps, III** from the University of Delaware has been awarded the 2016 **John H. Dillon Medal** from the American Physical Society "for significant advancement in the control, characterization, and understanding of polymer nanoscale-structure and energetics" Epps is the Thomas and Kipp Gutshall Associate Professor of Chemical and Biomolecular Engineering and Associate Professor of Materials Science and Engineering at the University of Delaware, and is a frequent user of the NCNR.



**Matthew E. Helgeson**, Assistant Professor of Chemical Engineering at the University of California at Santa Barbara, has been awarded the **Unilever Award** by the American Chemical Society at their 90th ACS Colloid & Surface Science Symposium. The award is given in recognition of fundamental work in colloid or surfactant science carried out in North America by researchers in the early stages of their careers. Matt's research is devoted to the design and processing of complex fluids and colloidal soft matter with well-specified mesostructure, and he makes frequent use of small angle scattering facilities at the NCNR.



**Prof. Kate Ross** was awarded the American Physical Society's 2016 **Valley Prize** "for the elucidation of quantum frustrated magnetism and its expression in the ground state selection of pyrochlore magnets." The biennial prize recognizes "one individual in the early stages of his or her career for an outstanding scientific contribution to physics that is deemed to have significant potential for a dramatic impact on the field." Kate was a recent post-doc at the NCNR and Johns Hopkins.



The European Colloid and Interface Society has awarded **Prof. Piero Baglioni** the 2016 **Overbeek Gold Medal** in recognition of his outstanding contributions to colloid and interface science. Piero is a Professor of Physical Chemistry at the University of Florence, and is a long time user of the NCNR and collaborator with NCNR staff.



**Prof. Norman Wagner** has been inducted as a fellow into the **National Academy of Inventors**, in ceremonies at the United States Patent and Trademark Office in Alexandria, Virginia. Wagner, who is the Unidel Robert Pigford Chaired Professor of Chemical and Biomolecular Engineering at the University of Delaware, has developed “super-hero” materials called shear-thickening fluids – some that he has developed into “liquid armor”, and studying these fluids using neutrons at the NCNR.



**Mircea Dincă**, Professor of Chemistry at MIT, has been selected by the NSF as the 2016 **Alan T. Waterman Award** winner. The award citation (in part) notes “Mircea’s research has demonstrated that metal organic frameworks (MOF) can store electrical energy – something previously unknown, and his research in microporous solids is revolutionizing how scientists approach this exciting new technology, opening the door for future discoveries.” He is a frequent user of the NCNR.



**Prof. Pengcheng Dai** of Rice University is the recipient of the 2016 **Sustained Research Prize** of the Neutron Scattering Society of America (NSSA) Prof. Dai is a frequent user of the NCNR, and was cited for: “his sustained and foundational contributions which have elucidated the magnetic properties of iron-based superconductors, cuprates, and other correlated electron materials.”



**Efrain E. Rodriguez**, Assistant Professor of Chemistry and Biochemistry at the University of Maryland has been selected as an **Emerging Investigator** by the Journal of Materials Chemistry C (Royal Society of Chemistry). He was recognized for “carrying out work with the potential to influence future directions in materials chemistry.” His research areas include iron-based superconductors, magnetic materials, transition metal oxides, crystallography, and make use of neutron scattering at the NCNR.



Two UMD graduate students working with Efrain Rodriguez received 2016 **Margaret C. Etter Student Lecturer Awards** at the recent meeting of the American Crystallographic Association. **Amber Larson**, who serves on the NCNR User Group Executive Committee, won in the area of Neutron Scattering for her presentation entitled “Complex magnetism and metal-insulator transitions in Hollandite transition-metal oxides.” **Daniel Taylor** won in the area of Powder Diffraction for his talk entitled “Oxygen storage properties of  $\text{La}_{1-x}\text{Sr}_x\text{FeO}_{3-\delta}$  for chemical-looping reactions.” **Daniel** was also awarded a 2016 **Ludo Frevel Crystallography Scholarship** from the International Centre for Diffraction Data for his thesis: “Reactivity and Oxygen Storage in Materials for Chemical Looping Processes.”





# Publications: August 1, 2015 to July 31, 2016

- Abebe, D.G., Liu, K.-Y., Mishra, S.R., Wu, A.H.F., Lamb, R.N., Fujiwara, T., "Time-Resolved SANS Analysis of Micelle Chain Exchange Behavior: Thermal Crosslink Driven by Stereocomplexation of PLA-PEG-PLA Micelles," *RSC Adv.* **5**(116), 96019 (2015).
- Alberca, A., Munuera, C., Azpeitia, J., Kirby, B., Nemes, N.M., Perez-Muñoz, A.M., Tornos, J., Mompean, F.J., Leon, C., Santamaria, J., Garcia-Hernandez, M., "Phase Separation Enhanced Magneto-Electric Coupling in  $\text{La}_{0.7}\text{Ca}_{0.3}\text{MnO}_3/\text{BaTiO}_3$  Ultra-Thin Films," *Sci. Rep.* **5**, 17926 (2015).
- Allen, A.J., Espinal, L., Wong-Ng, W., Queen, W.L., Brown, C.M., Kline, S.R., Kauffman, K.L., Culp, J.T., Matranga, C., "Flexible Metal-Organic Framework Compounds: *In situ* Studies for Selective  $\text{CO}_2$  Capture," *J. Alloy Compd.* **647**, 24 (2015). [CHNRNS]
- Alley, O.J., Plunkett, E., Kale, T.S., Guo, X., McClintock, G., Bhupathiraju, M., Kirby, B.J., Reich, D.H., Katz, H.E., "Synthesis, Fabrication, and Heterostructure of Charged, Substituted Polystyrene Multilayer Dielectrics and Their Effects in Pentacene Transistors," *Macromolecules* **49**(9), 3478 (2016).
- Anovitz, L.M., Cole, D.R., "Characterization and Analysis of Porosity and Pore Structures," *Rev. Mineral. Geochem.* **80**, 61 (2015). [CHNRNS]
- Anovitz, L.M., Cole, D.R., Sheets, J.M., Swift, A., Elston, H.W., Welch, S., Chipera, S.J., Littrell, K.C., Mildner, D.F.R., Wasbrough, M.J., "Effects of Maturation on Multiscale (Nanometer to Millimeter) Porosity in the Eagle Ford Shale," *Interpretation* **3**(3), SU59 (2015). [CHNRNS]
- Arif, M., Hussey, D.S., Baltic, E.M., Jacobson, D.L., "Neutron Imaging Facility Development and Research Trend at NIST," in *Physics Procedia* **69**, 210 (2015).
- Ashenfelter, J., Balantekin, B., Baldenegro, C.X., Band, H.R., Barclay, G., Bass, C.D., Berish, D., Bowden, N.S., Bryan, C.D., Cherwinka, J.J., Chu, R., Classen, T., Davee, D., Dean, D., Deichert, G., Dolinski, M.J., Dolph, J., Dwyer, D.A., Fan, S., Gaison, J.K., Galindo-Uribarri, A., Gilje, K., Glenn, A., Green, M., Han, K., Hans, S., Heeger, K.M., Heffron, B., Jaffe, D.E., Kettell, S., Langford, T.J., Littlejohn, B.R., Martinez, D., McKeown, R.D., Morrell, S., Mueller, P.E., Mumm, H.P., Napolitano, J., Norcini, D., Pushin, D., Romero, E., Rosero, R., Saldana, L., Seilhan, B.S., Sharma, R., Stemen, N.T., Surukuchi, P.T., Thompson, S.J., Varner, R.L., Wang, W., Watson, S.M., White, B., White, C., Wilhelmi, J., Williams, C., Wise, T., Yao, H., Yeh, M., Yen, Y.-R., Zhang, C., Zhang, X., "Background Radiation Measurements at High Power Research Reactors," *Nucl. Instrum. Meth. A* **806**, 401 (2016).
- Ashenfelter, J., Balantekin, B., Band, H.R., Barclay, G., Bass, C.D., Berish, D., Bowden, N.S., Bowes, A., Brodsky, J.P., Bryan, C.D., Cherwinka, J.J., Chu, R., Classen, T., Commeford, K., Davee, D., Dean, D., Deichert, G., Diwan, M.V., Dolinski, M.J., Dolph, J., Dwyer, D.A., Gaison, J.K., Galindo-Uribarri, A., Gilje, K., Glenn, A., Goddard, B.W., Green, M., Han, K., Hans, S., Heeger, K.M., Heffron, B., Jaffe, D.E., Langford, T.J., Littlejohn, B.R., Martinez Caicedo, D.A., McKeown, R.D., Mendenhall, M.P., Mueller, P., Mumm, H.P., Napolitano, J., Neilson, R., Norcini, D., Pushin, D., Qian, X., Romero, E., Rosero, R., Saldana, L., Seilhan, B.S., Sharma, R., Sheets, S., Stemen, N.T., Surukuchi, P.T., Varner, R.L., Viren, B., Wang, W., White, B., White, C., Wilhelmi, J., Williams, C., Wise, T., Yao, H., Yeh, M., Yen, Y.R., Zangakis, G., Zhang, C., Zhang, X., "Light Collection and Pulse-Shape Discrimination in Elongated Scintillator Cells for the PROSPECT Reactor Antineutrino Experiment," *JINST* **10**(11), P11004 (2015).
- Bakaimi, I., Brescia, R., Brown, C.M., Tsirlin, A.A., Green, M.A., Lappas, A., "Hydration-Induced Spin-Glass State in a Frustrated Na-Mn-O Triangular Lattice," *Phys. Rev. B* **93**(18), 184422 (2016).
- Bales, M.J., Alarcon, R., Bass, C.D., Beise, E.J., Breuer, H., Byrne, J., Chupp, T.E., Coakley, K.J., Cooper, R.L., Dewey, M.S., Gardner, S., Gentile, T.R., He, D., Mumm, H.P., Nico, J.S., O'Neill, B., Thompson, A.K., Wietfeldt, F.E., "Precision Measurement of the Radiative  $\beta$  Decay of the Free Neutron," *Phys. Rev. Lett.* **116**(24), 242501 (2016).
- Balz, C., Lake, B., Reuther, J., Luetkens, H., Schönmann, R., Herrmannsdörfer, T., Singh, Y., Nazmul Islam, A.T.M., Wheeler, E.M., Rodriguez-Rivera, J.A., Guidi, T., Simeoni, G.G., Baines, C., Ryll, H., "Physical Realization of a Quantum Spin Liquid Based on a Complex Frustration Mechanism," *Nat. Phys.*, in press. [CHNRNS]
- Barker, J.G., Mildner, D.F.R., "Survey of Background Scattering from Materials Found in Small-Angle Neutron Scattering," *J. Appl. Crystallogr.* **48**(4), 1055 (2015). [CHNRNS]
- Barnett, G.V., Qi, W., Amin, S., Lewis, E.N., Razinkov, V.I., Kerwin, B.A., Liu, Y., Roberts, C.J., "Structural Changes and Aggregation Mechanisms for Anti-Streptavidin IgG1 at Elevated Concentration," *J. Phys. Chem. B* **119**(49), 15150 (2015). [CHNRNS]

- Barros, M., Heinrich, F., Datta, S.A.K., Rein, A., Karageorgos, I., Nanda, H., Lösche, M., "Membrane Binding of HIV-1 Matrix Protein: Dependence on Bilayer Composition and Protein Lipidation," *J. Virol.* **90**(9), 4544 (2016).
- Bellur, K., Médici, E.F., Kulshreshtha, M., Konduru, V., Tyrewala, D., Tamilarasan, A., McQuillen, J., Leão, J.B., Hussey, D.S., Jacobson, D.L., Scherschligt, J., Hermanson, J.C., Choi, C.K., Allen, J.S., "A New Experiment for Investigating Evaporation and Condensation of Cryogenic Propellants," *Cryogenics* **74**, 131 (2016).
- Bellur, K., Médici, E., Allen, J., Choi, C.K., Hermanson, J., Tamilarasan, A., Hussey, D., Jacobson, D., Leão, J.B., McQuillen, J., "Neutron Radiography of Condensation and Evaporation of Hydrogen in a Cryogenic Condition," *J. Heat Transf.* **137**(8), 080901 (2015).
- Bellur, K., Konduru, V., Kulshreshtha, M., Tyrewala, D., Médici, E., Allen, J.S., Choi, C.K., Hussey, D.S., Jacobson, D.C., Leão, J.B., McQuillen, J., Hermanson, J., Tamilarasan, A., "Contact Angle Measurement of Liquid Hydrogen (LH<sub>2</sub>) in Stainless Steel and Aluminum Cells," *J. Heat Transf.* **138**(2), 020904 (2016).
- Bertrand, C.E., Godfrin, P.D., Liu, Y., "Direct Observation of Critical Adsorption on Colloidal Particles," *J. Chem. Phys.* **143**(8), 084704 (2015). [CHNRNS]
- Bertrand, C.E., Self, J.L., Copley, J.R.D., Faraone, A., "Dynamic Signature of Molecular Association in Methanol," *J. Chem. Phys.* **145**(1), 014502 (2016). [CHNRNS]
- Bhatti, K.P., Srivastava, V., Phelan, D.P., El-Khatib, S., James, R.D., Leighton, C., "Magnetic Phase Competition in Off-Stoichiometric Martensitic Heusler Alloys: The Ni<sub>50-x</sub>Co<sub>x</sub>Mn<sub>25+y</sub>Sn<sub>25-y</sub> System," in "Heusler Alloys Vol. 222 of the Series Springer Series in Materials Science," edited by Felser, C., Hirohata, A., (Springer International Publishing, Cham) Chap. **8**, 193 (2015).
- Bingham, P., Polsky, Y., Anovitz, L., Carmichael, J., Bilheux, H., Jacobson, D., Hussey, D., "Neutron Radiography of Fluid Flow for Geothermal Energy Research," *Physics Procedia*, **69**, 464 (2015).
- Blasic, J.R., Worcester, D.L., Gawrisch, K., Gurnev, P., Mihailescu, M., "Pore Hydration States of KcsA Potassium Channels in Membranes," *J. Biol. Chem.* **290**(44), 26765 (2015).
- Bloch, E.D., Queen, W.L., Hudson, M.R., Mason, J.A., Xiao, D.J., Murray, L.J., Flacau, R., Brown, C.M., Long, J.R., "Hydrogen Storage and Selective, Reversible O<sub>2</sub> Adsorption in a Metal-Organic Framework with Open Chromium(II) Sites," *Angew. Chem. Int. Ed.* **55**(30), 8605 (2016).
- Borg, C.K.H., Zhou, X., Eckberg, C., Campbell, D.J., Saha, S.R., Paglione, J., Rodriguez, E.E., "Strong Anisotropy in Nearly Ideal Tetrahedral Superconducting FeS Single Crystals," *Phys. Rev. B* **93**(9), 094522 (2016).
- Brookes, E.H., Anjum, N., Curtis, J.E., Marru, S., Singh, R., Pierce, M., "The GenApp Framework Integrated with Airavata for Managed Compute Resource Submissions," *Concurr. Comp.-Pract. E.* **27**(16), 4292 (2015).
- Broom, D.P., Webb, C.J., Hurst, K.E., Parilla, P.A., Gennett, T., Brown, C.M., Zacharia, R., Tylanakis, E., Klontzas, E., Froudakis, G.E., Steriotis, Th.A., Trikalitis, P.N., Anton, D.L., Hardy, B., Tamburello, D., Corgnale, C., van Hassell, B.A., Cossement, D., Chahine, R., Hirscher, M., "Outlook and Challenges for Hydrogen Storage in Nanoporous Materials," *Appl. Phys. A-Mater.* **122**(3), 151 (2016).
- Brown, P., Bromberg, L., Rial-Hermida, M.I., Wasbrough, M., Hatton, T.A., Alvarez-Lorenzo, C., "Magnetic Surfactants and Polymers with Gadolinium Counterions for Protein Separations," *Langmuir* **32**(3), 699 (2016). [CHNRNS]
- Burgess, S.A., Kassie, A., Baranowski, S.A., Fritzsche, K.J., Schmidt-Rohr, K., Brown, C.M., Wade, C.R., "Improved Catalytic Activity and Stability of a Palladium Pincer Complex by Incorporation into a Metal-Organic Framework," *J. Am. Chem. Soc.* **138**(6), 1780 (2016).
- Butch, N.P., Paglione, J., Chow, P., Xiao, Y., Marianetti, C.A., Booth, C.H., Jeffries, J.R., "Pressure-Resistant Intermediate Valence in the Kondo Insulator SmB<sub>6</sub>," *Phys. Rev. Lett.* **116**(15), 156401 (2016).
- Calabrese, M.A., Wagner, N.J., Rogers, S.A., "An Optimized Protocol for the Analysis of Time-Resolved Elastic Scattering Experiments," *Soft Matter* **12**(8), 2301 (2016). [CHNRNS]
- Calabrese, M.A., Rogers, S.A., Murphy, R.P., Wagner, N.J., "The Rheology and Microstructure of Branched Micelles under Shear," *J. Rheol.* **59**(5), 1299 (2015). [CHNRNS]
- Cao, F., Liu, Y., Xu, J., He, Y., Hammouda, B., Qiao, R., Yang, B., "Probing Nanoscale Thermal Transport in Surfactant Solutions," *Sci. Rep.* **5**, 16040 (2015). [CHNRNS]
- Cao, W., Huang, Q., Rong, Y., Wang, Y., Deng, J., Chen, J., Xing, X., "Structure, Phase Transition and Negative Thermal Expansion in Ammoniated ZrW<sub>2</sub>O<sub>8</sub>," *Inorg. Chem. Front* **3**(6), 856 (2016).
- Carrillo, J.-M.Y., Sakwa-Novak, M.A., Holewinski, A., Potter, M.E., Rother, G., Jones, C.W., Sumpter, B.G., "Unraveling the Dynamics of Aminopolymer/Silica Composites," *Langmuir* **32**(11), 2617 (2016). [CHNRNS]
- Castañeda, C.A., Chaturvedi, A., Camara, C.M., Curtis, J.E., Krueger, S., Fushman, D., "Linkage-Specific Conformational Ensembles of Non-Canonical Polyubiquitin Chains," *Phys. Chem. Chem. Phys.* **18**(8), 5771 (2016). [CHNRNS]
- Castañeda, C.A., Dixon, E.K., Walker, O., Chaturvedi, A., Nakasone, M.A., Curtis, J.E., Reed, M.R., Krueger, S., Cropp, T.A., Fushman, D., "Linkage via K27 Bestows Ubiquitin Chains with Unique Properties Among Polyubiquitins," *Structure* **24**(3), 423 (2016).

- Chang, G., Wen, H., Li, B., Zhou, W., Wang, H., Alfooty, K., Bao, Z., Chen, B., "A Fluorinated Metal-Organic Framework for High Methane Storage at Room Temperature," *Cryst. Growth Des.* **16**(6), 3395 (2016).
- Chang, G., Li, B., Wang, H., Bao, Z., Yildirim, T., Yao, Z., Xiang, S., Zhou, W., Chen, B., "A Microporous Metal-Organic Framework with Polarized Trifluoromethyl Groups for High Methane Storage," *Chem. Commun.* **51**(79), 14789 (2015).
- Chen, T., Foley, B.J., Ipek, B., Tyagi, M., Copley, J.R.D., Brown, C.M., Choi, J.J., Lee, S.-H., "Rotational Dynamics of Organic Cations in the  $\text{CH}_3\text{NH}_3\text{PbI}_3$  Perovskite," *Phys. Chem. Chem. Phys.* **17**(46), 31278 (2015). [CHNRS]
- Chen, X., Harriger, L., Sefat, A., Birgeneau, R.J., Wilson, S.D., "Strain-Activated Structural Anisotropy in  $\text{BaFe}_2\text{As}_2$ ," *Phys. Rev. B* **93**(14), 144118 (2016).
- Chen, X., Hogan, T., Walkup, D., Zhou, W., Pokharel, M., Yao, M., Tian, W., Ward, T.Z., Zhao, Y., Parshall, D., Opeil, C., Lynn, J.W., Madhavan, V., Wilson, S.D., "Influence of Electron Doping on the Ground State of  $(\text{Sr}_{1-x}\text{La}_x)_2\text{IrO}_4$ ," *Phys. Rev. B* **92**(7), 075125 (2015).
- Chiang, W.-S., Fratini, E., Baglioni, P., Georgi, D., Chen, J.-H., Liu, Y., "Methane Adsorption in Model Mesoporous Material, SBA-15, Studied by Small-Angle Neutron Scattering," *J. Phys. Chem. C* **120**(8), 4354 (2016). [CHNRS]
- Chisnell, R., Helton, J.S., Freedman, D.E., Singh, D.K., Demmel, F., Stock, C., Nocera, D.G., Lee, Y.S., "Magnetic Transitions in the Topological Magnon Insulator  $\text{Cu}(1,3\text{-bdc})$ ," *Phys. Rev. B* **93**(21), 214403 (2016).
- Chisnell, R., Helton, J.S., Freedman, D.E., Singh, D.K., Bewley, R.I., Nocera, D.G., Lee, Y.S., "Topological Magnon Bands in a Kagome Lattice Ferromagnet," *Phys. Rev. Lett.* **115**(14), 147201 (2015).
- Chiu, C.-C., Vogt, T., Zhao, L., Genest, A., Rösch, N., "Structure and Electronic Properties of MoVO Type Mixed-Metal Oxides - a Combined View by Experiment and Theory," *Dalton T.* **44**(31), 13778 (2015).
- Clark, C.W., Barankov, R., Huber, M.G., Arif, M., Cory, D.G., Pushin, D.A., "Controlling Neutron Orbital Angular Momentum," *Nature* **525**(7570), 504 (2015).
- Clark, G.A., Henderson, J.M., Heffern, C., Akgün, B., Majewski, J., Lee, K.Y.C., "Synergistic Interactions of Sugars/Polyols and Monovalent Salts with Phospholipids Depend upon Sugar/Polyol Complexity and Anion Identity," *Langmuir* **31**(46), 12688 (2015).
- Cleveland, IV, T.E., Kelman, Z., "Isotopic Labeling of Proteins in *Halobacterium Salinarum*," in "Methods in Enzymology, Volume 565," edited by Abelson, J.N., Simon, M.I., *et al.*, (Academic Press, Waltham, MA) Chap. **7**, 147 (2015).
- Clifton, L.A., Holt, S.A., Hughes, A.V., Daulton, E.L., Arunmanee, W., Heinrich, F., Khalid, S., Jefferies, D., Charlton, T.R., Webster, J.R.P., Kinane, C.J., Lackey, J.H., "An Accurate in Vitro Model of the *E. Coli* Envelope," *Angew. Chem. Int. Edit.* **54**, 11952 (2015).
- Coakley, K.J., Dewey, M.S., Huber, M.G., Huffer, C.R., Huffman, P.R., Marley, D.E., Mumm, H.P., O'Shaughnessy, C.M., Schelhammer, K.W., Thompson, A.K., Yue, A.T., "Survival Analysis Approach to Account for Non-Exponential Decay Rate Effects in Lifetime Experiments," *Nucl. Instrum. Meth. A* **813**, 84 (2016).
- Cook, J.C., Barker, J.G., Rowe, J.M., Williams, R.E., Gagnon, C., Lindstrom, R.M., Ibberson, R.M., Neumann, D.A., "Experimental Characterization of the Advanced Liquid Hydrogen Cold Neutron Source Spectrum of the NBSR Reactor at the NIST Center for Neutron Research," *Nucl. Instrum. Meth. A* **792**, 15 (2015).
- Cui, X., Chen, K., Xing, H., Yang, Q., Krishna, R., Bao, Z., Wu, H., Zhou, W., Dong, X., Han, Y., Li, B., Ren, Q., Zaworotko, M.J., Chen, B., "Pore Chemistry and Size Control in Hybrid Porous Materials for Acetylene Capture from Ethylene," *Science* **353**(6295), 141 (2016).
- Cui, Y., Li, B., He, H., Zhou, W., Chen, B., Qian, G., "Metal-Organic Frameworks as Platforms for Functional Materials," *Accounts Chem. Res.* **49**(3), 483 (2016).
- Cunningham, N.J., Alinger, M.J., Klingensmith, D., Wu, Y., Odette, G.R., "On Nano-Oxide Coarsening Kinetics in the Nanostructured Ferritic Alloy MA957: A Mechanism Based Predictive Model," *Mater. Sci. Eng. A*, **655**, 355 (2016).
- Dahal, A., Gunasekera, J., Harriger, L., Singh, D.K., Singh, D.J., "Metallic Nickel Silicides: Experiments and Theory for NiSi and First Principles Calculations for other Phases," *J. Alloy Compd.* **672**, 110 (2016).
- de Jongh, P.E., Blanchard, D., Matsuo, M., Udovic, T.J., Orimo, S., "Complex Hydrides as Room-Temperature Solid Electrolytes for Rechargeable Batteries," *Appl. Phys. A-Mater.* **122**(3), 251 (2016).
- de la Iglesia, P., Jaeger, V.W., Xi, Y., Pfaendtner, J., Pozzo, L.D., "Structure Characterization and Properties of Metal-Surfactant Complexes Dispersed in Organic Solvents," *Langmuir* **31**(33), 9006 (2015). [CHNRS]
- Del Buffa, S., Fratini, E., Ridi, F., Faraone, A., Baglioni, P., "State of Water in Hydrating Tricalcium Silicate Pastes: The Effect of a Cellulose Ether," *J. Phys. Chem. C* **120**(14), 7612 (2016).
- Deng, S., Sun, Y., Wang, L., Wu, H., Shi, K., Hu, P., Huang, Q., Wang, C., "Near-Zero Temperature Coefficient of Resistivity Associated with Magnetic Ordering in Antiperovskite  $\text{Mn}_{3+x}\text{Ni}_{1-x}\text{N}$ ," *Appl. Phys. Lett.* **108**(4), 041908 (2016).



- Deng, S., Sun, Y., Wang, L., Shi, Z., Wu, H., Huang, Q., Yan, J., Shi, K., Hu, P., Zaoui, A., Wang, C., "Frustrated Triangular Magnetic Structures of  $\text{Mn}_3\text{ZnN}$ : Applications in Thermal Expansion," *J. Phys. Chem. C* **119**(44), 24983 (2015).
- Dharmaraj, V.L., Godfrin, P.D., Liu, Y., Hudson, S.D., "Rheology of Clustering Protein Solutions," *Biomicrofluidics* **10**(4), 043509 (2016).
- Dick, R.A., Barros, M., Jin, D., Lösche, M., Vogt, V.M., "Membrane Binding of the Rous Sarcoma Virus Gag Protein is Cooperative and Dependent on the Spacer Peptide Assembly Domain," *J. Virol.* **90**(5), 2473 (2016).
- Dick, R.A., Datta, S.A.K., Nanda, H., Fang, X., Wen, Y., Barros, M., Wang, Y.-X., Rein, A., Vogt, V.M., "Hydrodynamic and Membrane Binding Properties of Purified Rous Sarcoma Virus Gag Protein," *J. Virol.* **89**(20), 10371 (2015).
- Dimitrievska, M., Ivetic, T.B., Litvinchuk, A.P., Fairbrother, A., Miljevic, B.B., Strbac, G.R., Pérez-Rodríguez, A., Lukic-Petrovic, S.R., "Eu-Doped Wide-Bandgap  $\text{ZnSnO}$  Semiconductor Nanoparticles: Structure and Luminescence," *J. Phys. Chem. C*, in press.
- Ding, C., Guo, S., Zhao, Y., Man, H., Fu, L., Gu, Y., Wang, Z., Liu, L., Frandsen, B.A., Cheung, S., Uemura, Y.J., Goko, T., Luetkens, H., Morenzoni, E., Zhao, Y., Ning, F.L., "The Synthesis and Characterization of 1111 Type Diluted Ferromagnetic Semiconductor  $(\text{La}_{1-x}\text{Ca}_x)(\text{Zn}_{1-x}\text{Mn}_x)\text{AsO}_4$ ," *J. Phys.: Condens. Matter* **28**(2), 026003 (2015).
- Diroll, B.T., Weigandt, K.M., Jishkariani, D., Cargnello, M., Murphy, R.J., Hough, L.A., Murray, C.B., Donnio, B., "Quantifying 'Softness' of Organic Coatings on Gold Nanoparticles using Correlated Small-Angle X-ray and Neutron Scattering," *Nano Lett.* **15**(12), 8008 (2015).
- Disseler, S.M., Chen, Y., Yeo, S., Gasparovic, G., Piccoli, P.M.B., Schultz, A.J., Qiu, Y., Huang, Q., Cheong, S.-W., Ratcliff, II, W., "One Dimensional(1D)-to-2D Crossover of Spin Correlations in the 3D Magnet  $\text{ZnMn}_2\text{O}_4$ ," *Sci. Rep.* **5**(17771), 1 (2015).
- Disseler, S.M., Lynn, J.W., Jardim, R.F., Torikachvili, M.S., Granado, E., "Spin Dynamics and Two-Dimensional Correlations in the FCC Antiferromagnetic  $\text{Sr}_2\text{YRuO}_6$ ," *Phys. Rev. B* **93**(14), 140407 (2016).
- Disseler, S.M., Luo, X., Gao, B., Oh, Y.S., Hu, R., Wang, Y., Quintana, D., Zhang, A., Huang, Q., Lau, J., Paul, R., Lynn, J.W., Cheong, S.-W., Ratcliff, II, W., "Multiferroicity in Doped Hexagonal  $\text{LuFeO}_3$ ," *Phys. Rev. B* **92**(5), 054435 (2015).
- Duncan, T.T., Berrie, B.H., Weiss, R.G., "Colloidal Properties of Aqueous Poly(Vinyl Acetate)-Borate Dispersions with Short-Chain Glycol Ethers," *Chem. Phys. Chem.*, in press.
- El-Khatib, S., Phelan, D., Barker, J.G., Zheng, H., Mitchell, J.F., Leighton, C., "Neutron-Scattering-Based Evidence for Interacting Magnetic Excitons in  $\text{LaCoO}_3$ ," *Phys. Rev. B* **92**(6), 060404 (2015). [CHRN]
- Eyers, B.D., Wu, Z., Kochunas, B., "Feasibility Investigation of Application of MPACT to Core Design Studies of NBSR-2, a Heavy Water-Reflected, Heterogeneous LEU Fuel Research Reactor," in "Proceedings of the PHYSOR 2016 Meeting in Sun Valley, ID, May 2016," (PHYSOR 2016: Unifying Theory and Experiments in the 21st Century, April 2016, Sun Valley, ID), 1631 (2016).
- Fajalia, A.I., Tsianou, M., "Self-Assembly Control via Molecular Recognition: Effect of Cyclodextrins on Surfactant Micelle Structure and Interactions Determined by SANS," *Colloid Surface. A* **480**, 91 (2015). [CHRN]
- Fajalia, A.I., Antoniou, E., Alexandridis, P., Tsianou, M., "Self-Assembly of Sodium Bis(2-Ethylhexyl) Sulfosuccinate in Aqueous Solutions: Modulation of Micelle Structure and Interactions by Cyclodextrins Investigated by Small-Angle Neutron Scattering," *J. Mol. Liq.* **210**, 125 (2015). [CHRN]
- Filippidi, E., DeMartini, D.G., Malo, de Molina, P., Danner, E.W., Kim, J., Helgeson, M.E., Waite, J.H., Valentine, M.T., "The Microscopic Network Structure of Mussel (*Mytilus*) Adhesive Plaques," *J. Roy. Soc. Interface* **12**(113), 20150827 (2015). [CHRN]
- Gao, J., Wagner, N.J., "Water Nanocluster Formation in the Ionic Liquid 1-Butyl-3-Methylimidazolium Tetrafluoroborate ( $[\text{C}_4\text{mim}][\text{BF}_4]$ )- $\text{D}_2\text{O}$  Mixtures," *Langmuir* **32**(20), 5078 (2016). [CHRN]
- Gaudet, J., Ross, K.A., Kermarrec, E., Butch, N.P., Ehlers, G., Dabkowska, H.A., Gaulin, B.D., "Gapless Quantum Excitations from an Icelike Splayed Ferromagnetic Ground State in Stoichiometric  $\text{Yb}_2\text{Ti}_2\text{O}_7$ ," *Phys. Rev. B* **93**(6), 064406 (2016).
- Ghimire, N.J., Cary, S.K., Eley, S., Wakeham, N.A., Rosa, P.F.S., Albrecht-Schmitt, T., Lee, Y., Janoschek, M., Brown, C.M., Civalé, L., Thompson, J.D., Ronning, F., Bauer, E.D., "Physical Properties of the  $\text{Ce}_3\text{MAl}_7\text{Ge}_4$  Heavy-Fermion Compounds ( $M = \text{Co}, \text{Ir}, \text{Ni}, \text{Pd}$ )," *Phys. Rev. B* **93**(20), 205141 (2016).
- Gilbert, D.A., Maranville, B.B., Balk, A.L., Kirby, B.J., Fischer, P., Pierce, D.T., Unguris, J., Borchers, J.A., Liu, K., "Realization of Ground-State Artificial Skyrmion Lattices at Room Temperature," *Nat. Commun.* **6**(8462), 8462 (2015).
- Gilbert, D.A., Olamit, J., Dumas, R.K., Kirby, B.J., Grutter, A.J., Maranville, B.B., Arenholz, E., Borchers, J.A., Liu, K., "Controllable Positive Exchange Bias via Redox-Driven Oxygen Migration," *Nat. Commun.* **7**, 11050 (2016).
- Gilbert, D.A., Grutter, A.J., Arenholz, E., Liu, K., Kirby, B.J., Borchers, J.A., Maranville, B.B., "Structural and Magnetic Depth Profiles of Magneto-Ionic Heterostructures Beyond the Interface Limit," *Nat. Commun.* **7**, 12264 (2016).

- Glassman, M.J., Olsen, B.D., "Arrested Phase Separation of Elastin-like Polypeptide Solutions Yields Stiff, Thermoresponsive Gels," *Biomacromolecules* **16**(12), 3762 (2015). [CHNRNS]
- Glinka, C.J., Barker, J.G., Mildner, D.F.R., "Comparison of Pinhole Collimation and Focusing Optics for SANS," *Nucl. Instrum. Meth. A* **795**, 122 (2015). [CHNRNS]
- Glor, E.C., Composto, R.J., Fakhraai, Z., "Glass Transition Dynamics and Fragility of Ultrathin Miscible Polymer Blend Films," *Macromolecules* **48**(18), 6682 (2015).
- Godfrin, P.D., Hudson, S.D., Hong, K., Porcar, L., Falus, P., Wagner, N.J., Liu, Y., "Short-Time Glassy Dynamics in Viscous Protein Solutions with Competing Interactions," *Phys. Rev. Lett.* **115**(22), 228302 (2015). [CHNRNS]
- Godfrin, P.D., Zarraga, I.E., Zarzar, J., Porcar, L., Falus, P., Wagner, N.J., Liu, Y., "Effect of Hierarchical Cluster Formation on the Viscosity of Concentrated Monoclonal Antibody Formulations Studied by Neutron Scattering," *J. Phys. Chem. B* **120**(2), 278 (2016). [CHNRNS]
- Goshima, H., Forney-Stevens, K.M., Liu, M., Qian, K.K., Tyagi, M., Cicerone, M.T., Pikal, M.J., "Addition of Monovalent Electrolytes to Improve Storage Stability of Freeze-Dried Protein Formulations," *J. Pharm. Sci.* **105**(2), 530 (2016). [CHNRNS]
- Greene, D.G., Modla, S., Wagner, N.J., Sandler, S.I., Lenhoff, A.M., "Local Crystalline Structure in an Amorphous Protein Dense Phase," *Biophys. J.* **109**(8), 1716 (2015). [CHNRNS]
- Grutter, A.J., "Perspective: Probing 2-D Magnetic Structures in a 3-D World," *APL Materials* **4**(3), 032402 (2016).
- Grutter, A.J., Vailionis, A., Borchers, J.A., Kirby, B.J., Flint, C.L., He, C., Arenholz, E., Suzuki, Y., "Interfacial Symmetry Control of Emergent Ferromagnetism at the Nanoscale," *Nano Lett.*, in press.
- Grutter, A.J., Gilbert, D.A., Alaan, U.S., Arenholz, E., Maranville, B.B., Borchers, J.A., Suzuki, Y., Liu, K., Kirby, B.J., "Reversible Control of Magnetism in  $\text{La}_{0.67}\text{Sr}_{0.33}\text{MnO}_3$  through Chemically-Induced Oxygen Migration," *Appl. Phys. Lett.* **108**(8), 082405 (2016).
- Gu, X., Mildner, D.F.R., "Ultra-Small-Angle Neutron Scattering with Azimuthal Asymmetry," *J. Appl. Crystallogr.* **49**(3), 934 (2016). [CHNRNS]
- Gu, X., Mildner, D.F.R., Cole, D.R., Rother, G., Slingerland, R., Brantley, S.L., "Quantification of Organic Porosity and Water Accessibility in Marcellus Shale using Neutron Scattering," *Energ. Fuel.* **30**(6), 4438 (2016). [CHNRNS]
- Gunasekera, J., Harriger, L., Dahal, A., Heitmann, T., Vignale, G., Singh, D.K., "Magnetic Fluctuations Driven Insulator-to-Metal Transition in  $\text{Ca}(\text{Ir}_{1-x}\text{Ru}_x)\text{O}_3$ ," *Sci. Rep.* **5**, 18047 (2015).
- Gunasekera, J., Harriger, L., Dahal, A., Maurya, A., Heitmann, T., Disseler, S.M., Thamizhavel, A., Dhar, S., Singh, D.J., Singh, D.K., "Electronic Nature of the Lock-in Magnetic Transition in  $\text{CeAl}_4\text{Si}_2$ ," *Phys. Rev. B* **93**(15), 155151 (2016).
- Guo, Z., Panda, D.K., Maity, K., Lindsey, D., Parker, T.G., Albrecht-Schmitt, T.E., Barreda-Esparza, J.L., Xiong, P., Zhou, W., Saha, S., "Modulating the Electrical Conductivity of Metal-Organic Framework Films with Intercalated Guest  $\pi$ -Systems," *J. Mater. Chem. C* **4**(5), 894 (2016).
- Gygi, D., Bloch, E.D., Mason, J.A., Hudson, M.R., González, M.I., Siegelman, R.L., Darwish, T.A., Queen, W.L., Brown, C.M., Long, J.R., "Hydrogen Storage in the Expanded Pore Metal-Organic Frameworks  $\text{M}_2(\text{dobpdc})$  (M = Mg, Mn, Fe, Co, Ni, Zn)," *Chem. Mater.* **28**(4), 1128 (2016).
- Habersberger, B.M., Hart, K.E., Gillespie, D., Huang, T., "Molecular Weight Dependence of Deuterium Exchange on Polyethylene: Direct Measurement and SANS Model," *Macromolecules* **48**(16), 5951 (2015). [CHNRNS]
- Hälg, M., Huvonen, D., Butch, N.P., Demmel, F., Zheludev, A., "Finite-Temperature Scaling of Spin Correlations in a Partially Magnetized Heisenberg  $S = 1/2$  Chain," *Phys. Rev. B* **92**(10), 104416 (2015).
- Hallas, A.M., Gaudet, J., Butch, N.P., Tachibana, M., Freitas, R.S., Luke, G.M., Wiebe, C.R., Gaulin, B.D., "Universal Dynamic Magnetism in Yb Pyrochlores with Disparate Ground States," *Phys. Rev. B* **93**(10), 100403 (2016).
- Hammouda, B., "Form Factors for Branched Polymers with Excluded Volume," *J. Res. Natl. Inst. Stan.* **121**, 139 (2016). [CHNRNS]
- He, Y., Downing, R.G., Wang, H., "3D Mapping of Lithium in Battery Electrodes using Neutron Activation," *J. Power Sources* **287**, 226 (2015).
- Heinrich, F., Chakravarthy, S., Nanda, H., Papa, A., Pandolfi, P.P., Ross, A.H., Harishchandra, R.K., Gericke, A., Lösche, M., "The PTEN Tumor Suppressor Forms Homodimers in Solution," *Structure* **23**, 1952 (2015).
- Heinrich, F., "Deuteration in Biological Neutron Reflectometry," in "Methods in Enzymology," edited by Kelman, Z., (American Press, Cambridge, MA) Chap. **7**, 212 (2016).
- Hester, G., Heitmann, T., Tyagi, M., Rathore, M., Dalvi, A., Mitra, S., "Neutron Scattering Studies of Lithium-Ion Diffusion in Ternary Phosphate Glasses," *MRS Advances*, in press. [CHNRNS]
- Hickey, R.J., Gillard, T.M., Irwin, M.T., Lodge, T.P., Bates, F.S., "Structure, Viscoelasticity, and Interfacial Dynamics of a Model Polymeric Bicontinuous Microemulsion" *Soft Matter* **12**(1), 53 (2016).

- Hore, M.J.A., Ye, X., Ford, J., Gao, Y., Fei, J., Wu, Q., Rowan, S.J., Composto, R.J., Murray, C.B., Hammouda, B., "Probing the Structure, Composition, and Spatial Distribution of Ligands on Gold Nanorods," *Nano Lett.* **15**(9), 5730 (2015). [CHNRNS]
- Horkay, F., Bassar, P.J., Hecht, A.-M., Geissler, E., "Effect of Calcium/Sodium Ion Exchange on the Osmotic Properties and Structure of Polyelectrolyte Gels," *P. I. Mech. Eng. H* **229**(12), 895 (2015). [CHNRNS]
- Horkay, F., "Interaction of Cartilage Biopolymers," *Macromol. Symp.* **358**(1), 78 (2015). [CHNRNS]
- Horkay, F., Bassar, P.J., Hecht, A.-M., Geissler, E., "Cartilage: Multiscale Structure and Biomechanical Properties," *MRS Advances* **1**(8), 509 (2016). [CHNRNS]
- Howell, S.C., Qiu, X., Curtis, J.E., "Monte Carlo Simulation Algorithm for B-DNA," *J. Comput. Chem.*, in press.
- Hrabe, N.W., Gnäupel-Herold, T.H., Quinn, T.P., "Fatigue Properties of a Titanium Alloy (Ti-6Al-4V) Fabricated Via Electron Beam Melting (EBM): Effects of Internal Defects and Residual Stress," in "World Materials Research Institutes Forum International Workshop for Young Scientists," in press.
- Hu, L., Chen, J., Sanson, A., Wu, H., Rodriguez, C.G., Olivi, L., Ren, Y., Fan, L., Deng, J., Xing, X., "New Insights into the Negative Thermal Expansion: Direct Experimental Evidence for the 'Guitar-String' Effect in Cubic  $\text{ScF}_3$ ," *J. Am. Chem. Soc.* **138**(27), 8320 (2016).
- Hu, L., Chen, J., Fan, L., Ren, Y., Huang, Q., Sanson, A., Jiang, Z., Zhou, M., Rong, Y., Wang, Y., Deng, J., Xing, X., "High-Curie-Temperature Ferromagnetism in  $(\text{Sc,Fe})\text{F}_3$  Fluorides and its Dependence on Chemical Valence," *Adv. Mater.* **27**(31), 4592 (2015).
- Hulvey, Z., Vlasisavljevich, B., Mason, J.A., Tsivion, E., Dougherty, T.P., Bloch, E.D., Head-Gordon, M., Smit, B., Long, J.R., Brown, C.M., "Critical Factors Driving the High Volumetric Uptake of Methane in  $\text{Cu}_3(\text{btc})_2$ ," *J. Am. Chem. Soc.* **137**(33), 10816 (2015).
- Hussey, D.S., Brocker, C., Cook, J.C., Jacobson, D.L., Gentile, T.R., Chen, W.C., Baltic, E., Baxter, D.V., Daskow, J., Arif, M., "A New Cold Neutron Imaging Instrument at NIST," in "Physics Procedia," edited by Lehmann, E.H., Kaestner, A.P., Mannes, D., (10 World Conference on Neutron Radiography, October 2014, Grindelwald, Switzerland) **69**, 48 (2015).
- Imai, T., Lee, Y.S., "Do Quantum Spin Liquids Exist?" *Phys. Today*, in press. [CHNRNS]
- Imel, A.E., Naskar, A.K., Dadmun, M.D., "Understanding the Impact of Poly(Ethylene Oxide) on the Assembly of Lignin in Solution Toward Improved Carbon Fiber Production," *ACS Appl. Mater. Interfaces* **8**(5), 3200 (2016).
- Indelicato, G., Wahome, N., Ringler, P., Müller, S.A., Nieh, M.-P., Burkhard, P., Twarock, R., "Principles Governing the Self-Assembly of Coiled-Coil Protein Nanoparticles," *Biophys. J.* **110**(3), 646 (2016). [CHNRNS]
- Jacobsen, H., Zaliznyak, I.A., Savici, A.T., Winn, B.L., Chang, S., Hücker, M., Gu, G.D., Tranquada, J.M., "Neutron Scattering Study of Spin Ordering and Stripe Pinning in Superconducting  $\text{La}_{1.93}\text{Sr}_{0.07}\text{CuO}_4$ " *Phys. Rev. B* **92**(17), 174525 (2015).
- Jeffries, J.R., Stillwell, R.L., Weir, S.T., Vohra, Y.K., Butch, N.P., "Emergent Ferromagnetism and  $T$ -Linear Scattering in  $\text{USb}_2$  at High Pressure," *Phys. Rev. B* **93**(18), 184406 (2016).
- Jeong, Y., Iadicola, M., Gnäupel-Herold, T., Creuziger, A., "Multiaxial Constitutive Behavior of an Interstitial-Free Steel: Measurements through X-ray and Digital Image Correlation," *Acta Mater.* **112**, 84 (2016).
- Jia, D., Zuo, T., Rogers, S., Cheng, H., Hammouda, B., Han, C.C., "Re-Entrance of Poly( $N,N$ -Diethylacrylamide) in  $\text{D}_2\text{O}/d$ -Ethanol Mixture at 27 °C," *Macromolecules* **49**(14), 5152 (2016). [CHNRNS]
- Jiang, N., Endoh, M.K., Koga, T., Masui, T., Kishimoto, H., Nagao, M., Satija, S.K., Taniguchi, T., "Nanostructures and Dynamics of Macromolecules Bound to Attractive Filler Surfaces," *ACS Macro Letters* **4**(8), 838 (2015). [CHNRNS]
- Jiang, N., Wang, J., Di, X., Cheung, J., Zeng, W., Endoh, M.K., Koga, T., Satija, S.K., "Nanoscale Adsorbed Structures as a Robust Approach for Tailoring Polymer Film Stability," *Soft Matter* **12**(6), 1801 (2016).
- Jones, S.Z., Bentz, D.P., Snyder, K.A., Martys, N.S., Hussey, D.S., Jacobson, D.L., "Service Life Modeling of Reinforced High Volume Fly Ash (HVFA) Concrete Structures Containing Cracks," in "Proceedings of the International Concrete Sustainability Conference," (International Concrete Sustainability Conference, April 2015, Miami, Florida) (2015).
- Kabirian, F., Khan, A.S., "Anisotropic Yield Criteria in  $\sigma$ - $\tau$  Stress Space for Materials with Yield Asymmetry," *Int. J. Solids Struct.* **67-68**, 116 (2015).
- Kabirian, F., Khan, A.S., Gnäupel-Herold, T.H., "Plastic Deformation Behavior of a Thermo-Mechanically Processed AZ31 Magnesium Alloy under a Wide Range of Temperature and Strain Rate," *J. Alloy Compd.* **673**, 327 (2016).
- Kaizu, K., Alexandridis, P., "Glucose-Induced Sphere to Ellipsoid Transition of Polyoxyethylene-Polyoxypropylene Block Copolymer Micelles in Aqueous Solutions," *Colloid Surface. A* **480**, 203 (2015). [CHNRNS]
- Karlsson, E.B., Hartmann, O., Chatzidimitriou-Dreismann, C.A., Abdul-Redah, T., "The Hydrogen Anomaly in Neutron Compton Scattering: New Experiments and a Quantitative Theoretical Explanation," *Meas. Sci. Technol.* **27**(8), 085501 (2016).



- Kepola, E.J., Loizou, E., Patrickios, C.S., Leontidis, E., Voutouri, C., Stylianopoulos, T., Schweins, R., Gradzielski, M., Krumm, C., Tiller, J.C., Kushnir, M., Wesdemiotis, C., "Amphiphilic Polymer Conetworks Based on End-Linked 'Core-First' Star Block Copolymers: Structure Formation with Long-Range Order," *ACS Macro Letters* **4**(10), 1163 (2015).
- Kermarrec, E., Maharaj, D.D., Gaudet, J., Fritsch, K., Pomaranski, D., Kycia, J.B., Qiu, Y., Copley, J.R.D., Couchman, M.M.P., Morningstar, A.O.R., Dabkowska, H.A., Gaulin, B.D., "Gapped and Gapless Short-Range- Ordered Magnetic States with  $(\frac{1}{2}, \frac{1}{2}, \frac{1}{2})$  Wave Vectors in the Pyrochlore Magnet  $\text{Tb}_{2+x}\text{Ti}_{2-x}\text{O}_{7+\delta}$ ," *Phys. Rev. B* **92**(24), 245114 (2015).
- Kirby, B.J., Belliveau, H.F., Belyea, D.D., Kienzle, P.A., Grutter, A.J., Riego, P., Berger, A., Miller, C.W., "Spatial Evolution of the Ferromagnetic Phase Transition in an Exchange Graded Film," *Phys. Rev. Lett.* **116**(4), 047203 (2016).
- Kline, S.R., "2015 NCNR Annual Report," NIST SP **1202**, 1 (2016).
- Kofu, M., Tyagi, M., Inamura, Y., Miyazaki, K., Yamamuro, O., "Quasielastic Neutron Scattering Studies on Glass-Forming Ionic Liquids with Imidazolium Cations," *J. Chem. Phys.* **143**(23), 234502 (2015). [CHRNS]
- Kofu, M., Yamamuro, O., "Hierarchical and Glassy Dynamics of Imidazolium-Based Ionic Liquids," *Nihon Kessho Gakkaishi* **58**(1), 18 (2016). [CHRNS]
- Konduru, V., Bellur, K., Médici, E.F., Allen, J.S., Choi, C.K., Hussey, D.S., Jacobson, D., Leão, J.B., McQuillen, J., Hermanson, J.C., "Examining Liquid Hydrogen Wettability using Neutron Imaging," *J. Heat Transfer*, in press.
- Koo, J., Koga, T., Li, B., Satija, S.K., Rafailovich, M.H., "Extending the Anomalous Dilation in  $\text{CO}_2$  to Thick Polymer Blend Films: A Neutron Reflectivity Study," *Macromolecules* **49**(9), 3433 (2016).
- Koo, J., Kim, H., Kim, K.-Y., Jang, Y.R., Lee, J.-S., Yoon, S.W., Suh, B.J., Yu, T., Bang, J., Yoon, K., Yuan, G., Satija, S.K., "Controlling the Magnetic Properties of Polymer-Iron Oxide Nanoparticle Composite Thin Films *via* Spatial Particle Orientation," *RSC Adv.*, in press.
- Kumari, H., Armitage, S.E., Kline, S.R., Damodaran, K.K., Kennedy, S.R., Atwood, J.L., Steed, J.W., "Fluorous 'Ponytails' Lead to Strong Gelators Showing Thermally Induced Structure Evolution," *Soft Matter* **11**(43), 8471 (2015).
- Kumari, H., Kline, S.R., Kennedy, S.R., Garvey, C., Raston, C.L., Atwood, J.L., Steed, J.W., "Manipulating Three-Dimensional Gel Network Entanglement by Thin Film Shearing," *Chem. Commun.* **52**(24), 4513 (2016).
- Kuo, Y.-C., Wu, H.-C., Hoang, D., Bentley, W.E., D'Souza, W.D., Raghavan, S.R., "Colloidal Properties of Nanoerythrocytes Derived from Bovine Red Blood Cells," *Langmuir* **32**(1), 171 (2016).
- Kupwade-Patil, K., Tyagi, M., Brown, C.M., Büyüköztürk, O., "Water Dynamics in Cement Paste at Early Age Prepared with Pozzolanic Volcanic Ash and Ordinary Portland Cement using Quasielastic Neutron Scattering," *Cement Concrete Res.*, in press. [CHRNS]
- Kwon, N.K., Park, C.S., Lee, C.H., Kim, Y.S., Zukoski, C.F., Kim, S.Y., "Tunable Nanoparticle Stability in Concentrated Polymer Solutions on the Basis of the Temperature Dependent Solvent Quality," *Macromolecules* **49**(6), 2307 (2016).
- Lam, C.N., Chang, D., Wang, M., Chen, W.-R., Olsen, B.D., "The Shape of Protein-Polymer Conjugates in Dilute Solution," *J. Polym. Sci. Pol. Chem.* **54**(2), 292 (2016).
- Lamontagne, L.K., Laurita, G., Gaultois, M.W., Knight, M., Ghadbeigi, L., Sparks, T.D., Gruner, M.E., Pentcheva, R., Brown, C.M., Seshadri, R., "High Thermopower with Metallic Conductivity in *p*-Type Li-Substituted  $\text{PbPdO}_2$ ," *Chem. Mater.* **28**(10), 3367 (2016).
- Langford, T.J., Beise, E.J., Breuer, H., Heimbach, C.R., Ji, G., Nico, J.S., "Development and Characterization of a High Sensitivity Segmented Fast Neutron Spectrometer (FaNS-2)," *JINST* **11**(01), P01006 (2016).
- Lavelle, C.M., Coplan, M., Miller, E.C., Thompson, A.K., Kowler, A., Vest, R., Yue, A., Koeth, T., Al-Sheikhly, M., Clark, C., "Neutron Detection with Noble Gas Scintillation: A Review of Recent Results," in "Proceedings of SPIE," edited by Franks, L., James, R., *et al.*, (Hard X-ray, Gamma-Ray, and Neutron Detector Physics XVII, July 2015, San Diego, CA) **9593**, 95930H (2015).
- Lawler, K.V., Hulvey, Z., Forster, P.M., "On the Importance of a Precise Crystal Structure for Simulating Gas Adsorption in Nanoporous Materials," *Phys. Chem. Chem. Phys.* **17**(29), 18904 (2015).
- Lee, J.S., Vlaisavljevich, B., Britt, D.K., Brown, C.M., Haranczyk, M., Neaton, J.B., Smit, B., Long, J.R., Queen, W.L., "Understanding Small-Molecule Interactions in Metal-Organic Frameworks: Coupling Experiment with Theory," *Adv. Mater.* **27**(38), 5785 (2015).
- Lee, Y.-W., Jang, T.-H., Dissanayake, S.E., Lee, S., Jeong, Y.H., "Magnetism and Magnetoelectricity in the Polar Oxide  $\alpha\text{-Cu}_2\text{V}_2\text{O}_7$ ," *Europhys. Lett.* **113**(2), 27007 (2016).
- Li, B., Wen, H.-M., Cui, Y., Zhou, W., Qian, G., Chen, B., "Emerging Multifunctional Metal-Organic Framework Materials," *Adv. Mater.*, in press.
- Li, B., Wen, H.-M., Wang, H., Wu, H., Yildirim, T., Zhou, W., Chen, B., "Porous Metal-Organic Frameworks with Lewis Basic Nitrogen Sites for High-Capacity Methane Storage," *Energ. Environ. Sci.* **8**(8), 2504 (2015).
- Li, B., Louca, D., Feygenson, M., Brown, C.M., Copley, J.R.D., Iida, K., "Local Jahn-Teller Distortions and Orbital Ordering in  $\text{Ba}_3\text{Cu}_{1+x}\text{Sb}_{2-x}\text{O}_9$  Investigated by Neutron Scattering," *Phys. Rev. B* **93**(1), 014423 (2016).

- Li, D., Hsu, R., Figura, B., Jacobs, R., Li, S., Horvath, S., Clifford, T., Chari, K., "Rheology and Structure of Surface Crosslinked Surfactant-Activated Microgels," *Soft Matter*, in press.
- Li, F., Parnell, S.R., Wang, T., Baxter, D.V., Pynn, R., "Magnetic Field Optimization and Design of a Superconducting Neutron Wollaston Prism," *J. Phys. Conf. Ser.* **711**(1), 012015 (2016).
- Li, F., Parnell, S.R., Bai, H., Yang, W., Hamilton, W.A., Maranville, B.B., Ashkar, R., Baxter, D.V., Cremer, J.T., Pynn, R., "Spin Echo Modulated Small-Angle Neutron Scattering using Superconducting Magnetic Wollaston Prisms," *J. Appl. Crystallogr.* **49**, 55 (2016).
- Li, H., Zhang, L.-L., Yi, Z., Fratini, E., Baglioni, P., Chen, S.-H., "Translational and Rotational Dynamics of Water Contained in Aged Portland Cement Pastes Studied by Quasi-Elastic Neutron Scattering," *J. Colloid Interf. Sci.* **452**, 2 (2015). [CHRS]
- Li, J., Medina, E.A., Stalick, J.K., Sleight, A.W., Subramanian, M.A., "Structural Studies of  $\text{CaAl}_{12}\text{O}_{19}$ ,  $\text{SrAl}_{12}\text{O}_{19}$ ,  $\text{La}_{2/3+\delta}\text{Al}_{12-8}\text{O}_{19}$ , and  $\text{CaAl}_{10}\text{NiTiO}_{19}$  with the Hibonite Structure; Indications of an Unusual Type of Ferroelectricity," *Z. Naturforsch. B* **71**(5), 475 (2016).
- Li, K., Arif, M., Cory, D.G., Huan, R., Heacock, B., Huber, M.G., Nsofini, J., Pushin, D.A., Saggu, P., Sarenac, D., Shahi, C.B., Skavysh, V., Snow, W.M., Young, A.R., "Neutron Limit on the Strongly-Coupled Chameleon Field," *Phys. Rev. D* **93**(6), 062001 (2016).
- Li, M.-R., Retuerto, M., Deng, Z., Stephens, P.W., Croft, M., Huang, Q., Wu, H., Deng, X., Kotliar, G., Sánchez-Benítez, J., Hadermann, J., Walker, D., Greenblatt, M., "Giant Magnetoresistance in the Half-Metallic Double-Perovskite Ferrimagnet  $\text{Mn}_2\text{FeReO}_6$ ," *Angew. Chem. Int. Edit.* **54**(41), 12069 (2015).
- Li, M., Chang, C.-Z., Kirby, B.J., Jamer, M.E., Cui, W., Wu, L., Wei, P., Zhu, Y., Heiman, D., Li, J., Moodera, J.S., "Proximity-Driven Enhanced Magnetic Order at Ferromagnetic-Insulator-Magnetic-Topological-Insulator Interface," *Phys. Rev. Lett.* **115**(8), 087201 (2015).
- Li, V.A., Dorrell, R., Duvall, M.J., Koblanski, J., Negrashov, S., Sakai, M., Wipperfurth, S.A., Engel, K., Jocher, G.R., Learned, J.G., Macchiarulo, L., Matsuno, S., McDonough, W.F., Mumm, H.P., Murillo, J., Nishimura, K., Rosen, M., Usman, S.M., Varner, G.S., "Invited Article: MiniTimeCube," *Rev. Sci. Instrum.* **87**(2), 021301 (2016).
- Li, Y., Nelson, A., Easton, C.D., Nisbet, D.R., Forsythe, J.S., Muir, B., "Probing the Interfacial Structure of Bilayer Plasma Polymer Films via Neutron Reflectometry," *Plasma Process Polym.* **13**(5), 534 (2016).
- Lin, K., Gong, P., Sun, J., Ma, H., Wang, Y., You, L., Deng, J., Chen, J., Lin, Z., Kato, K., Wu, H., Huang, Q., Xing, X., "Thermal Expansion and Second Harmonic Generation Response of the Tungsten Bronze  $\text{Pb}_2\text{AgNb}_5\text{O}_{15}$ ," *Inorg. Chem.* **55**(6), 2864 (2016).
- Liu, D.M., Zhang, Z.L., Zhou, S.L., Huang, Q.Z., Deng, X.J., Yue, M., Liu, C.X., Zhang, J.X., Lynn, J.W., "A Pathway to Optimize the Properties of Magnetocaloric  $\text{Mn}_{2-x}\text{Fe}_x\text{P}_{1-y}\text{Ge}_y$  for Magnetic Refrigeration," *J. Alloy Compd.* **666**, 108 (2016).
- Liu, D.X., Cao, L.R., Co, A.C., "Demonstrating the Feasibility of Al as Anode Current Collector in Li-Ion Batteries via *In Situ* Neutron Depth Profiling," *Chem. Mater.* **28**(2), 556 (2016).
- Liu, D.X., Co, A.C., "Revealing Chemical Processes Involved in Electrochemical (De)Lithiation of Al with *In Situ* Neutron Depth Profiling and X-ray Diffraction," *J. Am. Chem. Soc.* **138**(1), 231 (2016).
- Liu, M., Chen, L., Lewis, S., Chong, S.Y., Little, M.A., Hasell, T., Aldous, I.M., Brown, C.M., Smith, M.W., Morrison, C.A., Hardwick, L.J., Cooper, A.I., "Three-Dimensional Protonic Conductivity in Porous Organic Cage Solids," *Nat. Commun.*, in press.
- López-Barrón, C.R., Beltramo, P.J., Liu, Y., Choi, S.-M., Lee, M.-J., "Mechanical, Dielectric and Structural Characterization of Cross-Linked PEG-Diacrylate/Ethylammonium Nitrate Ionogels," *Polymer* **87**, 300 (2016).
- López-Barrón, C.R., Chen, R., Wagner, N.J., Beltramo, P.J., "Self-Assembly of Pluronic F127 Diacrylate in Ethylammonium Nitrate: Structure, Rheology, and Ionic Conductivity Before and After Photo-Cross-Linking," *Macromolecules* **49**(14), 5179 (2016).
- López-Barrón, C.R., Eberle, A.P.R., Yakovlev, S., Bons, A.-J., "Structural Origins of Mechanical Properties and Hysteresis in SIS Triblock Copolymers/Polystyrene Blends with Spherical Morphology," *Rheol. Acta* **55**(2), 103 (2016).
- Lorenzo, A.T., Ponnampati, R., Chatterjee, T., Krishnamoorti, R., "Structural Characterization of Aqueous Solution Poly(Oligo(Ethylene Oxide) Monomethyl Methacrylate)-Grafted Silica Nanoparticles," *Faraday Discuss.* **186**, 311 (2016). [CHRS]
- Lu, J., Bates, F.S., Lodge, T.P., "Addition of Corona Block Homopolymer Retards Chain Exchange in Solutions of Block Copolymer Micelles," *Macromolecules* **49**(4), 1405 (2016).
- Lu, Q.M., Yue, M., Zhang, H.G., Wang, M.L., Yu, F., Huang, Q.Z., Ryan, D.H., Altounian, Z., "Intrinsic Magnetic Properties of Single-Phase  $\text{Mn}_{1+x}\text{Ga}$  ( $0 < x < 1$ ) Alloys," *Sci. Rep.* **5**, 17086 (2015).
- Lucero, C.L., Bentz, D.P., Hussey, D.S., Jacobson, D.L., Weiss, W.J., "Using Neutron Radiography to Quantify Water Transport and the Degree of Saturation in Entrained Air Cement Based Mortar," in "Physics Procedia," edited by Lehmann, E.H., Kaestner, A.P., Mannes, D., (10 World Conference on Neutron Radiography, September 2014, Grindelwald, Switzerland) **69**, 542 (2015).

- Luo, F., Yan, C., Dang, L., Krishna, R., Zhou, W., Wu, H., Dong, X., Han, Y., Hu, T.-L., O'Keeffe, M., Wang, L., Luo, M., Lin, R.-B., Chen, B., "UTSA-74: A MOF-74 Isomer with Two Accessible Binding Sites per Metal Center for Highly Selective Gas Separation," *J. Am. Chem. Soc.* **138**(17), 5678 (2016).
- Lynn, J.W., Zhou, X., Borg, C.K.H., Saha, S.R., Paglione, J., Rodriguez, E.E., "Neutron Investigation of the Magnetic Scattering in an Iron-Based Ferromagnetic Superconductor," *Phys. Rev. B* **92**(6), 060510 (2015).
- MacLaughlin, D.E., Bernal, O.O., Shu, L., Ishikawa, J., Matsumoto, Y., Wen, J.-J., Mourigal, M., Stock, C., Ehlers, G., Broholm, C.L., Machida, Y., Kimura, K., Nakatsuji, S., Shimura, Y., Sakakibara, T., "Unstable Spin-Ice Order in the Stuffed Metallic Pyrochlore  $\text{Pr}_{2-x}\text{Ir}_{2-x}\text{O}_{7-\delta}$ ," *Phys. Rev. B* **92**(5) 054432 (2015).
- Mahdavi, M., Baniassadi, M., Baghani, M., Dadmun, M., Tehrani, M., "3D Reconstruction of Carbon Nanotube Networks from Neutron Scattering Experiments," *Nanotechnology* **26**(38), 385704 (2015). [CHNRNS]
- Mallamace, F., Corsaro, C., Mallamace, D., Wang, Z., Chen, S.-H., "The Boson Peak in Confined Water: An Experimental Investigation of the Liquid-Liquid Phase Transition Hypothesis," *Front. Phys.* **10**(5), 106103 (2015).
- Malo de Molina, P., Lad, S., Helgeson, M.E., "Heterogeneity and its Influence on the Properties of Difunctional Poly(Ethylene Glycol) Hydrogels: Structure and Mechanics," *Macromolecules* **48**(15), 5402 (2015). [CHNRNS]
- Malo de Molina, P., Zhang, M., Bayles, A.V., Helgeson, M.E., "Oil-in-Water-in-Oil Multinanoemulsions for Templating Complex Nanoparticles," *Nano Lett.*, in press. [CHNRNS]
- Mamontov, E., Sharma, V.K., Borreguero, J.M., Tyagi, M., "Protein-Style Dynamical Transition in a Non-Biological Polymer and a Non-Aqueous Solvent," *J. Phys. Chem. B* **120**(2), 3232 (2016). [CHNRNS]
- Manson, J.L., Huang, Q.-Z., Brown, C.M., Lynn, J.W., Stone, M.B., Singleton, J., Xiao, F., "Magnetic Structure and Exchange Interactions in Quasi-One-Dimensional  $\text{MnCl}_2(\text{urea})_2$ ," *Inorg. Chem.* **54**(24), 11897 (2015).
- Maranville, B.B., Kirby, B.J., Grutter, A.J., Kienzle, P.A., Majkrzak, C.F., Liu, Y., Dennis, C.L., "Measurement and Modeling of Polarized Specular Neutron Reflectivity in Large Magnetic Fields," *J. Appl. Crystallogr.*, in press.
- Mariani, G., Schweins, R., Gröhn, F., "Structure Tuning of Electrostatically Self-Assembled Nanoparticles through pH," *J. Phys. Chem. B* **120**(7), 1380 (2016). [CHNRNS]
- Martin, T.B., Mongcopa, K.I.S., Ashkar, R., Butler, P., Krishnamoorti, R., Jayaraman, A., "Wetting-Dewetting and Dispersion-Aggregation Transitions Are Distinct for Polymer Grafted Nanoparticles in Chemically Dissimilar Polymer Matrix," *J. Am. Chem. Soc.* **137**(33), 10624 (2015). [CHNRNS]
- Mason, J.A., Oktawiec, J., Taylor, M.K., Hudson, M.R., Rodriguez, J., Bachman, J.E., Gonzalez, M.I., Cervellino, A., Guagliardi, A., Brown, C.M., Llewellyn, P.L., Masciocchi, N., Long, J.R., "Methane Storage in Flexible Metal-Organic Frameworks with Intrinsic Thermal Management," *Nature* **527**(7578), 357 (2015).
- McTaggart, M., Malardier-Jugroot, C., Jugroot, M., "Self-Assembled Biomimetic Nanoreactors I: Polymeric Template," *Chem. Phys. Lett.* **636**, 216 (2015). [CHNRNS]
- McTaggart, M., Malardier-Jugroot, C., Jugroot, M., "Self-Assembled Biomimetic Nanoreactors II: Noble Metal Active Centers," *Chem. Phys. Lett.* **636**, 221 (2015). [CHNRNS]
- Medina, E.A., Li, J., Stalick, J.K., Subramanian, M.A., "Intense Turquoise Colors of Apatite-Type Compounds with  $\text{Mn}^{5+}$  in Tetrahedral Coordination," *Solid State Sci.* **52**, 97 (2016).
- Michor, E.L., Berg, J.C., "Temperature Effects on Micelle Formation and Particle Charging with Span Surfactants in Apolar Media," *Langmuir* **31**(35), 9602 (2015). [CHNRNS]
- Müller, W., Wu, L.S., Kim, M.S., Orvis, T., Simonson, J.W., Gamża, M., McNally, D.M., Nelson, C.S., Ehlers, G., Podlesnyak, A., Helton, J.S., Zhao, Y., Qiu, Y., Copley, J.R.D., Lynn, J.W., Zaliznyak, I., Aronson, M.C., "Magnetic Structure of  $\text{Yb}_2\text{Pt}_2\text{Pb}$ : Ising Moments on the Shastry-Sutherland Lattice," *Phys. Rev. B* **93**(10), 104419 (2016).
- Mikita, R., Aharen, T., Yamamoto, T., Takeiri, F., Ya, T., Yoshimune, W., Fujita, K., Yoshida, S., Tanaka, K., Batuk, D., Abakumov, A.M., Brown, C.M., Kobayashi, Y., Kageyama, H., "Topochemical Nitridation with Anion Vacancy-Assisted  $\text{N}^{3-}/\text{O}^{2-}$  Exchange," *J. Am. Chem. Soc.* **138**(9), 3211 (2016).
- Milner, J.L., Gnäupel-Herold, T., Skovron, J.D., "Residual Stresses in Flow Drill Screwdriving of Aluminum Alloy Sheets," in "Proceedings of the ASME 2016 International Manufacturing Science and Engineering Conference," (ASME 2016 International Manufacturing Science and Engineering Conference, May 2016, Blacksburg, VA) **MSEC2016**, 8823 (2016).
- Mink, J., Lin, Y.-C., Karlsson, M., Österberg, C., Udovic, T.J., Fahlquist, H., Häussermann, U., "Vibrational Properties of  $\beta\text{-KSiH}_3$  and  $\beta\text{-RbSiH}_3$ : A Combined Raman and Inelastic Neutron Scattering Study," *J. Raman Spectrosc.*, in press.
- Mirri, F., Orloff, N.D., Forster, A.M., Ashkar, R., Headrick, R.J., Bengio, E.A., Long, C.J., Choi, A., Luo, Y., Hight Walker, A.R., Butler, P., Migler, K.B., Pasquali, M., "Lightweight, Flexible, High-Performance Carbon Nanotube Cables Made by Scalable Flow Coating," *ACS Appl. Mater. Interfaces* **8**(7), 4903 (2016).



- Mondal, T., Ashkar, R., Butler, P., Bhowmick, A.K., Krishnamoorti, R., "Graphene Nanocomposites with High Molecular Weight Poly( $\epsilon$ -Caprolactone) Grafts: Controlled Synthesis and Accelerated Crystallization," *ACS Macro Letters* **5**(3), 278 (2016). [CHNRS]
- Morgan, B., Dadmun, M.D., "Illumination of Conjugated Polymer in Solution Alters Its Conformation and Thermodynamics," *Macromolecules* **49**(9), 3490 (2016). [CHNRS]
- Motokawa, R., Endo, H., Nagao, M., Heller, W.T., "Neutron Polarization Analysis for Biphasic Solvent Extraction Systems," *Solvent Extr. Ion Exc.*, in press. [CHNRS]
- Mumm, H.P., Huber, M.G., Bauder, W., Abrams, N., Deibel, C.M., Huffer, C.R., Huffman, P.R., Schelhammer, K.W., Janssens, R., Jiang, C.L., Scott, R.H., Pardo, R.C., Rehm, K.E., Vondrasek, R., Swank, C.M., O'Shaughnessy, C.M., Paul, M., Yang, L., "High-Sensitivity Measurement of  $^3\text{He}$ - $^4\text{He}$  Isotopic Ratios for Ultracold Neutron Experiments," *Phys. Rev. C* **93**(6), 065502 (2016).
- Murphy, R.J., Weigandt, K.M., Uhrig, D., Alsayed, A., Badre, C., Hough, L., Muthukumar, M., "Scattering Studies on Poly(3,4-Ethylenedioxythiophene) - Polystyrenesulfonate in the Presence of Ionic Liquids," *Macromolecules* **48**(24), 8989 (2015). [CHNRS]
- Nambu, Y., Gardner, J.S., MacLaughlin, D.E., Stock, C., Endo, H., Jonas, S., Sato, T.J., Nakatsuji, S., Broholm, C., "Spin Fluctuations from Hertz to Terahertz on a Triangular Lattice," *Phys. Rev. Lett.* **115**(12), 127202 (2015). [CHNRS]
- Nandjou, F., Poirot-Crouvezier, J.-P., Chandesris, M., Rosini, S., Hussey, D.S., Jacobson, D.L., LaManna, J.M., Morin, A., Bultel, Y., "A Pseudo-3D Model to Investigate Heat and Water Transport in Large Area PEM Fuel Cells - Part 2: Application on an Automotive Driving Cycle," *Int. J. Hydrogen Energ.*, in press.
- NaraseGowda, S., Brown, C.M., Tyagi, M., Jenkins, T., Dobbins, T.A., "Quasi-Elastic Neutron Scattering Studies of Hydrogen Dynamics for Nanoconfined  $\text{NaAlH}_4$ ," *J. Phys. Chem. C* **120**(27), 14863 (2016). [CHNRS]
- Natarajan, B., Orloff, N.D., Ashkar, R., Doshi, S., Twedt, K., Krishnamurthy, A., Davis, C., Forster, A.M., Thostenson, E., Obrzut, J., Sharma, R., Liddle, J.A., "Multiscale Metrologies for Process Optimization of Carbon Nanotube Polymer Composites," *Carbon*, in press. [CHNRS]
- Navarre-Sitchler, A., Brantley, S.L., Rother, G., "How Porosity Increases During Incipient Weathering of Crystalline Silicate Rocks," *Rev. Mineral. Geochem.* **80**, 331 (2015). [CHNRS]
- Need, R.F., Isaac, B.J., Kirby, B.J., Borchers, J.A., Stemmer, S., Wilson, S.D., "Interface-Driven Ferromagnetism within the Quantum Wells of a Rare Earth Titanate Superlattice," *Phys. Rev. Lett.* **117**(3), 037205 (2016).
- Norman, A.I., Ivkov, R., Forbes, J.G., Greer, S.C., "Erratum: 'The Polymerization of Actin: Structural Changes from Small-Angle Neutron Scattering' [*J. Chem. Phys.* **123**, 154904 (2005)]," *J. Chem. Phys.* **144**(22), 229902 (2016). [CHNRS]
- Nsofini, J., Sarenac, D., Wood, C.J., Cory, D.G., Arif, M., Clark, C.W., Huber, M.G., Pushin, D.A., "Spin-Orbit States of Neutron Wave Packets," *Phys. Rev. A* **94**(1), 013605 (2016).
- Nykaza, J.R., Ye, Y., Nelson, R.L., Jackson, A.C., Beyer, F.L., Davis, E.M., Page, K., Sharick, S., Winey, K.I., Elabd, Y.A., "Polymerized Ionic Liquid Diblock Copolymers: Impact of Water/Ion Clustering on Ion Conductivity," *Soft Matter* **12**(4), 1133 (2016).
- Obermeyer, A.C., Mills, C.E., Dong, X.-H., Flores, R.J., Olsen, B.D., "Complex Coacervation of Supercharged Proteins with Polyelectrolytes," *Soft Matter* **12**(15), 3570 (2016). [CHNRS]
- Olsson, A., Rennie, A.R., "Boron Carbide Composite Apertures for Small-Angle Neutron Scattering made by Three-Dimensional Printing," *J. Appl. Crystallogr.* **49**(2), 696 (2016).
- Österberg, C., Fahlquist, H., Häussermann, U., Brown, C.M., Udovic, T.J., Karlsson, M., "Dynamics of Pyramidal  $\text{SiH}_3^-$  Ions in  $\text{ASiH}_3$  ( $A = \text{K}$  and  $\text{Rb}$ ) Investigated with Quasielastic Neutron Scattering," *J. Phys. Chem. C* **120**(12) 6369 (2016).
- Pan, L., Laurita, N.J., Ross, K.A., Gaulin, B.D., Armitage, N.P., "A Measure of Monopole Inertia in the Quantum Spin Ice  $\text{Yb}_2\text{Ti}_2\text{O}_7$ ," *Nat. Phys.* **12**(4), 361 (2016).
- Paul, R.L., "Prompt Gamma-Ray Activation Analysis for Certification of Sulfur in Fuel Oil SRMs," *J. Radioanal. Nucl. Chem.*, in press.
- Peng, H.-G., Daga, V.K., Lin, Y., Watkins, J.J., Wu, W.-L., Soles, C.L., "Distributions of a Linear Homopolymer Additive in an Ordered Block Copolymer Matrix as Quantified by Small-Angle Neutron Scattering," *Macromolecules* **48**(20), 7574 (2015).
- Phillips, II, D.G., Snow, W.M., Babu, K., Banerjee, S., Baxter, D.V., Bereziani, Z., Bergevin, M., Bhattacharya, S., Brooijmans, G., Castellanos, L., Chen, M.-C., Coppola, C.E., Cowsik, R., Crabtree, J.A., Das, P., Dees, E.B., Dolgov, A., Ferguson, P.D., Frost, M., Gabriel, T., Gal, A., Gallmeier, F., Ganezer, K., Golubeva, E., Greene, G., Hartfiel, B., Hawari, A., Heilbronn, L., Johnson, C., Kamyshkov, Y., Kerbikov, B., Kitaguchi, M., Kopeliovich, B.Z., Kopeliovich, V.B., Kuzmin, V.A., Liu, C.-Y., McGaughey, P., Mocko, M., Mohapatra, R., Mokhov, N., Muhler, G., Mumm, H.P., Okun, L., Pattie, Jr., R.W., Quigg, C., Ramberg, E., Ray, A., Roy, A., Ruggles, A., Sarkar, U., Saunders, A., Serebrov, A.P., Shimizu, H.M., Shrock, R., Sikdar, A.K., Sjue, S., Striganov, S., Townsend, L.W., Tschirhart, R., Vainshtein, A., Van Kooten, R., Wang, Z., Young, A.R., "Neutron-Antineutron Oscillations: Theoretical Status and Experimental Prospects," *Physics Reports* **612**, 1 (2016).

- Plumb, K.W., Hwang, K., Qiu, Y., Harriger, L.W., Granroth, G.E., Kolesnikov, A.I., Shu, G.J., Chou, F.C., Rüegg, Ch., Kim, Y.B., Kim, Y.-J., "Quasiparticle-Continuum Level Repulsion in a Quantum Magnet," *Nat. Phys.* **12**(3), 224 (2016).
- Prabhu, V., Venkataraman, S., Yang, Y.Y., Hedrick, J.L., "Equilibrium Self-Assembly, Structure and Dynamics of Clusters of Star-Like Micelles," *ACS Macro Letters* **4**(10), 1128 (2015).
- Prabhu, V.M., Venkataraman, S., Yang, Y.Y., Hedrick, J.L., "Star-Like Structure of Oligocarbonate-Fluorene End-Functionalized Poly(Ethylene Glycol) ABA Triblock Copolymers Below the Gel Point," *Macromol. Symp.* **358**(1), 157 (2015).
- Preta, G., Jankunec, M., Heinrich, F., Griffin, S., Sheldon, I.M., Valincius, G., "Tethered Bilayer Membranes as a Complementary Tool for Functional and Structural Studies: the Pyolysin Case," *Biochim. Biophys. Acta, Biomembr.*, in press.
- Prévost, D., Wu, Z., Williams, R.E., "Feasibility Studies on a Hexagonal-Lattice Core for a World-Class Cold Neutron Source," *T. Am. Nucl. Soc.* **114**, 671 (2016).
- Qiu, J., Mulligan, P., Lin, C.-H., Brillson, L., Downing, R.G., Cao, L., "Intrinsic Neutron Sensitivity of GaN and Radiation Effects on Forward-Biased Devices," in "Annual Meeting Proceedings of the Institute of Nuclear Materials Management," (56th Annual Meeting of the Nuclear Materials Management, June 2016, Indian Wells, CA) **2**, 1331 (2016).
- Rai, D.K., Beaucage, G., Ratkanthwar, K., Beaucage, P., Ramachandran, R., Hadjichristidis, N., "Quantification of Interaction and Topological Parameters of Polyisoprene Star Polymers under Good Solvent Conditions," *Phys. Rev. E* **93**(5), 052501 (2016).
- Ranka, M., Brown, P., Hatton, T.A., "Responsive Stabilization of Nanoparticles for Extreme Salinity and High-Temperature Reservoir Applications," *ACS Appl. Mater. Interfaces* **7**(35), 19651 (2015). [CHNRNS]
- Rappaport, S.M., Teijido, O., Hoogerheide, D.P., Rostovtseva, T.K., Berezhkovskii, A.M., Bezrukov, S.M., "Conductance Hysteresis in the Voltage-Dependent Anion Channel," *Eur. Biophys. J.* **44**(6), 465 (2015).
- Ratcliff, II, W.D., Lynn, J.W., "Chapter 5: Multiferroics," in "Experimental Methods in the Physical Sciences, Vol. 48," edited by Fernandez-Alonso, F. and Price, D.L. (Academic Press, New York, New York) Chap. **5**, 291 (2015).
- Ratcliff, W., Lynn, J.W., Kiryukhin, V., Jain, P., Fitzsimmons, M.R., "Magnetic Structures and Dynamics of Multiferroic Systems Obtained with Neutron Scattering," *NPJ* **1**(16003), 1 (2016).
- Reznik, D., Parshall, D., Park, S.R., Lynn, J.W., Wolf, Th., "Absence of Magnetic Field Dependence of the Anomalous Bond-Stretching Phonon in  $\text{YBa}_2\text{Cu}_3\text{O}_{6.6}$ ," *J. Supercond. Nov. Magn.* **29**(3), 643 (2016).
- Robertson, A.E., Phan, D.H., Macaluso, J.E., Kuryakov, V.N., Jouravleva, E.V., Bertrand, C.E., Yudin, I.K., Anisimov, M.A., "Mesoscale Solubilization and Critical Phenomena in Binary and Quasi-Binary Solutions of Hydrotropes," *Fluid Phase Equilib.* **407**, 243 (2016). [CHNRNS]
- Roh, J.H., Tyagi, M., Aich, P., Kim, K., Briber, R.M., Woodson, S.A., "Charge Screening in RNA: An Integral Route for Dynamical Enhancements," *Soft Matter* **11**(45), 8741 (2015). [CHNRNS]
- Roh, J.H., "Dynamics of Biopolymers: Role of Hydration and Electrostatic Interactions," *Macromol. Chem. Phys.* **217**(2), 256 (2016). [CHNRNS]
- Rønneest, A.K., Peters, G.H., Hansen, F.Y., Taub, H., Miskowicz, A., "Structure and Dynamics of Water and Lipid Molecules in Charged Anionic DMPG Lipid Bilayer Membranes," *J. Chem. Phys.* **144**(14), 144904 (2016). [CHNRNS]
- Ross, K.A., Bordelon, M.M., Terho, G., Neilson, J.R., "Nanosized Helical Magnetic Domains in Strongly Frustrated  $\text{Fe}_3\text{PO}_4\text{O}_3$ ," *Phys. Rev. B* **92**(13), 134419 (2015).
- Ross, K.A., Krizan, J.W., Rodriguez-Rivera, J.A., Cava, R.J., Broholm, C.L., "Static and Dynamic XY-Like Short-Range Order in a Frustrated Magnet with Exchange Disorder," *Phys. Rev. B* **93**(1), 014433 (2016). [CHNRNS]
- Roudebush, J.H., Ross, K.A., Cava, R.J., "Iridium Containing Honeycomb Delafossites by Topotactic Cation Exchange," *Dalton T.* **45**(21), 8783 (2016).
- Rubinson, K.A., Faraone, A., "The Relative Diffusive Transport Rate of  $\text{SrI}_2$  in Water Changes over the Nanometer Length Scale as Measured by Coherent Quasielastic Neutron Scattering," *Phys. Chem. Chem. Phys.* **18**(18), 12707 (2016).
- Rubinson, K.A., Bühlmann, P., Allison, T.C., "One-Dimensional Ionic Self-Assembly in a Fluorous Solution: The Structure of Tetra-*n*-butylammonium Tetrakis[3,5-Bis(perfluorohexyl)phenyl]borate in Perfluoromethylcyclohexane by Small-Angle Neutron Scattering (SANS)," *Phys. Chem. Chem. Phys.* **18**(14), 9470 (2016). [CHNRNS]
- Runčevski, T., Kapelewski, M.T., Torres-Gavosto, R.M., Tarver, J.D., Brown, C.M., Long, J.R., "Adsorption of Two Gas Molecules at a Single Metal Site in a Metal-Organic Framework," *Chem. Commun.* **52**(53), 8251 (2016).
- Şahin, D., Ünlü, K., Ivanov, K., "Neutron Analysis of the PSBR using a Burnup-Coupled MCNP Simulation with MURE," *Nucl. Technol.* **194**(3), 000 (2016).
- Samant, S.P., Grabowski, C.A., Kisslinger, K., Yager, K.G., Yuan, G., Satija, S.K., Durstock, M.F., Raghavan, D., Karim, A., "Directed Self-Assembly of Block Copolymers for High Breakdown Strength Polymer Film Capacitors," *ACS Appl. Mater. Interfaces* **8**(12), 7966 (2016).

- Santamaria, A.D., Becton, M.K., Cooper, N.J., Weber, A.Z., Park, J.W., "Effect of Cross-Flow on PEFC Liquid-Water Distribution: An In-Situ High-Resolution Neutron Radiography Study," *J. Power Sources* **293**, 162 (2015).
- Sarker, S., Chandra, D., Hirscher, M., Dolan, M., Isheim, D., Wermer, J., Viano, D., Baricco, M., Udovic, T.J., Grant, D., Palumbo, O., Paolone, A., Cantelli, R., "Developments in the Ni-Nb-Zr Amorphous Alloy Membranes," *Appl. Phys. A-Mater.* **122**(3), 168 (2016).
- Schantz, M.M., Cleveland, D., Heckert, N.A., Kucklick, J.R., Leigh, S.D., Long, S.E., Lynch, J.M., Murphy, K.E., Ofiaz, R., Pinar, A.L., Porter, B.J., Rabb, S.A., Vander Pol, S.S., Wise, S.A., Zeisler, R., "Development of Two Fine Particulate Matter Standard Reference Materials (<4  $\mu\text{m}$  and <10  $\mu\text{m}$ ) for the Determination of Organic and Inorganic Constituents," *Anal. Bioanal. Chem.* **408**(16), 4257 (2016).
- Scheie, A., Sanders, M., Krizan, J., Qiu, Y., Cava, R.J., Broholm, C., "Effective Spin- $\frac{1}{2}$  Scalar Chiral Order on Kagome Lattices in  $\text{Nd}_3\text{Sb}_3\text{Mg}_2\text{O}_{14}$ ," *Phys. Rev. B* **93**(18), 180407 (2016). [CHNRS]
- Scherger, J.D., Evans, E.A., Dura, J.A., Foster, M.D., "Extending Nanoscale Spectroscopy with Titanium Nitride Probes," *J. Raman Spectrosc.*, in press.
- Schneeloch, J.A., Xu, Z., Winn, B., Stock, C., Gehring, P.M., Birgeneau, R.J., Xu, G., "Phonon Coupling to Dynamic Short-Range Polar Order in a Relaxor Ferroelectric Near the Morphotropic Phase Boundary," *Phys. Rev. B* **92**(21), 214302 (2015).
- Scott, D.R., Silin, V., Nanda, H., "Reconstitution of Functionalized Transmembrane Domains of Receptor Proteins into Biomimetic Membranes," *Langmuir* **31**(33), 9115 (2015).
- Senses, E., Faraone, A., Akcora, P., "Microscopic Chain Motion in Polymer Nanocomposites with Dynamically Asymmetric Interphases," *Sci. Rep.* **6**, 29326 (2016). [CHNRS]
- Shahi, C.B., Arif, M., Cory, D.G., Mineeva, T., Nsofini, J., Sarenac, D., Williams, C.J., Huber, M.G., Pushin, D.A., "A New Polarized Neutron Interferometry Facility at the NCNR," *Nucl. Instrum. Meth. A* **813**, 111 (2016).
- Sharma, V.K., Mamontov, E., Tyagi, M., Qian, S., Rai, D.K., Urban, V.S., "Dynamical and Phase Behavior of a Phospholipid Membrane Altered by an Antimicrobial Peptide at Low Concentration," *J. Phys. Chem. Lett.* **7**(13), 2394 (2016). [CHNRS]
- Sharma, V.K., Mamontov, E., Tyagi, M., Urban, V.S., "Effect of  $\alpha$ -Tocopherol on the Microscopic Dynamics of Dimyristoylphosphatidylcholine Membrane," *J. Phys. Chem. B* **120**(1), 154 (2016). [CHNRS]
- Shen, Y., Barros, M., Vennemann, T., Gallagher, D.T., Yin, Y., Linden, S.B., Heselpoth, R.D., Spencer, D.J., Donovan, D.M., Moulton, J., Fischetti, V.A., Heinrich, F., Lösche, M., Nelson, D.C., "A Bacteriophage Endolysin that Eliminates Intracellular Streptococci," *eLIFE* **5**, e13152 (2016).
- Shen, Y., Wang, Q., Hao, Y., Pan, B., Feng, Y., Huang, Q., Harriger, L.W., Leão, J.B., Zhao, Y., Chisnell, R.M., Lynn, J.W., Cao, H., Hu, J., Zhao, J., "Structural and Magnetic Phase Diagram of CrAs and its Relationship with Pressure-induced Superconductivity," *Phys. Rev. B* **93**(6), 060503 (2016).
- Shetty, M., Şahin, D., "Data Acquisition and Analysis Software for Gamma Coincidence Spectrometry," *J. Radioanal. Nucl. Chem.* **309**(1), 243 (2016).
- Shi, K., Sun, Y., Yan, J., Deng, S., Wang, L., Wu, H., Hu, P., Lu, H., Malik, M.I., Huang, Q., Wang, C., "Baromagnetic Effect in Antiperovskite  $\text{Mn}_3\text{Ga}_{0.95}\text{N}_{0.94}$  by Neutron Powder Diffraction Analysis," *Adv. Mater.* **28**(19), 3761 (2016).
- Shrestha, U.R., Bhowmik, D., Copley, J.R.D., Tyagi, M., Leão, J.B., Chu, X.-Q., "Effects of Pressure on the Dynamics of an Oligomeric Protein from Deep-Sea Hyperthermophile," *P. Natl. A. Sci. USA* **112**(45), 13886 (2015). [CHNRS]
- Silin, V., Kasianowicz, J.J., Michelman-Ribeiro, A., Panchal, R.G., Bavari, S., Robertson, J.W.F., "Biochip for the Detection of *Bacillus Anthracis* Lethal Factor and Therapeutic Agents against Anthrax Toxins," *Membranes* **6**(3), 36 (2016).
- Skipov, A.V., Skoryunov, R.V., Solonin, A.V., Babanova, O.A., Tang, W.S., Stavila, V., Udovic, T.J., "Anion Reorientations and Cation Diffusion in  $\text{LiCB}_{11}\text{H}_{12}$  and  $\text{NaCB}_{11}\text{H}_{12}$ :  $^1\text{H}$ ,  $^7\text{Li}$ , and  $^{23}\text{Na}$  NMR Studies," *J. Phys. Chem. C* **119**(48), 26912 (2015).
- Smaha, R.W., Roudebush, J.H., Herb, J.T., Seibel, E.M., Krizan, J.W., Fox, G.M., Huang, Q., Arnold, C.B., Cava, R.J., "Tuning Sodium Ion Conductivity in the Layered Honeycomb Oxide  $\text{Na}_{3-x}\text{Sn}_{2-x}\text{Sb}_x\text{NaO}_6$ ," *Inorg. Chem.* **54**(16), 7985 (2015).
- Snow, W.M., Anderson, E., Barron Palos, L., Bass, C.D., Crawford, B.E., Crawford, C., Esposito, D., Fox, W., Fry, J., Gardiner, H., Haddock, C., Heckel, B.R., Holley, A.T., Lieffers, J., Maldonado-Velazquez, M., Malone, R., Markoff, D., Mumm, H.P., Nico, J.S., Olek, D., Paudel, C., Penn, S., Rout, P.C., Santra, S., Sarsour, M.G., Sprow, A., Swanson, H.E., Vanderwerp, J., van Sciver, S., "Searches for Exotic Spin-Dependent Interactions of Slow Neutrons with Matter using Neutron Spin Rotation," *J. Phys. Soc. Jpn.* **8**, 026003 (2015).
- Soetaert, F., Dupré, L., Ivkov, R., Crevecoeur, G., "Computational Evaluation of Amplitude Modulation for Enhanced Magnetic Nanoparticle Hyperthermia," *Biomed. Eng.-Biomed. Tech.* **60**(5), 491 (2015).



- Song, C., Liu, H., Jiao, J., Bai, D., Zhou, W., Yildirim, T., He, Y., "High Methane Storage and Working Capacities in a NbO-Type Metal-Organic Framework," *Dalton T.* **45**(18), 7559 (2016).
- Sowards, J.W., Gnäupel-Herold, T., McColskey, J.D., Pereira, V.F., Ramirez, A.J., "Characterization of Mechanical Properties, Fatigue-Crack Propagation and Residual Stresses in a Microalloyed Pipeline-Steel Friction-Stir Weld," *Materials and Design* **88**, 632 (2015).
- Stalick, J.K., Waterstrat, R.M., "Crystal Structures and Phase Equilibria in the Hafnium-Palladium System," *J. Phase Equilib. Diff.*, in press.
- Stock, C., Rodriguez, E.E., Lee, N., Green, M.A., Demmel, F., Ewings, R.A., Fouquet, P., Laver, M., Niedermayer, Ch., Su, Y., Nemkovski, K., Rodriguez-Rivera, J.A., Cheong, S.-W., "Solitary Magnons in the  $S = 5/2$  Antiferromagnet  $\text{CaFe}_2\text{O}_4$ ," *Phys. Rev. Lett.* **117**(1), 017201 (2016). [CHRNS]
- Sumino, Y., Yamada, N.L., Nagao, M., Honda, T., Kitahata, H., Melnichenko, Y.B., Seto, H., "Mechanism of Spontaneous Blebbing Motion of Oil-Water Interface: Elastic Stress Generated by a Lamellar-Lamellar Transition," *Langmuir* **32**(12), 2891 (2016).
- Sun, J.E.P., Stewart, B., Litan, A., Lee, S.J., Schneider, J.P., Langhans, S.A., Pochan, D.J., "Sustained Release of Active Chemotherapeutics from Injectable-Solid  $\beta$ -Hairpin Peptide Hydrogel," *Biomater. Sci.* **4**(5), 839 (2016). [CHRNS]
- Sun, L., Akgun, B., Hu, R., Browning, J.F., Wu, D.T., Foster, M.D., "Scaling Behavior and Segment Concentration Profile of Densely Grafted Polymer Brushes Swollen in Vapor," *Langmuir* **32**(2), 5623 (2016).
- Sunday, D.F., Hannon, A.F., Tein, S., Kline, R.J., "Thermodynamic and Morphological Behavior of Block Copolymer Blends with Thermal Polymer Additives," *Macromolecules* **49**(13), 4898 (2016).
- Suzuki, T., Chisnell, R., Devarakonda, A., Liu, Y.-T., Feng, W., Xiao, D., Lynn, J.W., Checkelsky, J.G., "Large Anomalous Hall Effect in a Half-Heusler Antiferromagnet," *Nat. Phys.*, in press.
- Takatsu, H., Onoda, S., Kittaka, S., Kasahara, A., Kono, Y., Sakakibara, T., Kato, Y., Fåk, B., Ollivier, J., Lynn, J.W., Taniguchi, T., Wakita, M., Kadowaki, H., "Quadrupole Order in the Frustrated Pyrochlore  $\text{Tb}_{2+x}\text{Ti}_{2-x}\text{O}_{7+y}$ ," *Phys. Rev. Lett.* **116**(21), 217201 (2016).
- Tan, C., James, R., Dong, B., Driver, M.S., Kelber, J.A., Downing, G., Cao, L.R., "Characterization of a Boron Carbide-Based Polymer Neutron Sensor," *Nucl. Instrum. Meth. A* **803**, 82 (2015).
- Tan, C., Leung, K.Y., Liu, D.X., Canova, M., Downing, R.G., Co, A.C., Cao, L.R., "Gamma Radiation Effects on Li-Ion Battery Electrolyte in Neutron Depth Profiling for Lithium Quantification," *J. Radioanal. Nucl. Ch.* **305**(2), 675 (2015).
- Tan, K.T., White, C.C., Hunston, D., Gorham, J.M., Imburgia, M.J., Forster, A.M., Voft, B.D., "Role of Salt on Adhesion of an Epoxy/Aluminum (Oxide) Interface in Aqueous Environments," *Polym. Eng. Sci.* **56**(1), 18, (2016).
- Tang, W.S., Matsuo, M., Wu, H., Stavila, V., Unemoto, A., Orimo, S.-I., Udovic, T.J., "Stabilizing Lithium and Sodium Fast-Ion Conduction in Solid Polyhedral-Borate Salts at Device-Relevant Temperatures," *Energy Storage Materials* **4**, 79 (2016). [CHRNS]
- Tang, W.S., Matsuo, M., Wu, H., Stavila, V., Zhou, W., Talin, A.A., Soloninin, A.V., Skoryunov, R.V., Babanova, O.A., Skripov, A.V., Unemoto, A., Orimo, S.-I., Udovic, T.J., "Liquid-Like Ionic Conduction in Solid Lithium and Sodium Monocarbonyl-Decaborates Near or at Room Temperature," *Adv. Energy Mater.* **6**(8), 1502237 (2016).
- Tang, W.S., Unemoto, A., Zhou, W., Stavila, V., Matsuo, M., Wu, H., Orimo, S.-I., Udovic, T.J., "Unparalleled Lithium and Sodium Superionic Conduction in Solid Electrolytes with Large Monovalent Cage-like Anions," *Energy Environ. Sci.* **8**(12), 3637 (2015).
- Tang, W.S., Udovic, T.J., Stavila, V., "Altering the Structural Properties of  $\text{A}_2\text{B}_{12}\text{H}_{12}$  Compounds via Cation and Anion Modifications," *J. Alloy Compd.* **645**, S200 (2015).
- Tassel, C., Goto, Y., Watabe, D., Tang, Y., Lu, H., Kuno, Y., Takeiri, F., Yamamoto, T., Brown, C.M., Hester, J., Kobayashi, Y., Kageyama, H., "High-Pressure Synthesis of Manganese Oxyhydride with Partial Anion Order," *Angew. Chem. Int. Edit.*, in press.
- Taylor, D.D., Schreiber, N.J., Brown, C.M., Arevalo-Lopez, A.M., Rodriguez, E.E., "Stabilization of Cubic  $\text{Sr}_2\text{FeMoO}_6$  through Topochemical Reduction," *Chem. Commun.* **51**(61), 12201 (2015).
- Trentelman, K., Janssens, K., van der Snickt, G., Szafran, Y., Woollett, A.T., Dik, J., "Rembrandt's *An Old Man in Military Costume*: the Underlying Image Re-Examined," *Appl. Phys. A-Mater.* **121**(3), 801 (2015).
- Tung, W.-S., Composto, R.J., Clarke, N., Winey, K.I., "Anisotropic Polymer Conformations in Aligned SWCNT/PS Nanocomposites," *ACS Macro Letters* **4**(9), 916 (2015).
- Turkoglu, D., Downing, R.G., Chen, W., Şahin, D., Cook, J., "A  $^3\text{He}$  Beam Stop for Minimizing Gamma-Ray and Fast-Neutron Background," *J. Radioanal. Nucl. Chem.*, in press.

- Tutolo, B.M., Mildner, D.F.R., Gagnon, C.V.L., Saar, M.O., Seyfried, Jr., W.E., "Nanoscale Constraints on Porosity Generation and Fluid Flow During Serpentinization," *Geology* **44**(2), 103 (2016). [CHNRNS]
- Uğur, G., Akgun, B., Jiang, Z., Narayanan, S., Satija, S., Foster, M.D., "Effect of Tethering on the Surface Dynamics of a Thin Polymer Melt Layer," *Soft Matter* **12**(24), 5372 (2016).
- Umeasiegbu, C.D., Balakotaiah, V., Krishnamoorti, R., "pH-Induced Re-Entrant Microstructural Transitions in Cationic Surfactant-Hydrotrope Mixtures," *Langmuir* **32**(3), 655 (2016).
- Unemoto, A., Wu, H., Udovic, T.J., Matsuo, M., Ikeshoji, T., Orimo, S.-I., "Fast Lithium-Ionic Conduction in a New Complex Hydride-Sulphide Crystalline Phase," *Chem. Commun.* **52**(3), 564 (2016). [CHNRNS]
- Unemoto, A., Ikeshoji, T., Yasaku, S., Matsuo, M., Stavila, V., Udovic, T.J., Orimo, S.-I., "Stable Interface Formation between  $\text{TiS}_2$  and  $\text{LiBH}_4$  in Bulk-Type All-Solid-State Lithium Batteries," *Chem. Mater.* **27**(15), 5407 (2015).
- Verdal, N., Udovic, T.J., Rush, J.J., Skripov, A.V., "Quasielastic Neutron Scattering Study of Tetrahydroborate Anion Dynamical Perturbations in Sodium Borohydride due to Partial Halide Anion Substitution," *J. Alloy Compd.* **645**, S513 (2015). [CHNRNS]
- Villani, C., Lucero, C., Bentz, D., Hussey, D., Jacobson, D., Weiss, W.J., "Neutron Radiography Evaluation of Drying in Mortars with and without Shrinkage Reducing Admixtures," in "Novel Characterization Techniques and Advanced Cementitious Materials: Tribute to James J. Beaudoin," (American Concrete Institute Fall Meeting 2014, October 2014, Washington, DC.) **1** (2015).
- Wagman, J.J., Carlo, J.P., Gaudet, J., Van Gastel, G., Abernathy, D.L., Stone, M.B., Granroth, G.E., Kolesnikov, A.I., Savici, A.T., Kim, Y.J., Zhang, H., Ellis, D., Zhao, Y., Clark, L., Kallin, A.B., Mazurek, E., Dabkowska, H.A., Gaulin, B.D., "Neutron Scattering Studies of Spin-Phonon Hybridization and Superconducting Spin Gaps in the High-Temperature Superconductor  $\text{La}_{2-x}(\text{Sr,Ba})_x\text{CuO}_4$ ," *Phys. Rev. B* **93**(9) 094416 (2016)
- Wallace, D.C., McQueen, T.M., "New Honeycomb Iridium(v) Oxides:  $\text{NiIrO}_3$  and  $\text{Sr}_3\text{CaIr}_2\text{O}_9$ ," *Dalton T* **44**(47) 20344 (2015).
- Wang, G., Persson, N., Chu, P.-H., Kleinhenz, N., Fu, B., Chang, M., Deb, N., Mao, Y., Wang, H., Grover, M.A., Reichmanis, E., "Microfluidic Crystal Engineering of  $\pi$ -Conjugated Polymers," *ACS Nano*, **9**(8), 8220 (2015).
- Wang, H., Li, B., Wu, H., Hu, T.-L., Yao, Z., Zhou, W., Xiang, S., Chen, B., "A Flexible Microporous Hydrogen-Bonded Organic Framework for Gas Sorption and Separation," *J. Am. Chem. Soc.* **137**(31), 9963 (2015).
- Wang, M., Yi, M., Cao, H., de la Cruz, C., Mo, S.K., Huang, Q.Z., Bourret-Courchesne, E., Dai, P., Lee, D.H., Shen, Z.X., Birgeneau, R.J., "Mott Localization in a Pure Stripe Antiferromagnet  $\text{Rb}_{1-8}\text{Fe}_{1.5-6}\text{S}_2$ ," *Phys. Rev. B* **92**(12) 121101 (2015).
- Wang, Q., Park, J.T., Feng, Y., Shen, Y., Hao, Y., Pan, B., Lynn, J.W., Ivanov, A., Chi, S., Matsuda, M., Cao, H., Birgeneau, R.J., Efremov, D.V., Zhao, J., "Transition from Sign-Reversed to Sign-Preserved Cooper-Pairing Symmetry in Sulfur-Doped Iron Selenide Superconductors," *Phys. Rev. Lett.* **116**(19), 197004 (2016).
- Wang, Z., Le, P., Ito, K., Leão, J.B., Tyagi, M., Chen, S.-H., "Dynamic Crossover in Deeply Cooled Water Confined in MCM-41 at 4 kbar and its Relation to the Liquid-Liquid Transition Hypothesis," *J. Chem. Phys.* **143**(11), 114508 (2015). [CHNRNS]
- Wei, M.-H., Li, B., Ameri David, R.L., Jones, S.C., Sarohia, V., Schmitgal, J.A., Kornfield, J.A., "Megasupramolecules for Safer, Cleaner Fuel by End Association of Long Telechelic Polymers," *Science* **350**(6256), 72 (2015). [CHNRNS]
- Weir, M.P., Johnson, D.W., Boothroyd, S.C., Savage, R.C., Thompson, R.L., Parnell, S.R., Parnell, A.J., King, S.M., Rogers, S.E., Coleman, K.S., Clarke, N., "Extrinsic Wrinkling and Single Exfoliated Sheets of Graphene Oxide in Polymer Composites," *Chem. Mater.* **28**(6), 1698 (2016). [CHNRNS]
- Wiener, C.G., Tyagi, M., Liu, Y., Weiss, R.A., Vogt, B.D., "Supramolecular Hydrophobic Aggregates in Hydrogels Partially Inhibit Ice Formation," *J. Phys. Chem. B* **120**(24), 5543 (2016). [CHNRNS]
- Williams, R.E., Middleton, M., Kopetka, P., Rowe, J.M., Brand, P.C., "Status of the Liquid Deuterium Cold Neutron Source for the NIST Research Reactor," in "European Research Reactor Conference," (European Research Reactor Conference, February 2016, Berlin, Germany) **0**, 618 (2016).
- Wong-Ng, W., Lynn, J.W., Huang, Q., Brown, C.M., Kaduk, J.A., Joshi, G., "Observation of Drastic Change of Generalized Phonon Density-of-States in Nanostructured Half-Heusler using Inelastic Neutron Scattering," *Appl. Phys. Lett.* **107**(21), 213901 (2015).
- Worcester, D.L., Weinrich, M., "Hydrostatic Pressure Promotes Domain Formation in Model Lipid Raft Membranes," *J. Phys. Chem. Lett.* **6**(21), 4417 (2015). [CHNRNS]
- Wu, H., Zhou, X., Rodriguez, E.E., Zhou, W., Udovic, T.J., Yildirim, T., Rush, J.J., "A New Family of Metal Borohydride Guanidinate Complexes: Synthesis, Structures and Hydrogen-Storage Properties," *J. Solid State Chem.*, in press.
- Wu, L.S., Gannon, W.J., Zaliznyak, I.A., Tselik, A.M., Brockmann, M., Caux, J.-S., Kim, M.S., Qiu, Y., Copley, J.R.D., Ehlers, G., Podlesnyak, A., Aronson, M.C., "Orbital-Exchange and Fractional Quantum Number Excitations in an f-electron Metal,  $\text{Yb}_2\text{Pt}_2\text{Pb}$ ," *Science* **352**(6290), 1206 (2016).

- Wu, R.-R., Bao, L.-F., Hu, F.-X., Wu, H., Huang, Q.-Z., Wang, J., Dong, X.-L., Li, G.-N., Sun, J.-R., Shen, F.-R., Zhao, T.-Y., Zheng, X.-Q., Wang, L.-C., Liu, Y., Zuo, W.-L., Zhao, Y.-Y., Zhang, M., Wang, X.-C., Jin, C.-Q., Rao, G.-H., Han, X.-F., Shen, B.-G., "Giant Barocaloric Effect in Hexagonal  $\text{Ni}_2\text{In}$ -Type Mn-Co-Ge-In Compounds Around Room Temperature," *Sci. Rep.* **5**, 18027 (2015).
- Wu, Y., Liang, J., Horkay, F., Libera, M., "Antimicrobial Loading into and Release from Poly(Ethylene Glycol)/Poly(Acrylic Acid) Semi-Interpenetrating Hydrogels," *J. Polym. Sci. Pol. Phys.* **54**(1), 64 (2016). [CHNRS]
- Wu, Z.P., Li, P.G., Tang, W.H., Li, L.H., Huang, Q.Z., "Study of Structure and Magnetic Ordering in Multiferroics  $\text{Tb}_{1-x}\text{Nd}_x\text{MnO}_3$  by Neutron Powder Diffraction," *J. Alloy Compd.* **644**, 13 (2015).
- Wu, Z., Williams, R.E., Rowe, J.M., "Hypothetical Accident Analyses of the Proposed Split Core at NIST using ANL-Paret Code," in "International Group Operating Research Reactors Conference," edited by IGORR, (International Group Operating Research Reactors Conference, February 2016, Berlin, Germany), 799 (2016).
- Wu, Z., Williams, R.E., Newton, T.H., "Reactivity Coefficient Calculation for a Low-Power LEU Research Reactor," *T. Am. Nucl. Soc.* **114**, 814 (2016).
- Wu, Z., Williams, R.E., "Core Design Studies on a Low-Enriched Uranium Reactor for Cold Neutron Sources at NIST," in "Proceedings on International Conference on Reactor Physics PHYSOR 2016," edited by ANS, (The Joint International Conference on Reactor Physics PHYSOR 2016, April 2016, Sun Valley, ID), 1583 (2016).
- Wu, Z., Williams, R.E., Rowe, J.M., "Preliminary Safety Analyses on a Conceptual LEU Fueled Research Reactor at NIST," in "Transactions of American Nuclear Society," edited by ANS, (American Nuclear Society National Winter Meeting, October 2015, Washington D.C.) **113**, 1397 (2015).
- Wu, Z., Williams, R.E., "Reactor Power Distribution Calculation in Research Reactors using MCNP," in "Transactions of American Nuclear Society," edited by ANS, (American Nuclear Society National Winter Meeting, October 2015, Washington D.C.) **113**, 1171 (2015).
- Xu, J., Li, X., Lu, F., Fu, H., Brown, C.M., Kuang, X., "Oxygen Interstitials and Vacancies in  $\text{LaSrGa}_3\text{O}_7$ -Based Melilites," *J. Solid State Chem.* **230**, 309 (2015).
- Yajima, T., Takeiri, F., Aidzu, K., Akamatsu, H., Fujita, K., Yoshimune, W., Ohkura, M., Lei, S., Gopalan, V., Tanaka, K., Brown, C.M., Green, M.A., Yamamoto, T., Kobayashi, Y., Kageyama, H., "A Labile Hydride Strategy for the Synthesis of Heavily Nitridized  $\text{BaTiO}_3$ ," *Nat. Chem.* **7**(12), 1017 (2015).
- Yamaguchi, T., Yonezawa, T., Yoshida, K., Yamaguchi, T., Nagao, M., Faraone, A., Seki, S., "Relationship between Structural Relaxation, Shear Viscosity, and Ionic Conduction of  $\text{LiPF}_6$  / Propylene Carbonate Solutions," *J. Phys. Chem. B* **119**(51), 15675 (2015). [CHNRS]
- Yang, J., Duan, C., Huang, Q., Brown, C., Neufeind, J., Louca, D., "Strong Correlations between Vacancy and Magnetic Ordering in Superconducting  $\text{K}_{0.8}\text{Fe}_{2-y}\text{Se}_2$ ," *Phys. Rev. B* **94**(2), 024503 (2016).
- Yang, J., Samarakoon, A., Dissanayake, S., Ueda, H., Klich, I., Iida, K., Pajeroski, D., Butch, N.P., Huang, Q., Copley, J.R.D., Lee, S.-H., "Spin Jam Induced by Quantum Fluctuations in a Frustrated Magnet," *P. Natl. A. Sci. USA* **112**(37), 11519 (2015).
- Yang, J., Samarakoon, A.M., Hong, K.W., Copley, J.R.D., Huang, Q., Tennant, A., Sato, T.J., Lee, S.-H., "Glassy Behavior and Isolated Spin Dimers in a New Frustrated Magnet  $\text{BaCr}_{9p}\text{Ga}_{12-9p}\text{O}_{19}$ ," *J. Phys. Soc. Jpn.*, in press.
- Yang, J., Duan, C., Copley, J.R.D., Brown, C.M., Louca, D., "The Magnetic Transitions and Dynamics in the Multiferroic  $\text{Lu}_{0.5}\text{Sc}_{0.5}\text{FeO}_3$ ," in "MRS advances," edited by Oyen, M.L., (MRS Advances, October 2015, Boston, MA) **1**, 565 (2016).
- Yang, K., Cai, Z., Tyagi, M., Feygenson, M., Neufeind, J.C., Moore, J.S., Zhang, Y., "Odd-Even Structural Sensitivity on Dynamics in Network-Forming Ionic Liquids," *Chem. Mater.* **28**(9), 3227 (2016). [CHNRS]
- Yang, Y.B., Liu, S.Q., Zhao, H., Yang, W.Y., Wu, R., Huang, Q.Z., Zhou, D., Du, H.L., Wang, C.S., Yang, Y.C., Xu, H., Zhu, J.L., Gourdon, O., Vogel, S., Yang, J.B., "Magnetic Structure and Phase Transition of  $\text{Ni}_2\text{Mn}_{1.48}\text{Sb}_{0.52}$  Magnetic Shape Memory Compound," *Scripta Mater.* **116**, 31 (2016).
- Yao, Z., Zhang, Z., Liu, L., Li, Z., Zhou, W., Zhao, Y., Han, Y., Chen, B., Krishna, R., Xiang, S., "Extraordinary Separation of Acetylene-Containing Mixtures with Microporous Metal-Organic Frameworks with Open O Donor Sites and Tunable Robustness through Control of the Helical Chain Secondary Building Units," *Chem.-Eur. J.* **22**, 5676 (2016).
- Yu, J., Mao, J., Yuan, G., Satija, S., Chen, W., Tirrell, M., "The Effect of Multivalent Counterions to the Structure of Highly Dense Polystyrene Sulfonate Brushes," *Polymer*, in press.
- Yu, J., Mao, J., Yuan, G., Satija, S., Jiang, Z., Chen, W., Tirrell, M., "Structure of Polyelectrolyte Brushes in the Presence of Multivalent Counterions," *Macromolecules*, in press.
- Yuan, G., Wang, X., Wu, D., Hammouda, B., "Structural Analysis of Dendrimers Based on Polyhedral Oligomeric Silsesquioxane and their Assemblies in Solution by Small-Angle Neutron Scattering: Fits to a Modified Two Correlation Lengths Model," *Macromolecules*, in press. [CHNRS]



- Zaccai, N.R., Sandlin, C.W., Hoopes, J.T., Curtis, J.E., Fleming, P.J., Fleming, K.G., Krueger, S., "Deuterium Labeling Together with Contrast Variation Small-Angle Neutron Scattering Suggests How Skp Captures and Releases Unfolded Outer Membrane Proteins," in "Methods in Enzymology, Vol. 566," (Elsevier, Oxford, Oxford) Chap. **6**, 159 (2016). [CHRNA]
- Zander, Z.K., Hua, G., Wiener, C.G., Vogt, B.D., Becker, M.L., "Control of Mesh Size and Modulus by Kinetically Dependent Cross-Linking in Hydrogels," *Adv. Mater.* **27**(40), 6283 (2015). [CHRNA]
- Zhang, C., Lv, W., Tan, G., Song, Y., Carr, S.V., Chi, S., Matsuda, M., Christianson, A.D., Fernandez-Baca, J.A., Harriger, L.W., Dai, P., "Electron Doping Evolution of the Neutron Spin Resonance in  $\text{NaFe}_{1-x}\text{Co}_x\text{As}$ ," *Phys. Rev. B* **93**(17), 174522 (2016).
- Zhang, F.Z., Winholtz, R.A., Black, W.J., Wilson, M.R., Taub, H., Ma, H.B., "Effect of Hydrophilic Nanostructured Cupric Oxide Surfaces on the Heat Transport Capability of a Flat-Plate Oscillating Heat Pipe," *J. Heat Transf.* **138**(6), 062901 (2016).
- Zhang, W., Shen, H., Guralnick, B.W., Kirby, B.J., Nguyen, N.A., Remy, R., Majkrzak, C.F., Mackay, M.E., "Correlation between Morphology and Device Performance of pBTTT:PC<sub>71</sub>BM Solar Cells," *Sol. Energ. Mat. Sol. C.*, in press. [CHRNA]
- Zhang, X., Liu, K., He, J.-Q., Wu, H., Huang, Q.-Z., Lin, J.-H., Lu, Z.-Y., Huang, F.-Q., "Antiperovskite Chalco-Halides  $\text{Ba}_3(\text{FeS}_4)\text{Cl}$ ,  $\text{Ba}_3(\text{FeS}_4)\text{Br}$ , and  $\text{Ba}_3(\text{FeSe}_4)\text{Br}$  with Spin Super-Super Exchange," *Sci. Rep.* **5**, 15910 (2015).
- Zhang, Y., Yamamoto, T., Green, M.A., Kageyama, H., Ueda, Y., "Interlayer Communication in Aurivillius Vanadate to Enable Defect Structures and Charge Ordering," *Inorg. Chem.* **54**(22), 10925 (2015).
- Zheng, X.Q., Wu, H., Chen, J., Zhang, B., Li, Y.Q., Hu, F.X., Sun, J.R., Huang, Q.Z., Shen, B.G., "The Physical Mechanism of Magnetic Field Controlled Magnetocaloric Effect and Magnetoresistance in Bulk PrGa Compound," *Sci. Rep.* **5**, 14970 (2015).
- Zheng, X., Zhang, B., Li, Y., Wu, H., Zhang, H., Zhang, J., Wang, S., Huang, Q., Shen, B., "Large Magnetocaloric Effect in  $\text{Er}_{12}\text{Co}_7$  Compound and the Enhancement of  $\delta T_{\text{FWHM}}$  by Ho-Substitution," *J. Alloy Compd.*, in press.
- Zhou, C., Toombes, G.E.S., Wasbrough, M.J., Hillmyer, M.A., Lodge, T.P., "Structure of Two-Compartment Hydrogels from Thermoresponsive ABC Triblock Terpolymers," *Macromolecules* **48**(16), 5934 (2015). [CHRNA]
- Zhou, X., Borg, C.K.H., Lynn, J.W., Saha, S.R., Paglione, J., Rodriguez, E.E., "The Preparation and Phase Diagrams of  $(\text{Li}_{1-x}\text{Fe}_x\text{OD})\text{FeSe}$  and  $(\text{Li}_{1-x}\text{Fe}_x\text{OH})\text{FeSe}$  Superconductors," *J. Mater. Chem. C* **4**(18), 3934 (2016).
- Zhukhovitskiy, A.V., Zhong, M., Keeler, E.G., Michaelis, V.K., Sun, J.E.P., Hore, M.J.A., Pochan, D.J., Griffin, R.G., Willard, A.P., Johnson, J.A., "Highly Branched and Loop-Rich Gels via Formation of Metal-Organic Cages Linked by Polymers," *Nat. Chem.* **8**, 33 (2016). [CHRNA]
- Zong, Y., Yuan, G., Han, C.C., "Asymmetrical Phase Separation and Gelation in Binary Mixtures of Oppositely Charged Colloids," *J. Chem. Phys.* **145**(1), 014904 (2016). [CHRNA]
- Zou, T., Cao, H.B., Liu, G.Q., Peng, J., Gottschalk, M., Zhu, M., Zhao, Y., Leão, J.B., Tian, W., Mao, Z.Q., Ke, X., "Pressure-Induced Electronic and Magnetic Phase Transitions in a Mott Insulator: Ti-Doped  $\text{Ca}_3\text{Ru}_2\text{O}_7$  Bilayer Ruthenate," *Phys. Rev. B* **94**(4), 041115 (2016).

# Instruments and Contacts

(name, tel. 301-975-xxxx, email)

## High resolution powder diffractometer (BT-1):

- J. K. Stalick, 6223, judith.stalick@nist.gov
- H. Wu, 2387, hui.wu@nist.gov
- Q. Z. Huang, 6164, qing.huang@nist.gov
- C. M. Brown, 5134, craig.brown@nist.gov

## Residual stress diffractometer (BT-8):

- T. Gnaeupel-Herold, 5380, thomas.gnaeupel-herold@nist.gov

## 30-m SANS instrument (NG-7):

- Y. Liu, 6235, yun.liu@nist.gov
- Y. Mao, 5250, yimin.mao@nist.gov
- J. R. Krzywón, 6650, jkrzywón@nist.gov

## 30-m SANS instrument (NG-B 30m) (CHRS):

- B. Hammouda, 3961, hammouda@nist.gov
- P. D. Butler, 2028, paul.butler@nist.gov
- S. Krueger, 6734, susan.krueger@nist.gov
- C. Gagnon, 2020, cedric.gagnon@nist.gov

## 10-m SANS instrument (NG-B) (nSoft):

- R. Jones, 4624, ronald.jones@nist.gov
- K. Weigandt, 8396, kathleen.weigandt@nist.gov

## USANS, Perfect Crystal SANS (BT-5) (CHRS):

- M. Bleuel, 5165, markus.bleuel@nist.gov
- P. D. Butler, 2028, paul.butler@nist.gov

## Polarized Beam Reflectometer/Diffractometer (NG-D):

- B. J. Kirby, 8395, brian.kirby@nist.gov
- J. A. Borchers, 6597, julie.borchers@nist.gov
- C. F. Majkrzak, 5251, cmajkrzak@nist.gov

## MAGIK, Off-Specular Reflectometer (NG-D):

- B. B. Maranville, 6034, brian.maranville@nist.gov
- J. A. Dura, 6251, joseph.dura@nist.gov

## Neutron reflectometer-horizontal sample (NG-7):

- S. K. Satija, 5250, satija@nist.gov

## Double-focusing triple-axis Spectrometer (BT-7):

- Y. Zhao, 2164, yang.zhao@nist.gov
- D. Parshall, 8097, daniel.parshall@nist.gov
- J. W. Lynn, 6246, jeff.lynn@nist.gov

## SPINS, Spin-polarized triple-axis spectrometer (NG-5):

- L. Harriger, 8360, leland.harriger@nist.gov

## Triple-axis spectrometer (BT-4):

- W. Ratcliff, 4316, william.ratcliff@nist.gov

## FANS, Filter-analyzer neutron spectrometer (BT-4):

- T. J. Udovic, 6241, udovic@nist.gov

## DCS, Disk-chopper time-of-flight spectrometer (NG-4):

- N. Butch, 4863, nicholas.butch@nist.gov
- W. Zhou, 8169, wei.zhou@nist.gov
- C. M. Brown, 5134, craig.brown@nist.gov

## HFBS, High-flux backscattering spectrometer (NG-2) (CHRS):

- M. Tyagi, 2046, madhusudan.tyagi@nist.gov

## NSE, Neutron spin echo spectrometer (NG-A) (CHRS):

- A. Faraone, 5254, antonio.faraone@nist.gov
- M. Nagao, 5505, michihiro.nagao@nist.gov

## MACS, Multi-angle crystal spectrometer (BT-9) (CHRS):

- J. A. Rodriguez-Rivera, 6019, jose.rodriguez@nist.gov
- Y. Qiu, 3274, yiming.qiu@nist.gov

## Cold-neutron prompt-gamma neutron activation analysis (NG-D):

- R. L. Paul, 6287, rpaul@nist.gov

## Thermal-neutron prompt-gamma activation analysis (VT-5):

- R. G. Downing, 3782, gregory.downing@nist.gov

## Other activation analysis facilities:

- P. Chu, 2988, pamela.chu@nist.gov

## Cold neutron depth profiling (NG-1):

- R. G. Downing, 3782, gregory.downing@nist.gov

## Thermal Neutron Imaging Station (BT-2):

- D. Jacobson, 6207, david.jacobson@nist.gov
- D. Hussey, 6465, daniel.hussey@nist.gov
- E. Baltic, 4842, eli.baltic@nist.gov
- J. Lamanna, 6809, jacob.lamanna@nist.gov
- M. Arif, 6303, muhammad.arif@nist.gov

## Cold Neutron Imaging Station (NG-6):

- D. Jacobson, 6207, david.jacobson@nist.gov
- D. Hussey, 6465, daniel.hussey@nist.gov
- E. Baltic, 4842, eli.baltic@nist.gov
- J. Lamanna, 6809, jacob.lamanna@nist.gov
- M. Arif, 6303, muhammad.arif@nist.gov

**Neutron interferometer (NG-7):**

- M. Huber, 5641, michael.huber@nist.gov
- D. Pushin, 4792, dmitry.pushin@nist.gov
- M. Arif, 6303, muhammad.arif@nist.gov

**Quantum-based neutron interferometer facility(NG-7):**

- M. Huber, 5641, michael.huber@nist.gov
- D. Pushin, 4792, dmitry.pushin@nist.gov
- M. Arif, 6303, muhammad.arif@nist.gov

**Fundamental neutron physics station (NG-C):**

- J. Nico, 4663, nico@nist.gov
- M. S. Dewey, 4843, maynard.dewey@nist.gov

**Fundamental neutron physics station (NG-6):**

- NG-6M: M. S. Dewey, 4843, mdewey@nist.gov
- NG-6A (MDM): M. Huber, 5641, michael.huber@nist.gov
- NG-6U: H. Mumm, 8355, hans.mumm@nist.gov

**Neutron test station (NG-7):**

- R. Erwin, 6245, ross.erwin@nist.gov
- K. Krycka, 8685, kathryn.krycka@nist.gov

**Theory and modeling:**

- J. E. Curtis, 3959, joseph.curtis@nist.gov
- T. Yildirim, 6228, taner@nist.gov

**Instruments under development:****vSANS instrument:**

- J. G. Barker, 6732, john.barker@nist.gov
- C. J. Glinka, 6242, charles.glinka@nist.gov

**CANDOR, White-beam reflectometer/diffractometer:**

- F. Heinrich, 4507, frank.heinrich@nist.gov
- C. F. Majkrzak, 5251, charles.majkrzak@nist.gov



# NIST Center for Neutron Research Contacts

Copies of annual reports, facility information, user information, and research proposal guidelines are available electronically.

Please visit our website: <http://www.ncnr.nist.gov>

## **For a paper copy of this report:**

Steve Kline  
301-975-6243  
[steven.kline@nist.gov](mailto:steven.kline@nist.gov)

## **For general information on the facility:**

Rob Dimeo  
301-975-6210  
[robert.dimeo@nist.gov](mailto:robert.dimeo@nist.gov)

Dan Neumann  
301-975-5252  
[dan.neumann@nist.gov](mailto:dan.neumann@nist.gov)

## **For information on visiting the facility and/or user access questions:**

Julie Keyser  
301-975-8200  
[julie.keyser@nist.gov](mailto:julie.keyser@nist.gov)

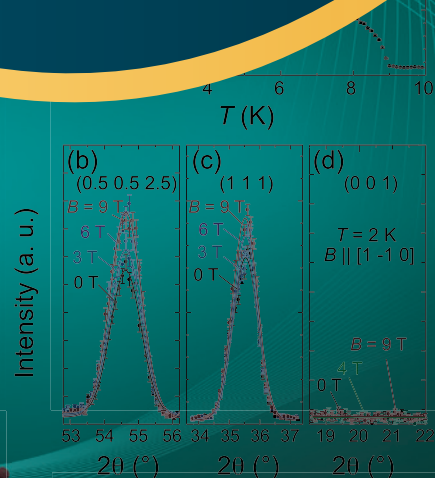
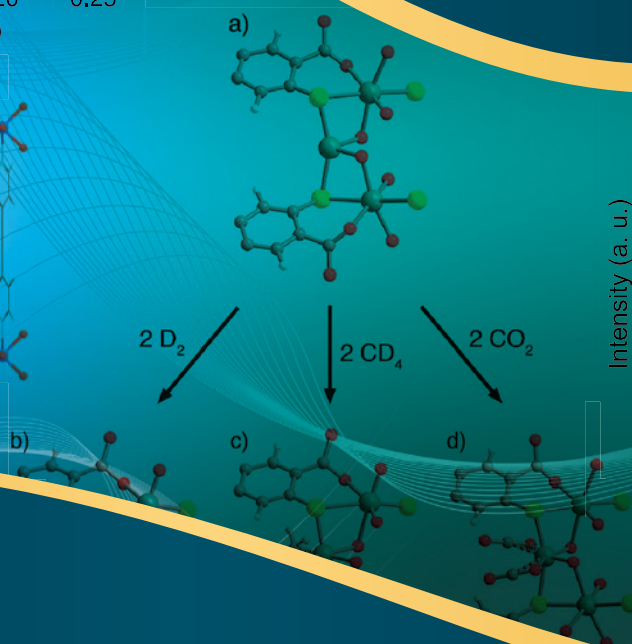
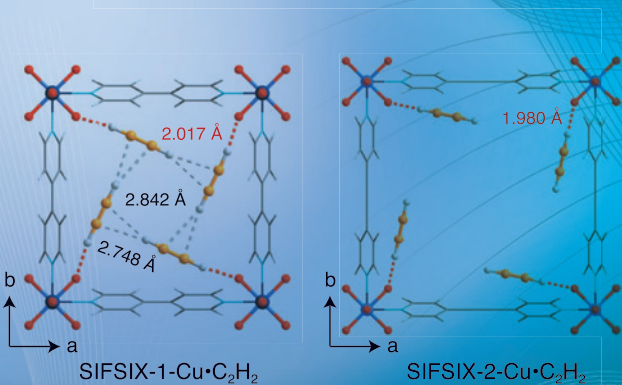
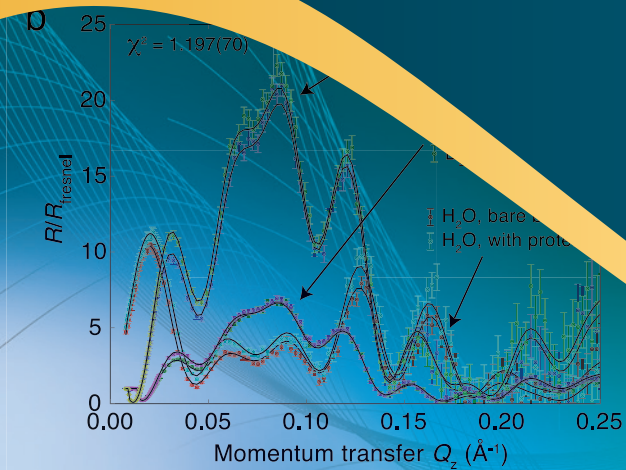
Mary Ann FitzGerald  
301-975-8200  
[maryann.fitzgerald@nist.gov](mailto:maryann.fitzgerald@nist.gov)

## **For information on performing research at the facility:**

Yamali Hernandez  
301-975-5295  
[yamali.hernandez@nist.gov](mailto:yamali.hernandez@nist.gov)

## **Facility address:**

NIST Center for Neutron Research  
National Institute of Standards and Technology  
100 Bureau Drive, Mail Stop 6100  
Gaithersburg, MD 20899-6100 USA



**NIST CENTER FOR NEUTRON RESEARCH**  
 National Institute of Standards and Technology  
 100 Bureau Drive, MS 6100  
 Gaithersburg, MD 20899-6100

[www.ncnr.nist.gov](http://www.ncnr.nist.gov)